AN INVESTIGATION OF DISTORTION-INDUCED FATIGUE CRACKS IN STEEL HIGHWAY BRIDGES: FROM CRACK DETECTION TO FATIGUE RETROFIT

By

Hayder Ibrahim Awad Al-Salih
B.S., University of Babylon, Babil, 2009
M.SC., University of Babylon, Babil, 2012

Submitted to the graduate degree program in Department of Civil, Environmental, and Architectural Engineering and the Graduate Faculty of the University of Kansas in partial fulfillment of the requirements for the degree of Doctor of Philosophy.

Chair: Dr. Caroline Bennett

Dr. William Collins

Dr. Adolfo Matamoros

Dr. Jian Li

Dr. Lin Liu

Date Defended: January 18, 2022

The dissertation committee for Hayder Ibrahim Awad Al-Salih certifies that this is the approved version of the following dissertation:

AN INVESTIGATION OF DISTORTION-INDUCED FATIGUE CRACKS IN STEEL HIGHWAY BRIDGES: FROM CRACK DETECTION TO FATIGUE RETROFIT

_____

Chair: Dr. Caroline Bennett

Date Approved: January 20, 2022

Abstract

Distortion-induced fatigue (DIF) cracking is the primary maintenance and structural safety concern in steel bridges built before the 1980s in the United States, requiring frequent inspections and costly repairs. Human visual inspections to characterize fatigue cracks have many drawbacks, including inconsistencies in identification, significant time and monetary costs, and safety risks posed to the lives of both inspectors and the traveling public due to lane closures. On the other hand, many retrofits aimed at mitigating the effects of DIF and stopping fatigue crack growth have been analyzed both experimentally and computationally; however, most of them require removal of the concrete deck, which disrupts the traveling public.

In this dissertation, a holistic study is presented aimed at advancing the state-of-the-art in advancing detection, characterization, and repair of distortion-induced fatigue in steel bridge structures. A digital image correlation (DIC) based methodology is proposed for detecting and monitoring fatigue cracks in steel bridges. Also, a numerical study of three types of finite element (FE) analysis computational measures (Hot Spot Stress (HSS) analysis, *J*-integrals, and Stress Intensity Factors (K)) was performed to evaluate their predictive capabilities for characterizing DIF cracking propensity. Moreover, an analytical study was conducted to assess the effectiveness of CFRP applied over cracked steel plates, and to determine the influence of various modeling parameters on the analytical solution. Finally, a novel Carbon Fiber Reinforced Polymer (CFRP)-Steel retrofit is proposed to repair complex patterns of DIF cracks in steel bridge web gaps without the need for bolting to the flange or concrete deck removal.

The DIC-based methodology was developed from in-plane compact fracture specimens then evaluated through a half-scale steel girder to cross-frame connection experimental test. The

laboratory test results verified that the proposed DIC methodology could robustly quantify the fatigue crack length. The FE results of the three computational measures (HSS, K, and J) showed good alignment with experimental observations, and they were capable of predicting and characterizing DIF cracking propensity. The FE results of strengthening cracked steel plates with CFRP showed effectiveness in reducing maximum principal stress and stress intensity factor at the crack tips and in reducing crack propagation rate. The experimental results of the novel CFRP-Steel retrofit showed that the retrofit was effective in preventing DIF crack initiation and propagation.

Acknowledgements

I would like to thank and acknowledge all of the following people who helped make this dissertation possible and a remarkable experience for me.

I would like to express my sincere gratitude and special appreciation to my major advisor Dr. Caroline Bennett for her guidance, patience, and motivation throughout my Ph.D. study. This includes not only research guidance but also professional life mentorship. Additionally, I would like to thank Dr. William Collins for his great contribution to my Ph.D. research. I would also like to thank my committee members, Dr. Jian Li, and Dr. Adolfo Matamoros, and Dr. Lin Liu, for their willingness to serve on my supervisory committee and provide me with their wise comments and recommendations.

I would like to acknowledge everyone in the Department of Civil, Environmental, and Architectural Engineering at the University of Kansas, with whom I have had the pleasure of working over my time in the Ph.D. program. I would like to thank Dr. Matt O'Reilly for his help during the first experiment set up and lab technicians Kent Dye, David Woody, and Josh Ostermann for their assistance in the laboratory. I would like to thank Susan Scott, Celeste Yaluk, and the ISS office for always being there to help and support.

I would also like to thank many friends and fellow graduate students who shared, helped, and supported me during my Ph.D. study: Danqing Yu, Zahra Andalib, Mary Juno, Landon Dellenbaugh, James Zhou, Katie McElrath, Kien Nguyen, Eugene Boadi-Danquah, Xiangxiong Kong, Cheng Chen, Hemin Mohammed, Mustafa Raheem, Luay Nazzal, Ali Abdul Baki, Abdalkader Alsabawy, Mustafa Al-Qadi, and many more. My gratitude goes to my dear friend,

Majid M.A. Khadim, for his help and support along the way. Thanks, extended to all my Iraqi friends around the US and in Iraq for their continuous support.

I am grateful for some of the lifelong friendships that have blossomed from my time at the University of Kansas in Lawrence, KS, especially my American families, the Harder family (Cliff Harder and Connie Harder); and the Heinbach family (Marvin Heinbach and Megan Heinbach) for making me welcomed at their homes and helping me understand and integrate in American culture.

Most importantly, I would like to thank my parents, brothers, and all of my family for their unconditional support and encouragement throughout all of my education. I am very thankful to my lovely wife and son for giving me the spirit to follow my dreams.

Finally, I would like to express gratitude to the Ministry of Higher Education and Scientific Research of Iraq (MOHESR) and the Mid-America Transportation Center (MATC) for the funding support.

I am proud to be a Jayhawk, Rock Chalk Jayhawk.

Table of Contents

List of Figures

List of Tables

Chapter 1: **Introduction**

Distortion-induced fatigue (DIF) cracking is a key maintenance and structural safety concern in steel bridges built prior to the mid-1980s in the United States. This type of damage is associated with a prevalent detailing practice at the time which avoided welding connection plates to girder flanges, ironically, to avoid fatigue cracks. The lack of connectivity and out-of-plane motion of the crossframe produce a flexible gap region in the girder web that is susceptible to fatigue cracking. These web gap regions can undergo substantial out-of-plane rotations due to differential deflection between adjacent girders generated by traffic loading. The DIF resulting from these repetitive out-of-plane rotations can cause severe cracking in the web gap detail, requiring frequent inspections and costly repairs.

Manual, hands-on inspections are currently the primary method used by Departments of Transportation and other bridge owners to identify and quantify fatigue cracks. Human visual inspections to characterize fatigue cracks have many drawbacks, including inconsistencies in identification, significant time and monetary costs, and safety risks posed to the lives of both inspectors and the traveling public due to lane closures. To improve the efficacy of fatigue crack inspections, previous research has proposed and examined numerous fatigue crack detection approaches, including both user-implemented technology and structural health monitoring methods. Digital image correlation (DIC) is a vision-based technology that has shown promise for identifying and characterizing fatigue cracks. Three-dimensional DIC measurements can capture full-field displacements and strains, allowing for detection and characterization of both in-plane and DIF cracks, offering the benefits of being low cost, non-contact, and deployable without human presence at the specific region of interest.

Many retrofits aimed at mitigating the effects of DIF and stopping fatigue crack growth have been analyzed both experimentally and computationally. The most common method of repair for DIF is to reduce localized stresses in the web gap region by attaching the connection plate (CP) and the top flange with bolted steel angles. This repair requires removal of the concrete deck to make the bolted connection, which causes disruption to the traveling public. The angles-with-plate retrofit is a more recent attachment technique that avoids interference with the concrete deck so installation can proceed with minimal disruption to traffic. In addition, the increased use of composite materials over the past two decades has sparked interest in strengthening steel structures with externally-bonded carbon fiber reinforced polymers (CFRP), including fatigue applications.

Using finite element (FE) analysis techniques, web-gap cracks may be modeled explicitly, and stress-based analysis techniques such as the Hot Spot Stress method may be used to evaluate retrofit performance. Inclusion of the Extended Finite Element Method (XFEM) in the finite element analysis software program Abaqus has enabled more accurate crack modeling to be conducted as well as fracture mechanics-based analyses such as utilization of the computation of *J*-integrals and Stress Intensity Factors, K. The basis of these techniques is well-established and commonly-used in various applications to characterize in-plane fatigue performance. However, there is little guidance in the literature regarding use of these computational measures for predicting DIF susceptibility. DIF is an inherently mixed-mode problem, and evidence is needed regarding what specific modeling methodologies and output quantities should be utilized with the various computational measures.

1.1 Research Objectives

In this dissertation, a Digital image correlation (DIC) based methodology is proposed for detecting and monitoring fatigue cracks in steel bridges. Also, a numerical study of three types of finite element (FE) analysis computational measures (Hot Spot Stress (HSS) analysis, *J*-integrals, and Stress Intensity Factors (K)) was performed to evaluate their predictive capabilities for characterizing DIF cracking propensity. Moreover, an analytical study was conducted to assess the effectiveness of CFRP applied over cracked steel plates, and to determine the influence of various modeling parameters on the analytical solution. Finally, a novel Carbon Fiber Reinforced Polymer (CFRP)-Steel retrofit is proposed to repair complex patterns of DIF cracks in steel bridge web gaps without the need for bolting to the flange or concrete deck removal.

The second chapter of this dissertation presents a digital image correlation-based methodology developed from in-plane compact fracture specimens for the detection and quantification of fatigue cracks. The effectiveness of the proposed methodology is further evaluated through experimental tests of a fatigue crack on a large-scale steel girder to cross-frame connection, similar to the out-of-plane fatigue cracks commonly found on steel highway bridges. Results indicate that the digital image correlation methodology can adequately characterize fatigue cracks, both in-plane and out-of-plane, in terms of crack length with reasonable error margin. Development of this methodology is intended to lay the groundwork for future research aimed at developing automatable systems capable of crack detection and characterization on in-service structures. This quantification from a non-contact inspection technology has the potential to lead to future automation of steel highway bridge fatigue inspections.

The third chapter of the dissertation describes an experimental study in which a half-scale steel girder-to-crossframe subassembly was subjected to DIF loading to produce multiple geometrically-complex bifurcated cracks. The objective of the study was to evaluate the ability and effectiveness of the previously developed DIC-based crack characterization methodology to quantify geometrically-complex multi-segment out-of-plane DIF cracks. The study included conducting a series of experimental tests on a 2845-mm (112-in.) long girder specimen subjected to out-of-plane fatigue loading to characterize DIF cracks under a wide range of load cases through DIC measurements. Eleven load cases were examined, both above and below what would be produced under design loads, to explore the performance of the DIC under a broad range of load cases. The crack pattern investigated in this study was a complex multi-segment crack pattern consisting of three bifurcated cracks emanating from the same crack initiation point and one web-to-flange crack. The crack length segments varied from 51 mm (2.00 in.) to 138.6 mm (5.45 in.) and occurred in different directions – horizontal, vertical, and inclined. The methodology was successful at characterizing cracks propagating in the girder web but struggled to characterize horizontal cracks. The aim of this research is to further expand the available toolkit of DIF crack detection that are implementable with minimal direct human involvement and minimal disruption to the traveling public.

The fourth chapter describes a numerical FE study of three types of computational measures to evaluate their predictive capabilities for characterizing DIF cracking propensity. The three computational measures studied were a modified Hot Spot Stress (HSS) analysis, *J*-integrals, and Stress Intensity Factors (K). This chapter presents the results from a suite of finite element simulations of girder-cross frame subassemblies, evaluating the three computational techniques (K, J, and HSS) as tools for DIF assessment. Benchmarked to previous experimental evaluations

of the subassembly, the models are also used to numerically evaluate different retrofit thicknesses that were not evaluated experimentally. The FE models included simulation of several crack states using XFEM and a comparison with actual crack growth data from a DIF experimental specimen, both with and without the retrofit applied. The numerical parametric study evaluated the effectiveness of the different retrofit thicknesses in lowering demand at the web gap region. Results indicated that the out-of-plane loading, Mode III, contributes to distortion-induced crack growth more than Modes I and II, and that equivalent Mode I stress intensity, $K_{Ieq(Ks)}$, values computed from a combination of K_I, K_{II}, K_{III}, are equivalent to those obtained from the *J*-integral, $K_{Ieq(J)}$, both correlating well with experimental behavior. Computational HSS values also predict fatigue crack demand and correspond with the findings of the experimental study. Results also showed the optimal component thickness for the angles-with-plate retrofit is 19 mm (0.75in.), which is more economic than the 25.4-mm (1-in.) thick retrofit with similar behavior.

The fifth chapter presents a numerical study of a steel plate with a single edge crack strengthened with Carbon Fiber Reinforced Polymer (CFRP) composites. The goal of the numerical study was to achieve a better understanding of the potential effectiveness of CFRP in reducing stress at the crack tip, as well as reducing crack growth rate. The study included a parametric analysis to explore the effect of different parameters on CFRP strengthening behavior. A continuum shell element was utilized to model the CFRP, a cohesive element used to model the adhesive layer, and the eXtended Finite Element Method (XFEM) was used to model the crack. Damage initiation of the adhesive and in the crack were modeled using traction-separation laws. The mixed-mode failure criterion, the quadratic strain damage initiation criterion, which takes into consideration both Mode I and Mode II failures, was utilized to model damage in the adhesive, whereas the maximum principal stress damage initiation criterion was utilized to model damage

at the steel crack. Damage to CFRP sheets was modeled using the "Damage and Failure for Fiber-Reinforced Composites" material model, which employs Hashin's failure criterion. Results showed that CFRP strengthening can be very effective in reducing maximum principal stress and stress intensity factor at the crack tips and in reducing crack propagation rate. The results showed that CFRP strengthening significantly increased the capacity of cracked steel plates for both isotropic CFRP and lamina CFRP strengthening. The parametric analysis showed that increasing the elastic modulus in the longitudinal direction of the CFRP led to an increase in capacity and reduced crack propagation lengths. Increased adhesive shear stiffness led to an increase in capacity and reduced crack propagation length.

The sixth chapter presents a study evaluating the use of CFRP in conjunction with steel sections to repair complex patterns of DIF cracks in steel bridge web gaps without the need for bolting to the flange or concrete deck removal. A steel girder-to-crossframe subassembly was tested in DIF to evaluate the performance of the retrofit measure. Realistic crack patterns were introduced by applying fatigue loading, and the efficacy of the repair method was evaluated by monitoring crack growth with the repair in place. Twelve test trials were performed: five in the unretrofitted condition to propagate the cracks and seven in the retrofitted condition to evaluate the performance of the repair. The study evaluated multiple crack patterns, different configurations of the retrofit, the presence or absence of mechanical anchorage to the flange, the footprint of the CFRP relative to the steel retrofit elements, and different surfaces connected by the CFRP. The results showed that the combined CFRP-steel retrofit measure was effective in preventing DIF crack initiation and propagation.

1.2 Publications, Contributions, and Novelty

Each chapter within this document contains published or articles in preparation for publishing. Earlier results from the study represented in Chapter 2 were presented at the World Steel Bridge Symposium, St. Louis, MO, April 4, 2019 and at the Structures Congress, American Society of Civil Engineers (ASCE), Orlando, Florida, April 26, 2019. The full results were published in the Journal of Bridge Engineering, volume 25, issue 9, in September 2020; I contributed as co-author in this journal article and was responsible for conducting and analyzing the experiments on the girder specimen. Earlier results from the study presented in Chapter 3 were presented at the 3rd International Conference on Structural Integrity, ICSI 2019, Funchal, Madeira, Portugal, and published in the Procedia Structural Integrity, volume 17, pages 682-689 on August 25, 2019. The full results were published in Fatigue & Fracture of Engineering Materials & Structures (FFEMS) as an invited review article on March 18, 2021. I am the first author of both of these articles. Chapter 4 and Chapter 5 are intended for future publications, and I will be the first author of both of these articles. The study reported in Chapter 4 represents a long-term research effort that earlier KU students have contributed important groundwork to, however, all of the models and analyses in Chapter 4 were independently constructed by my myself. Earlier results of the study presented in Chapter 6 were presented at the Structures Congress, American Society of Civil Engineers (ASCE), Fort Worth, Texas, April 21, 2018. Later results were published in the proceedings of the Structures Congress, American Society of Civil Engineers (ASCE), St. Louis, Missouri, April 5–8, 2020 as a conference paper. The full results represented in Chapter 6 were published in the Journal of Constructional Steel Research, volume 182, pages 106642 on March 27, 2021. I am the first author of both of the proceeding and the journal article.

Despite the fact that many researchers have examined DIF crack detection, evaluation, and retrofitting, the methodology, parameters, and measures discussed in this dissertation represent novel contributions. The work presented here is an original and novel contribution to DIF crack detection, evaluation and retrofitting that adds to the available body of knowledge and literature, and it represents significant and promising advancement in the field of structural engineering.

Chapter 2: **Development of a Distortion-Induced Fatigue Crack Characterization Methodology using Digital Image Correlation**

Landon Dellenbaugh[1], Xiangxiong Kong[2], Hayder Al-Salih[3], William Collins[4], Caroline Bennett[5], Jian Li[6], Elaina J. Sutley[7]

[1] Graduate Research Assistant, Department of Civil, Environmental, and Architectural Engineering, University of Kansas, 2150 Learned Hall, 1530 W. 15th St., Lawrence, KS 66045

[2]Assistant Professor, School of Engineering, University of Guam, English Language Institute, Room 202, UOG Station, Mangilao, GU 96923

[3] Graduate Research Assistant, Department of Civil, Environmental, and Architectural Engineering, University of Kansas, 2150 Learned Hall, 1530 W. 15th St., Lawrence, KS 66045

[4]Assistant Professor, Department of Civil, Environmental, and Architectural Engineering, University of Kansas, 2150 Learned Hall, 1530 W. 15th St., Lawrence, KS 66045 (corresponding author). E-mail: william.collins@ku.edu

[5] Professor, Department of Civil, Environmental, and Architectural Engineering, University of Kansas, 2150 Learned Hall, 1530 W. 15th St., Lawrence, KS 66045

[6] Associate Professor, Department of Civil, Environmental, and Architectural Engineering, University of Kansas, 2150 Learned Hall, 1530 W. 15th St., Lawrence, KS 66045

[7]Assistant Professor, Department of Civil, Environmental, and Architectural Engineering, University of Kansas, 2150 Learned Hall, 1530 W. 15th St., Lawrence, KS 66045

2.1 Abstract

Distortion-induced fatigue cracking is a primary maintenance and structural safety concern in steel bridges built prior to the 1980s in the United States. Manual, hands-on inspections are currently the primary method departments of transportation and other bridge owners use to identify and quantify fatigue cracks. To improve the efficacy of fatigue crack inspections, previous research has proposed and examined numerous fatigue crack detection approaches, including both user-implemented technology and structural health monitoring methods. However, these approaches typically require human presence and active participation at the location of interest, or prolonged

mechanical contact and continuous monitoring of the structure. This limits the effectiveness and flexibility of these approaches for inspecting the large number of fatigue susceptible regions found on steel bridges. Recently, vision-based sensing technologies have been explored for applications related to damage detection and health assessment in civil infrastructure, as they offer the benefits of being low cost, non-contact, and deployable without human presence at the specific region of interest. This paper presents a digital image correlation-based methodology developed from in-plane compact fracture specimens for the detection and quantification of fatigue cracks. The effectiveness of the proposed methodology is further evaluated through experimental tests of a fatigue crack on a large-scale steel girder to cross-frame connection, similar to the out-of-plane fatigue cracks commonly found on steel highway bridges. Results indicate that the digital image correlation methodology can adequately characterize fatigue cracks, both in-plane and out-of-plane, in terms of crack length. This quantification from a non-contact inspection technology has the potential to lead to future automation of steel highway bridge fatigue inspections.

Keywords

Fatigue; cracking; bridge; steel; inspection; digital image correlation

2.2 Introduction

Bridges serve a critical role in maintaining many vital functions of modern society, but due to repetitive loads and long service lives they are prone to damage and deterioration. A recent report issued by the American Society of Civil Engineers assigned U.S. bridges a grade of C+, with over 9 percent of the inventory considered to be structurally deficient (American Society of Civil Engineers 2017). For these structures to perform as needed up to and beyond their intended service lives, it is clear that they must be properly maintained and rehabilitated.

One of the biggest structural concerns for many aging steel bridges in the United States is the initiation and propagation of fatigue cracks (Fisher 1984). Caused by cyclic traffic loading, fatigue cracks are initially very small and often difficult to detect through visual inspection. However, if cracks go undetected and are allowed to propagate to critical size, fatigue cracking can compromise the structural integrity of an entire bridge putting human lives at risk. The majority of these cracks occur in the web-gap region between flanges and transverse stiffeners or connections plates, as shown in Figure 2-1. These distortion-induced fatigue cracks are caused by differential vertical movement between adjacent longitudinal girders under traffic loading. Due to design practices of the era, distortion-induced fatigue cracks are commonly found in steel U.S. bridges built prior to the 1980s (Zhao and Roddis 2004).

Visual inspection is the most common approach used for fatigue crack detection on steel bridges. Inspected on either a 24-month or 48-month cycle (Federal Highway Administration (FHWA) 2004), fatigue damage in steel bridges is intended to be identified and monitored over time, with repairs made prior to cracks reaching critical size. In practice, however, visual inspections for fatigue cracks present a number of challenges. In addition to having a low probability of detection, visual inspections are labor intensive, costly, and dangerous for inspectors and the traveling public(Whitehead 2015; Zhao and Haldar 1996).

Efforts to improve the efficacy of fatigue crack inspections through detection and monitoring have been undertaken in both the structural health monitoring (SHM) and non-destructive testing (NDT) research communities. A variety of sensing technologies have shown promise in detecting and monitoring cracks, both those induced by in-plane and out-of-plane fatigue loading. However, the majority of these approaches rely on sensors that are physically attached to the monitored structure. This reliance on discretized physical attachment limits the

ability to efficiently and cost-effectively monitor a large number of fatigue-susceptible regions on a structure. Vision-based, non-contact sensing technologies overcome these limitations, allowing technologies to be deployed over large areas of a given structure. While numerous vision-based crack detection and characterization methods are described in the literature, the majority of studies have been conducted under idealized conditions examining in-plane fatigue loading or cracks in non-metallic materials (Nowell et al. 2010; Rupil et al. 2011; Vanlanduit et al. 2009). Very few have examined fatigue cracks in steel structures loaded through a realistic distortion-induced mechanism that commonly occurs in geometrically-complex steel bridge connections. The present work helps fill this gap by offering the results and analysis of a vision-based, non-contact fatigue crack evaluation on a steel bridge system under realistic loading conditions.

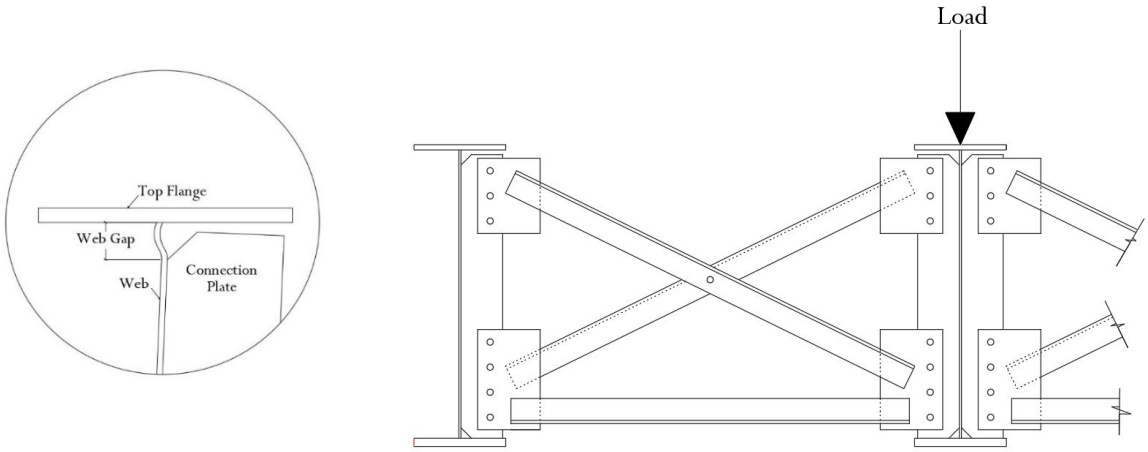

Figure 2-1. Distortion-induced fatigue mechanism

2.3 Digital Image Correlation Background and Application

Digital image correlation (DIC) is a vision-based technology which uses image analysis software to produce full-field surface displacement and strain measurements. DIC requires application of a high contrast random surface pattern and compares a series of images collected

while the patterned surface deforms. The success of a DIC analysis is based on the uniqueness of the surface pattern with non-repetitive, high contrast patterns yielding more accurate results. DIC analysis functions by discretizing the digital images into small groups of neighboring pixels, known as subsets. These subsets each contain a distinct high contrast surface pattern, and the DIC analysis compares the subsets of an undeformed image with a subsequent deformed image, maximizing a similarity function between the different patterns. This process quantifies the deformation occurring within the subset, which allows for displacement and strain characterization of the entire material surface. More in-depth discussions of the digital image correlation processes and calculations can be found in the literature (Schreier et al. 2009). DIC-based measurement approaches have previously been evaluated and applied in the context of civil infrastructure. An overview of relevant work is presented in the following, organized by applications to in-plane measurements, out-of-plane measurements, and fatigue crack characterization.

2.3.1 In-Plane Displacement Measurements

DIC has been used in previous studies to evaluate the in-plane displacement measurement of target surfaces on a variety of civil infrastructure. One of the primary applications of DIC is in measuring deflections of critical bridge members under service loads. (Pan et al. 2016) combined DIC and an inverse compositional algorithm to measure bridge deflections through digital videos. The proposed method was validated through in-service testing of a railway bridge. (Dhanasekar et al. 2019) investigated the serviceability deflections of two historic masonry arch bridges under operating conditions using an advanced DIC system. Similar work was performed by (Busca et al. 2014) and (Alipour et al. 2019). Despite the successful applications of these studies, some challenges to field deployment have been identified, including lighting conditions (Ribeiro et al.

2014) and limitations on the distance between the camera and the material surface (Lee and Shinozuka 2006).

2.3.2 Out-of-Plane Displacement Measurements

When equipped with multiple cameras, DIC can be an effective tool to measure out-of-plane displacements. (Chen et al. 2013) achieved accurate solutions when using a four-camera test setup to measure out-of-plane displacements, albeit sacrificing experimental configuration flexibility and ease of calibration due to test setup complexity. (Helfrick et al. 2011) used a stereoscopic camera setup with a high-speed shutter to measure full-field out-of-plane vibrations, noting significant image resolution tradeoffs with camera speed. In an effort to examine the performance of DIC applied in complex loading scenarios, Sutton et al. (2007) developed clevis fixtures allowing for mixed-mode loading of compact (C(T)) specimens. Displacement results obtained from DIC were found to be in good agreement with those obtained from a 3D finite element model of the region surrounding the crack for Mode I opening and Mode II in-plane shear loading.

2.3.3 Fatigue Crack Detection and Characterization

Extensive research has been performed regarding the applicability of using DIC to detect and identify fatigue cracks in metallic materials under controlled laboratory settings. Previous studies have primarily examined fatigue cracks under in-plane (Mode I) loading conditions, attempting to either identify or characterize crack conditions. Recent studies in which DIC was applied in this in-plane loading context include tests of aluminum channels (Vanlanduit et al. 2009) as well as steel C(T) specimens (Nowell et al. 2010; Rupil et al. 2011), tension plates with center-drilled bolt holes (Hutt and Cawley 2009; Lorenzino et al. 2014), and notched tension specimens

(Carroll et al. 2009; Carroll et al. 2013). DIC methods have also shown promise as an approach to experimentally determine stress intensity factors (Hamam et al. 2007; Zhang and He 2012).

These studies have been foundational in understanding the capabilities and limitations of DIC with respect to crack detection, resulting in qualitative identification and characterization of cracks. However, automated methodologies are still urgently needed to quantitatively evaluate cracks in in-service bridges. Furthermore, the effectiveness of DIC for detecting and quantifying cracking under out-of-plane fatigue loading conditions resulting in mixed-mode cracking has not been thoroughly researched. Researchers have postulated that this lack of experimental evaluation is potentially due to the inherent complexity required for the out-of-plane test setups (Sutton et al. 2007).

2.4 Objective and Scope

The objective of this study was to investigate the effectiveness and limitations of DIC when applied to the problem of distortion-induced fatigue cracks in steel bridges, progressing towards development of a crack detection methodology robust enough to assist with and eventually serve as a potential replacement to human-based visual inspections. A quantifiable approach to out-of-plane fatigue characterization using DIC is required before this overarching long-term goal can be realized. This study presents a methodology that can be applied to detect fatigue cracks and quantify crack lengths under in-plane and distortion-induced fatigue loading. The methodology described here was first developed using in-plane fatigue specimens and was then evaluated using a bridge component specimen tested under realistic out-of-plane fatigue loading. Development of this methodology is intended to lay the groundwork for future research aimed at developing automatable systems capable of crack detection and characterization on in-service structures.

2.5 Overall Experimental Approach

The methodology presented in this study was (1) developed through tests performed using DIC applied to in-plane C(T) specimens, and (2) validated through tests performed using DIC applied to a bridge component specimen subjected to distortion-induced fatigue. In the in-plane loading development stage, C(T) specimens were cyclically loaded to initiate and propagate Mode I fatigue cracks, where crack propagation was paused at discrete intervals of experimentally-known crack lengths and documented using DIC. DIC data was collected and evaluated for multiple load ranges at each increment of crack length. Vision-based algorithms were then applied and data analysis procedures developed to identify the crack path and the crack tip location, allowing for the calculation of crack length from DIC data.

Next, a half-scale bridge girder-to-cross-frame connection specimen was used to evaluate the methodology's effectiveness for detection of distortion-induced fatigue cracking. The cross-frame connection simulated both the geometry and out-of-plane loading conditions commonly found on steel bridges. The girder specimen was cycled under out-of-plane loading until fatigue cracking initiated in the web-gap region. The developed methodology was then applied to the girder specimen to detect and characterize the fatigue crack on this geometrically-complex test setup. The following sections present the methodology development, corresponding testing conditions, and validation.

2.6 In-Plane Fatigue Crack

2.6.1 In-Plane Test Specimen Description

The initial testing was performed on steel C(T) specimens loaded in a uniaxial servo-controlled closed-loop hydraulic load frame. These tests were performed to develop the crack

length quantification methodology in an idealized test environment with a simple specimen geometry for later application to the complex out-of-plane geometry. The C(T) specimen was 6.4-mm (0.25-in.) thick with a width of 127 mm (5.0 in.), allowing for the possibility of long cracks. In typical fatigue and fracture mechanics testing crack length is defined from the load line, which for a C(T) specimen is at the centerline of the loading pins, to the crack tip. However, this length includes a portion of the machined notch, a geometric feature that does not exist on bridge components. In the context of using DIC to identify and characterize a fatigue crack, a different convention is more applicable. In this study, all crack lengths on C(T) specimens were measured from the tip of the notch where fatigue crack initiation occurred, as shown in Figure 2-2.

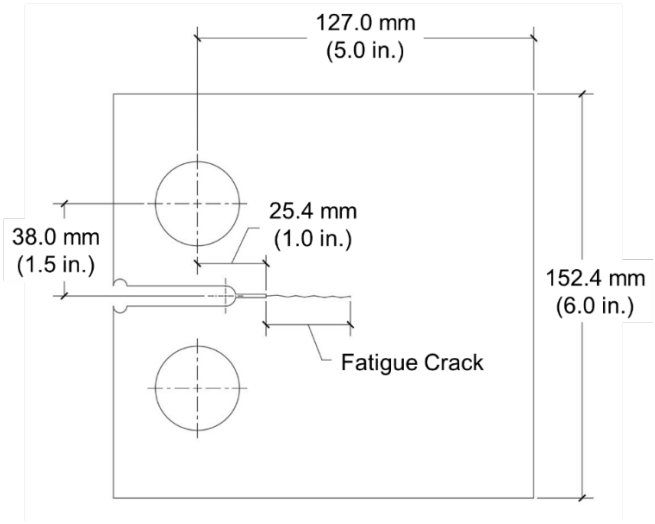

Figure 2-2. C(T) specimen dimensions

2.6.2 In-Plane Loading Protocol

Truck loading on highway bridges is highly variable, so a fatigue crack inspection methodology needs to function over a range of load magnitudes. To evaluate the effectiveness of DIC in identifying and characterizing fatigue cracks, a loading protocol was developed to examine

a range of realistic load scenarios. Crack propagation was conducted at low levels of stress intensity to avoid the influence of excessive crack tip plasticity, and to represent realistic cracks in steel bridge infrastructure. Five load cases, designated C(T)-LC1 through C(T)-LC5, were defined by applied stress intensity ranges (ΔK_I) of 11, 22, 33, 44, and 55 MPa√m (10, 20, 30, 40, and 50 ksi√in), as shown in Table 2-1. Each load case used an *R*-ratio, the ratio of minimum to maximum load, of 0.1. All load cases were examined at each of four crack lengths ranging from 12.7 to 50.8 mm (0.5 to 2.0 in.), in 12.7-mm (0.5-in.) long increments. All stress intensity-based load calculations and corresponding crack length measurements were computed based on compliance equations validated and accepted for the given specimen geometry (ASTM International 2018). For each crack length, crack tip plasticity was limited during testing by first applying the smallest loading range, C(T)-LC1, and successively increasing to the greatest, C(T)-LC5. Once testing was concluded for each crack length, crack growth was reinitiated at a low stress intensity range and the crack was propagated to the next desired increment of crack length, ensuring crack extension beyond any previously-induced plastic zone.

Table 2-1. Convergence of in-plane specimens for multiple crack lengths

Load Case	Stress Intensity Factor Range, ΔKI MPa√m (ksi√in)	Crack Length mm (in.)			
		12.7 (0.5)	25.4 (1.0)	38.1 (1.5)	50.8 (2.0)
C(T)-LC1	11 (10)	90.9%	98.3%	98.9%	99.3%
C(T)-LC2	22 (20)	67.6%	94.7%	99.6%	99.3%
C(T)-LC3	33 (30)	86.7%	92.9%	89.9%	99.7%
C(T)-LC4	44 (40)	68.5%	85.8%	94.8%	97.7%
C(T)-LC5	55 (50)	61.5%	91.2%	91.4%	95.0%

2.6.3 In-Plane DIC Configuration

The DIC analyses performed on C(T) specimens tested under in-plane loading were conducted using a single camera setup, consistent with the 2D testing approach, as shown in Figure 2-3. The PGR Grasshopper3 camera used a Sony IMX250 complementary metal oxide semiconductor (CMOS) sensor and was equipped with a 17 mm (0.67 in.) lens and was mounted on an adjustable tripod. Details regarding the cameras, lenses, and lighting sources are presented in Table 2-2. External adjustable LED lighting panels were used to eliminate shadows induced by ambient laboratory lighting as well as to provide the necessary contrast for data analysis. A high contrast random pattern was applied to the specimen by coating the surface with white paint and then applying black spray paint in a random, speckle pattern. Black speckle sizes ranged from approximately 0.5 to 2.5 mm^2 (0.0007 to 0.04 $in.^2$), and covered approximately one third of the specimen surface. System calibration was performed prior to testing with a calibration plate provided by the system manufacturer, Correlated Solutions (Correlated Solutions Inc. 2016). Prior to each test, the setup conditions and resulting noise level were examined through an uncertainty estimate, and system resolution was typically on the order of 0.0002 mm (0.000008 in.) or better. Analysis of the collected images utilized Correlated Solutions' VIC-2D software with a subset size of 29 pixels and a step size of 7 pixels. These values are the default settings automatically calculated within the software. The combination of a 29 pixel subset and 7 pixel step size allowed for the maintaining of spatial resolution while optimizing processing time. As these analysis settings produced a resolution level that was multiple orders of magnitude smaller than the crack sizes being examined, they were considered appropriate for the current study. Post-processing performed within the DIC analysis software was limited to coordinate transformation, aligning the y-axis to the direction of the load line and the x-axis to the crack path, as denoted in Figure 2-4.

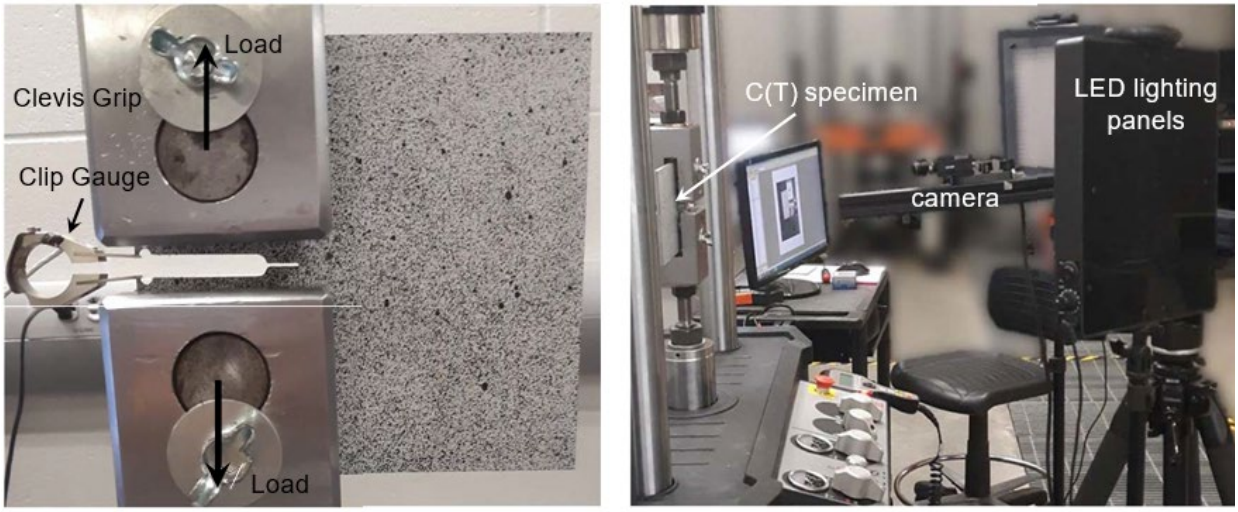

(a) (b)

Figure 2-3 a) C(T) specimen with high-contrast surface pattern and b) DIC hardware placement

Table 2-2. Camera, lens, and lighting details

Equipment	Description	Specification
Camera	Model	PGR Grasshopper3
	Sensor	Sony IMX250 CMOS
	Resolution (megapixels)	5
	Resolution (horizontal x vertical) (pixels)	2,448 x 2,048
	Frame Rate (frame/s)	75
Lens	Model	Schneider Xenoplan
	Focal Length (mm)	17
	Iris range/ aperture	f1.4
Light	Model	Light Emitting Diode (LED) 500k Bescor lighting system

2.6.4 Development of Crack Characterization Methodology

Methods of interpreting DIC data, typically examined in terms of displacement or calculated strain, vary between researchers, but generally still require some operator visual

identification. While the crack location was readily visually identifiable from either strain or displacement data in this case, as observable in Figure 2-4, automation of an inspection tool requires utilization of algorithms independent of operator interaction.

Although DIC results for strain produced images where the crack could be visualized, allowing for a qualitative understanding of behavior around fatigue cracks, exact geometric localization of the crack from this data proved difficult due to erroneously large strain values calculated at the free edges of the crack surfaces as the crack opened. As DIC algorithms calculate surface displacements over an entire subset of pixels, the extremely large strains calculated for crack faces spread beyond the exact location of the crack surfaces, making localization difficult. Displacement data do not have this issue, and are thus more suitable for crack localization. As illustrated in the following sections, an edge detection algorithm can identify the general crack path with high accuracy using the displacement image, offering a great advantage in future automation of this methodology, while achieving the same result with the strain image would be challenging. For this reason, displacement-based DIC data were used in the present study. The

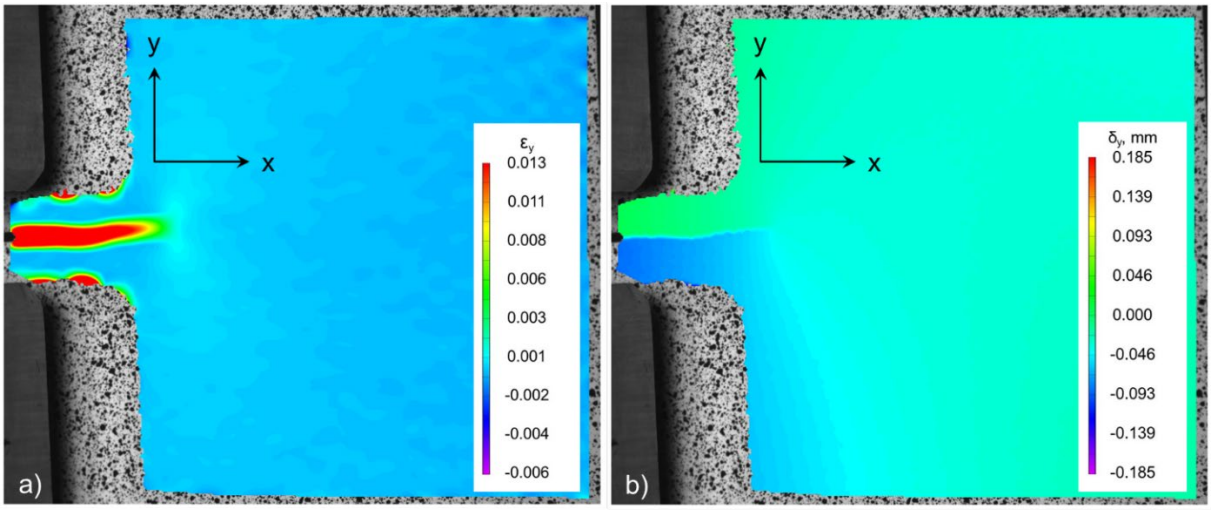

Figure 2-4. Typical visualized DIC results of in-plane specimen in terms of y-direction a) strain and b) displacement

methodology used to determine crack length from DIC data is schematically illustrated in Figure 2-5.

To initially identify the crack path, a matrix of y-axis displacement contours corresponding to the direction of crack opening was imported into MATLAB (MathWorks, Natick, Massachusetts) from the DIC analysis software. A basic Sobel edge detection algorithm (Parker 2010) was applied to the contour data within MATLAB, and outputs provided a localization of the crack path along specific x-y coordinates, represented schematically as the bi-linear line in Figure 2-5a, and linearly extending beyond the crack path termination defined by edge detection. This edge detection process, rather than manual visual identification, was used for crack path localization to allow for future automation of the methodology. Although the process did involve manual manipulation in the current study, it is anticipated that more refinement of the edge detection process will allow for fully-automated fatigue crack characterization of DIC data without manual intervention. Once the initial crack path was identified through the edge detection process, data export paths orthogonal to the crack path were defined at discrete intervals along the crack path, shown as dashed lines in Figure 2-5 a. Displacement values resulting from the DIC analyses were examined along each orthogonal path to determine the relative displacement occurring across the crack. Relative displacement for each orthogonal path was defined as the difference between plateau values on either side of the crack, shown in Figure 2-5b. Relative displacement extracted from the orthogonal paths was then plotted along the length of the crack path, creating figures similar to that in Figure 2-5c.

Each value of relative displacement along the crack path, Δ_i, was divided by the maximum relative displacement along the crack path, Δ_{max}, which typically occurs at the crack initiation site. This ratio was then subtracted from 100%, as presented in Equation 2-1, resulting in the

convergence of relative displacement along the crack path, shown in Figure 2-5d. Convergence of relative displacement should theoretically approach 100% at the crack tip.

$$\text{Convergence} = 100\% - \frac{\Delta_i}{\Delta_{max}} \tag{2-1}$$

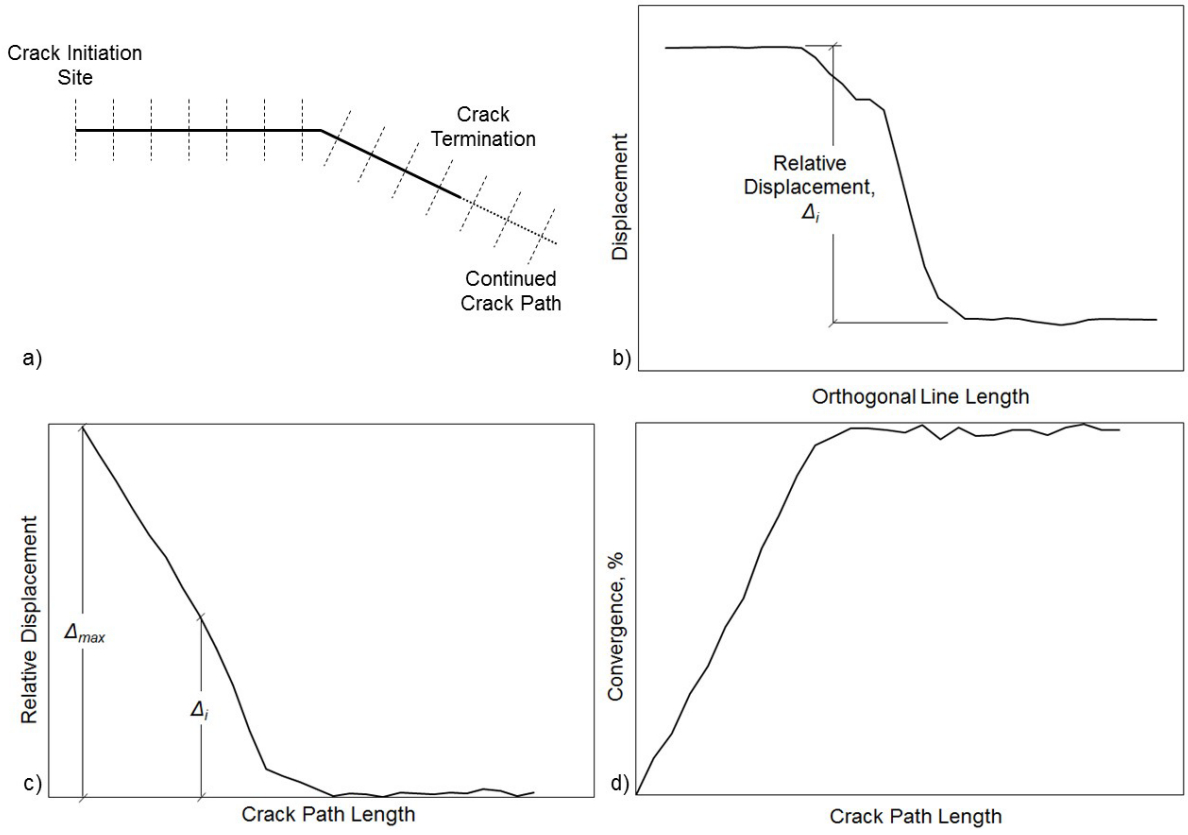

Figure 2-5. a) Crack path and data export lines, b) Displacement values along a data export line, c) Relative displacement along crack path, and d) Convergence along crack path

2.6.5 Discussion and Results for In-Plane Testing

The described crack characterization methodology was applied for each load case within each crack length increment. Typical relative displacement and convergence plots for the specimen with a 25.4-mm (1.0-in.) long crack are shown in Figure 2-6 and Figure 2-7. The dotted vertical line indicates the crack length as measured through specimen compliance and verified optically.

Convergence values at known crack lengths were evaluated for each load case and are presented in Table 2-1 for the in-plane specimen trials.

At crack lengths of 25.4, 38.1, and 50.8 mm (1.0, 1.5, and 2.0 in.), the majority of load cases resulted in convergence values over 90%, with many over 95%. Data for the 12.7-mm (0.5-in.) crack length did not converge as well, likely due to proximity to the machined notch and the resulting localized displacement behavior. As load range increased, calculated convergence values at the known crack length generally decreased, indicating that some relative displacement continued beyond the visibly-observable crack tip. It is well known that plasticity can influence behavior, with specimens exhibiting behavior corresponding to crack lengths longer than the physical crack size (Irwin 1960). Plasticity corrections are often used in linear-elastic fracture analyses (Anderson 1995), and iterative approximations commonly use a crack length increased by half of the plastic zone size (Collins et al. 2016). Therefore, the reduction in calculated convergence at higher values of stress intensity are likely to have been caused by crack tip plasticity. However, an investigation into the full quantification of any plasticity influence is beyond the scope of this paper.

2.7 Distortion-Induced Fatigue Crack

2.7.1 Out-of-Plane Test Specimen Description

The DIC inspection process and crack characterization methodology developed on the in-plane C(T) specimens was subsequently applied to a distortion-induced fatigue test setup for validation. An I-shaped plate girder subassembly was used as the test specimen, schematically presented in Figure 2-8a. Fabricated from A36 steel (ASTM International 2019), the half-scale girder was 2845-mm (112-in.) long, 917-mm (36.1-in.) deep, and had a web thickness of 10 mm (0.375 in.).

Attachments between cross-section elements were made with 5-mm (0.1875-in.) fillet welds. The girder subassembly was tested upside-down, such that the length of the bottom flange was connected rigidly to the laboratory floor, simulating the lateral stiffness provided by a concrete deck.

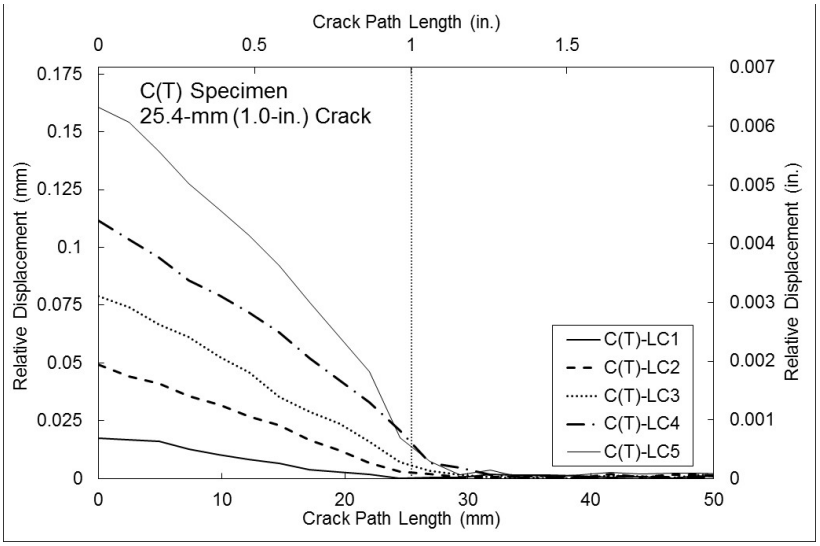

Figure 2-6. Relative displacement along crack path for an in-plane specimen with a 25.4-mm (1.0-in.) long crack

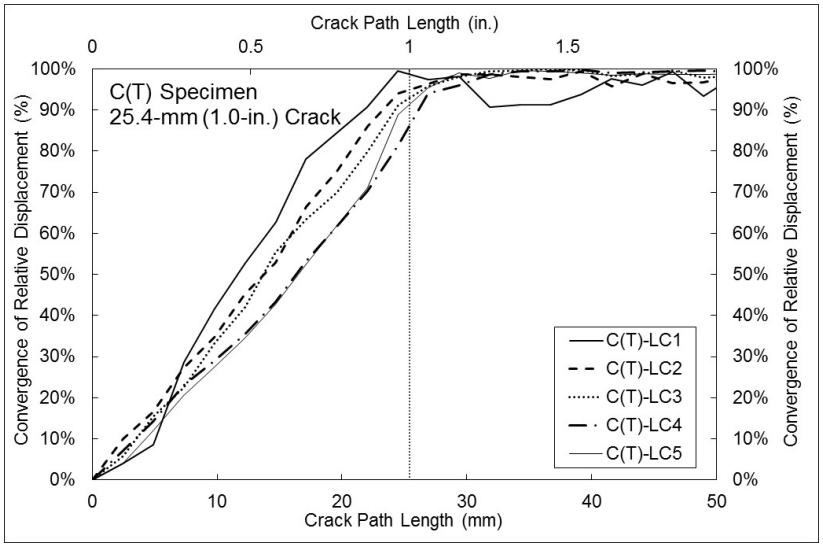

Figure 2-7. Convergence of relative displacement for an in-plane specimen with a 25.4-mm (1.0-in.) long crack

A cross-frame was installed at mid-span of the girder, attached through a connection plate welded only to the girder web. The girder was loaded out-of-plane by applying a vertical load at the far end of the cross-frame, the direction of which is indicated in Figure 2-8a, producing a distortion-induced fatigue mechanism in the web-gap region between the flange and connection plate. Additional details characterizing the general distortion-induced fatigue test configuration can be found in Alemdar et al. (2014a).

Prior to collection of DIC measurements, the girder was loaded for 21,000 cycles at a load range of 2.2 kN to 25.5 kN (0.5 kip to 5.75 kip), resulting in the initiation and propagation of a fatigue crack in the web-gap region. The location of the crack is represented schematically in Figure 2-8b. As the location of the crack was known, the use of fluorescent dye penetrant allowed for a visual measurement of the fatigue crack located between the connection plate weld and the girder web. The total length of the observed distortion-induced fatigue crack was 44.5 mm (1.75 in.) and it consisted of three segments. Dimensions of each crack segment, reasonably idealized as linear and designated with letters in Figure 2-8b, were A = 9.7 mm (0.38 in.), B = 14.2 mm (0.56 in.), and C = 20.6 mm (0.81 in.).

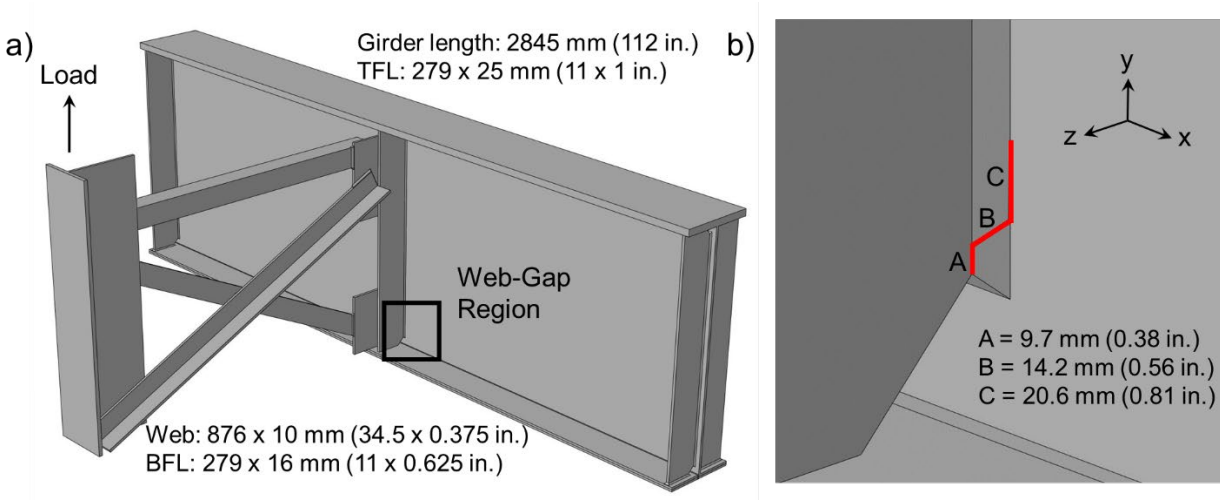

Figure 2-8. a) Out-of-plane girder subassembly and b) Crack location and geometry

2.7.2 Out-of-Plane Loading Protocol

Similar to the in-plane C(T) specimen tests, it was necessary to develop loading protocols representative of real steel bridge applications for the distortion-induced fatigue setup. Determination of appropriate load levels for the distortion-induced fatigue test was accomplished through the use of a finite element bridge model that was based on the full-scale proportions of the test setup. The modeled structure was a two-span continuous, non-skewed steel plate girder bridge with four girder lines and a concrete deck. Linear-elastic material models were used for both the steel and deck elements, and the model contained approximately 4 million elements with 27 million degrees of freedom. Analytical models were based on those developed and validated as part of a previous study, additional details of which can be found in (Hassel et al. 2013). A load representative of the AASHTO fatigue truck (American Association Of State Highway Transportation Officials 2014) was applied in the finite element model, so that realistic levels of differential vertical deflections between adjacent girders could be examined. From the finite element model, a representative value of differential girder deflection in the full-scale bridge system was found to be 2.5 mm (0.1 in.). Scaling down for the half-scale specimen resulted in a realistic target deflection of 1.3 mm (0.05 in.), which corresponded to an applied actuator load of 6.6 kN (1.5 kips) in the physical test setup. Seven load cases, DIF-LC1 through DIF-LC7, were then defined, applying load both above and below this value, as presented in Table 2-3 and schematically represented in Figure 2-9. The minimum applied load for all cases was 0.89 kN (0.2 kips), simulating the presence of dead load.

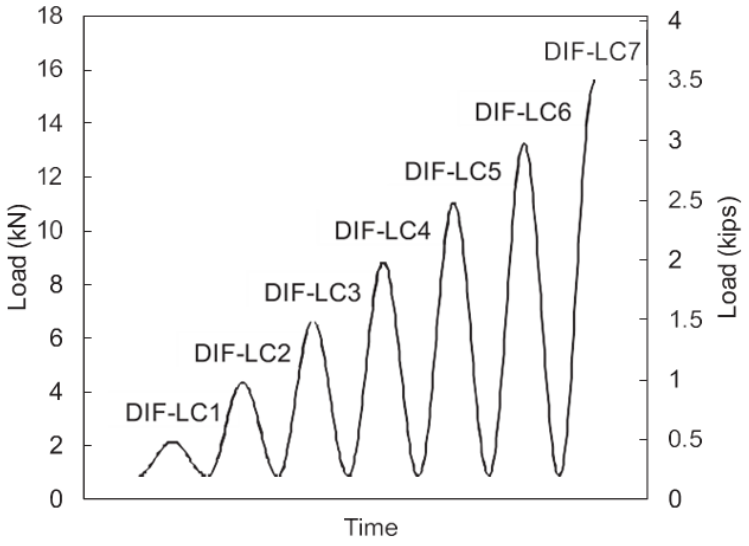

Figure 2-9. Schematic distortion-induced fatigue loading protocol

2.7.3 Out-of-Plane DIC Configuration

The configuration of the DIC setup for the distortion-induced fatigue tests was very similar to that used on the in-plane C(T) specimens, with a major difference being the use of a two-camera stereo setup. The distortion-induced fatigue specimen is shown in Figure 2-10 a, with application of the high contrast surface pattern shown in Figure 2-10 b. The web-gap region of the distortion-induced fatigue specimen was painted with a white background to allow for the application of a random, high contrast pattern. Spray paint was used to apply the black speckle pattern over the white background, with sizes ranging from 0.5 to 8.4 mm^2 (0.0007 to 0.013 $in.^2$), with the black pattern covering approximately one-third of the white-painted area. Manufacturer-provided calibration plates were used to calibrate the DIC system prior to the start of testing. The DIC hardware setup is shown in Figure 2-10c and Figure 2-10d, with the two cameras attached to vertical mounting bars connected to the tripod. The two cameras were separated by approximately 200 mm (8 in.) at a stereo angle of 31 degrees. As two cameras were used for the out-of-plane

tests, VIC-3D was used to analyze the data. Processing subset and step size were the same as that used for the in-plane analyses, resulting in system resolution of 0.0003 mm (0.00001 in.) or better. Although this represents a slight decrease in resolution compared with the in-plane analyses, it was considered sufficient within the context of the cracks being examined. Post-processing of the DIC data for coordinate transformation resulted in the x-axis located along the web-to-flange weld, the y-axis located along the stiffener-to-web weld, and the z-axis aligned with the direction of the cross-frame, as indicated in Figure 2-8b.

Figure 2-10. a) Distortion-induced fatigue test frame, b) Applied high-contrast surface pattern, c) DIC hardware placement, and d) Detailed orientation of DIC hardware seen from above

2.7.4 Application of Crack Characterization Methodology

The methodology initially developed for the case in which DIC was applied to the in-plane specimens was applied here to all load cases for the distortion-induced fatigue specimen. Z-axis displacement contour measurements were imported into the edge-detecting crack path algorithm. Although geometrically more complex than the crack on the C(T) specimen, the crack path obtained from the edge detection algorithm agreed with results from visual inspection. Typical visualized results obtained by DIC for the distortion-induced fatigue specimen are presented in Figure 2-11 in terms of maximum principal strain and displacement corresponding to the z-axis. Note that the horizontal discontinuities observable in Figure 2-11 are strain gage wires attached to the girder web during testing. Similar to the in-plane test results, strain-based DIC results allowed for a qualitative understanding of crack behavior, but were found to be of limited usefulness in the context of crack localization. Therefore, displacement data were used in the developed methodology. Relative displacements orthogonal to each segment of the crack tip were computed, extending beyond the crack tip perceived by the edge detection algorithm, and convergence values were calculated.

2.7.5 Discussion and Results of Distortion-Induced Fatigue Testing

Relative displacement along the crack path for each load case is shown in Figure 2-12, and convergence values for load cases DIF-LC2 through DIF-LC7 are presented in Figure 2-13. Relative displacements measured during DIF-LC1 were observed to be very small along the entire crack path length, resulting in high variability in convergence. This finding indicated that the methodology is not effective at this low load level, and established a threshold of applicability. Convergence values for DIF-LC1 are not presented in Figure 2-13.

Table 2-3. Distortion-induced fatigue crack length characterization

Load Case	Load Range kN (kips)	90% Convergence		95% Convergence	
		Computed Crack Length, mm (in.)	Error, %	Computed Crack Length, mm (in.)	Error, %
DIF-LC1	0.89-2.2 (0.2-0.5)	N/A	N/A	N/A	N/A
DIF-LC2	0.89-4.4 (0.2-1.0)	41.2 (1.62)	-7	46.1 (1.81)	4
DIF-LC3	0.89-6.7 (0.2-1.5)	39.7 (1.56)	-11	43.4 (1.71)	-2
DIF-LC4	0.89-8.9 (0.2-2.0)	44.4 (1.75)	0	50.6 (1.99)	14
DIF-LC5	0.89-11.1 (0.2-2.5)	36.7 (1.44)	-18	42.8 (1.69)	-4
DIF-LC6	0.89-13.3 (0.2-3.0)	38.9 (1.53)	-13	41.2 (1.62)	-7
DIF-LC7	0.89-15.6 (0.2-3.5)	42.8 (1.69)	-4	46.1 (1.81)	4
Average		40.6 (1.59)	-9	45.0 (1.77)	1

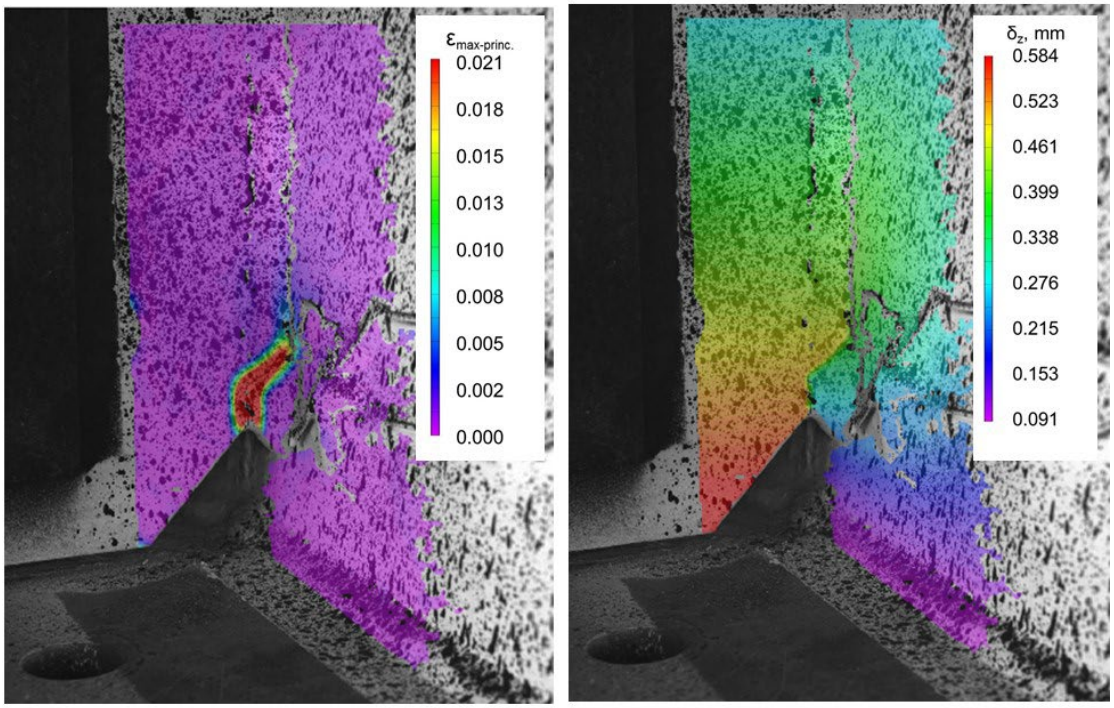

(a) (b)

Figure 2-11. Typical visualized DIC results of distortion-induced fatigue specimen in terms of a) maximum principal strain and b) z-direction displacement

Based on results from tests of the in-plane C(T) specimen, convergence thresholds of 90% and 95% were examined for the distortion-induced fatigue specimen. Table 2-3 presents results for these cases of 90% and 95% convergence compared with the optically-measured crack length of 44.5 mm (1.75 in.). Generally, using the 90% convergence threshold under-predicted crack length while using 95% convergence over-predicted crack length. The average crack length value corresponding to 90% convergence was 40.6 mm (1.59 in.), a 9% under-prediction. Evaluation of 95% convergence resulted in an average crack length of 45.0 mm (1.77 in.), only 1% greater than the optically-measured length. Although calculated convergence at known crack lengths in the C(T) specimens generally decreased, this was not the case for the distortion-induced fatigue specimen. This is seen in Table 2-3, where there is no clear trend in computed crack length error for the different load cases. Plastic zone size and shape are dependent on loading mode, and the mixed-mode loading of distortion-induced fatigue did not result in the same behavior as that observed for the in-plane C(T) specimens.

2.8 Comparison of In-plane and Distortion-Induced Results

To facilitate a comparison between results from the DIC crack detection methodology applied to in-plane C(T) specimen and those from the out-of-plane fatigue specimen, applied stress intensity values were calculated for the distortion-induced load cases.

Finite element analyses (Alemdar et al. 2014b) were used to determine Modes I, II, and III stress intensities at the crack tip for each load case, and an equivalent applied Mode I stress intensity was calculated. Modeling and data extraction techniques were validated based on known closed-form solutions of stress intensity for traditional fracture mechanics specimens (ASTM International 2018). Applied stress intensity ranges for in-plane testing varied from 11 to 55 MPa$\sqrt{m}$ (10 to 50

ksi√in) and values for distortion-induced fatigue testing were found to be between 10.1 and 40.5 MPa√m (9.2 and 36.9 ksi√in), providing adequate overlap to make a meaningful comparison.

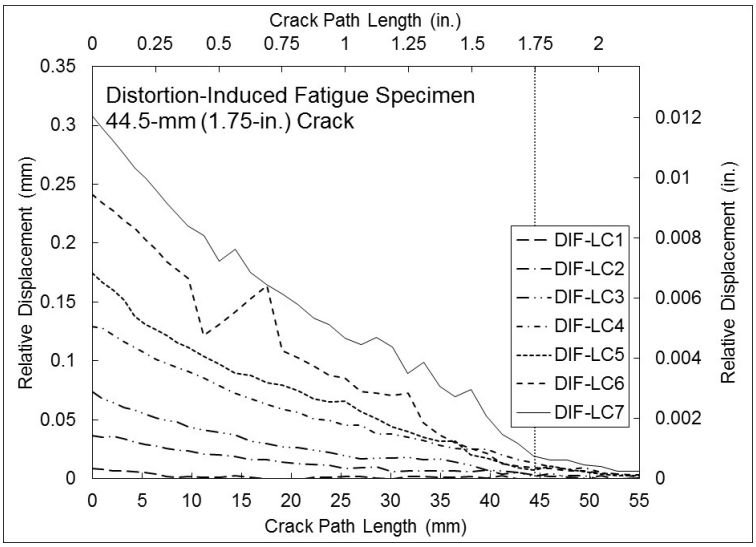

Figure 2-12. Relative displacement along crack path length for distortion-induced fatigue specimen

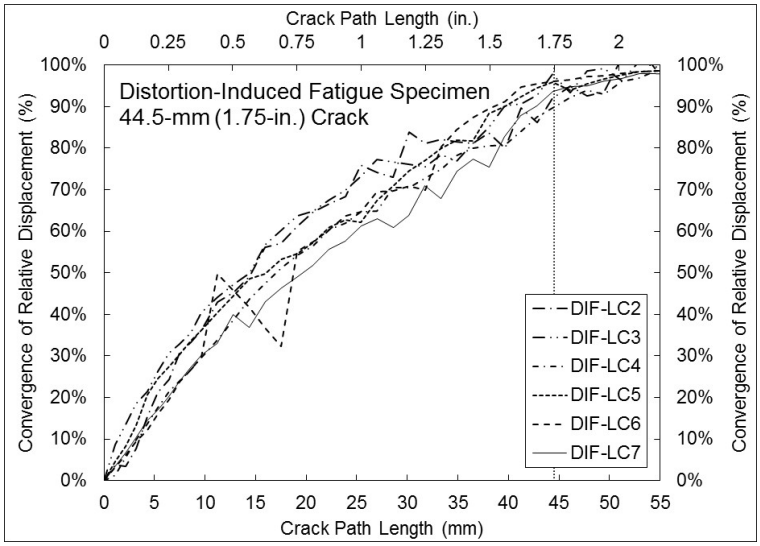

Figure 2-13. Convergence of relative displacement for distortion-induced fatigue specimen

Computed crack lengths were divided by the known crack lengths and plotted against applied stress intensity. This was done for each of the four in-plane crack lengths and for the distortion-induced fatigue crack. Evaluations of predicted crack length are presented for values of 90% and

95% convergence in Figure 2-14. Results of in-plane C(T) specimens are represented by the open symbols, while the distortion-induced fatigue results are represented by the filled symbols. All data points are connected with dashed lines to enhance clarity, and a solid horizontal line at 100% indicates an exact crack prediction. Data falling below the horizontal line signifies a prediction short of the physical crack length, while data above the line indicates a predicted crack length longer than the actual crack size.

Crack length predictions at both 90% and 95% convergence for the in-plane C(T) specimen with a 12.7-mm (0.5-in.) crack resulted in crack lengths longer than the physical crack size. For the majority of the in-plane specimens, however, 90% convergence resulted in crack lengths shorter than the physical crack size. The distortion-induced fatigue results were consistent with this behavior, with all predicted crack lengths shorter than the physical crack size. Predicted crack results at 95% convergence did not exhibit a consistent trend. Disregarding the 12.7-mm (0.5-in.) specimen, half of the in-plane results over-predicted crack length at 95% convergence, while the other half under-predicted crack length. Similar behavior was observed in the results of the out-of-plane distortion-induced fatigue specimen, with half of the load cases over-predicting and half under-predicting. In general, application of the crack characterization methodology to a distortion-induced fatigue specimen resulted in results similar to those for the case in which the methodology was applied to the in-plane specimens, indicating that the method developed is robust enough to be applied meaningfully to realistic fatigue applications.

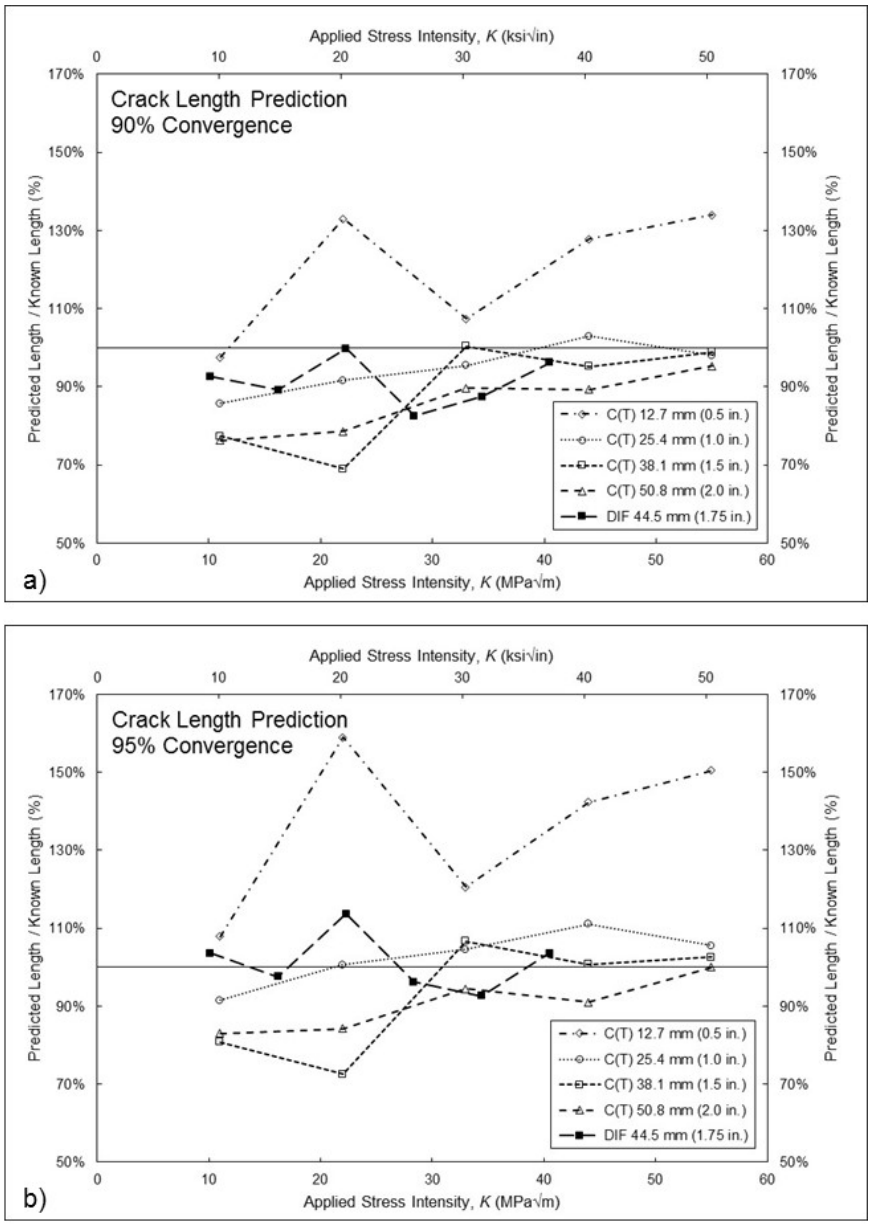

Figure 2-14. Crack length prediction at a) 90% and b) 95% convergence

2.9 Conclusions and Future Work

This study presented the development of a methodology for using digital image correlation data as a crack detection and characterization tool. The methodology was initially developed in the context of in-plane fatigue testing C(T) specimens, and was then applied to a distortion-induced

fatigue test specimen. Edge detection algorithms were applied to DIC displacement data contours to determine the crack path, and relative displacements orthogonal to the crack path were used to calculate a value of convergence, used to identify the crack tip. A theoretical convergence value of 100% should indicate the crack tip, where no relative displacement is occurring orthogonal to the crack path. However, results of in-plane testing indicated convergence between 90% and 95% corresponding to the actual crack length. Both the 90% and 95% convergence thresholds were investigated for the distortion-induced fatigue crack. For the load cases examined, 90% convergence resulted in a -9% error in crack length prediction, while 95% convergence produced an average crack length prediction only 1% beyond the known crack length. The threshold of applicability with respect to load was identified on the distortion-induced fatigue specimen, as the lowest load case examined was unable to produce adequate results. However, this threshold was found to be below fatigue loads expected on steel highway bridges, indicating the developed methodology has the potential for future bridge inspection application in the field.

Refinements to the methodology, continued examination of the impact of in-service conditions, and further development of fully automated algorithms and protocols are necessary prior to implementation of this methodology as a fatigue crack inspection tool. Further work in determining limits of the developed methodology should be undertaken, including the physical limits of DIC to produce data that can be analyzed. This should include variations in surface condition, lighting, and camera focus. As used in this study, DIC requires a precise setup and operator interaction to provide the resolution presented. Further work is needed to develop a deployment mechanism capable of collecting DIC data with limited physical interaction, allowing for a potentially non-contact, automated inspection process. Additionally, the ability of 2D DIC utilizing a single camera setup to collect data on distortion-induced fatigue cracks should be

examined. Investigating additional crack lengths and complex crack geometries, such as bifurcated distortion-induced fatigue cracks, would provide further insight into the potential strengths and weaknesses of the methodology. As used in this study, DIC requires extensive setup and operator interaction to provide the resolution presented.

Although previous research has examined the applicability of DIC analyses to fatigue crack identification and characterization, the vast majority has focused on in-plane loading. Additionally, most previous analyses resulted in qualitative measures of fatigue cracks. The work presented here represents a significant advancement in this area, with quantitative crack characterization applied to out-of-plane distortion-induced fatigue cracks. Advances are necessary to develop a fully automated methodology for detecting cracks on in-service steel highway bridges. The ability to quantify and characterize distortion-induced fatigue cracks with the use of DIC data demonstrates potential for the developed methodology to be fully automated in the future, improving the practice of fatigue inspection on steel bridges.

2.10 Data Availability Statement

Some or all data, models, or code generated or used during the study are available in a repository online in accordance with funder data retention policies. (https://matc.unl.edu/research/research_search.php)

2.11 Acknowledgements

Funding for this study was provided in part through the Mid-America Transportation Center via a grant from the U.S. Department of Transportation's University Transportation Centers Program, and this support is gratefully acknowledged. The views expressed in this paper are those of the authors, and do not reflect the position of the sponsoring agency.

2.12 References

Alemdar, F., Nagati, D., Matamoros, A., Bennett, C., and Rolfe, S. (2014-I). "Repairing Distortion-Induced Fatigue Cracks in Steel Bridge Girders using Angles-with-Plate Retrofit Technique, Part I: Physical Simulations." *Journal of Structural Engineering*, 140(5).

Alemdar, F., Overman, T., Matamoros, A., Bennett, C., and Rolfe, S. (2014-II). "Repairing Distortion-Induced Fatigue Cracks in Steel Bridge Girders using Angles-with-Plate Retrofit Technique, Part II: Computer Simulations." *Journal of Structural Engineering*, 140(5).

Alipour, M., Washlesky, S. J., and Harris, D. (2019). "Field Deployment and Laboratory Evaluation of 2D Digital Image Correlation for Deflection Sensing in Complex Environments." *J. Bridge Eng.*, 24(4).

American Association Of State Highway Transportation Officials (2014). "AASHTO LRFD Bridge Design Specifications " *7th Edition*, AASHTO, Washington DC.

American Society of Civil Engineers (2017). "Infrastructure Report Card – Bridges." ASCE, Reston, VA.

Anderson, T. L. (1995). "Fracture Mechanics: Fundamentals and Applications." CRC Press, Boca Raton.

ASTM International (2018). "Standard Test Method for Fracture Toughness." *ASTM E1820-18*, ASTM, West Conshohocken, PA.

ASTM International (2019). "Standard Specification for Carbon Structural Steel." *ASTM A36-19*, ASTM, West Conshohocken, PA.

Busca, G., Cigada, A., Mazzoleni, P., and Zappa, E. (2014). "Vibration Monitoring of Multiple Bridge Points by Means of a Unique Vision-Based Measuring System." *An International Journal*, 54(2), 255-271.

Carroll, J., Efstathiou, C., Lambros, J., Sehitoglu, H., Hauber, B., Spottswood, S., and Chona, R. (2009). "Investigation of fatigue crack closure using multiscale image correlation experiments." *Engineering Fracture Mechanics*, 76(15), 2384-2398.

Carroll, J. D., Abuzaid, W., Lambros, J., and Sehitoglu, H. (2013). "High resolution digital image correlation measurements of strain accumulation in fatigue crack growth." *International Journal of Fatigue*, 57, 140-150.

Chen, F., Chen, X., Xie, X., Feng, X., and Yang, L. (2013). "Full-field 3D measurement using multi-camera digital image correlation system." *Optics and Lasers in Engineering*, 51(9), 1044-1052.

Collins, W., Sherman, R., Leon, R., and Connor, R. (2016). "State-of-the-Art Fracture Characterization. I: Master Curve Analysis of Legacy Bridge Steels." *Journal of Bridge Engineering*, 21(12), 04016097.

Correlated Solutions Inc. (2016). "Correlated Solutions VIC Suite [Computer Software]. Retrieved from https://www.correlatedsolutions.com/." Irmo, South Carolina USA, .

Dhanasekar, M., Prasad, P., Dorji, J., and Zahra, T. (2019). "Serviceability Assessment of Masonry Arch Bridges Using Digital Image Correlation." *J. Bridge Eng.*, 24(2).

Federal Highway Administration (FHWA) (2004). "National bridge inspection standards." *Federal Register*, 69(239), 74419–74439.

Fisher, J. W. (1984). "Fatigue and fracture in steel bridges : case studies."

Hamam, R., Hild, F., and Roux, S. (2007). "Stress Intensity Factor Gauging by Digital Image Correlation: Application in Cyclic Fatigue." *Strain*, 43(3), 181-192.

Hassel, H., Bennett, C., Matamoros, A., and Rolfe, S. (2013). "Parametric Analysis of Cross-Frame Layout on Distortion-Induced Fatigue in Skewed Steel Bridges." *Journal of Bridge Engineering*, 18(7), 601-611.

Helfrick, M. N., Niezrecki, C., Avitabile, P., and Schmidt, T. (2011). "3D digital image correlation methods for full-field vibration measurement." *Mechanical Systems and Signal Processing*, 25(3), 917-927.

Hutt, T., and Cawley, P. (2009). "Feasibility of digital image correlation for detection of cracks at fastener holes." *NDT & E International*, 42(2), 141-149.

Irwin, G. (1960). "Plastic Zone Near a Crack Tip and Fracture Toughness, Sagamore Ordnance Material Conference, pp." *Used for Measuring the Indirect Tensile Strength of Rocks. Rock Mechanics and Rock Engineering*, 48(5), 1849-1866.

Lee, J. J., and Shinozuka, M. (2006). "A vision-based system for remote sensing of bridge displacement." *NDT & E International*, 39(5), 425-431.

Lorenzino, P., Beretta, G., and Navarro, A. (2014). "Application of Digital Image Correlation (DIC) in resonance machines for measuring fatigue crack growth." *Frattura ed Integrità Strutturale*, 8(30), 369-374.

Nowell, D., Paynter, R. J. H., and De Matos, P. F. P. (2010). "Optical methods for measurement of fatigue crack closure: moiré interferometry and digital image correlation." *Fatigue & Fracture of Engineering Materials & Structures*, 33(12), 778-790.

Pan, B., Tian, L., and Song, X. (2016). "Real-time, non-contact and targetless measurement of vertical deflection of bridges using off-axis digital image correlation." *NDT and E International*, 79, 73-80.

Parker, J. R. (2010). Algorithms for image processing and computer vision, John Wiley & Sons.

Ribeiro, D., Calçada, R., Ferreira, J., and Martins, T. (2014). "Non-contact measurement of the dynamic displacement of railway bridges using an advanced video-based system." *Engineering Structures*, 75, 164-180.

Rupil, J., Roux, S., Hild, F., and Vincent, L. (2011). "Fatigue microcrack detection with digital image correlation." *The Journal of Strain Analysis for Engineering Design*, 46(6), 492-509.

Schreier, H., Orteu, J., and Sutton, M. (2009). Image Correlation for Shape, Motion and Deformation Measurements: Basic Concepts,Theory and Applications, Springer.

Sutton, M. A., Yan, J., Deng, X., Cheng, C.-S., and Zavattieri, P. (2007). "Three-dimensional digital image correlation to quantify deformation and crack-opening displacement in ductile aluminum under mixed-mode I/III loading." *Optical Engineering*, 46(5), 051003.

Vanlanduit, S., Vanherzeele, J., Longo, R., and Guillaume, P. (2009). "A digital image correlation method for fatigue test experiments." *Optics and Lasers in Engineering*, 47(3-4), 371-378.

Whitehead, J. (2015). "Probability of detection study for visual inspection of steel bridges." R. J. Connor, M. Bowman, and G. Washer, eds., ProQuest Dissertations Publishing.

Zhang, R., and He, L. (2012). "Measurement of mixed-mode stress intensity factors using digital image correlation method." *Optics and Lasers in Engineering*, 50(7), 1001-1007.

Zhao, Y., and Roddis, W. (2004). "Fatigue Prone Steel Bridge Details: Investigation and Recommended Repairs." Final Rep. No. K-TRAN: KU-99-2. Topeka, KS: Kansas Dept. of Transportation.

Zhao, Z., and Haldar, A. (1996). "Bridge fatigue damage evaluation and updating using non-destructive inspections." *Engineering fracture mechanics*, 53(5), 775-788.

Chapter 3: **Application of a Digital Image Correlation Bridge Inspection Methodology on Geometrically-Complex Bifurcated Distortion-Induced Fatigue Cracking**

Hayder Al-Salih[1] , Mary Juno[1] , William Collins PhD, PE[1] , Caroline Bennett PhD, PE [1] , Jian Li PhD, PE [1]

[1] Department of Civil, Environmental, and Architectural Engineering, University of Kansas, Lawrence, Kansas 66045, USA

Correspondence: William Collins, Department of Civil, Environmental, and Architectural Engineering, University of Kansas, Lawrence, KS 66045, USA.

Email: william.collins@ku.edu

Funding information: Mid-America Transportation Center (MATC), Grant/Award Number 69A3551747107

3.1 Abstract

Distortion-induced fatigue cracking is a concern for many aging steel bridges in the United States. Human visual inspections to characterize fatigue cracks have many drawbacks including inconsistencies in identification, significant time and monetary costs, and safety risks posed to the lives of both inspectors and the traveling public due to lane closures. Digital image correlation (DIC) is a vision-based technology which has shown promise for identifying and characterizing fatigue cracks. Three-dimensional DIC measurements can capture full-field displacements and strains, allowing for detection and characterization of both in-plane and distortion-induced fatigue cracks. This paper describes an experimental study in which a half-scale steel girder-to-crossframe subassembly was subjected to distortion-induced fatigue loading to produce multiple geometrically-complex cracks. A DIC-based crack characterization methodology was applied to quantify the cracks, which was successful at characterizing cracks propagating in the girder web but struggled to characterize horizontal cracks. Additional work is needed to improve the accuracy of the DIC-based crack characterization methodology to use as an automated bridge inspection tool.

Keywords

Fatigue; fatigue crack growth; non-destructive characterization; fatigue cracks; multiaxial fatigue; digital image correlation.

3.2 Introduction and Background

3.2.1 Fatigue Cracking and Bridge Inspections

One of the main structural concerns regarding aging steel bridges in the United States (U.S.) is the initiation and propagation of fatigue cracks, particularly distortion-induced fatigue (DIF) cracks ((Fisher 1984). Distortion-induced fatigue cracks account for the majority of cracks occurring in steel bridges built in the U.S. prior to the 1980s, as they were often designed to have no connection between girder flanges and connection plates (CPs). When bridges without this connection experience traffic loading, differential deflection between girders causes the crossframe to push or pull on girder webs. In the weak web-gap regions, shown in Figure 3-2(a), differential deflection induces secondary out-of-plane stresses, resulting in distortion-induced fatigue. Steel bridges built prior to the mid-1980's undergo regular inspections to monitor the potential impact of distortion-induced fatigue, and repairs and protective retrofitting are often required.

Proper maintenance and repair are vital for ensuring that bridges can remain in-service for the entirety of their intended service life or longer. Visual inspection, mandated on a 24- or 48-month cycle (Federal Highway Administration (FHWA) 2004), is the most common approach to detecting fatigue cracks on bridges. A challenge with visual inspections is that fatigue cracks are initially small and thus difficult to detect. Although bridge inspections are necessary to ensure the safety of bridge infrastructure through the identification and monitoring of cracks over time, visual inspections are associated with significant time and monetary costs, as well as the introduction of safety risks to both inspectors and the traveling public. Additionally, visual identification of fatigue

cracks has been shown to be extremely difficult and inconsistent (Campbell et al. 2020; Whitehead 2015; Zhao and Haldar 1996). It is worth noting that distortion-induced fatigue crack patterns can be very geometrically complex. Generally, distortion-induced fatigue cracks consist of several different crack fronts, including horizontal web-to-flange cracks, vertical CP-to-web cracks, and branched cracks that bifurcate from the vertical cracks and grow horizontally or diagonally into the girder web. An example of these different crack segments can be seen in Figure 3-3, which presents the distortion-induced fatigue cracks examined in this study.

Researchers interested in both structural health monitoring and non-destructive testing have studied technologies aimed at detecting and monitoring cracks. Sensing technologies have been successfully used to detect and monitor cracking, but many of these approaches require the use of sensors or other components that are physically attached to the bridge, limiting the scope of detection. A vision-based, non-contact approach that does not require physical attachment would allow for large areas of bridges to be monitored in a more safe and efficient manner.

While some research has been conducted on vision-based crack detection methods, testing has primarily been conducted under idealized conditions limited to in-plane fatigue loading or at cracks in non-metallic materials (Nowell et al. 2010; Rupil et al. 2011; Vanlanduit et al. 2009). Few research programs have evaluated vision-based crack detection methods on out-of-plane loading with the complex geometries found on steel highway bridges. In this paper, the efficacy of a vision-based crack detection methodology is examined on a girder-to-crossframe test setup with a geometrically-complex, multi-segment distortion-induced fatigue crack.

3.2.2 Computer Vision

Computer vision encompasses the branch of technology that utilizes optics and computer algorithms to gather information from pictures and videos. Various forms of computer vision have been used in civil engineering applications to characterize mechanical parameters, with the majority of studies focusing on macro-indicators of damage, such as concrete deck deterioration, corrosion, and large displacements caused by substructure movement (Alipour et al. 2019; Busca et al. 2014; Dhanasekar et al. 2019; Pan et al. 2016).

Researchers have evaluated the potential of using computer vision for crack detection using a variety of materials. Edge detection methodologies have been used to successfully find discontinuous features in digital images, allowing for the detection and localization of cracks in concrete surfaces (Abdel-Qader et al. 2003). Research has been conducted to develop algorithms to remove short, thick, or exceedingly linear edges that are indicative of not being caused by cracking, in the hopes of creating a reliable crack detection method (Yu et al. 2007). Other researchers have created complex algorithms to detect cracking in concrete and asphalt pavement (Cha et al. 2017; Yamaguchi and Hashimoto 2010; Zou et al. 2012).

Cracks in metallic materials are often very thin, making application of edge detection methodologies significantly more challenging than in other civil material applications; for example, this is less of a challenge in concrete and asphalt components, which often develop relatively large crack openings and corresponding high contrast levels in digital images. Because of this, edge detection in metallic materials has a high rate of false positives, resulting from inadvertent detection of component boundaries, defects, corrosion, and other surface textures (Yeum and Dyke 2015). Kong and Li (2018) developed a computer vision strategy to detect fatigue

cracks by tracking structural surface motion in video format, but crack tip identification remains a challenge.

3.2.3 Digital Image Correlation

Digital image correlation (DIC) is a specific application of computer vision that utilizes medium- to high-resolution cameras and computer software to analyze images and generate full-field surface displacement measurements, which can be used to develop three-dimensional strain fields. Depending on the number of cameras used during data collection, two-dimensional (2D) and three-dimensional (3D) data can be utilized. DIC algorithms are applied to compare a series of images collected during loading to obtain relative displacement and strain for each point on the image.

DIC has been widely used to measure deformations and strain during material testing, and it is regularly used as an alternative or supplement to traditional sensing technology, such as strain gauges or extensometers (Yuan et al. 2014). With respect to cracking, DIC has been used to detect cracking in concrete structures, (Küntz et al. 2006) and to calculate stress intensity factors (Zhang and He 2012). 3D-DIC has also been used with unmanned aerial vehicle delivery to examine cracking on a concrete bridge (Reagan et al. 2017).

While research on vision-based crack detection methods have been conducted, testing has primarily occurred under idealized conditions looking at in-plane loading or at cracks in non-metallic materials. In-plane loading studies have been performed on steel compact (C(T)) specimens (J´er´emie Rupil et al. 2011), aluminum channels (Vanlanduit et al. 2009), notched tension specimens (Carroll et al. 2009; Carroll et al. 2013), and plates with drilled bolt holes (Hutt and Cawley 2009; Lorenzino et al. 2014). These studies have demonstrated the abilities and limitations of DIC for crack detection, but minimal research has focused on use with out-of-plane

loading and complex geometries characteristic of steel highway bridges, at least in part due to the challenges associated with creating and implementing such experimental setups (Sutton et al. 2007). Dellenbaugh et al. (2020) developed a DIC-based methodology for characterizing out-of-plane distortion-induced fatigue cracks, and evaluated DIC for crack detection in a test setup that included complex crack patterns and realistic steel bridge girder geometry. The results of that study indicated that the developed methodology was able to characterize distortion-induced fatigue crack lengths to within 2% to 14%, depending on loading conditions, with an average error of 5.8% (Dellenbaugh et al. 2020).

To obtain accurate results when using DIC, specimen preparation, camera setup, calibration, and image collection all must be optimized. Specimen preparation involves applying a high-contrast, random speckle pattern on the material surface, creating points of reference for image comparison as the specimen surface undergoes deformations. The required camera setup is dependent on the complexity of the specimen being tested. For two-dimensional analysis, one camera is sufficient since no out-of-plane deformations are expected, but two or more cameras are required to calculate a three-dimensional strain field such as is present in distortion-induced fatigue applications. Calibration of the system is necessary to establish the location of the two cameras in relation to each other and to convert images from pixels into dimensional units.

3.3 DIC Crack Characterization Methodology

3.3.1 Methodology Development and Initial Testing

Initial development and testing of the methodology used in this study utilized a single-camera DIC setup on a C(T) specimen subjected to in-plane loading in a servo-hydraulic testing machine, discussed in detail in Dellenbaugh et al. (2020). The C(T) specimen was 6.35 mm (0.25 in.) thick

with a width of 127 mm (5.0 in.). The size of the specimen was able to accommodate extensive crack growth, allowing for testing at multiple crack lengths on a single specimen. To emulate the high variability of bridge loadings, multiple load cases were defined and applied to achieve stress intensity ranges of 11, 22, 33, 44, and 55 MPa√m (10, 20, 30, 40, and 50 ksi√in). Crack tip plasticity during testing was controlled by testing first at the lowest load case, progressing to the highest. DIC data was recorded for each load case at crack lengths from 12.7 to 50.8 mm (0.5 to 2.0 in.) in 12.7 mm (0.5 in.) increments. Although the general crack location could be visually identified in the processed DIC images, the goal of automation prompted the development of a crack detection methodology to quantifiably characterize crack length from the DIC data. The 20 sets of in-plane data were used to develop the crack length quantification methodology.

3.3.2 Crack Characterization Methodology

When attempting to identify fatigue cracks on steel bridges using edge detection algorithms, the algorithms often produce false positive results; however, edge detection algorithms can work well for images analyzed with DIC. DIC-derived surface displacement contours were analyzed using MATLAB edge detection algorithms to initially identify the path of the fatigue crack. The crack path coordinates were extended linearly beyond the end of the crack tip determined through edge detection. The linear extension of the crack path accounted for the inability of the edge detection process to accurately identify the crack tip location. Following crack path identification, surface displacement data was extracted along orthogonal lines across the crack. More details about the methodology development can be found in Dellenbaugh et al. (2020). Data from these orthogonal extraction paths were used to determine the relative displacement between crack surfaces at discrete points along the crack path, schematically represented in Figure 3-1(a). The relative displacement at each point along the crack path, Δ_i, was divided by the maximum relative

displacement, Δ_{max}. A convergence value was defined as the difference between the ratio of relative displacements and 100%, represented in Equation (3-1) and plotted in Figure 3-1(b).

$$Convergence = 100\% - \frac{\Delta_i}{\Delta_{max}} \tag{3-1}$$

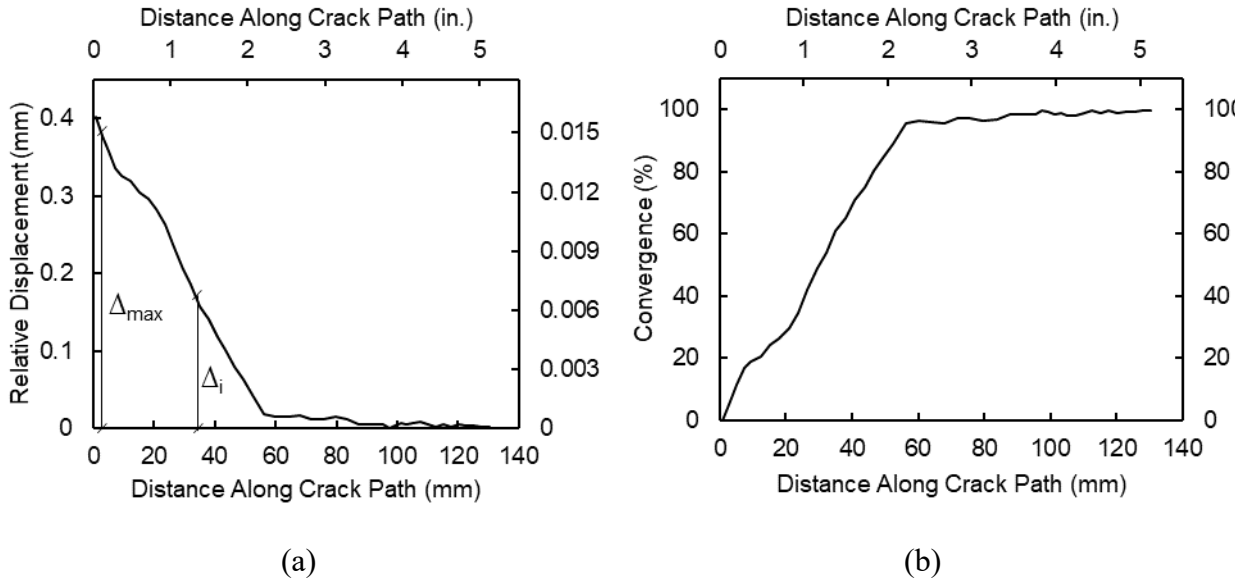

Figure 3-1. (a) Relative displacement and (b) Convergence along length of the crack path

Convergence values were then plotted along the crack path and evaluated at the known crack length. At the tip of the crack convergence should theoretically be equal to 100%, as the crack opening should be zero. However, results from C(T) specimens indicated that crack tip locations typically corresponded with convergence values between 90% and 95%, indicating that relative displacement is occurring beyond the end of the crack, likely due to a combination of crack tip plasticity and DIC measurement noise. The developed methodology was then evaluated on distortion-induced fatigue cracks under varying loads (Al-Salih et al. 2019; Dellenbaugh et al. 2020). Results from Dellenbaugh et al. (2020) indicated the developed methodology was, on

average, capable of characterizing a single DIF crack to within 5.8% of its length. However, results from Al-Salih et al. (2019) indicated that a bifurcated DIF crack with two crack fronts proved more difficult to accurately characterize, with results indicating 10% error for the horizontal branched crack and 38% error for the vertical crack (Al-Salih et al. 2019). Percent error is highly dependent on the dominant crack at the time of testing. In the first study the vertical crack was the dominant crack as the branched crack had not yet initiated. In the second study the horizontal branched crack become the dominant propagating crack, reducing the driving force experienced by the vertical branch of the crack. This in turn reduced crack opening when subjected to loading, leading to higher error in the vertical crack characterization.

3.4 Objective and Scope

The objective of this study was to evaluate the ability and effectiveness of a DIC-based crack characterization methodology (Dellenbaugh et al. 2020) to quantify geometrically-complex multi-segment out-of-plane distortion-induced fatigue cracks. The scope of this study included conducting a series of experimental tests on a 2845-mm (112-in.) long girder specimen subjected to out-of-plane fatigue loading to characterize distortion-induced fatigue cracks under a wide range of load cases through DIC measurements. Eleven load cases were examined, both above and below what would be produced under design loads, to explore the performance of the DIC under a broad range of load cases. The crack pattern was initiated and propagated under out-of-plane fatigue loading, and DIC data was collected under varying load cases. The crack pattern investigated in this study was a complex multi-segment crack pattern, consisting of three bifurcated cracks emanating from the same crack initiation point and one web-to-flange crack. The crack length segments varied from 51 mm (2.00 in.) to 138.6 mm (5.45 in.), and occurred in different directions – horizontal, vertical, and inclined.

The objective of this research is to further expand the available 'toolkit' of distortion-induced fatigue crack detection that are implementable with minimal direct human involvement and minimal disruption to the traveling public.

3.5 Experimental Approach

3.5.1 Girder Test Setup

A half-scale girder-to-crossframe subassembly fabricated from A36 steel (ASTM International 2019) was used for out-of-plane distortion-induced fatigue testing. Shown in Figure 3-2, the test setup had a length of 2845 mm (112 in.), a depth of 917 mm (36.1 in.), and a web thickness of 10 mm (3/8 in.). The bottom flange of the girder was connected to the strong floor of the laboratory via a grid of steel channels, restraining it from motion, approximating the top flange of a real bridge that is restrained by the concrete deck. A crossframe was attached at the center of the girder through a connection plate. The connection plate was welded to the girder web only and no connection was provided between it and the girder flanges, producing a fatigue-susceptible web-gap region, as shown in Figure 3-2(a) and Figure 3-3.

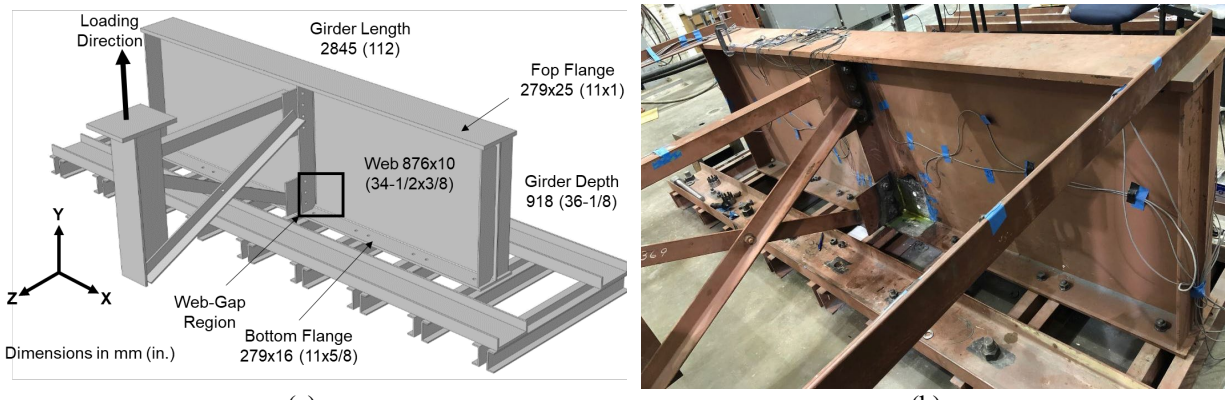

(a) (b)

Figure 3-2. Distortion-induced fatigue test setup: (a) schematic; (b) lab model

A vertical upward cyclic loading was applied to the far end of the crossframe by a servo-controlled hydraulic actuator, representing differential girder displacement and causing the girder to be

loaded out-of-plane, producing distortion-induced fatigue cracking in the web-gap region. Additional details regarding the distortion-induced fatigue test frame can be found in Alemdar et al. (2014a);(Al-Salih et al. 2021); Al-Salih et al. (2020); (Al-Salih et al. 2019), and Dellenbaugh et al. (2020)

3.5.2 Complex Crack Pattern

Prior to data collection, multiple fatigue cracks were initiated and propagated on the girder by loading cyclically at a load range of 2.2 to 25.5 kN (0.50 to 5.75 kips) for about 1,700,000 cycles. Fatigue cracks propagated in the web-gap region along both the CP-to-web weld and the web-to-flange weld. The crack in the CP-to-web weld bifurcated in three distinct branches, with one that continued to grow vertically along the CP-to-web weld, and two others that branched out into the girder web. The crack pattern is shown in Figure 3-3, where white lines have been drawn over the fatigue cracks for clarity, and letters have been assigned to designate the different crack segments. For the purposes of crack characterization, these bifurcated cracks were evaluated as three separate cracks with a shared initiation site at the bottom of the connection plate. The naming convention used for the three bifurcated cracks, as well as the web-to-flange crack and the location and length of all cracks is shown in Table 3-1. The lengths were determined using visual inspection with dye penetrant in the loaded condition.

Table 3-1. Crack Designations and Lengths

Crack Name	Crack Location	Crack Length mm (in.)
Vertical Crack	A-B-C-D-E-G	104.9 (4.14)
Branched Crack 1	A-B-C-D-F	111.9 (4.41)
Branched Crack 2	A-B-C-D-E-H	138.6 (5.45)
Horizontal Crack	I-J	51.0 (2.00)

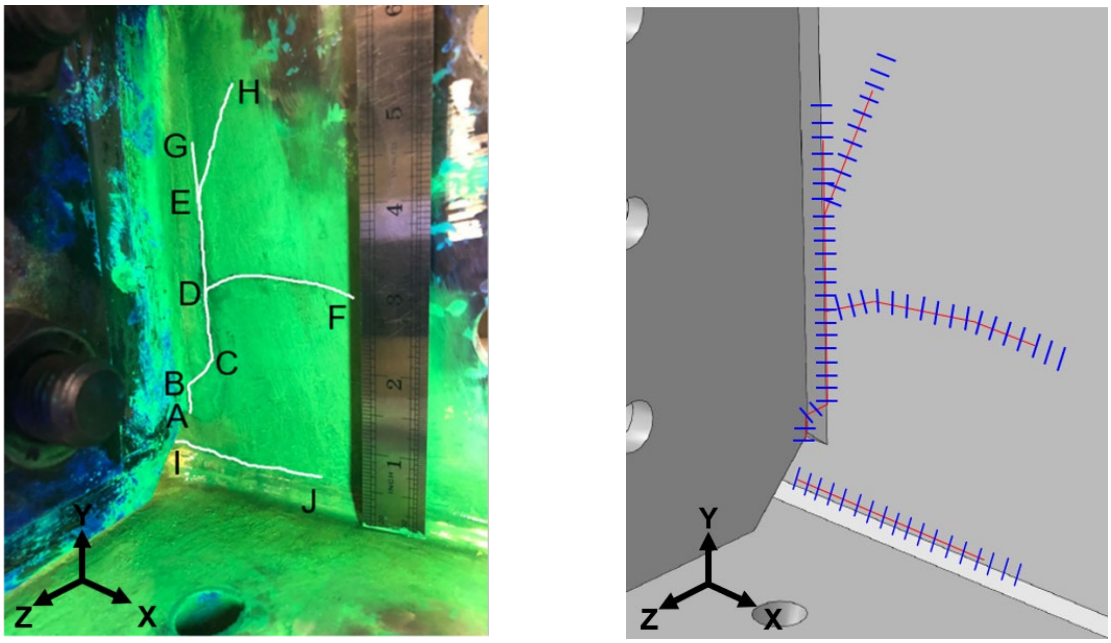

(a) (b)

Figure 3-3. (a) Fatigue cracks in web-gap region with ruler for scale displaying length in inches; (b) schematic of crack path and orthogonal data extraction lines

3.5.3 Loading Protocol for Data Collection

A loading protocol was developed to examine the crack characterization methodology under realistic distortion-induced fatigue load levels. A finite element (FE) model of a highway bridge was evaluated under AASHTO fatigue truck loading (American Association Of State Highway Transportation Officials 2014), evaluating the differential vertical deflections occurring between adjacent girders. The FE model was a full scale two-span non-skewed built-up steel plate girder bridge, with four girder lines and a concrete deck. The bridge was modeled using Abaqus Version 6.8.2. Both the steel and concrete deck elements were modeled using linear-elastic material properties. The model consisted of approximately 4 million elements with 27 million degrees of freedom. The FE model was developed and validated as part of a previous study, and additional details can be found in Hassel et al. (2013). As the half-scale distortion-induced fatigue test setup was based on the same full-scale bridge used in the analytical model, scaling differential deflections obtained by the FE analysis provides realistic levels of bridge loading. The differential

deflection under fatigue loading in the full-scale bridge FE model was found to be 2.6 mm (0.102 in.). This deflection was scaled for the half-scale girder-to-crossframe specimen, resulting in a target deflection of 1.3 mm (0.051 in.), corresponding to an applied actuator load of 7.8 kN (1.75 kips) in the initial configuration of the experimental test setup. Eleven load cases, LC1 through LC11, were defined. The maximum applied loads varied from 2.2 kN (0.5 kips) to 24.5 kN (5.5 kips), corresponding to differential girder deflection both above and below that estimated from the analytical model. A minimum load of 0.89 kN (0.2 kips) was applied in each load case to simulate dead load. Load cases and corresponding actuator displacements developed for the girder-to-crossframe specimen are presented in Table 3-2.

Table 3-2. Load Cases

Load Case	Load Range kN (kips)	Displacement Range mm (in.)
LC1	0.9-2.2 (0.2-0.5)	0.025-0.046 (0.001-0.0018)
LC2	0.9-4.4 (0.2-1.0)	0.025-0.074 (0.001-0.0029)
LC3	0.9-6.7 (0.2-1.5)	0.025-0.965 (0.001-0.038)
LC4	0.9-8.9 (0.2-2.0)	0.025-1.651 (0.001-0.065)
LC5	0.9-11.1 (0.2-2.5)	0.025-2.464 (0.001-0.097)
LC6	0.9-13.3 (0.2-3.0)	0.025-3.302 (0.001-0.130)
LC7	0.9-15.6 (0.2-3.5)	0.025-4.141(0.001-0.163)
LC8	0.9-17.8 (0.2-4.0)	0.025-4.902 (0.001-0.193)
LC9	0.9-20.0 (0.2-4.5)	0.025-5.741 (0.001-0.226)
LC10	0.9-22.2 (0.2-5.0)	0.025-6.553 (0.001-0.258)
LC11	0.9-24.5 (0.2-5.5)	0.025-7.315 (0.001-0.288)

3.5.4 Crack Characterization Methodology

The methodology applied for analyzing the complex multi-segment out-of-plane crack was similar to that described above. Analysis of the collected DIC images was performed using coordinate transformation, defining the x-axis along the web-to-flange weld, the y-axis along the CP-to-web weld, and the z-axis perpendicular to the plane of the web, shown in Figure 3-2 and Figure 3-3. Due to the complex geometry and movements associated with distortion-induced fatigue, displacements in all the three directions were analyzed. From the three-dimensional data, W displacement along the z-axis, V displacement along the y-axis, U displacement along the x-axis

were analyzed, as shown in Figure 3-4. Additionally, the resultant displacement, R, of all displacements in the three directions was calculated and evaluated.

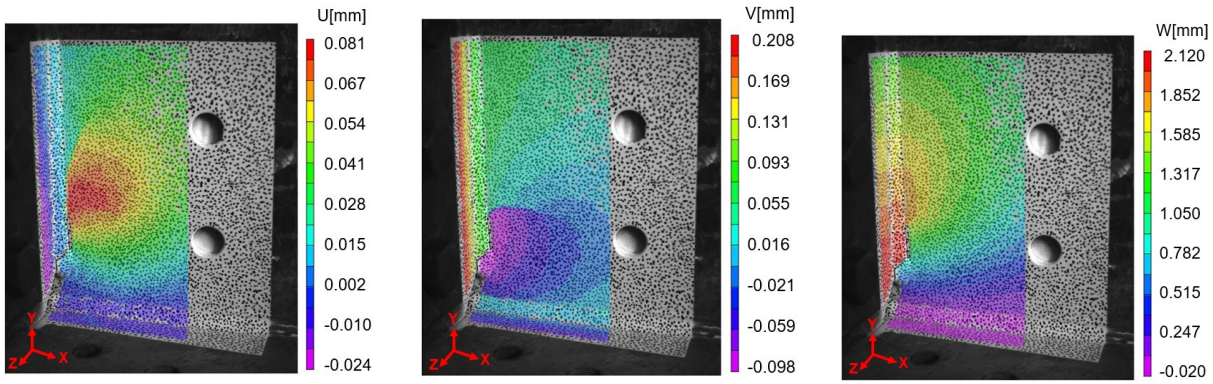

(a) (b) (c)

Figure 3-4. Typical visualized DIC displacements results in all the three principal directions: (a) U displacement in the x-axis; (b) V displacement in the y-axis; (c) W displacement in the z-axis

As the multi-segment out-of-plane cracks were more geometrically complex than the cracks previously evaluated, there were challenges in applying the crack characterization methodology. Specifically, the edge detection algorithms available in MATLAB were not able to clearly detect the paths corresponding to the cracks found through visual inspection. Therefore, the crack paths were visually identified based on the visualized strain data resulting from DIC analysis, see Figure 3-6. Following the previously developed procedures, orthogonal data extraction lines were defined along the crack path, extending beyond the perceived crack tip, and relative displacements across the cracks were calculated. The differential displacement between the sides of the crack were then used to determine convergence along the crack path.

3.5.5 DIC System Configuration and Specifications

3.5.5.1 DIC System

Tests were conducted using two cameras connected to an adjustable tripod via one horizontal and two vertical mounting bars. The two cameras were spaced 241.3 mm (9.5 in.) apart at a 21.6 degree

stereo angle. The distance from the cameras to the specimen was approximately 508 mm (20 in.). The configuration of the DIC hardware setup is shown in Figure 3-5.

The cameras used in the study were five megapixel (2448 x 2048 pixels) PGR Grasshopper3 cameras with a Sony IMX250 (CMOS) sensor and a frame rate of 75 frames/s. Schneider Xenoplan 1.4/17mm Compact Series were used with the cameras with a focal length of 17 mm (0.67 in.) and iris range/aperture of f1.4, resulting in a field of view of 240 x 200 mm (9.41 x 7.87 in.). External adjustable light-emitting diode (LED) lighting panels were used to provide the necessary contrast on the specimen surface and to eliminate shadows. Additional details of the DIC setup are presented in Table 3-3.

3.5.5.2 DIC Configuration, Calibration and Postprocessing

Prior to testing, stereo calibration was performed for the camera setup. This process ensures that the two cameras are in a known location relative to each other and that the setup is adequate for analysis by the DIC software. Additionally, the calibration process serves to remove any existing lens distortion and measurement bias, as well as defining a 3D coordinate system. A high contrast speckled surface pattern was also applied to the specimen prior to data collection. The web-gap region where the crack developed was painted white and a black marker was used to create the random, high contrast speckle pattern. Speckle diameters ranged from 1.5 mm to 2.0 mm (0.06 in. to 0.08 in.) and covered approximately 37% of the area of interest. Images were collected during cyclic loading and analyzed using Correlated Solutions' VIC-3D (V.08) software (Correlated Solutions Inc. 2016). Processing of the collected DIC images was started by using coordinate transformation as previously described, the adopted coordinate directions are shown in Figure 3-2 and Figure 3-3.

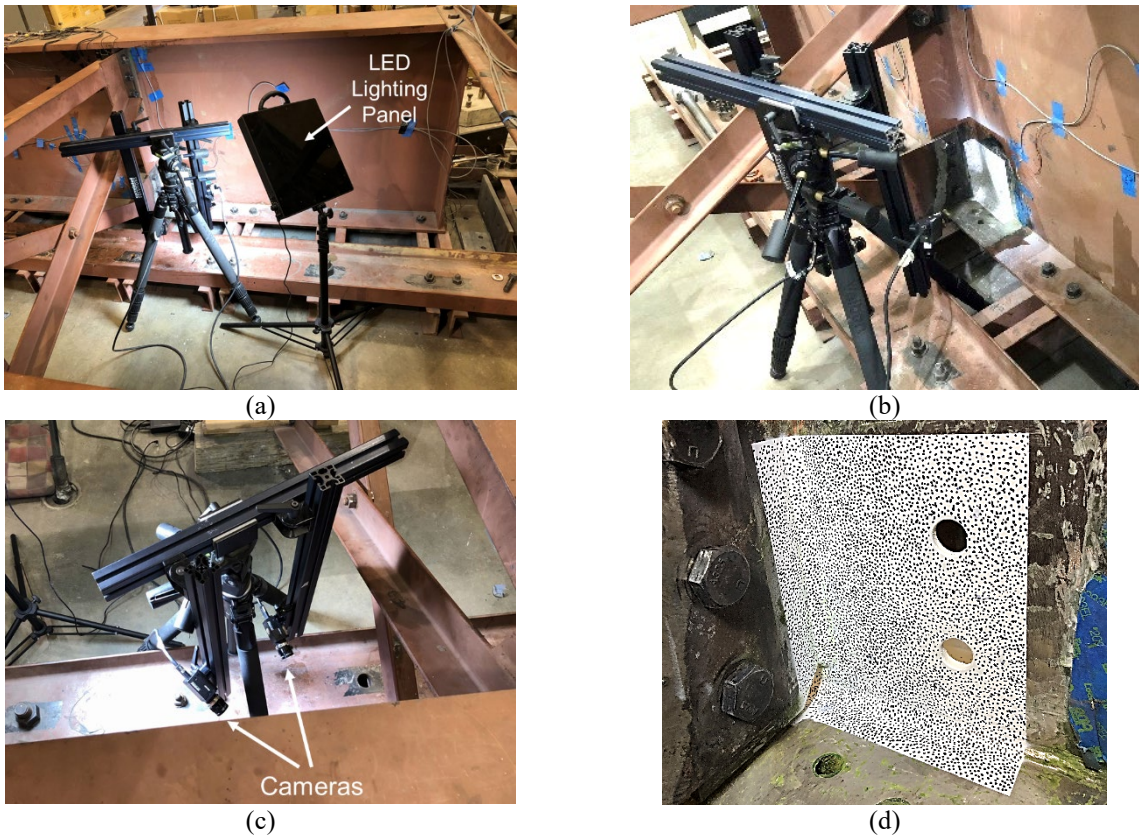

(a) (b)

(c) (d)

Figure 3-5. DIC hardware placement, and orientation: (a) front view; (b) side view, (c) top view; (d) random high-contrast speckle pattern in web-gap region.

Two other important parameters for DIC postprocessing are the subset size and the step size. Subset size is the width and height of the square of data being compared between the reference image and the deformed image. The step size is the distance between subset centers, which controls the spacing of the points being analyzed. The subset size used in this study was 29 pixels by 29 pixels, and the step size was 7 pixels. It was found that these values for subset and step size maintained a high-quality spatial resolution while optimizing computation time. Additionally, the values resulted in low uncertainty and a resolution level that was multiple orders of magnitude smaller than the crack sizes under consideration.

3.5.5.3 Noise and Uncertainty

The accuracy of DIC data can be improved by optimizing multiple parameters, including lighting, camera focus, and the applied high-contrast pattern. To minimize noise and uncertainty during testing, special attention was given to these parameters. The cameras were carefully focused during testing, utilizing prime midrange (17mm) focal length lenses. The adopted lighting condition, typically 250 ± 35 lux, combined with camera exposure time limited to 1 ms, produced the lowest uncertainty level in the resulting data.

Table 3-3. DIC system specifications, parameters, and details

Equipment /Parameter	Description/Feature	Specification/Value
Camera	Model	PGR Grasshopper3
	Resolution (Megapixels)	5
	Resolution (Horizontal x Vertical), pixels	2448 x 2048
	Frame Rate, frame/s	75
	Sensor	Sony IMX250 (CMOS)
	Distance between cameras center, mm (in.)	241 (9.49)
	Distance between camera and the specimen, mm (in.)	508 (20)
	Stereo angle, deg	21.6
	Field of view, mm (in.)	240 x 200 (9.41 x 7.87)
Lens	Model	Schneider Xenoplan Compact Series (2/3" Sensor) Lenses
	Focal Length, mm (in.)	17 (0.67)
	Iris range/aperture	f1.4
Light	Model	Light-emitting diode (LED) 500k Bescor lighting system
	Light intensity (Lux)	250±35

System accuracy can be determined by computing confidence intervals during postprocessing to obtain Sigma-X, which represents one standard deviation of displacement uncertainty in the X-axis. Similar uncertainty estimates for the Y- and Z-axes, Sigma-Y and Sigma-Z, can be obtained. These Sigma values, which represent the uncertainty level in the VIC 3D software, were used as an estimate to quantify the noise. It was found that Sigma-X ranged from 0.00018 mm to 0.00217 mm (7.1e-6 in. to 8.5e-5 in.), Sigma-Y ranged from 0.0002 mm to 0.0031 mm (7.9e-6 in. to 1.2e-4 in.), and Sigma-Z ranged 0.0004 mm to 0.00486 mm (1.6e-5 in to 1.9e-4 in.). The majority of

the area of interest was on the lower bound of the noise and uncertainty range, and these ranges were considered very low within the context of the crack lengths.

3.6 Results and Discussion

3.6.1 Visualization of Results

Strains obtained by DIC for the complex crack test are presented in Figure 3-6. The majority of the crack pattern is clearly visible in the images, except for the last segment of the vertical crack, segment E-G, which was also found to be difficult to identify visually. Although von Mises strain (Figure 3-6f) was able to reveal the majority of the crack pattern, it is important to note that this computation does not readily reveal differences between tensile and compression; for example, the region surrounding the web-to-flange crack in Figure 3-6 f is shown as red, but it is representative of compressive stresses rather than tensile. FE study conducted by Liu (2015) found that web-to-flange crack is under compression on the CP side and under tension on the fascia side. Similarly, maximum principal strain only provides a clear picture if it is combined with minimum principal strain.

3.6.2 Crack Characterization Results

As previously described, differential displacements were computed along data extraction lines arranged orthogonal to the crack path, and convergence for those displacements values was calculated along the length of the crack path. Because of the complex geometry of web-gap region and the multi-segment crack, displacements for all three principal directions were examined. The resultant differential displacements were calculated and evaluated for the crack characterization methodology. Resultant displacements produced similar trends and compliance magnitudes when

compared with the W displacement results, because the W displacement magnitude was significantly higher than that for the V and U directions, dominating the resultant calculation. Therefore, results based on resultant displacement have not been presented in this paper. Additionally, as load was applied in the YZ plane, the U displacements were found to be small magnitude, creating highly variable convergence curves for most load cases. Therefore, U displacement convergence was also not considered to be a useful indicator for crack detection for this crack pattern.

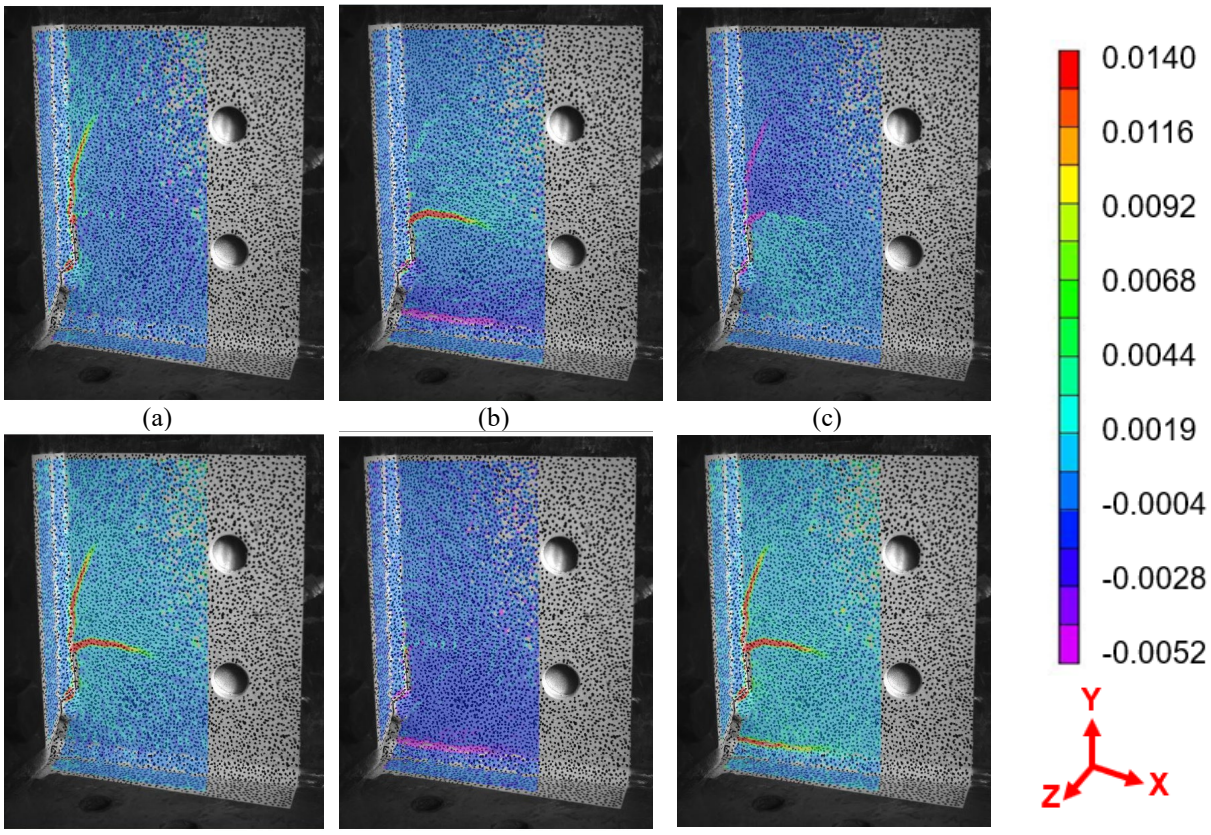

Figure 3-6. Typical visualized DIC strains, (a) Strain in x-axis (exx); (b) Strain in y-axis (eyy); (c) Strain in xy plane (exy); (d) Max principal strain (e1); (e) Min principal strain (e2); (f) Von Mises Strain.

The approach applied here was found to perform well under a broad range of applied loads, but a threshold to its applicability was identified as occurring at the lowest-magnitude load case studied

(LC1). Relative displacements in all the three directions measured under LC1 were extremely small, resulting in highly variable convergence values and indicating that the displacement-driven process was ineffective at this low load range. This level of loading was identified as the threshold of applicability in the development of this approach, as the variability in convergence did not allow for a characterization of crack lengths (Dellenbaugh et al. 2020). Although graphically presented in relative displacement and convergence plots, data from LC1 has been excluded from further consideration and is not used to characterize crack lengths. It should be noted that for most load cases, the relative displacements values in all the three directions approached zero well before the known crack tip location, resulting in an under-prediction of crack length at 90% and 95% convergence values. For this reason, crack lengths at convergence values of 98% were also examined. Only 95% and 98% convergence values will be presented in this paper.

3.6.2.1 Vertical Crack Characterization Results

W- and V-direction relative displacements for the vertical crack are presented in Figure 3-7 (a) and (c), with convergence curves for the same directions shown in Figure 3-7 (b) and (d). The crack segment lengths as determined through traditional visual inspection without the assistance of DIC have been represented by a vertical dotted line in the figures. Table 3-4 presents the predicted crack lengths and the percentage of error for 95% and 98% convergence results for both the V and W displacement compared with the visually measured crack length of 105 mm (4.14 in.). Both relative displacement and convergence in the V-direction display a step-like trend for the diagonal second crack segment, B-C. This is caused by the low levels of vertical relative displacement occurring in the vertical segments on either side of B-C, compared with a much larger amount of vertical displacement within the segment.

Table 3-4. Vertical Crack length characterization (Actual length from inspection= 104.9 mm (4.14in.))

Load Case	95% Convergence				98% Convergence			
	Computed Crack from V Displacement		Computed Crack from W Displacement		Computed Crack from V Displacement		Computed Crack from W Displacement	
	Length [mm (in.)]	Error [%]	Length [mm (in.)]	Error [%]	Length [mm (in.)]	Error [%]	Length [mm (in.)]	Error [%]
LC2	59.5 (2.34)	-43%	52.1 (2.05)	-50%	98.8 (3.89)	-6%	87.3 (3.44)	-17%
LC3	71.8 (2.83)	-32%	61.3 (2.41)	-42%	86.9 (3.42)	-17%	87.2 (3.43)	-17%
LC4	81.0 (3.19)	-23%	55.6 (2.19)	-47%	83.6 (3.29)	-20%	85.3 (3.36)	-19%
LC5	86.2 (3.39)	-18%	55.8 (2.20)	-47%	98.2 (3.87)	-6%	86.1 (3.39)	-18%
LC6	87.0 (3.43)	-17%	56.1 (2.21)	-47%	104.9 (4.13)	0%	86.2 (3.39)	-18%
LC7	95.7 (3.77)	-9%	58.3 (2.30)	-44%	104.0 (4.09)	-1%	86.9 (3.42)	-17%
LC8	96.7 (3.81)	-8%	65.2 (2.57)	-38%	104.1 (4.10)	-1%	87.2 (3.43)	-17%
LC9	96.4 (3.80)	-8%	67.5 (2.66)	-36%	103.7 (4.08)	-1%	86.4 (3.40)	-18%
LC10	96.7 (3.81)	-8%	66.0 (2.60)	-37%	103.8 (4.09)	-1%	87.7 (3.45)	-16%
LC11	96.8 (3.81)	-8%	65.4 (2.57)	-38%	103.8 (4.09)	-1%	87.0 (3.43)	-17%
Avg. (abs)	86.8 (3.42)	17%	60.3 (2.37)	42%	99.2 (3.91)	5%	86.7 (3.41)	17%

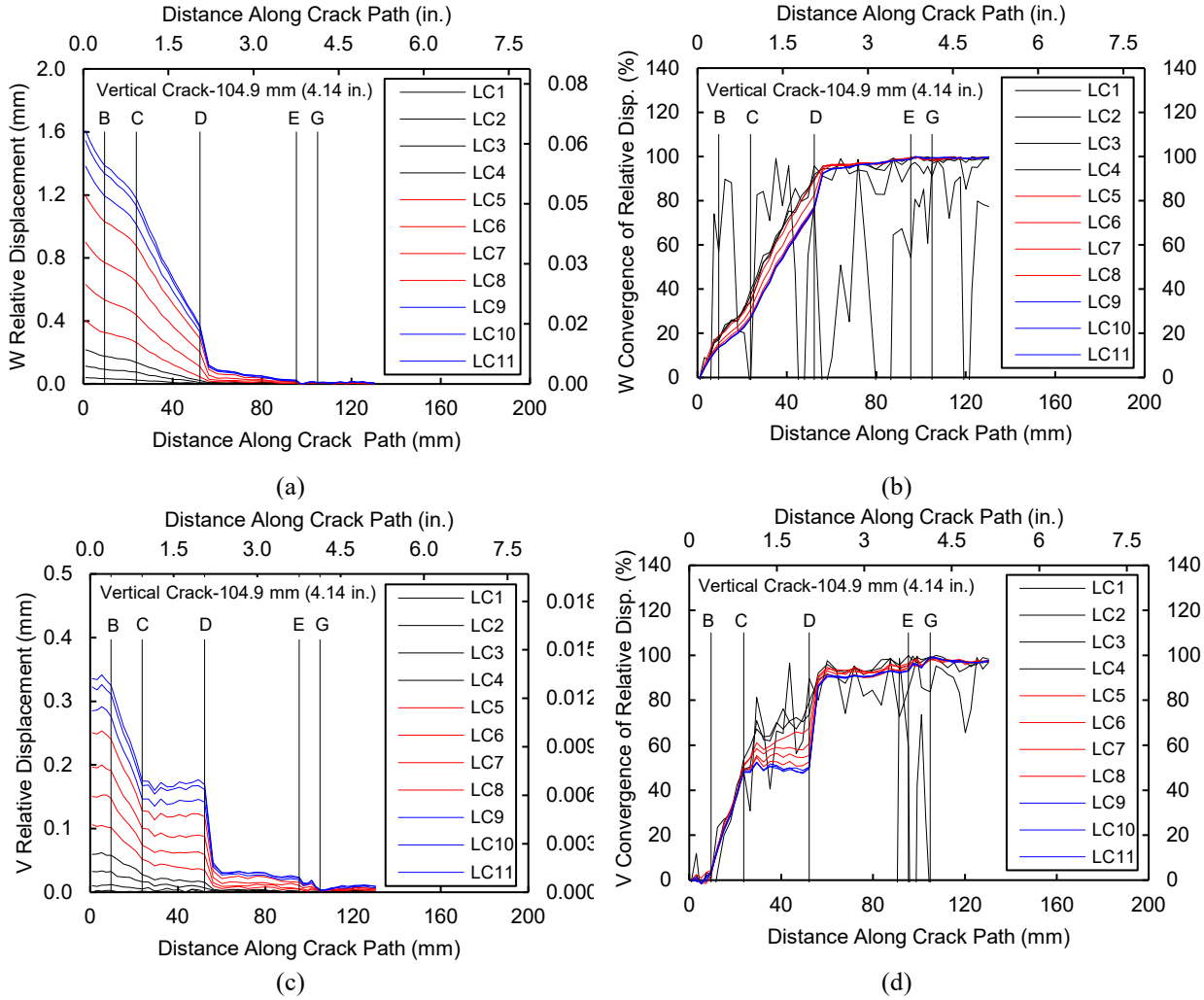

Figure 3-7. Vertical Crack, (a) W Relative displacement; (b) Convergence of W relative displacement; (c) V Relative displacement; (d) Convergence of V relative displacement.

As shown in the Table 3-4 and Figure 3-7, 95% convergence under-predicted vertical crack lengths by an absolute average of 17% based of V-displacement values, and 42% based on W-displacement values, as evident in Figure 3-11. The 98% convergence level resulted in a better predication of the vertical crack length, under-predicting the length by an absolute average of only 5% based of V-displacement values, and 17% based on W-displacement values.

3.6.2.2 Branched Crack 1 Characterization Results

The relative displacements and convergence values based on W- and V-displacements for Branched Crack 1 are shown in Figure 3-8. The lengths of actual crack segments are represented by vertical dotted lines in the figures. Table 3-5 shows the predicted crack lengths and the percentage of error compared with the visually-measured Branched Crack 1 length of 112 mm (4.41 in.) for 95% and 98% convergence based on V- and W-displacement. Again, the results based on V-direction displacement produce a step in the relative displacement and convergence curves for segment B-C.

Table 3-5. Branched Crack 1 length characterization (Actual length from inspection= 111.9 mm (4.41 in.))

Load Case	95% Convergence				98% Convergence			
	Computed Crack from V Displacement		Computed Crack from W Displacement		Computed Crack from V Displacement		Computed Crack from W Displacement	
	Length [mm (in.)]	Error [%]	Length [mm (in.)]	Error [%]	Length [mm (in.)]	Error [%]	Length [mm (in.)]	Error [%]
LC2	69.4 (2.73)	-38%	52.1 (2.05)	-53%	105.2 (4.14)	-6%	69.5 (2.74)	-38%
LC3	67.0 (2.64)	-40%	54.1 (2.13)	-52%	90.8 (3.57)	-19%	68.5 (2.70)	-39%
LC4	67.1 (2.64)	-40%	64.5 (2.54)	-42%	86.1 (3.39)	-23%	68.5 (2.70)	-39%
LC5	81.7 (3.22)	-27%	64.2 (2.53)	-43%	90.3 (3.56)	-19%	71.5 (2.81)	-36%
LC6	102.0 (4.02)	-9%	69.1 (2.72)	-38%	119.1 (4.69)	6%	79.7 (3.14)	-29%
LC7	106.6 (4.20)	-5%	74.6 (2.94)	-33%	123.5 (4.86)	10%	105.0 (4.13)	-6%
LC8	116.0 (4.57)	4%	75.4 (2.97)	-33%	124.4 (4.90)	11%	109.9 (4.33)	-2%
LC9	118.4 (4.66)	6%	75.6 (2.98)	-32%	124.0 (4.88)	11%	110.2 (4.34)	-1%
LC10	118.9 (4.68)	6%	75.7 (2.98)	-32%	124.8 (4.91)	11%	111.1 (4.37)	-1%
LC11	120.1 (4.73)	7%	75.9 (2.99)	-32%	125.4 (4.94)	12%	111.0 (4.37)	-1%
Avg. (abs)	96.7 (3.81)	18%	68.1 (2.68)	39%	111.4 (4.39)	13%	90.5 (3.56)	19%

This flat section is again caused by the large vertical displacements in the diagonal segment relative to the two vertical crack segments surrounding it. Predicted crack lengths and associated errors for Branched Crack 1 are presented in Table 3-5. The absolute average error in predicted crack length values was 18% for 95% convergence, based on V-displacement values, and 39% for 95%, based on W-displacement values, as shown in Figure 3-11. Evaluating crack lengths at 98% convergence resulted in less error, underpredicting crack length by an absolute average of only 13% based on V-displacement values and 19% based on W-displacement values.

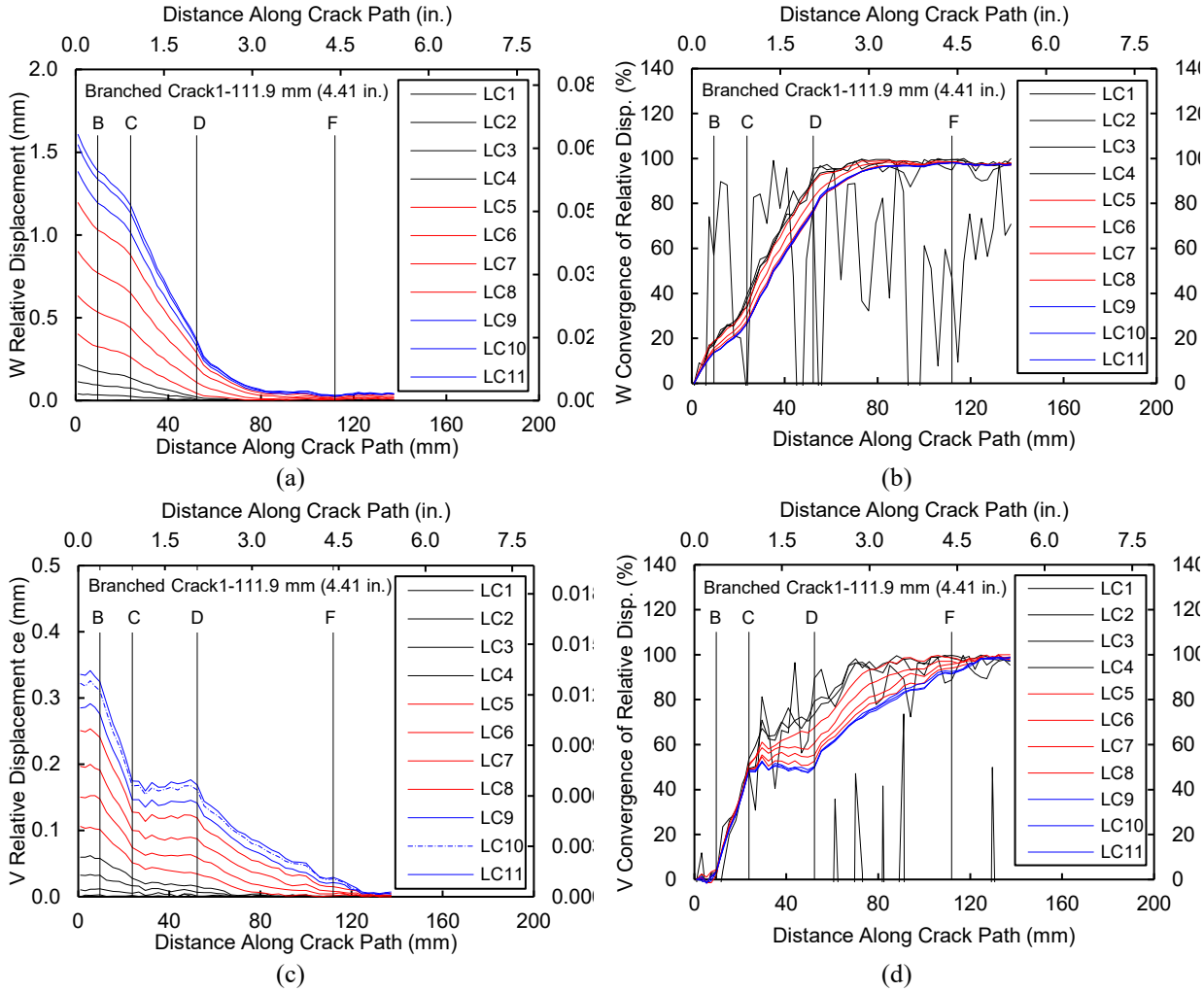

Figure 3-8. Branched Crack1, (a) W Relative displacement; (b) Convergence of W relative displacement; (c) V Relative displacement; (d) Convergence of V relative displacement

3.6.2.3 Branched Crack 2 Characterization Results

The W- and V-direction relative displacement and convergence values for Branched Crack 2 are shown in Figure 3-9. The vertical dotted lines in the figures represent lengths of actual crack segments. The predicted crack lengths and the percentage of error compared with the visually-measured Branched Crack 2 length of 139 mm (5.45 in.) for 95% and 98% convergence results for V and W displacement are shown in Table 3-6.

Table 3-6. Branched Crack 2 length characterization (Actual length from inspection= 138.6 mm (5.45 in.))

Load Case	95% Convergence				98% Convergence			
	Computed Crack from V Displacement		Computed Crack from W Displacement		Computed Crack from V Displacement		Computed Crack from W Displacement	
	Length [mm (in.)]	Error [%]	Length [mm (in.)]	Error [%]	Length [mm (in.)]	Error [%]	Length [mm (in.)]	Error [%]
LC2	59.5 (2.34)	-57%	52.1 (2.05)	-62%	132.8 (5.23)	-4%	63.6 (2.50)	-54%
LC3	71.8 (2.83)	-48%	61.3 (2.41)	-56%	86.9 (3.42)	-37%	87.2 (3.43)	-37%
LC4	81.0 (3.19)	-42%	55.6 (2.19)	-60%	83.6 (3.29)	-40%	85.3 (3.36)	-38%
LC5	86.2 (3.39)	-38%	55.8 (2.20)	-60%	99.7 (3.93)	-28%	86.1 (3.39)	-38%
LC6	87.0 (3.42)	-37%	56.1 (2.21)	-60%	97.7 (3.85)	-30%	86.2 (3.39)	-38%
LC7	95.7 (3.77)	-31%	58.3 (2.30)	-58%	145.3 (5.72)	5%	86.9 (3.42)	-37%
LC8	96.9 (3.81)	-30%	65.2 (2.57)	-53%	147.1 (5.79)	6%	87.2 (3.43)	-37%
LC9	97.9 (3.85)	-29%	67.5 (2.66)	-51%	146.0 (5.75)	5%	86.4 (3.40)	-38%
LC10	97.3 (3.83)	-30%	66.0 (2.60)	-52%	147.4 (5.80)	6%	87.7 (3.45)	-37%
LC11	97.4 (3.84)	-30%	65.4 (2.57)	-53%	146.0 (5.75)	5%	87.0 (3.43)	-37%
Avg. (abs)	87.1 (3.43)	37%	60.3 (2.37)	56%	123.2 (4.85)	17%	84.4 (3.32)	39%

Again, there is a step-like trend for the second segment, B-C, in both the V-direction relative displacement and convergence curves, shown in Figure 3-9 (c) and Figure 3-9 (d), respectively. This is again attributed to low-magnitude vertical relative displacements between the boundary of the vertical segments of the cracks compared to the amount of vertical relative displacements between the boundary of the diagonal segment B-C. Although segment E-H is not perfectly vertical it exhibits the step-like trend, which can be attributed to the fact that E-H has a very little vertical relative displacement. This corresponds with experimental observations, which indicate segment E-H has small opening that made it very hard to measure during the visual inspection.

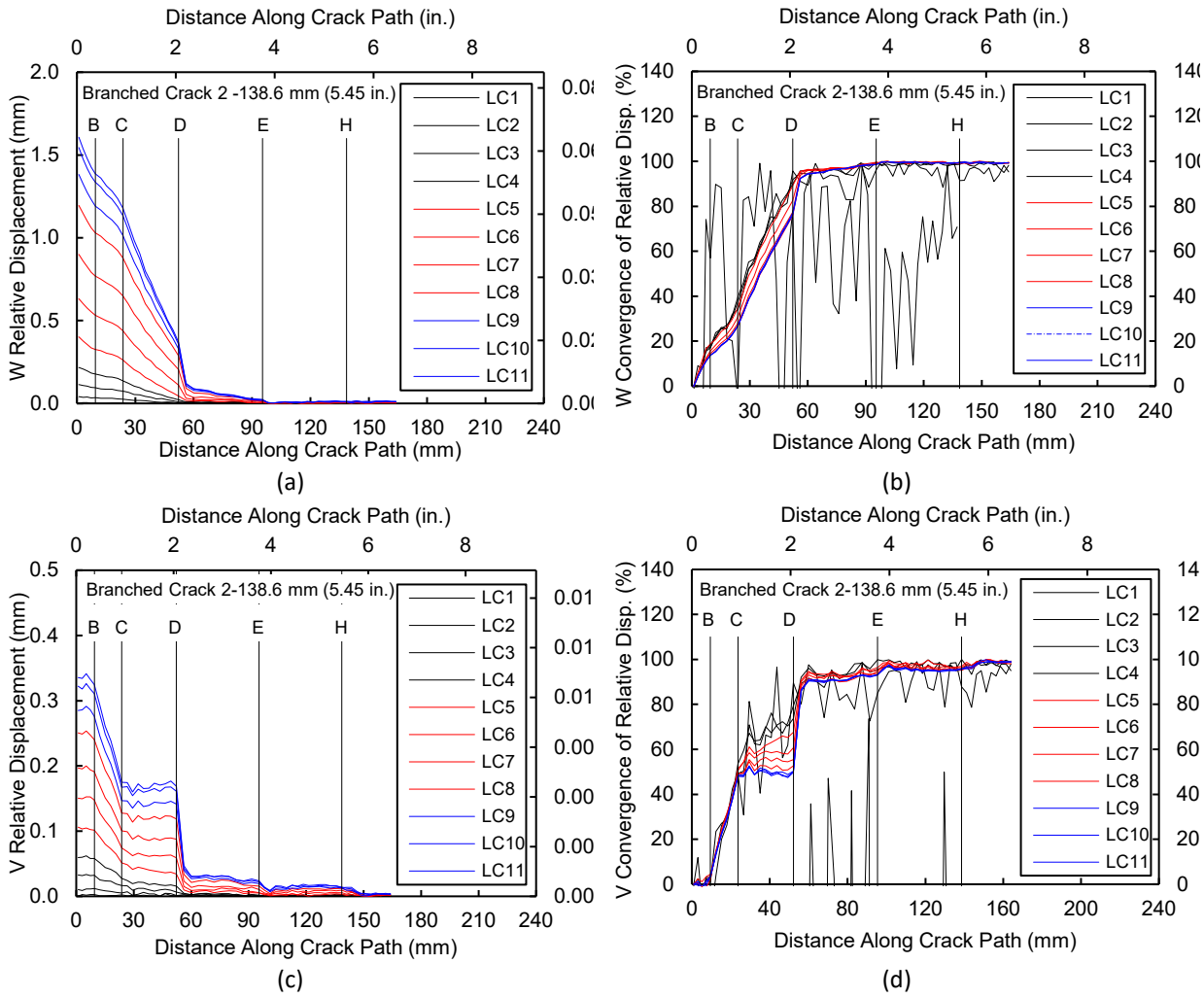

Figure 3-9. Branched Crack 2: (a) W Relative displacement; (b) Convergence of W relative displacement; (c) V Relative displacement; (d) Convergence of V relative displacement.

As presented in Table 3-6, Figure 3-9, and Figure 3-11, the 95% and 98% convergence underpredicted the Branched Crack 2 length by 37% and 17%, respectively, based on V-direction displacement values, and by 56% and 39%, respectively, based on W-direction displacement values.

3.6.2.4 Horizontal Web-to-Flange Crack Characterization Results

The relative displacement and convergence values based determined in the V-direction for the horizontal web-to-flange crack are shown in Figure 3-10. The vertical dotted line in the figures represent the length of the actual horizontal web-to-flange crack, based on visual inspection of the

specimen. It is clear that horizontal web-to-flange crack results exhibited a high level of noise and did not converge well compared to the application of the crack characterization technique for other cracks in the girder specimen. W-, R-, and U- displacements were also found to be very noisy and did not approach the 95% convergence level, and for V-direction displacements more than half of the load combinations examined did not produce convergence levels of 95%. These results are attributed to a few different reasons. First, relative displacements between the crack boundaries were very small. For example, the maximum relative W-displacements for the horizontal crack were found to be 0.08 mm (0.003 in.), as compared to 1.6 mm (0.06 in.) for other cracks. This corresponds with experimental observation, where the opening of the horizontal web-to-flange crack was extremely small and nearly invisible, making it very difficult to detect during visual inspections. Second, as discussed previously with regard to the strain visualization results, the horizontal crack is under compression on the interior side of the girder, producing crack closure under loading rather than opening. This behavior was confirmed with finite element analyses (Liu 2015) that showed the horizontal crack is under compression on the interior side of the girder and under tension on the fascia side. For these reasons, the horizontal web-to-flange was not able to be well-characterized using this DIC-based methodology, with convergence values never reaching 95% or 98%. Table 3-7 presents the calculated convergence percentage for each load case associated with the actual crack length. Figure 3-11 presents a summary for the predicted cracks lengths and the corresponding percent of error for the Vertical Crack, Branched Crack 1, and Branched Crack 2. Figure 3-11 (a) presents the absolute average percent error between predicted and actual crack lengths for 95% and 98% convergence levels for relative V- and W-displacements, while Figure 3-11 (b) presents the predicted crack lengths based on 95% and 98%

convergence levels for relative V- and W- displacements. The dotted lines represent the actual crack lengths.

Table 3-7. Horizontal Crack length characterization (Actual length from inspection= 51 mm (2 in.))

Load Case	Convergence percentages associated with the actual crack length	
	Computed Crack from V Displacement	Computed Crack from W Displacement
LC2	69.8	47.4
LC3	94.9	63.0
LC4	90.6	86.9
LC5	94.2	74.6
LC6	83.2	81.7
LC7	84.2	75.8
LC8	87.4	66.3
LC9	85.0	69.1
LC10	84.7	66.4
LC11	81.9	67.3
Avg.	85.6	69.9

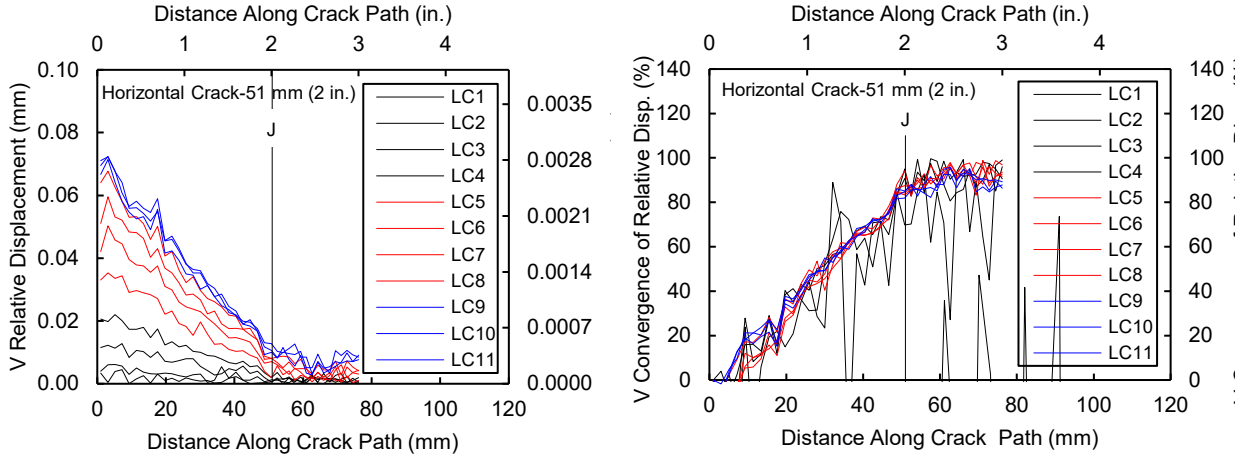

(a) (b)

Figure 3-10. Horizontal Web-to-Flange Crack: (a) V Relative displacement; (b) Convergence of V relative displacement.

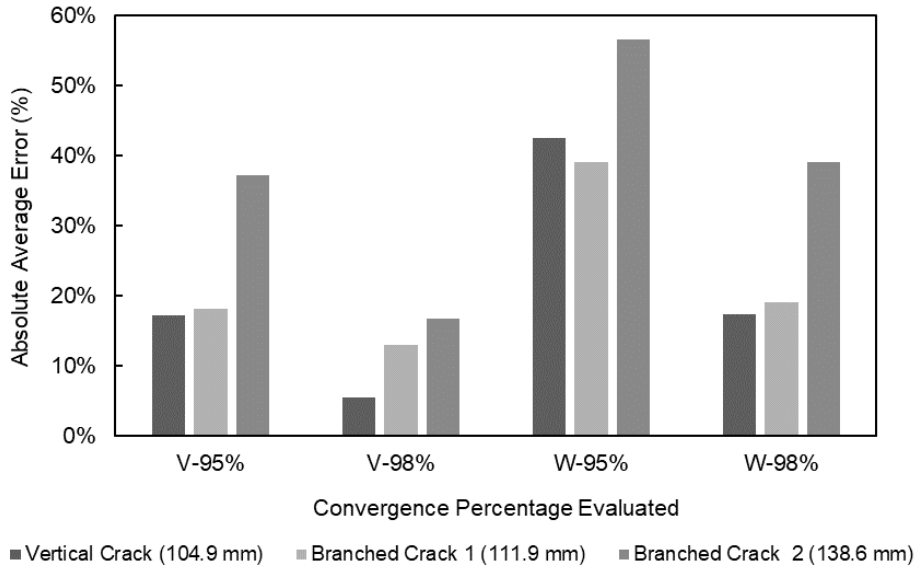

(a)

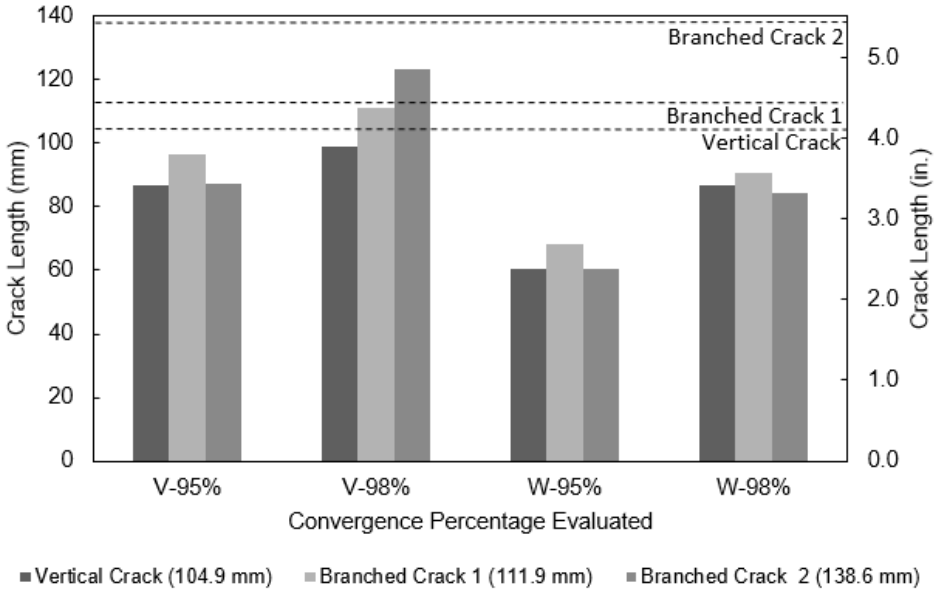

(b)

Figure 3-11. (a) Absolute average percent error between predicted and actual crack lengths for 95%, and 98% convergence for V and W relative displacement; (b) Predicted crack lengths based on 95%, and 98% convergence for V and W relative displacement

Initial load cases, which produce very little crack opening displacements, resulted in higher levels of error in the convergence calculations. The loading threshold where crack length prediction error approaches 10% appears to be between LC4 and LC5 for the Vertical Crack, LC5 and LC6 for

Branched Crack 1, and LC6 and LC7 for Branched Crack 2. Lower load ranges did not produce crack opening along the full crack length, making it difficult to detect the displacement difference occurring at crack edges, which resulted in crack length underestimation.

3.7 Conclusions and Future Work

This study has evaluated the ability of a previously developed DIC-based methodology for characterizing geometrically complex bifurcated distortion-induced fatigue cracks in steel bridges. The methodology utilizes relative displacement between crack edges to determine length of the crack. The methodology was successful at characterizing bifurcated cracks propagating in the girder web, but characterization of a horizontal crack at the web-to-flange connection was found to be a limitation of the technique. The following conclusions have been drawn from the study:

1- A convergence of 98% was found to provide a more accurate estimation of the crack length on a steel girder loaded out-of-plane with complex fatigue crack geometry compared with 95% convergence. Due to this increased accuracy, 98% convergence is recommended for crack length characterization when used in similar crack patterns and applications.

2- The methodology was found to result in more accurate results when V-direction displacements were used rather than U- and W-direction displacements, which can be attributed to the V-direction corresponding to the direction of loading.

3- On average, 98% convergence based on V-direction displacement data resulted in underprediction of crack lengths with 5%, 13%, and 17% error for the Vertical Crack, Branched Crack 1, and Branched Crack 2, respectively.

4- The crack characterization methodology was found to not converge well for the horizontal web-to-flange crack under this mode of loading. This was because the web-to-flange crack experienced crack closure on the interior face of the girder, and relative displacements were extremely small along the crack length.

5- Load cases with low load levels resulted in greater error in terms of crack length determination. The threshold of adequate loading for use with this technique appears to be between LC4 and LC5 for the Vertical Crack, LC5 and LC6 for Branched Crack 1, and LC6 and LC7 for Branched Crack 2, as load levels below this did not produce crack opening along the full length of the crack.

For the proposed methodology to be employed for in-service inspections of highway bridges, the associated hands-on work needs to be minimized. As the described work is still an early step towards using DIC in this application, it is recognized that additional work is needed to realize the potential of the system. Ongoing work is also examining the necessity of the painted-on high contrast pattern, instead utilizing existing surface defects for DIC analysis. Additional ongoing work is examining the limitations of the methodology discussed in this paper, primarily regarding the adequate levels of lighting and focus necessary for detecting and characterizing fatigue cracks.

Identifying and characterizing distortion-induced fatigue cracks using an automated methodology that does not rely on hands-on human visual inspection would benefit bridge owners and stakeholders as it has the potential to decrease the time and cost of performing inspections, as well as reduce the risk for inspectors and the traveling public. This methodology could potentially be used as a stand-alone tool, in conjunction with other inspection techniques, and/or as an early warning that will trigger more invasive manual inspections. Work described in this paper constitutes an important step to accomplishing this goal.

3.8 Acknowledgment

Funding for this study was provided in part through the Mid-America Transportation Center via a grant from the U.S. Department of Transportation's University Transportation Centers Program,

and this support is gratefully acknowledged. The views expressed in this paper are those of the authors, and do not reflect the position of the sponsoring agency.

3.9 Data Availability

Some or all data, models, or code generated or used during the study are available in a repository online in accordance with funder data retention policies (https://matc.unl.edu/research/research_search.php).

3.10 References

Abdel-Qader, I., Abudayyeh, O., and Kelly, M. E. (2003). "Analysis of edge-detection techniques for crack identification in bridges." *Journal of Computing in Civil Engineering*, 17(4), 255-263.

Al-Salih, H., Bennett, C., and Matamoros, A. (2021). "Evaluation of novel combined CFRP-steel retrofit for repairing distortion-induced fatigue." *Journal of Constructional Steel Research*, 182, 106642.

Al-Salih, H., Bennett, C., Matamoros, A., Collins, W., and Li, J. (2020). "Repairing Distortion-Induced Fatigue in Steel Bridges Using a CFRP-Steel Retrofit." *Structures Congress 2020*, 273-284.

Al-Salih, H., Juno, M., Collins, W., Bennett, C., Li, J., and Sutley, E. J. (2019). "Evaluation of a Digital Image Correlation Bridge Inspection Methodology on Complex Distortion-Induced Fatigue Cracking." *ICSI 2019 The 3rd International Conference on Structural Integrity*, Elsevier B.V., Funchal, Madeira, Portugal, 682-689.

Alemdar, F., Nagati, D., Matamoros, A., Bennett, C., and Rolfe, S. (2014 Part I). "Repairing Distortion-Induced Fatigue Cracks in Steel Bridge Girders using Angles-with-Plate Retrofit Technique, Part I: Physical Simulations." *Journal of Structural Engineering*, 140(5).

Alipour, M., Washlesky, S. J., and Harris, D. (2019). "Field Deployment and Laboratory Evaluation of 2D Digital Image Correlation for Deflection Sensing in Complex Environments." *J. Bridge Eng.*, 24(4).

American Association Of State Highway Transportation Officials (AASHTO) (2014). "AASHTO LRFD Bridge Design Specifications (8th Edition)."

ASTM International (2019). "Standard Specification for Carbon Structural Steel." *ASTM A36 / A36M-19,* West Conshohocken, PA,.

Busca, G., Cigada, A., Mazzoleni, P., and Zappa, E. (2014). "Vibration Monitoring of Multiple Bridge Points by Means of a Unique Vision-Based Measuring System." *An International Journal*, 54(2), 255-271.

Campbell, L. E., Connor, R. J., Whitehead, J. M., and Washer, G. A. (2020). "Benchmark for Evaluating Performance in Visual Inspection of Fatigue Cracking in Steel Bridges." *Journal of Bridge Engineering*, 25(1).

Carroll, J., Efstathiou, C., Lambros, J., Sehitoglu, H., Hauber, B., Spottswood, S., and Chona, R. (2009). "Investigation of fatigue crack closure using multiscale image correlation experiments." *Engineering Fracture Mechanics*, 76(15), 2384-2398.

Carroll, J. D., Abuzaid, W., Lambros, J., and Sehitoglu, H. (2013). "High resolution digital image correlation measurements of strain accumulation in fatigue crack growth." *International Journal of Fatigue*, 57, 140-150.

Cha, Y. J., Choi, W., and Büyüköztürk, O. (2017). "Deep learning-based crack damage detection using convolutional neural networks." *Computer-Aided Civil and Infrastructure Engineering*, 32(5), 361-378.

Correlated Solutions Inc. (2016). "Correlated Solutions VIC Suite [Computer Software]. Retrieved from https://www.correlatedsolutions.com/." Irmo, South Carolina USA, .

Dellenbaugh, L., Kong, X., Al-Salih, H., Collins, W., Bennett, C., Li, J., and Sutley, E. J. (2020). "Development of a Distortion-Induced Fatigue Crack Characterization Methodology Using Digital Image Correlation." *Journal of Bridge Engineering*, 25(9), 04020063.

Dhanasekar, M., Prasad, P., Dorji, J., and Zahra, T. (2019). "Serviceability Assessment of Masonry Arch Bridges Using Digital Image Correlation." *J. Bridge Eng.*, 24(2).

Federal Highway Administration (FHWA) (2004). "National bridge inspection standards." *Federal Register*, 69(239), 74419–74439.

Fisher, J. W. (1984). "Fatigue and fracture in steel bridges : case studies."

Hassel, H. L., Bennett, C. R., Matamoros, A. B., and Rolfe, S. T. (2013). "Parametric Analysis of Cross-Frame Layout on Distortion-Induced Fatigue in Skewed Steel Bridges." *J. Bridge Eng.*, 18(7), 601-611.

Hutt, T., and Cawley, P. (2009). "Feasibility of digital image correlation for detection of cracks at fastener holes." *NDT & E International*, 42(2), 141-149.

J´er´emie Rupil, St´ephane Roux, Fran¸cois Hild, and Vincent, L. (2011). "Fatigue microcrack detection with digital image correlation." *The Journal of Strain Analysis for Engineering Design*, 46(6), 492-509.

Kong, X., and Li, J. (2018). "Vision-Based Fatigue Crack Detection of Steel Structures Using Video Feature Tracking." *Computer-Aided Civil and Infrastructure Engineering*, 33(9), 783-799.

Küntz, M., Jolin, M., Bastien, J., Perez, F., and Hild, F. (2006). "Digital image correlation analysis of crack behavior in a reinforced concrete beam during a load test." *Canadian Journal of Civil Engineering*, 33(11), 1418-1425.

Liu, H. (2015). "A Finite-Element-Based Approach to Modeling Cracking & Repairs for Distortion-Induced Fatigue in Steel Bridges."Ph.D., University of Kansas, Ann Arbor.

Lorenzino, P., Beretta, G., and Navarro, A. (2014). "Application of Digital Image Correlation (DIC) in resonance machines for measuring fatigue crack growth." *Frattura ed Integrità Strutturale*, 8(30), 369-374.

Nowell, D., Paynter, R. J. H., and De Matos, P. F. P. (2010). "Optical methods for measurement of fatigue crack closure: moiré interferometry and digital image correlation." *Fatigue & Fracture of Engineering Materials & Structures*, 33(12), 778-790.

Pan, B., Tian, L., and Song, X. (2016). "Real-time, non-contact and targetless measurement of vertical deflection of bridges using off-axis digital image correlation." *NDT and E International*, 79, 73-80.

Reagan, D., Sabato, A., and Niezrecki, C. (2017). "Feasibility of using digital image correlation for unmanned aerial vehicle structural health monitoring of bridges." *Structural Health Monitoring*, 17(5), 1056-1072.

Rupil, J., Roux, S., Hild, F., and Vincent, L. (2011). "Fatigue microcrack detection with digital image correlation." *The Journal of Strain Analysis for Engineering Design*, 46(6), 492-509.

Sutton, M. A., Yan, J., Deng, X., Cheng, C.-S., and Zavattieri, P. (2007). "Three-dimensional digital image correlation to quantify deformation and crack-opening displacement in ductile aluminum under mixed-mode I/III loading." *Optical Engineering*, 46(5), 051003.

Vanlanduit, S., Vanherzeele, J., Longo, R., and Guillaume, P. (2009). "A digital image correlation method for fatigue test experiments." *Optics and Lasers in Engineering*, 47(3-4), 371-378.

Whitehead, J. (2015). "Probability of detection study for visual inspection of steel bridges." R. J. Connor, M. Bowman, and G. Washer, eds., ProQuest Dissertations Publishing.

Yamaguchi, T., and Hashimoto, S. (2010). "Fast crack detection method for large-size concrete surface images using percolation-based image processing." *Machine Vision and Applications*, 21(5), 797-809.

Yeum, C. M., and Dyke, S. J. (2015). "Vision-Based Automated Crack Detection for Bridge Inspection." *Computer-Aided Civil and Infrastructure Engineering*, 30(10), 759-770.

Yu, S.-N., Jang, J.-H., and Han, C.-S. (2007). "Auto inspection system using a mobile robot for detecting concrete cracks in a tunnel." *Automation in Construction*, 16(3), 255-261.

Yuan, Y., Huang, J., Peng, X., Xiong, C., Fang, J., and Yuan, F. (2014). "Accurate displacement measurement via a self-adaptive digital image correlation method based on a weighted ZNSSD criterion." *Optics and Lasers in Engineering*, 52, 75-85.

Zhang, R., and He, L. (2012). "Measurement of mixed-mode stress intensity factors using digital image correlation method." *Optics and Lasers in Engineering*, 50(7), 1001-1007.

Zhao, Z., and Haldar, A. (1996). "Bridge fatigue damage evaluation and updating using non-destructive inspections." *Engineering fracture mechanics*, 53(5), 775-788.

Zou, Q., Cao, Y., Li, Q., Mao, Q., and Wang, S. (2012). "CrackTree: Automatic crack detection from pavement images." *Pattern Recognition Letters*, 33(3), 227-238.

Chapter 4: **Evaluation of Three Computational Techniques for Quantifying Distortion-Induced Fatigue Crack Propensity Using Finite Element Analysis**

Hayder Al-Salih P.E.[1], Hao Liu, Ph.D., P.E.[2], John Przywara, P.E.[3], Caroline Bennett, Ph.D., P.E.[4], William Collins, Ph.D., P.E.[5], Jian Li, Ph.D., P.E. [6], Adolfo Matamoros, Ph.D., P.E.[7]

Abstract

In many bridges built prior to 1985, distortion-induced fatigue near transverse connection plate web-gaps is a serious problem. Many retrofits aimed at mitigating the effects of distortion-induced fatigue and stopping fatigue crack growth have been analyzed, both experimentally and computationally. When finite element analysis techniques are used, web-gap cracks may be modeled explicitly and stress-based analysis techniques such as the Hot Spot Stress (HSS) method may be used to evaluate retrofit performance. Inclusion of the extended finite element method (XFEM) in the finite element analysis software program Abaqus has enabled for modeling of changing discontinuities, including propagating fatigue cracks without the need for remeshing. Additionally, analytical computation of fracture mechanics-based parameters, such as the *J*-integral and stress intensity factors for multiple modes, K_I, K_{II}, and K_{III}, allow for accurate modeling of cracks. This paper presents the results from a suite of finite element simulations of girder-cross frame subassemblies, evaluating the three computational techniques (K, J, and HSS)

Department of Civil, Environmental, and Architectural Engineering
University of Kansas, 1530 W. 15th St, Lawrence, KS 66045
Tel. (785) 864-3235, Fax. (785) 864-5631

[1] Hayder Al-Salih, P.E., Graduate Research Assistant, University of Kansas, hia@ku.edu
[2] Hao Liu, P.E.,
[3] John Przywara, P.E.,
[4] Caroline Bennett, Ph.D., P.E., Corresponding Author, Professor, University of Kansas, crb@ku.edu
[5] William Collins, Ph.D., P.E., Associate Professor, University of Kansas, william.collins@ku.edu
[6] Jian Li, Ph.D., P.E., Associate Professor, University of Kansas, william.collins@ku.edu
[7] Adolfo Matamoros, Ph.D., P.E., Professor, University of Texas at San Antonio, adolfo.matamoros@utsa.edu

as tools for distortion-induced fatigue assessment. Benchmarked to previous experimental evaluations of the subassembly, the models are also used to numerically evaluate different retrofit thicknesses that were not evaluated experimentally. The FE models included simulation of several crack states modeled using XFEM and comparing them with actual crack growth data from a distortion-induced fatigue experimental specimen, both with and without the retrofit applied. The numerical parametric study evaluated the effectiveness of the different retrofit thicknesses in lowering the demand at the web gap region. The three computational measures (K, J, and HSS) were utilized in the simulations to analyze the performance of the retrofit with varying thicknesses. Results indicate the out-of-plane loading, Mode III, contributes to distortion-induced crack growth more than Modes I and II, and that equivalent Mode I stress intensity, K_{Ieq}, values computed from a combination of K_I, K_{II}, K_{III}, are equivalent to those obtained from the *J*-integral, with both correlating well with experimental behavior. Computational HSS values also predict fatigue crack demand and correspond with the findings of the experimental study. Results also showed the optimal component thickness for the angles-with-plate retrofit is 19 mm (0.75in.), which is more economic than the 25.4 mm (1 in.) thick retrofit with similar behavior.

Keywords:

Fatigue, Bridges, XFEM, *J*-integral, Stress Intensity Factor, Hot Spot Stress, Distortion-Induced Fatigue, Steel Bridges

4.1 Introduction

Distortion-induced fatigue cracking is one of the major threats to the longevity of steel highway bridges. In many bridges, a commonly-used detail to laterally transfer traffic loads and prevent lateral-torsional buckling during construction involves attaching cross-frames or diaphragms to transverse connection plates (Tedesco et al. 1995). In bridges built prior to 1985, transverse connection plates were typically not welded to tension flanges due to historic concerns

associated with susceptibility to brittle fracture (Castiglioni et al. 1988). However, the detail created by not attaching connection plates to adjacent flanges, known as the web-gap, has accounted for the greatest proportion of fatigue cracking in steel bridges (Jajich and Schultz 2003; Keating 1994). Distortion-induced fatigue is produced when a girder experiences greater in-plane bending deformation than an adjacent girder, such that significant out-of-plane stress concentrations are generated in the web-gap between the transverse connection plate and either flange during each loading cycle. In time, fatigue cracks initiate and propagate in web-gap regions, decreasing the fatigue life of the bridge and necessitating maintenance in the form of repair or retrofit.

Distortion-induced fatigue cracking is a failure mode that has proven difficult to repair because of two challenges: (1) selection of an effective and appropriate repair technique is challenging, and (2) adequate repairs are often difficult to properly implement.

Regarding the first challenge, repairing distortion-induced fatigue cracking is a difficult task because the performance of repair techniques has been shown to be sensitive to bridge layout and connection details (Hassel et al. 2013; Hassel et al. 2010). For this reason, custom repair solutions are often developed by engineers for distortion-induced fatigue cracking. To do this, finite element (FE) models are created for the bridge needing repair, and ideally the FE model is informed and complemented by field testing. This process is time-consuming and expensive, driven in large part by the need for complementing field studies which require specialized equipment and personnel. Nonetheless, this approach is often necessary because there is little guidance in the literature regarding appropriate modeling techniques and outputs that are well-correlated with predicting distortion-induced fatigue behavior or the performance of retrofits aimed at mitigating crack growth. If such guidance was available, costs associated with designing

effective repairs for distortion-induced fatigue would be significantly lower than they are today, because analytically-derived solutions would be associated with greater confidence.

Regarding the second challenge, many distortion-induced fatigue retrofits are difficult to correctly implement, and therefore are expensive. One of the most common retrofit mechanisms for providing an alternate load path around a web-gap region is to weld or bolt angles between the transverse connection plate and the adjacent girder flange. This kind of repair is commonly understood to be effective, but can necessitate removal of portions of the concrete bridge deck (Keating and Fisher 1987) (Fisher 1990).

The authors have been focused on developing solutions to both of these challenges. A recently developed repair technique for distortion-induced fatigue with significant installation advantages is the angles-with-plate retrofit technique, which provides connectivity between the transverse connection plate and the girder web but does not require removal of the concrete deck. A study was performed in which the angles-with-plate retrofit was applied to 2.7-m (9-ft) girder specimens, and results were examined to determine the effectives of the retrofit for repairing distortion-induced fatigue (Alemdar et al. 2014a; Alemdar et al. 2014b). This work was primarily focused on overcoming the challenges associated with retrofit installation. The study described in this current paper is focused on addressing the problem associated with the lack of information regarding analytical modeling of distortion-induced fatigue behavior and repairs, and both complements and expands upon the experimental dataset presented in Alemdar et al. (2014a).

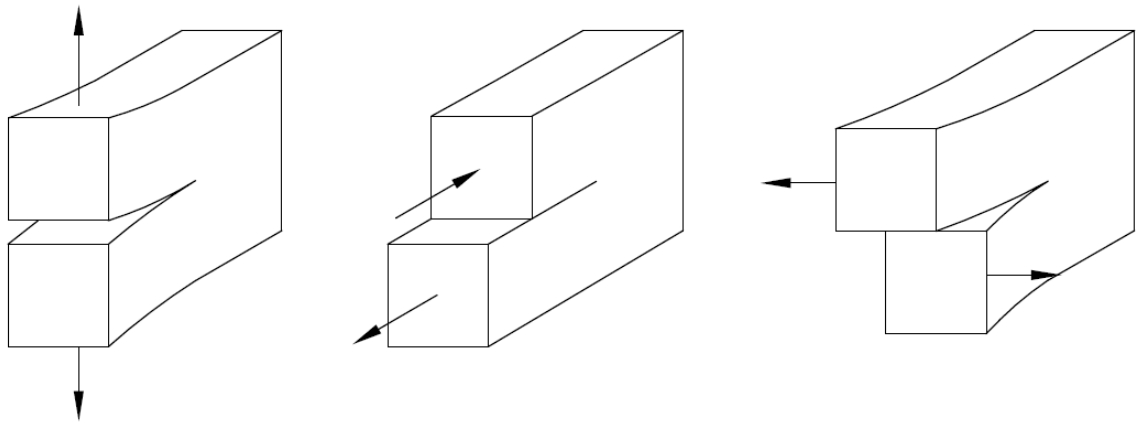

(a) (b) (c)

Figure 4-1: Crack opening (a) Mode I, (b) Mode II, and (c) Mode III

In contrast to in-plane fatigue where a nominal stress approach can be used to assess fatigue susceptibility, distortion-induced fatigue is an inherently mixed-mode problem. Because of this, a nominal stress approach cannot simply be applied to distortion-induced fatigue, and other computational techniques are needed to assess likelihood of crack propagation for both retrofitted and unretrofitted details. Three modes of fatigue crack deformation, Modes I, II, and III, describe the local deformation behavior ahead of the crack tip. Mode I is associated with tensile opening of the crack surfaces, Mode II describes in-plane shear of the crack surfaces, and Mode III refers to out-of-plane shear or tearing of the crack surfaces, as shown in Figure 4-1. In quantifying distortion-induced fatigue cracking propensity, it is critical to consider approaches that represent the three-dimensional loading demands that characterize distortion-induced fatigue.

4.2 Objective and Scope

The objectives of this study were twofold. The first objective was to evaluate three types of finite element analysis computational measures based on their predictive capabilities for characterizing distortion-induced fatigue cracking propensity in the web-gap region of bridge

girders. The three computational measures evaluated were modified Hot Spot Stresses (HSS), *J*-integrals, and Stress Intensity Factors, *K*. The second objective was to investigate the performance of angles-with-plate retrofits in terms of their ability to halt the propagation of distortion-induced fatigue cracking. This analytical study evaluated the impact of component thickness on retrofit efficacy, examining physical parameters not experimentally evaluated in previous studies.

To accomplish these objectives, detailed finite element models of experimentally-tested 2.7-m (9-ft) girder specimens were created using the commercially-available finite element modeling software Abaqus 2017 (SIMULIA 2017). These models included simulated cracks along the connection plate-to-web welds and the flange-to-web welds at varying lengths, and cases with and without a retrofit were considered. The three computational measures were examined and compared against results from physical testing to evaluate their suitability for predicting distortion-induced fatigue cracking propensity. Additionally, a parametric study using a suite of finite element models was conducted to evaluate the influence of differing component thicknesses utilized within angles-with-plate retrofits. The three computational measures of crack driving force (K, J, and HSS) were utilized in the simulations to evaluate the performance of the retrofit to determine the optimal component thickness resulting in the lowest demand in the web gap region.

4.3 Background and Computational Measures

Two different methods can be used to simulate web-gap cracks in the computational models created in the finite element modeling software Abaqus 2017. The first method involves explicitly modeling cracks by removing thin sections of elements in the web at crack locations. The second method utilizes components of the Extended Finite Element Method (XFEM) theory

available in Abaqus 2017, which can be used to model crack discontinuities independent of the model mesh.

The XFEM concept was first developed in 1999 (Moes et al. 1999) and implemented in v.6.9 of Abaqus. When cracking is simulated using XFEM, the discontinuity can be modeled independently from the mesh geometry. In other words, cracks can be modeled as occurring through individual elements as opposed to having to occur at element boundaries, and thus are mesh-independent. The XFEM algorithm accomplishes this by enhancing the finite element approximation by adding discontinuous functions to the solution at nodes in elements cut by a crack or a crack tip. XFEM was used in all the computational simulations of this study.

4.3.1 Hot Spot Stresses

A hot spot refers to a point where fatigue cracking is likely to initiate, such as a weld toe, and the HSS refers to the combined multi-directional stress at that point (Marquis and Kahonen 1996). Traditionally, HSS approaches have primarily been applied to uncracked details to characterize the likelihood of crack initiation. However, there is a clear need with distortion-induced fatigue to be able to assess the performance of retrofits on cracked bridge girders and to characterize the susceptibility of an unrepaired, cracked girder to further cracking. Therefore, the traditional HSS approach is adapted here for use in finite element models that include cracks near weld toes.

Since direct stress computations are mesh-sensitive and stresses of interest often occur within regions of geometric discontinuities and steep stress gradients, HSS are determined by extrapolating stresses at elements sufficiently away from the discontinuity to reduce mesh sensitivity error and to avoid stress singularity. A variety of methods exist to evaluate HSS in finite

element analyses (Adams 2010), and these methods have all been shown to be somewhat sensitive to mesh geometry (Bhargava 2010). To estimate fatigue stress demand in the vicinity of a weld toe, the HSS technique utilizes either a one-point procedure or a two-point extrapolation procedure. In the one-point HSS procedure, the stress values are extracted from a single point at a predetermined distance away from the weld toe. In the two-point procedure, stress is extracted at two predefined distances from the weld toe, and then a straight through line that passes through the two points is extrapolated until it intersects the weld toe. The extrapolated stress at this point is the HSS. The predefined distances in both procedures are usually a function of plate thickness or of plate thickness and weld length (Adams 2010; Bhargava 2010). Adams (2010) investigated many two-point and one-point HSS procedures for distortion-induced fatigue and concluded that the one-point procedure, with stresses extracted at a distance of one-half material thickness, $0.5t$, was a reasonable selection for distortion-induced fatigue applications. Therefore, in this study, a one-point analysis procedure was used.

4.3.2 *J*-integrals

A *J*-integral is an energy approach wherein behavior at a crack tip is inferred by computing relationships at an elastic region sufficiently removed from the plastic zone around the crack tip (Anderson 1995; Barsom and Rolfe 1999). In a purely elastic state, the *J*-integral is equivalent to the quantity *G*, which is the strain energy release rate per unit crack extension. This energy-based approach is attractive in cases such as this one, where the geometry is complex, and loading is multi-directional. The *J*-integral is computed in Abaqus 2017 by applying a surface integral that encloses the crack front from one crack surface to the other, and is represented by the following mathematical expression:

$$J(s) = \lim_{\Gamma \to 0} c_l(s) \int_{\Gamma(s)} \left(W \delta_{lj} - \sigma_{ij} u_{i,l}\right) n_j d\Gamma \quad (4\text{-}1)$$

Where s is a point along the crack front, Γ is any contour surrounding the crack, W is the work per unit volume done by loading, and σ_{ij} is the stress field (Rice 1968). The loading work per unit volume, W, is represented by the following expression:

$$W = \int_0^{\varepsilon} \sigma d\varepsilon \quad (4\text{-}2)$$

While computing the *J*-integral quantities may be useful for directly quantifying demand in the case of distortion-induced fatigue, where both loading, and geometry are complex, there is a need to transform the *J*-integral quantities into a framework where they can be benchmarked against resistance. The most practical way of accomplishing this is to transform *J* into an equivalent *K* value. This approach is also beneficial as most practicing engineers are more familiar with the concepts of stress intensity factors than the *J*-integral.

Since linear-elastic behavior was assumed for steel in this study, which is a reasonable assumption given that distortion-induced fatigue cracking generally occurs at low stress ranges within the elastic regime, the *J*-integral computed is the same as *G*. Therefore, a *J*-integral parameter, ΔJ_I, can be defined as the energy required to grow a crack and can be related to the Mode I stress intensity factor range, ΔK_I, by the following expression:

$$\Delta J_I = \Delta G_I = \frac{(1-\nu^2)\Delta K_I^2}{E} \quad (4\text{-}3)$$

Where E and ν are the elastic modulus and Poisson's ratio, respectively, and were taken as 200 GPa (29,000 ksi) and 0.3. Rearranging Equation 3 enables the computed *J*-integral range to be converted into an elastic-plastic equivalent Mode I stress intensity factor range, $\Delta K_{I,eq,(J)}$.

4.3.3 Stress Intensity Factors

The third analysis technique used in this study was the evaluation of Mode I, II, and III stress intensity factors: ΔK_I, ΔK_{II}, and ΔK_{III}. Abaqus uses an interaction integral method to extract the Mode I, II, and III stress intensity factors by relating the real and auxiliary stress fields (Shih and Asaro 1988). The interaction integral is given by the following expression:

$$I(s) = \lim_{\Gamma \to 0} c_l(s) \int_{\Gamma(s)} \left(\sigma_{ik} \varepsilon_{ik}^{aux} \delta_{lj} - \sigma_{ij} u_{i,l}^{aux} - u_{i,l} \sigma_{ij}^{aux}\right) n_j d\Gamma \quad (4\text{-}4)$$

Where σ_{ij}^{aux} is the auxiliary stress field, ε_{ij}^{aux} is the auxiliary strain field, and u_i^{aux} is the auxiliary displacement field. Abaqus computes the interaction integral and then substitutes the definitions of the actual and auxiliary fields into Equation 4-5 to yield an expression for the interaction integral in terms of the actual and auxiliary Mode I, II, and III stress intensity factors:

$$I(s) = \frac{2(1-\nu^2)}{E} (\Delta K_I \Delta K_I^{aux} + \Delta K_{II} \Delta K_{II}^{aux}) + \frac{1}{G} \Delta K_{III} \Delta K_{III}^{aux} \quad (4\text{-}5)$$

To determine ΔK_I, ΔK_I^{aux} was set to 1 while ΔK_{II}^{aux} and ΔK_{III}^{aux} were set to 0 (Gosz 2005). ΔK_{II} and ΔK_{III} were determined in the same manner.

Knowledge regarding the Mode I, II, and III stress intensity factors around a crack can provide descriptive information about the contribution of different modes of loading. However, material fatigue and fracture resistances are typically evaluated for Mode I. Therefore, to make a comparison between load and resistance, relationships must be applied to quantify the additional contribution of ΔK_{II} and ΔK_{III} on demand at the crack tip. Thus, the influence of Mode I, II, and III stress intensity factors at a crack could be examined as a single, equivalent $K_{I,eq(Ks)}$ range. Assuming material homogeneity and isotropy, the following equation can be derived from the *J*-integral expression provided by (Shih and Asaro 1988; Sih and Cha 1974; Sih and Macdonald 1974; SIMULIA 2017).

$$\Delta K_{I,eq(Ks)} = \sqrt[2]{(\Delta K_I^2 + \Delta K_{II}^2) + \frac{E}{2G(1-v^2)}\Delta K_{III}^2} \quad (4\text{-}6)$$

4.4 Finite Element Models

4.4.1 Girder-Cross Frame Subassemblies Models

All finite element models discussed in this paper were based off 2.7-m (9-ft) long experimental girder-cross frame assemblies used in physical testing. The subassemblies were designed to represent a segment of an external girder in a composite bridge. In a bridge, the top flange of the girder is restrained against lateral motion by the bridge deck. This boundary condition was simulated in the test by inverting the girder and bolting the top flange to a series of channels attached to the laboratory strong floor. One of the effects of supporting the girder in this manner is that longitudinal bending of the girder was prevented, leaving only out-of-plane loads applied via the cross-frame element. The resulting stress field is representative of the behavior near inflection points in bridges or points where the bending stresses due to live loads are very small compared to the stresses induced by out-of-plane forces.

Detailed three-dimensional finite element models were created using the commercially-available finite element modeling software Abaqus 2017 to simulate the behavior of the experimental test girders. The girders modeled in this study were 2.7-m (9-ft) long built-up I-sections, with an 876-mm x 10-mm (34 ½-in. x 3/8-in.) web, a 279-mm x 16-mm (11-in. x 5/8-in.) top flange, and a 279-mm x 25-mm (11-in. x 1-in.) bottom flange. 5-mm (3/16-in.) fillet welds were used to attach the flanges to the web. Three L76x76x10-mm (L3x3x3/8-in.) angles constituting the cross frame were attached to two 305-mm x 191-mm x 10-mm (12-in. x 7 ½-in. x 3/8-in.) gusset plates by 5-mm (3/16-in.) fillet welds, which were, in turn, bolted to a 876-mm x 127-mm x 10-mm (34 ½-in. x 5-in. x 3/8-in.) connection plate (CP). The connection plate was

welded all-around to the web with a 5-mm (3/16-in.) fillet weld but was not welded to either flange. The opposite end of the three angles constituting the cross bracing were bolted to a heavy WT section attached to an actuator that was used to apply a vertical load to the cross frame. The girder subassembly and the finite element model of the subassembly are shown in Figure 4-2. The actuator was modeled with steel properties and an 86x86-mm (3.4x3.4-in) square cross-section with a length of 584 mm (23 in.). It was capable of moving in the vertical plane, and a 22.2-kN (5-kip) linearly progressing upward load was applied to it to simulate half of one cycle of the actual loading.

All steel sections and welds were modeled as isotropic, linear-elastic materials having an elastic modulus of 200 GPa (29,000 ksi) and a Poisson's ratio of 0.3. The laboratory floor was the only component of the finite element models modeled as concrete, and it was simulated to be an isotropic, linear-elastic material with an elastic modulus of 27,780 MPa (4,030 ksi) with Poisson's ratio taken as 0.2.

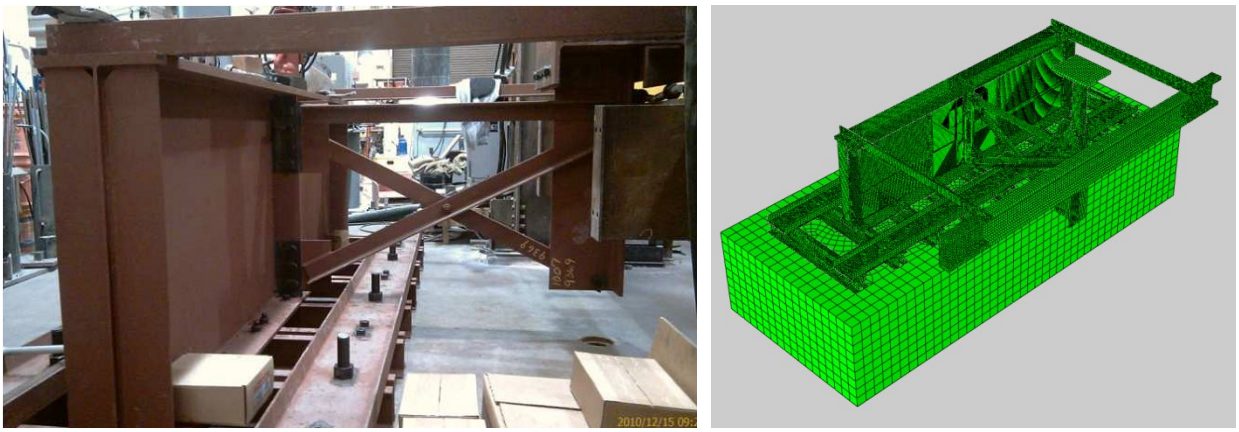

(a) (b)

Figure 4-2: (a) Experimental girder subassembly and (b) the finite element model of the test setup

4.4.2 Elements, Meshes, Contacts and Cracks

Eight-node, linear brick elements (C3D8R) each with 24 degrees of freedom were used wherever possible to model the physical geometry. In some instances, four-node, tetrahedral elements having 12 degrees of freedom were utilized to conform to special geometric aspects of the set-up. All fillet welds were modeled as right triangle cross-sections and tie constraints were used to connect the fillet welds to the surfaces that they joined.

A finer mesh was used near the connection plate in the web gap region where fatigue damage occurred, while a coarser mesh was used away from the connection region. A mesh convergence study was conducted to investigate the effect of element size on the stress in the web gap region, and it was found that the mesh was well-converged at an element size of 0.635 mm (0.025 in.) in the densest region. The mesh transitioned to a coarser mesh 2.54 mm (0.1 in) around the web gap region, then transitioned to the coarsest mesh of 9.5 mm (0.375 in) for the remainder of the web.

Surfaces in the model expected to make contact with one another were assigned interaction properties with a coefficient of friction of 0.35 to simulate hard contact.

Cracks were modeled using XFEM and crack lengths and locations were chosen based on observed cracks in experimental specimens. As shown in Figure 4-3, cracks were observed to occur in two locations: around the CP-to-web weld (Type 1) and along the flange-to-web weld (Type 2). In the web gap region, Crack Type 1 is also often referred to as a U-shaped, horseshoe, or vertical crack, and Crack Type 2 is often referred to as a horizontal crack. All cracks were modeled as through-thickness. Each crack was modeled as being a small distance ($0.5t$ = 4.8mm [0.1875 in.], or six elements) away from the weld toe. This is an important necessity when K and

J values are to be computed, as there must be enough elements between the crack tip and other points of discontinuity to ensure convergence of the *K* and *J* computations.

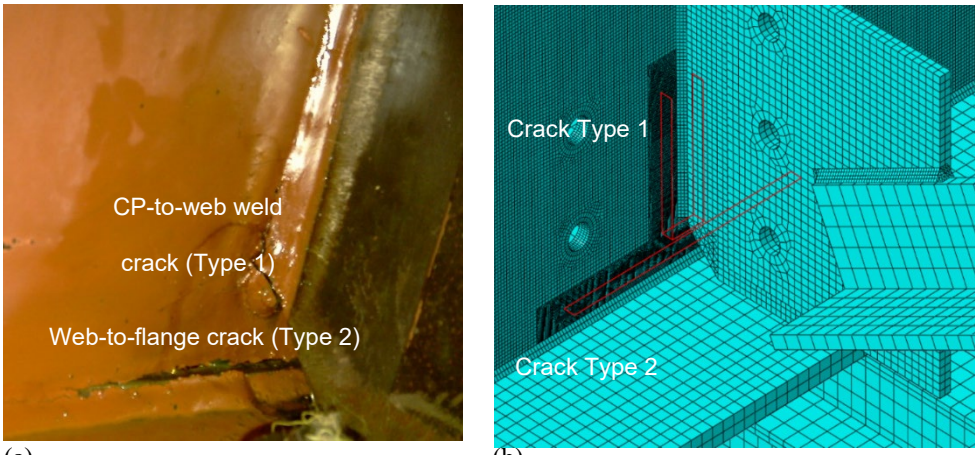

(a) (b)

Figure 4-3:(a) Cracks on the experimental girder subassembly and (b) cracks in the FE model of the subassembly

4.4.3 Models Names, Cracks, and Retrofits Combinations

Several different crack combinations were modeled to compare against physical testing. Experimental testing of the retrofits was performed for multiple crack lengths. Nine combinations of Type 1 and Type 2 cracks were employed in this study as described in Table 4-1. It should be noted that the length "a1" of the Type 1 crack, refers to the length of one leg of the "U" shape, and the length "a2" of the Type 2 crack, refers to half of the horizontal crack on one side of the connection plate.

For each of these crack combinations, three variations of the angles-with-plate retrofit were investigated, each with angles L152x127x*t* mm (L6x5x*t* in.) and a backing plate 457x203x*t* mm (18x8x*t* in.). The thickness of the angle and backing plate, *t*, was considered to be 13-mm (1/2-in.) noted as 0.5R, 19-mm (3/4-in.) noted as 0.75R, and 25-mm (1-in.) noted as 1.0R. The version of the angles-with-plate retrofit tested experimentally had *t*=19-mm (¾-in.), and the other two

thicknesses were modeled to bound the behavior of the tested retrofit. Models with each combination of cracks but no retrofit (noted as UR) were also examined, as well as one model representing the uncracked, unretrofitted configuration of the girder, noted as UR-UC. Therefore, a total of 33 models were examined, one uncracked model and 32 cracked models (8 of them unretrofitted and 24 retrofitted), the cracked models divided into two groups, one has a1=2a2 and the other has a1=a2. Results from these simulations were compared with the experimental observations. Figure 4-4 shows the angles and back plate layout

Table 4-1 Summary of modeled crack combinations and retrofits

Crack Combinations	Type 1, a1 mm (in.)	Type 2, a2 mm (in.)	(UR) UnRetrofitted	(0.5R)Retrofit of 13 mm (0.5in.)	(0.75R) Retrofit of 19 mm (0.75in.)	(1.0R) Retrofit of 25 mm (1.0in.)
UnCracked (UC)	0 (0)	0 (0)	UR-UC			
a1=2a2=0.5	13 (0.5)	6 (0.25)	UR-a1=2a2=0.5	0.5R-a1=2a2=0.5	0.75R-a1=2a2=0.5	1.0R-a1=2a2=0.5
a1=2a2=1	25 (1)	13 (0.5)	UR-a1=2a2=1	0.5R-a1=2a2=1	0.75R-a1=2a2=1	1.0R-a1=2a2=1
a1=2a2=2	51 (2)	25 (1)	UR-a1=2a2=2	0.5R-a1=2a2=2	0.75R-a1=2a2=2	1.0R-a1=2a2=2
a1=2a2=4	102 (4)	51 (2)	UR-a1=2a2=4	0.5R-a1=2a2=4	0.75R-a1=2a2=4	1.0R-a1=2a2=4
a1=a2=0.5	13 (0.5)	13 (0.5)	UR-a1=a2=0.5	0.5R-a1=a2=0.5	0.75R-a1=a2=0.5	1.0R-a1=a2=0.5
a1=a2=1	25 (1)	25 (1)	UR-a1=a2=1	0.5R-a1=a2=1	0.75R-a1=a2=1	1.0R-a1=a2=1
a1=a2=2	51 (2)	51 (2)	UR-a1=a2=2	0.5R-a1=a2=2	0.75R-a1=a2=2	1.0R-a1=a2=2
a1=a2=4	102 (4)	102 (4)	UR-a1=a2=4	0.5R-a1=a2=4	0.75R-a1=a2=4	1.0R-a1=a2=4

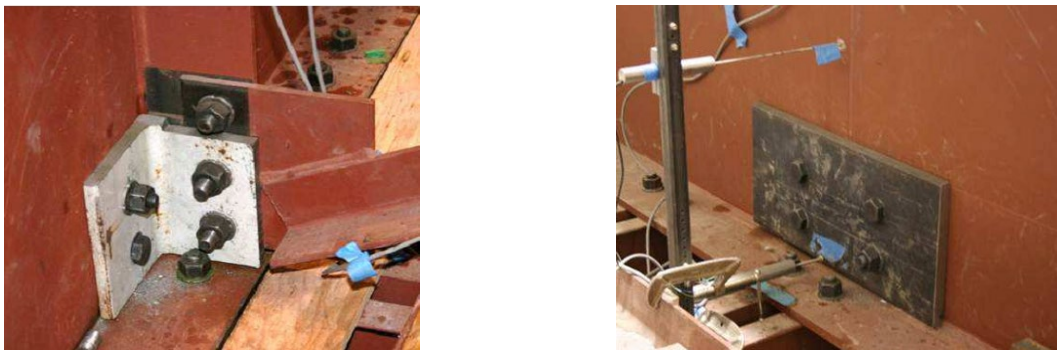

(a) (b)

Figure 4-4: Angles-with-plate retrofit: (a) Angles layout; (b) Back plate layout

4.5 Computational Measures Details

4.5.1 Hot Spot Stresses Characterization

As mentioned previously, observation of the experimental test girders showed that distortion-induced fatigue resulted in two primary cracking patterns along welds in the bottom web gap of the specimens. One crack formed a U-shape around the CP-to-web weld in the web base metal (Type 1), while the other ran horizontally along the flange-to-web weld, also in the web base metal (Type 2). Consequently, path1 was used to determine the peak stress for the Type 1 and path2 was used to determine the peak stress for the Type 2.

Directional stresses, shear stresses, von Mises, maximum principal stress, mimium principal stress and absolutate maximum principal stress were extracted from the two HSS paths in the web gap region to evaluate each as an indicator for crack propensity, see Figure 4-5. The stress patterns for S11, S22, and S33 corresponded reasonably favorably to the experimentally-observed crack patterns (Figure 4-3 (a)), and shared similar patterns with each other, but varied magnitudes. The plot of von Mises stresses also appeared reasonable when compared against physical observations, however, it does not reveal differences between tensile and compression; for instance, the region nearby the web-to-flange crack is shown as red on the interior side, but it is representative of compressive stresses rather than tensile. All stress patterns for S11, S22, and S33 show that web-to-flange crack is under compression on the interior side and under tension on the fascia side. Also, von Mises stresses appeared to over-predict stresses at the fascia side of the stiffener, where cracking did not ever first initiate in physical tests. The maximum principal stress distribution was found to have the best correlation with crack patterns observed in the experimental specimens, and the analytical stresses match those measured from strain gauge No. 4, located in

web gap region 16.5 mm (0.65 in.) from the CP. Therefore, peak maximum principal stress was extracted along each of these paths to determine the two stress values used in the HSS analyses. Other researchers have adopted the use of maximum principal stresses in HSS analyses of DIF applications Adams (2010); Alemdar et al. (2014b); Hartman et al. (2013); Hartman et al. (2010); Liu (2015); Przywara (2013)

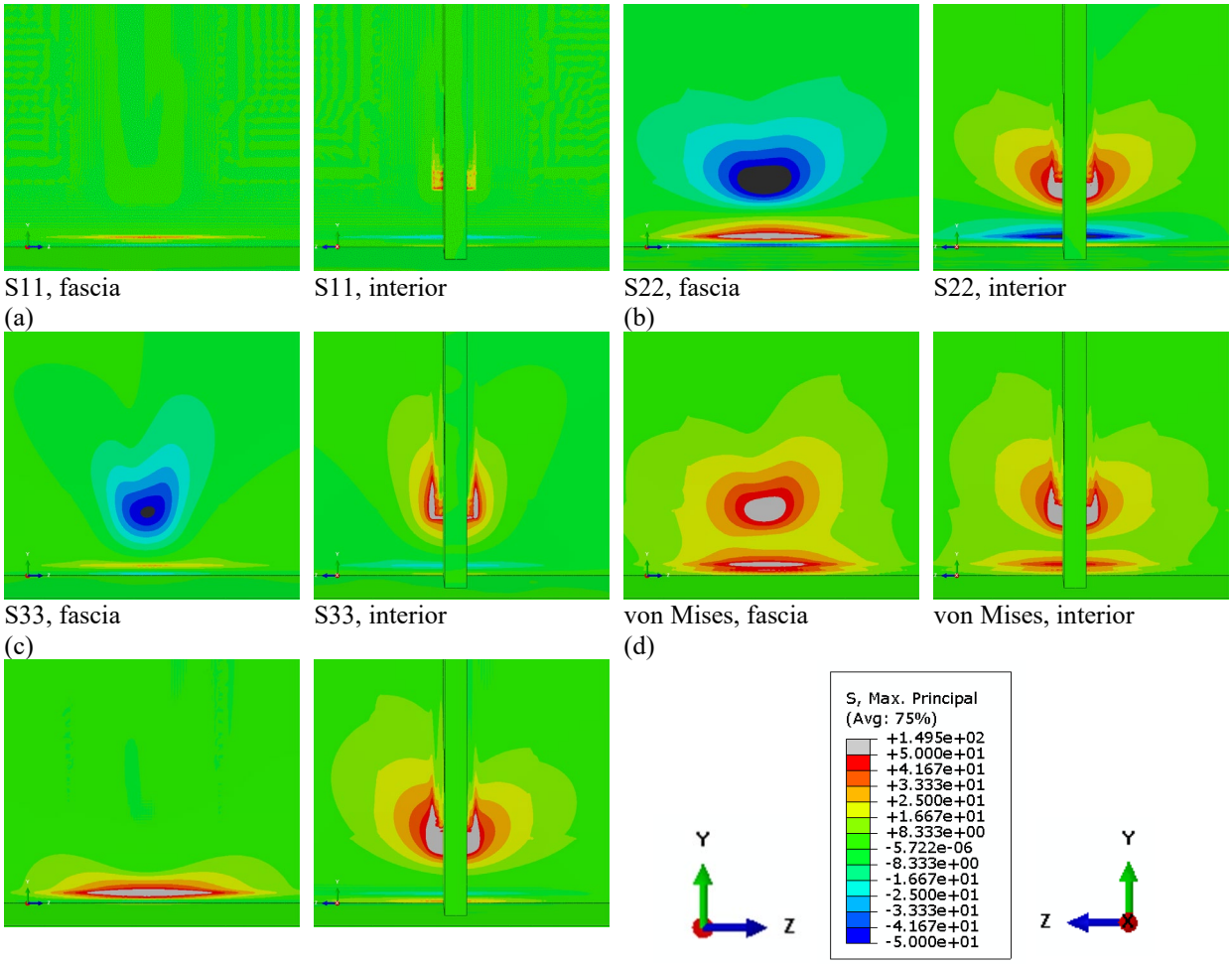

S11, fascia
(a)

S11, interior

S22, fascia
(b)

S22, interior

S33, fascia
(c)

S33, interior

von Mises, fascia
(d)

von Mises, interior

Max principal stress, fascia
(e)

Max principal stress, interior

Directions, interior

Directions, fascia

Figure 4-5: Different stresses on the web gap region on the fascia side and interior, (a)S11, (b) S22, (c) S33, (d) von Mises, (e) Max principal stress

4.5.2 Convergence of J and K Computations

It is important to ensure that contour integrals taken for the determination of the *J*-integral and *K* values are removed enough from the crack tip to provide a realistic estimate of demand. A convergence study for *J*-integral and *K* values was performed; Figure 4-6 shows a typical example of contours around a crack tip for the *J*-integral for the unretrofitted model with a1=102-mm (4-in.) CP-to-web crack and a2= 102-mm (4-in.) web-to-flange crack. The mesh size around the crack tip was 0.635-mm (0.025-in). It was found that the results for *K* and *J* were well-converged by the third contour (third ring of elements at distance of 1.91 mm (0.075in.) from crack tip), and thus values were extracted at Contour 3 for all models.

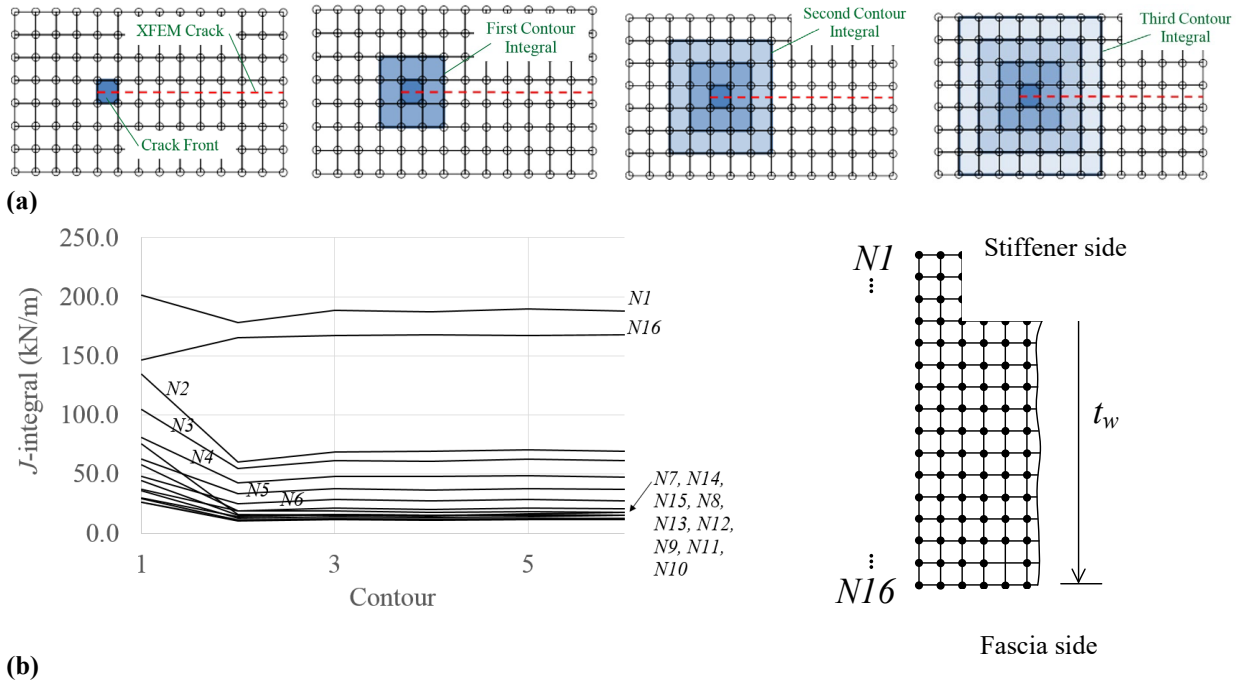

Figure 4-6: (a) Illustration of how contour integrals were taken in a finite element convergence study for *J*-integral values (Contours 1-6) through-thickness (Nodes 1-16) of the unretrofitted model with a1=102-mm (4-in.) Type 1 and a2=102-mm (4-in.) Type 2 cracks

Sixteen values each for *K* and *J* were computed through the thickness of the web at Contour 3, since the web mesh was fifteen elements (sixteen nodes) thick. Data was ignored for the first, second, fifteenth and sixteenth contours (nodes associated with the extreme elements) because

those results were found to be impacted by the contact constraint between the web and the angles & back plate. Finally, the remaining twelve through-thickness values were averaged for the final result.

4.6 Results and Discussion

4.6.1 Experimental Results

Tests on four physical girder-to-cross frame specimens were performed and the results are used for comparison with computational techniques. Each test was conducted by first initiating cracks in the web gap region of the specimen, and then performing a series of trials, alternating the unretrofitted condition so that cracks could freely initiate and propagate, and the retrofitted condition. Since cracking was allowed to freely propagate in the unretroffited state after each retrofitted trial, testing each retrofitted trial incorporated different crack lengths. Loading was applied to each retrofitted test trial for 1.2 million cycles. The unretrofitted trials were shorter and varied in duration, depending on crack propagation rates. A detailed exploration of the physical testing program is provided in (Al-Salih et al. 2021; Al-Salih et al. 2020; Alemdar et al. 2014a). Figure 4-7 presents the crack propagation data for one of the four specimens (Specimen 3) with crack lengths approximately matching those of the FE models. Crack growth rates in Figure 4-7 show that cracks propagated very rapidly during unretrofitted trials, as indicated by the line segments with a steep slope. No observed crack propagation occurred in the bottom web-gap during each 1.2 million cycle trials with the retrofit in place, as indicated by the horizontal line segments. This behavior is indicative of all experimental specimens, and full detailed results and discussion of the physical testing program are provided in Alemdar et al. (2014a)

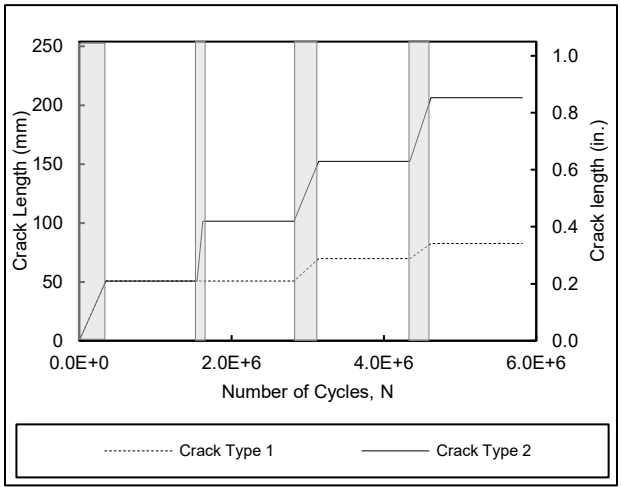

Figure 4-7: Crack propagation data for specimen 3 in both retrofitted and unretrofitted conditions (Alemdar et al. 2014a)

4.6.2 Hot Spot Stresses

Numerical model geometries approximated crack locations of the physical test specimens. Cracks were modeled at a distance equal to half the web thickness (0.5*t*=4.8mm [0.185 in.]) away from the weld toe, so maximum principal stresses were extracted from two paths along the two cracks at distances slightly greater than 0.5*t* from each of the cracked weld toes. Two distances were adapted 0.53*t* [5mm (0.2in.)] and 0.6*t* [5.7mm (0.225in.)]. Path1 that was used to determine the peak stress for the Type 1 crack paralleled the U-shaped crack path around the connection plate-to-web weld for a length of 284-mm (11.2-in.) which represent the longest U shape crack of 102mm (4-in) along both sides of the connection plate plus 25mm (1-in) beyond the crack tips from each side. Path2 that used to determine the peak stress for the Type 2 crack paralleled the horizontal path along the flange-to-web weld for a length of 254-mm (10-in.) which represent the longest horizontal crack 203-mm (8-in) plus 25mm (1-in) beyond the crack tips from each side, see Figure 4-8. Each of Path1 and Path2 were extracted on both of stiffener and fascia sides at 0.53*t* and 0.6*t*. Therefore, 0.53tPath1S represent Path1 on stiffener side at 0.53*t* distance and

0.6tPath2F represent Path2 on fascia side at 0.6t distance. From the stress contours Figure 4-5 (e) and from the maximum principal stresses distribution along the paths it has been found the most critical spots are on stiffener side for crack Type1 and on fascia side for crack Type2. Also, from the extracted paths results comparison it has been found that the most critical paths are the ones with closer distance to the crack (i.e. at 0.53t), hence 0.53tPath1S and 0.53tPath2F are the critical paths.

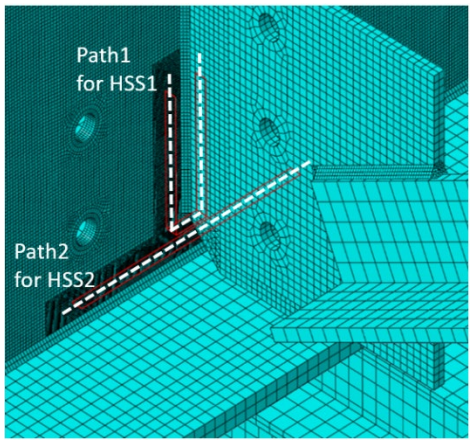

Figure 4-8: Paths for HSS along Crack Type1 and Crack Type2

To avoid the severe stress spikes in the HSS data corresponding to the location of crack tips, results from the data extraction path were truncated at different distances, TD, from the tips of the crack. After the data were truncated the maximum value of the remaining data represents the HSS. It has been found that the stress to the outside of the crack (beyond the crack tip) is distributed better than to the inside of the crack. Additionally, 2 mm (0.075 in.) is the same distance from the crack tip that the K and J values were extracted, providing consistency between the different analytical methods.

Figure 4-9 shows the modified Hot Spot Stresses as a function of Type 1 and Type 2 crack lengths. It is important to note that Type 1 and Type 2 cracks were modeled as occurring simultaneously, reflecting observations from experimental tests. For the scenario in which there was no retrofit,

Figure 4-9 (a) and (b) shows that the hot spot stresses increased significantly at both welds of interest for longer crack combinations, and that the stresses were always higher at Crack Type 1 than at Crack Type 2, indicating higher crack driving demand at this location. However, it can be observed that the slope of HSS generally deceases with increasing crack length, indicating a reduced crack driving demand. This is consistent with observed experimental results, as crack growth rates were reduced as cracks extended, as seen in Figure 4-7. The crack propagation data in Figure 4-7 is typical of that observed for all specimens and is fairly well-predicted by the FE-derived HSS trends with increasing crack length.

The HSS data for retrofitted conditions in Figure 4-9 (a) and (b) is much lower in magnitude than for unretrofitted conditions, and tends to decrease with crack length, which imply that the retrofit works very well at distributing stress demand at the crack tip, reducing crack propagation. This behavior was corroborated by the experimental data as propagation of cracks occurred at both the CP and the web-to-flange welds during unretrofitted trials, as presented in Figure 4-7, and no crack growth occurred in the retrofitted condition for any crack length. Therefore, the HSS data for both the retrofitted and unretrofitted conditions match the physical test results, indicating HSS could be used to predict distortion-induced fatigue damage propensity.

Figure 4-9 (c) presents the ratio of Crack Type 1 and Crack Type 2 hot spot stresses in the unretrofitted condition. It is clear from this figure that there is an interaction between the Type 1 and Type 2 cracks at shorter crack lengths. This interaction is due to the proximity of the two crack tips at short crack lengths. As the cracks propagate, the crack tips move farther from each other, minimizing this interaction effect. Figure 4-9 (d) presents the percent of reduction in HSS due to the application of the 19 mm (0.75 in.) thick retrofit (0.75R). The data indicate the retrofit has a

much higher effect at reducing the HSS at longer crack lengths, which is consistent with trends seen on Figure 4-9 (a) and (b), and also align with experimental observations.

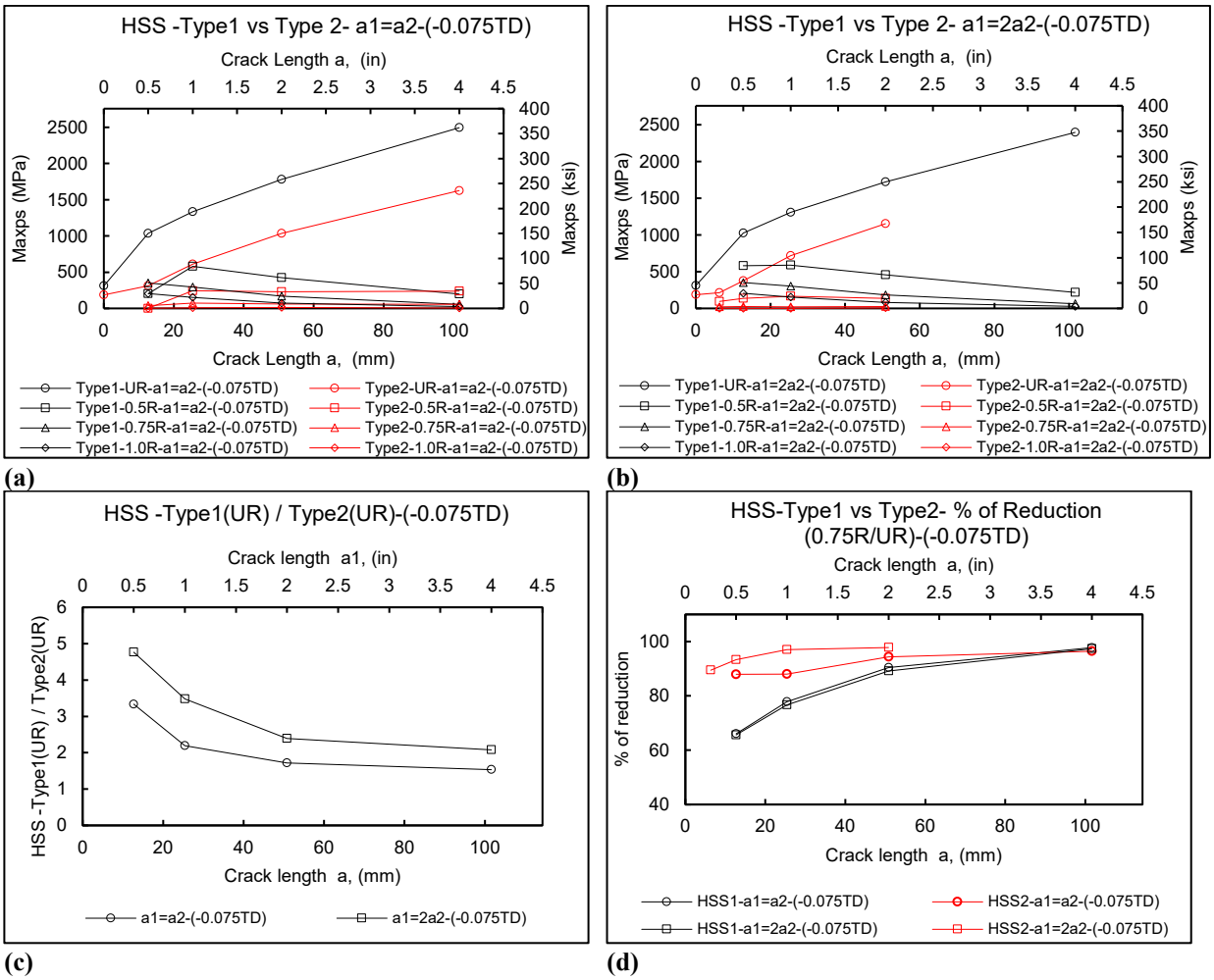

Figure 4-9: (a) HSS -Type1 vs Type 2- a1=a2-(-0.075TD); (b) HSS -Type1 vs Type 2- a1=2a2-(-0.075TD); (c) HSS -Type1(UR) / Type2(UR)-(-0.075TD); (d) HSS-Type1 vs Type2- % of Reduction (0.75R/UR)-(-0.075TD)

4.6.3 Stress Intensity Factors

As previously mentioned, the values for different modes of K (K_I, K_{II}, and K_{III}) were well-converged by the third contour (third ring of elements at distance of 1.91 mm (0.075in.) from crack tip), and thus values were extracted at Contour 3 for all models. The Mode I, Mode II, and Mode

III stress intensity factors (K_I, K_{II}, and K_{III}) compared for the Type 1 and Type 2 cracks for unretrofitted models as well as retrofitted models are presented in Figure 4-10 (a)-(f) . Results indicates that for longer crack combinations in unretrofitted condition, the K (K_I, K_{II}, and K_{III}) values increased significantly at both welds of interest. However, as crack lengths increase, the rate of change of stress intensity, represented by the slope of K, decreases, indicating a lower crack driving demand. This is consistent with the HSS findings. This is supported by experimental findings, which show that when cracks get longer, crack growth rates decreased, as shown in Figure 4-7. Results indicated that Mode III loading, the out-of-plane tearing mode, is the predominant driving demand for both Type 1 and Type 2 cracks, as seen in Figure 4-10 (e) and (f). This is consistent with observations of out-of-plane deformations in unretrofitted web-gaps. Results showed that the K_{III} values for Crack Type 1 were always greater than K_{III} values for Crack Type 2, indicating that Crack Type 1 experiences more crack driving demand than Crack Type 2. This is consistent with the findings of the HSS analyses.

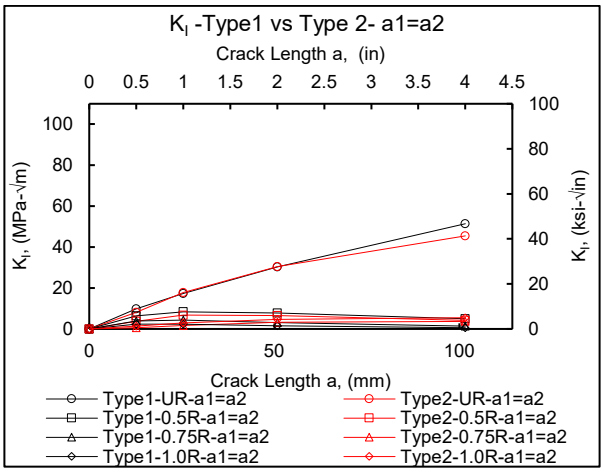

(a)

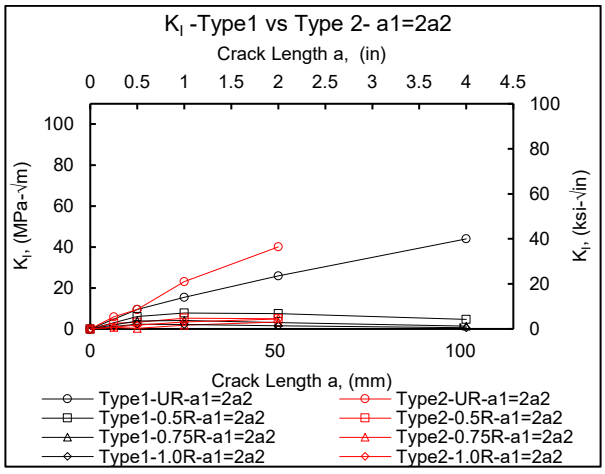

(b)

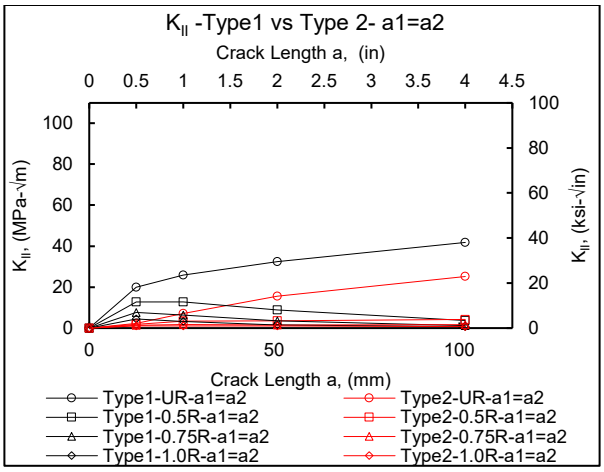

(c)

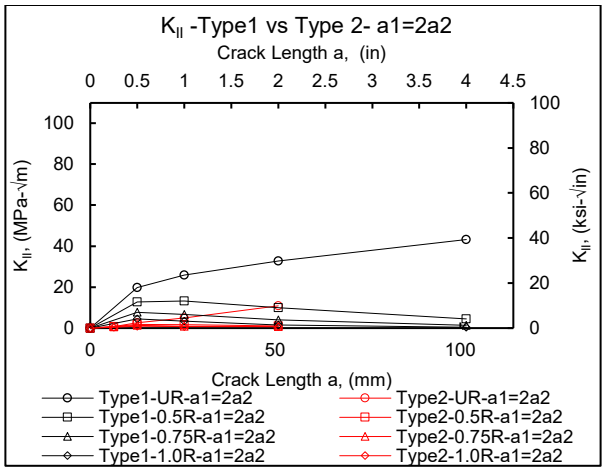

(d)

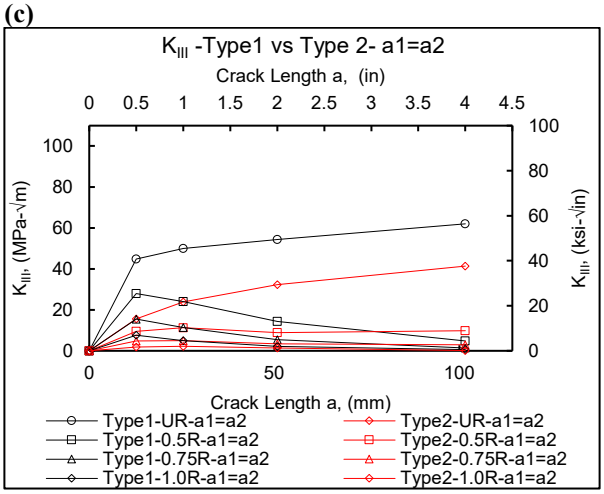

(e)

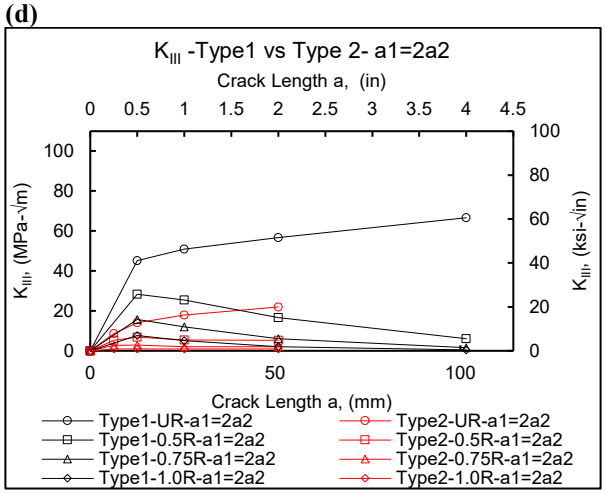

(f)

Figure 4-10: Stress intensity factors: (a) K_I -Type1 vs Type 2- a1=a2; (b) K_I -Type1 vs Type 2- a1=2a2 ; (c) K_{II} -Type1 vs Type 2- a1=a2 ; (d) K_{II} -Type1 vs Type 2- a1=2a2 ; (e) K_{III} -Type1 vs Type 2- a1=a2 ; (f) K_{III} -Type1 vs Type 2- a1=2a2

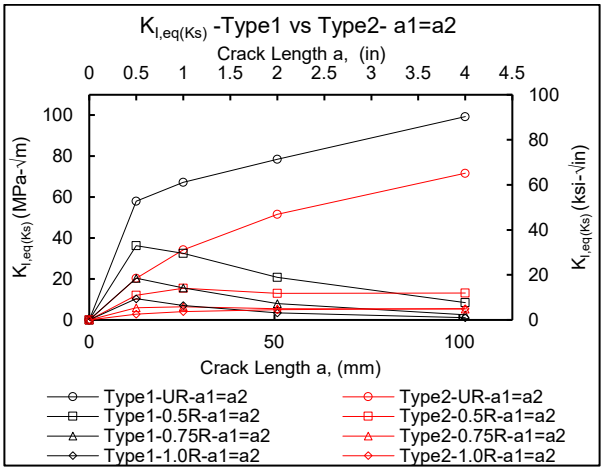

(a)

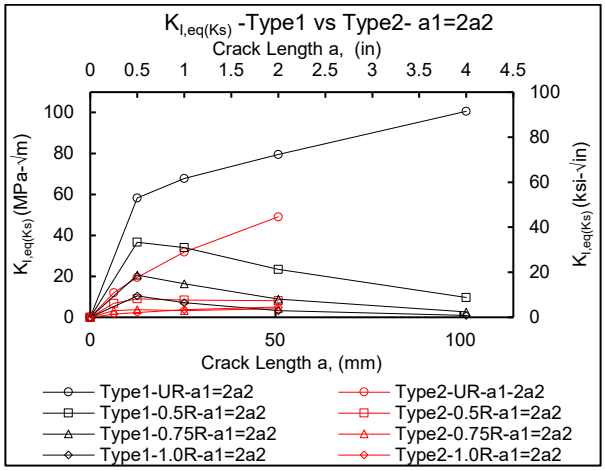

(b)

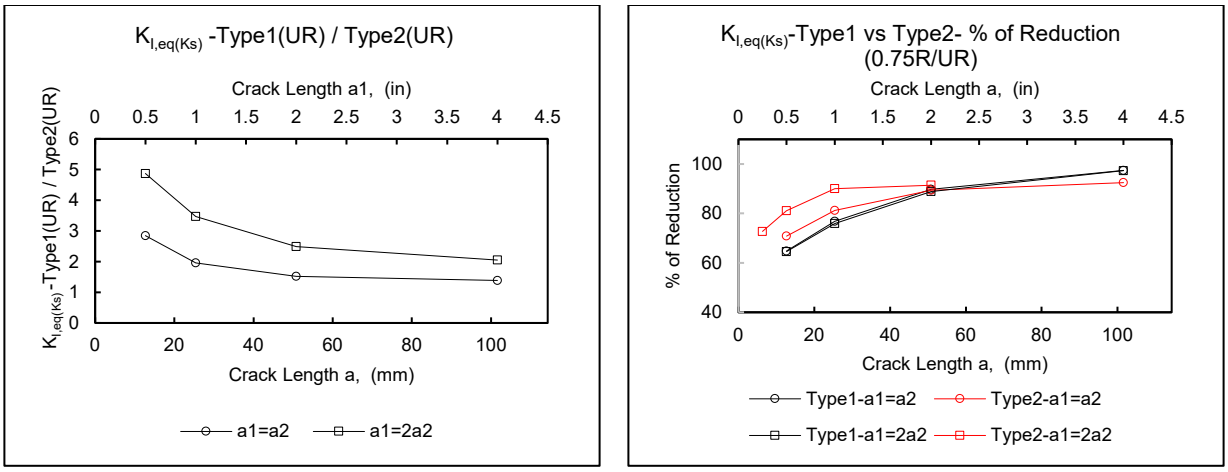

(c) **(d)**

Figure 4-11: Stress intensity factors: (a) $K_{I,eq(Ks)}$ -Type1 vs Type 2- a1=a2 ; (b) $K_{I,eq(Ks)}$ -Type1 vs Type 2- a1=2a2; (c) $K_{I,eq(Ks)}$ -Type1(UR) / Type2(UR); (d) $K_{I,eq(Ks)}$-Type1 vs Type2- % of Reduction (0.75R/UR)

Figure 4-11 (a) and (b) present the computed equivalent Mode I stress intensity factors, $K_{I,eq,(Ks)}$, comparing Type 1 and Type 2 cracks for both the unretrofitted and retrofitted conditions. The $K_{I,eq,(Ks)}$ results indicated there was a high propensity for crack growth in the unretrofitted condition for all crack lengths studied. However, similar to the HSS results and consistent with experimental observations, the demand decreases with crack extension. With the retrofit in place, the values for $K_{I,eq(Ks)}$ were significantly reduced, and the level of retrofit effectiveness was influenced by crack length, see Figure 4-11 (a) and (b). The $K_{I,eq(Ks)}$ results for the 19-mm (3/4-in.) thick retrofit were dramatically smaller than for the unretrofitted case for all crack lengths.. These findings indicate that little or no fatigue crack growth should occur under the retrofit, resulting in a favorable comparison with the experimental results.

The ratio of $K_{I,eq(Ks)}$ for Type 1 and Type 2 unretrofitted cracks is presented in Figure 4-11 (c). Similar to the behavior observed in the HSS analyses, the figure shows there is an interaction between Type 1 and Type 2 cracks at shorter crack lengths. Again, this is because the tips of each crack type are close to each other at shorter crack lengths, causing this interaction between the stress intensity factors. As the crack lengths increase, the crack tips move further apart, minimizing

this interaction effect. Figure 4-11 (d) illustrates the percent reduction in $K_{I,eq(Ks)}$ caused by the 19 mm (0.75 in.) thick retrofit (0.75R). The plot shows that the retrofit has a considerably greater effect in reducing $K_{I,eq(Ks)}$ in the longer crack lengths, which is consistent with experimental observations.

4.6.4 *J*-integrals

Similar to extracted stress intensity values, the *J*-integral values were well-converged by the third contour (third ring of elements at distance of 1.91 mm (0.075 in.) from crack tip), so values were extracted at Contour 3 for all models. The computed *J*-integrals compared for Type 1 and Type 2 cracks for retrofitted and unretrofitted conditions are presented in Figure 4-12 (a) and (b). It is clear from the figure that the difference between the *J*-integral values for unretrofitted models and retrofitted models became larger with increasing crack length. This finding indicated that the level of improvement experienced due to the retrofits increased with increasing crack length, which is consistent with the results of both the HSS and stress intensity analyses.

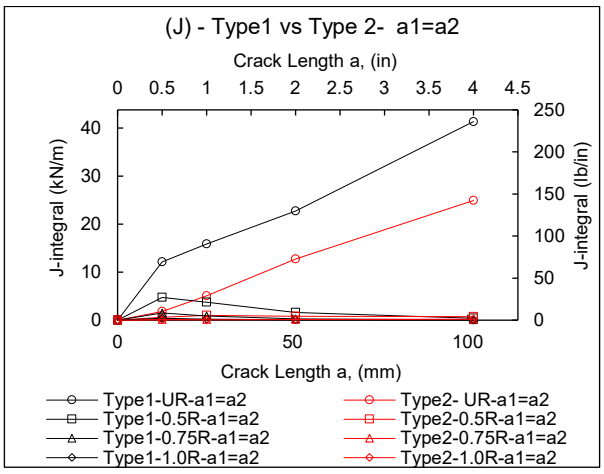

(a)

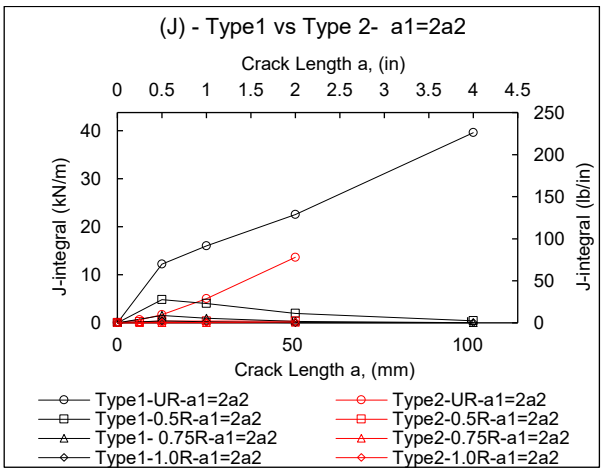

(b)

Figure 4-12: (a) *J*-integrals - Type1 vs Type 2- a1=a2 ; (b) *J*-integrals - Type1 vs Type 2- a1=2a2

Figure 4-13(a) and (b) present the *J*-integral values converted into equivalent Mode I stress intensity factors, $K_{I,eq(J)}$, for Type 1 and Type 2 crack for retrofitted and unretrofitted conditions. For all crack lengths investigated, the $K_{I,eq(J)}$ results showed a significant propensity for crack growth in the unretrofitted condition. However, the demand reduces with crack extension, aligning with both HSS and K results, as well as experimental observations. The $K_{I,eq(J)}$ results for all three retrofit thicknesses indicated a significant improvement over unretrofitted performance, thus predicting that little or no crack propagation would occur in the retrofitted condition. This was corroborated by the experimental results, as no crack propagation occurred in the retrofitted condition for any crack length.

Error! Reference source not found. (c) presents the ratio of $K_{I,eq(J)}$ in the unretrofitted state between Type 1 and Type 2 cracks. Similar to previous results, an interaction between the two crack types is seen at shorter crack lengths, with this behavior dissipating as cracks extend. The percent of reduction in $K_{I,eq(J)}$ due to the 19 mm (0.75 in.) thick retrofit (0.75R) is shown in **Error! Reference source not found.** (d). Again, similar to the results from HSS and stress intensity, the plot reveals that the retrofit is more effective at lowering the demand in longer crack lengths, which is in line with experimental findings.

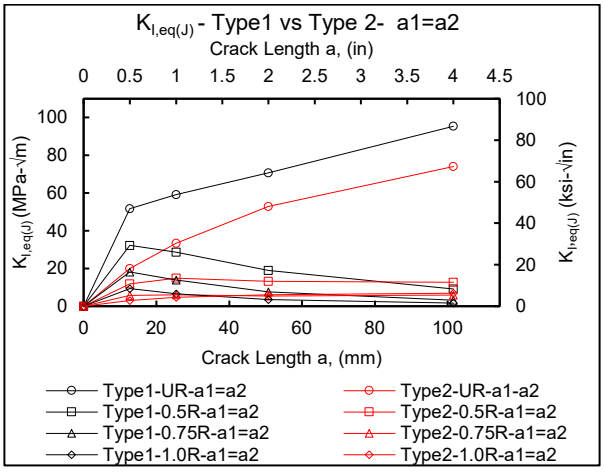

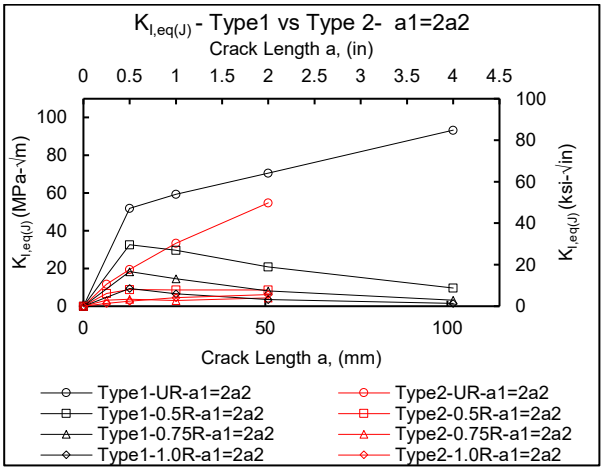

(a)

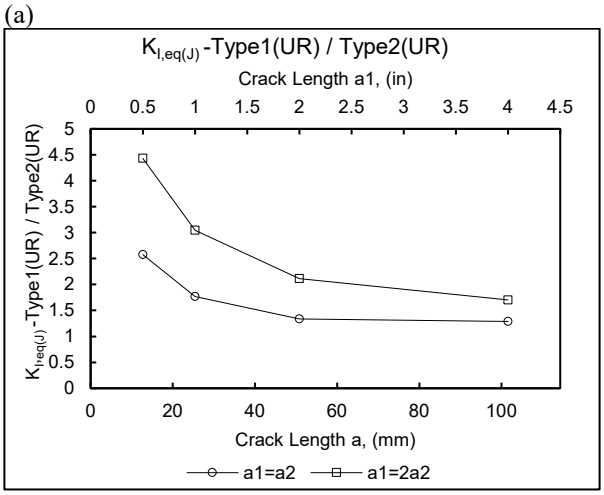

(b)

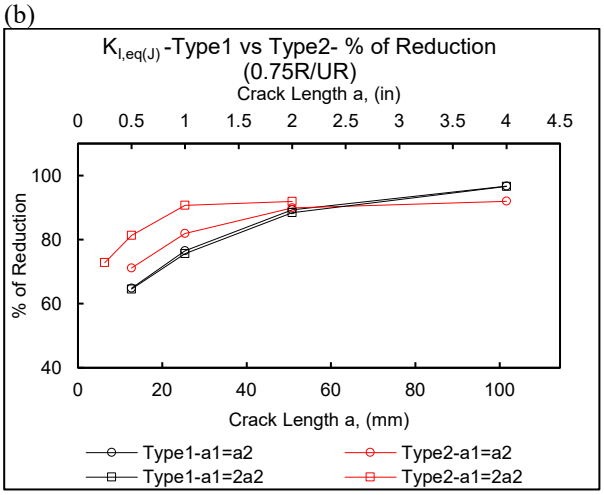

(c) (d)

Figure 4-13: (a) $K_{I,eq(J)}$ - Type1 vs Type 2- a1=a2; (b) $K_{I,eq(J)}$ - Type1 vs Type 2- a1=2a2; (c) $K_{I,eq(J)}$ -Type1(UR) / Type2(UR); (d) $K_{I,eq(J)}$ -Type1 vs Type2- % of Reduction (0.75R/UR)

4.6.5 Comparison Between Techniques and Experimental Results

The modified HSS results show generally similar trends for the unretrofitted and retrofitted cases as found from the *K* and *J*-integral computations. The demand at unretrofitted Type 1 cracks was consistently greater than the demand at unretrofitted Type 2 cracks for all *K*, *J,* and modified HSS computations. In the experimental tests, the Type 2 cracks propagated at a rate less than that for Type 1 cracks, showing a good alignment between the experimental and analytical results.

The advantage of the *J*-integral and Stress Intensity Factor analysis techniques is the *J*-integral values and the Stress Intensity factors can be automatically computed as output parameters by Abaqus 2017 for the contours surrounding each crack tip in the model. However, the need for a contour convergence study was apparent, and must be performed around the crack tips to minimize the sensitivity of results to mesh size.

A comparison between the $K_{I,eq(Ks)}$ values obtained from computed K_I, K_{II}, and K_{III} values and $K_{I,eq(J)}$ values obtained from *J*-integral shows that the $K_{I,eq(Ks)}$ and $K_{I,eq(J)}$ values are quite

similar. Both *K* and *J* results aligned well with experimental findings. There may be a slight advantage to using computed *J*-integral values since the conversion to $K_{I,eq(J)}$ was slightly more direct, and requires manipulation of fewer quantities. However, the Stress Intensity Factor analysis is effective at determining the contribution of each of Mode I, Mode II, and Mode III crack growth modes to overall crack growth.

Figure 4-14 (a) and (b) below shows a comparison of the HSS, $K_{I,eq(Ks)}$, and $K_{I,eq(J)}$ versus the crack propagation data from experimental test (specimen 3) for Crack Type 1 and Crack Type 2, respectively. The primary vertical axis represents the crack length in mm, the horizontal axis represents the number of cycles associated with the specific crack length, and the secondary vertical axis represent HSS, $K_{I,eq(Ks)}$, and $K_{I,eq(J)}$ values, normalized through division by the highest extracted value. To create these plots, the crack lengths in FE models were approximated to the closest crack lengths in the experimental results, and the number of cycles associated with this specific crack length was used as the horizontal axis values to plot HSS, $K_{I,eq(Ks)}$, and $K_{I,eq(J)}$ that correspond to the specific retrofitting condition.

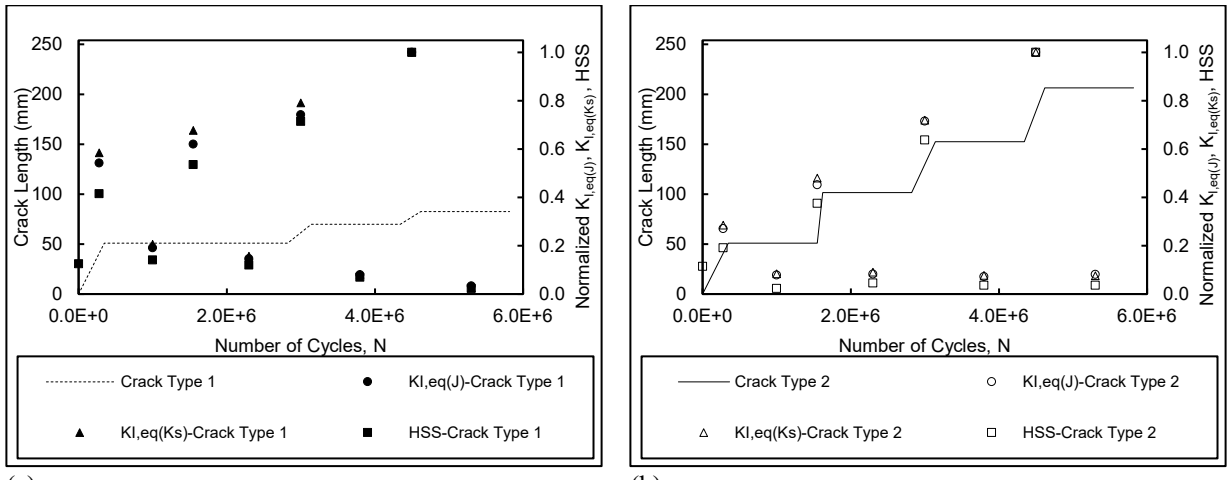

(a) (b)

Figure 4-14: (a) Crack Type 1 propagation data for Specimen 3 (Alemdar et al. 2014a) verses $K_{I,eq(J)}$, $K_{I,eq(Ks)}$ and HSS simulation results; (b) Crack Type 2 propagation data for Specimen 3 (Alemdar et al. 2014a) verses $K_{I,eq(J)}$, $K_{I,eq(Ks)}$ and HSS simulation results

The stair-like lines represent the experimental crack propagation data, indicating rapid propagation occurring during unretrofitted trials, with no observed propagation with the retrofit installed. The results indicate all of $K_{I,eq(J)}$, $K_{I,eq(Ks)}$ and HSS have higher magnitudes in the unretrofitted condition and much lower magnitudes when the retrofit is in place, aligning well with observed experimental behavior. Also, the results showed a trend of reduced $K_{I,eq(J)}$, $K_{I,eq(Ks)}$, and HSS at longer crack lengths with the retrofit in place, indicating the retrofit is more effective for the longer crack lengths considered in this study.

4.7 Conclusions

Implementation of the Extended Finite Element Method (XFEM) for modeling cracks in Abaqus has enabled more detailed analyses to be performed in investigating distortion-induced fatigue and retrofits aimed at mitigating distortion-induced fatigue. This has made implementation of analysis techniques such as the computation of *J*-integrals and the computation of Mode I, Mode II, and Mode III stress intensity factors more accessible for evaluating and predicting performance. This study had two goals. The first goal was to assess three FE computational techniques (Hot Spot Stresses (HSS), *J*-integrals, and Stress Intensity Factors, K) for their ability to predict DIF cracking propensity in bridge girders' web-gap regions. To achieve this goal, numerical simulations were conducted for a 2.7-m (9-ft) girder subassembly experiencing DIF cracking. These numerical models contained simulated cracks at various lengths along the connection plate-to-web and flange-to-web welds, as well as cases with and without a retrofit. The three computational metrics were studied and compared to findings from experimental testing, to determine their effectiveness for predicting DIF cracking propensity. Based on the results; several conclusions have been reached:

1. All evaluated analysis techniques, HSS, K, and *J*-integral, showed higher magnitudes of crack driving force in the unretrofitted condition. This corresponds well with findings from the experimental study, and indicates all methods are suitable for estimating crack propagation likelihood in distortion-induced fatigue.

2. The values for $K_{I,eq(Ks)}$ obtained from K_I, K_{II}, K_{III} were equivalent to $K_{I,eq(J)}$ obtained from J, and both were well-correlated with experimental behavior.

3. HSS, $K_{I,eq(Ks)}$ and $K_{I,eq(J)}$ slopes decreased with crack extension, and correlated well with findings from the corresponding experiments for the crack lengths considered in this study.

4. The HSS approach is a valuable alternative to fracture mechanics approaches for DIF crack propensity, because it is relatively simple to apply, engineers are familiar with stress analysis, and does not require knowledge of fracture mechanics.

The second goal was to investigate the effectiveness of angles-with-plate retrofits to halt the propagation DIF cracking. To achieve this goal, a numerical parametric study was conducted on a 2.7-m (9-ft) girder subassembly experiencing DIF cracking in the web gap region to evaluate different angles-with-plate retrofit thicknesses and their effectiveness at lowering the crack-driving demand in the web gap region. The retrofit performance was evaluated at several different crack states using XFEM. The three computational measures (K, J, and HSS) were used in the simulations to analyze the performance of the angles-with-plate retrofit with varying angle and back plate thicknesses. These simulations were compared to experimental findings and the following conclusions have been drawn based on the findings of the parametric study:

5. The results indicated that all of $K_{I,eq(J)}$, $K_{I,eq(Ks)}$, and HSS had higher magnitudes in the unretrofitted condition and much lower magnitudes with the retrofit installed. This aligns well with experimental observations, as no crack propagation occurred in the retrofitted condition for any crack length.

6. Analyses indicate that for each of the three retrofit thicknesses being considered in this study, the optimal angles-with-plate retrofit thickness was 19 mm (0.75in.). This retrofit thickness was just as effective as the 25.4 mm (1 in.) thick retrofit in preventing the crack propagation, but is more economic.

Adding HSS approach to the available toolkit to evaluate DIF crack propensity is an important and promising measure, because almost all the engineers are familiar with stress analysis, it easy and does not require fracture mechanics knowledge. Although *K* and *J* are extremely meaningful in terms of material behavior and fracture mechanics, they are unfamiliar concepts for the majority of bridge engineers. Further investigations are recommended to study the sensitivity of the HSS technique to different welding details, crack locations, metal thicknesses, and mesh sizes.

4.8 References

Adams, C. (2010). "Finite Element Study on Bridge Details Susceptible to Distortion-Induced Fatigue." M.S., University of Kansas, Lawrence, KS.

Al-Salih, H., Bennett, C., and Matamoros, A. (2021). "Evaluation of novel combined CFRP-steel retrofit for repairing distortion-induced fatigue." *Journal of Constructional Steel Research*, 182, 106642.

Al-Salih, H., Bennett, C., Matamoros, A., Collins, W., and Li, J. (2020). "Repairing Distortion-Induced Fatigue in Steel Bridges Using a CFRP-Steel Retrofit." *Structures Congress 2020*, 273-284.

Alemdar, F., Nagati, D., Matamoros, A., Bennett, C., and Rolfe, S. (2014a). "Repairing Distortion-Induced Fatigue Cracks in Steel Bridge Girders using Angles-with-Plate Retrofit Technique, Part I: Physical Simulations." *Journal of Structural Engineering*, 140(5).

Alemdar, F., Overman, T., Matamoros, A., Bennett, C., and Rolfe, S. (2014b). "Repairing Distortion-Induced Fatigue Cracks in Steel Bridge Girders using Angles-with-Plate Retrofit Technique, Part II: Computer Simulations." *Journal of Structural Engineering*, 140(5).

Anderson, T. L. (1995). *Fracture Mechanics: Fundamentals and Applications*, CRC Press, Boca Raton, FL.

Barsom, J. M., and Rolfe, S. T. (1999). *Fracture and Fatigue Control in Structures: Application of Fracture Mechanics*, ASTM, West Conshohocken, PA.

Bhargava, A. (2010). "Fatigue Analysis of Steel Bridge Details: Hot Spot Stress Approach." Ph.D., George Washington University, Washington DC.

Castiglioni, C., Fisher, J. W., and Yen, B. T. (1988). "Evaluation of fatigue cracking at cross diaphragms of a multigirder steel bridge." *Journal of Constructional Steel Research*, 9(2), 95-110.

Fisher, J. W. (1990). "NCHRP Report 336: Distortion-induced fatigue cracking in steel bridges." Transportation Research Board Washington DC.

Gosz, M. "An Interaction Integral Method for Computation of T-Stress Along the Fronts of General Non-Planar Cracks in Three-Dimensions." *Proc., 11th International Conference on Fracture*.

Hartman, A., Bennett, C., Matamoros, A., and Rolfe, S. (2013). "Innovative Retrofit Technique for Distortion Induced Fatigue Cracks in Steel Girder Web Gaps." *Bridge Structures*, 9, 57-71.

Hartman, A. S., Hassel, H. L., Adams, C. A., Bennett, C. R., Matamoros, A. B., and Rolfe, S. T. (2010). "Effects of Cross-Frame Placement and Skew on Distortion-Induced Fatigue in Steel Bridges." *Transportation Research Record: Journal of the Transportation Research Board*, 2200(1), 62-68.

Hassel, H., Bennett, C., Matamoros, A., and Rolfe, S. (2013). "Parametric Analysis of Cross-Frame Layout on Distortion-Induced Fatigue in Skewed Steel Bridges." *Journal of Bridge Engineering*, 18(7), 601-611.

Hassel, H., Hartman, A., Bennett, C., Matamoros, A., and Rolfe, S. "Distortion-induced fatigue in steel bridges: causes, parameters, and fixes." *Proc., ASCE Structures Congress*, ASCE.

Jajich, D., and Schultz, A. (2003). "Measurement and Analysis of Distortion-Induced Fatigue in Multigirder Steel Bridges." *Journal of Bridge Engineering*, 8(2), 84-91.

Keating, P., and Fisher, J. W. (1987). "Fatigue behavior of variable loaded bridge details near the fatigue limit." *Transportation Research Record*(1118), 56-64.

Keating, P. B. (1994). "Focusing on Fatigue." *Civil Engineering - ASCE*, 64(11), 54-57.

Liu, H. (2015). "A Finite-Element-Based Approach to Modeling Cracking and Repairs for Distortion-Induced Fatigue in Steel Bridges." Ph.D., The Univeristy of Kansas

Marquis, G., and Kahonen, A. (1996). "Fatigue testing and analysis using the hot spot method." " *VTT Publications*, 239, 3-39.

Moes, N., Dolbow, J., and Belytschko, T. (1999). "A finite element method for crack growth without remeshing." *International Journal for Numerical Methods in Engineering*, 46, 131-150.

Przywara, J. (2013). "Applications of The Extended Finite Element Method (XFEM) for the Analysis of Distortion-Induced Fatigue Cracking in Highway Bridge Girders." M.Sc., The University of Kansas.

Rice, J. R. (1968). "A Path Independent Integral and the Approximate Analysis of Strain Concentration by Notches and Cracks." *Journal of Applied Mechanics*, 35, 379-386.

Shih, C., and Asaro, R. (1988). "Elastic-Plastic Analysis of Cracks on Bimaterial Interaces: Part I—Small Scale Yielding." *Journal of Applied Mechanics*, 55(2), 299-316.

Sih, G., and Cha, B. (1974). "A fracture criterion for three-dimensional crack problems." *Engineering Fracture Mechanics*, 6(4), 699-723.

Sih, G., and Macdonald, B. (1974). "Fracture mechanics applied to engineering problems—strain energy density fracture criterion." *Engineering Fracture Mechanics*, 6(2), 361-386.

SIMULIA (2017). "SIMULIA™ Support Documentation - Dassault Systèmes®, Abaqus, Version 2017." <http://simulia.com>.

Tedesco, J., Stallings, J., and Tow, D. (1995). "Finite Element Method Analysis of Bridge Girder-Diaphragm Interaction." *Computers and Structures*, 56(2-3), 461-473.

Chapter 5: **Numerical Study on Strengthening of Cracked Steel Plate Using CFRP Composites**

Hayder Al-Salih[1] P.E., Caroline Bennett[2], Ph.D., P.E.

[1]Graduate Research Assistant, University of Kansas, Department of Civil, Environmental, and Architectural Engineering, 1530 W. 15th St., Lawrence, Kansas, 66045, E-mail: hia@ku.edu

[2]Professor, University of Kansas, Department of Civil, Environmental, and Architectural Engineering, 1530 W. 15th St., Lawrence, Kansas, 66045, E-mail: crb@ku.edu (Corresponding Author)

5.1 Abstract

Fiber Reinforced Polymers (FRP) composite materials for strengthening steel structures have received a significant amount of attention in recent decades. This chapter covers an introduction focused on the development of FRP composite materials for structural applications, a literature review on using externally bonded FRP composites for strengthening steel members, and a numerical study of a steel plate with a single edge crack strengthened with Carbon Fiber Reinforced Polymer (CFRP) composites. The goal of the numerical study was to achieve a better understanding of the effectiveness of the CFRP in reducing stress at the crack tip, as well as reducing crack growth rate. The study includes a parametric analysis to explore the effect of different factors on CFRP strengthening behavior. A continuum shell element was utilized to model the CFRP, a cohesive element used to model the adhesive layer, and the eXtended Finite Element Method (XFEM) was used to model the crack. Damage initiation of the adhesive and in the crack were modeled using traction-separation laws. The mixed mode failure criterion (quadratic strain damage initiation criterion), which takes into consideration both mode I and mode II failures, was utilized to model damage in the adhesive, whereas maximum principal stress damage initiation criterion was utilized to model damage in the steel substrate. Damage to CFRP sheets was modeled using the "Damage and Failure for Fiber-Reinforced Composites" material

model, which employs Hashin's failure criterion. Results showed that CFRP strengthening was effective in reducing maximum principal stress and the stress intensity factor at the crack, and in reducing the crack propagation rate. CFRP strengthening significantly increased the capacity of cracked steel plate for both isotropic and lamina CFRP models. The parametric analysis showed that increasing the elastic modulus in the longitudinal direction of the CFRP led to an increase in capacity and reduced crack propagation length. Likewise, increasing adhesive shear stiffness increased capacity and reduced crack propagation length.

5.2 Introduction and Background

Fiber reinforced polymers are commonly referred to as composite materials or composites. The word composite comes from the Latin word "*componere,"* which means 'put together' (Carolin 2003). A composite is a material formed of two or more distinct parts working together. Often one of the parts is harder and stronger (fiber) while the other is more of a force transferring material (matrix) (Nordin 2003). There are several materials available for the fibers, e.g. AFRP (Aramid Fiber Reinforced Polymer), CFRP (Carbon Fiber Reinforced Polymer), and GFRP (Glass Fiber Reinforced Polymer) (Lundqvist 2007). Combining fibers and a polymer matrix produces a composite material with desirable strength and stiffness properties.

The main function of the polymer matrix is to bind the fibers together, transfer forces between the fibers, and protect the fibers from external mechanical and environmental damage. The shear forces carried between the fibers are limited to the properties of the matrix. The matrix is also the limiting factor when applying forces perpendicular to the fibers. It is important that the matrix has the capability to accommodate higher strains than the fibers, otherwise, cracks will form in the matrix before the fibers fail and the fibers will be unprotected (Nordin 2003). Common matrix

materials in civil engineering applications are divided into two categories of resins: *thermoset resins* (most common for structural uses) and *thermoplastic resins*. Common thermoset resin types are polyester (least cost), vinyl ester (industry standard), polyurethane (premium cost), and epoxy (greatest cost and commonly used in aerospace applications and structural strengthening) (Tavakkolizadeh and Saadatmanesh 2003).

The need for retrofitting and strengthening of buildings and bridge structures continually increases as our built infrastructure matures. Many structures undergo use changes which may require higher load-carrying capacity than they were originally designed for. As a result, such structures must be re-evaluated and may require strengthening to meet increased capacity requirements.

The restoration of historic buildings in the late 1950s represents the introduction of FRP composites to building structure applications. The rehabilitation of bridge columns, decks, beams, tunnel and marine pier repairs in Europe, Japan, and the United States in the 1970s and 1980s represents the beginning of FRP composite technology being used in infrastructure markets (MAPEI 2011). Use of FRP composites for repair or strengthening concrete and steel members has matured as a promising technology for infrastructure rehabilitation since 1987 when the initial development of FRP-strengthening technique took place in Switzerland, under the leadership of Meier (1987). By 1997, more than 1500 concrete structures worldwide had been reinforced with externally-bonded FRP composites (Fukuyama et al. 1997).

FRP materials possess many advantages over other materials in civil engineering. They are lightweight, have high tensile strength (high strength-to-weight ratio), and high tensile stiffness (high stiffness-to-weight ratio). FRP materials exhibit excellent fatigue properties and are resistant to corrosion and chemicals (Khan et al. 2004; Lundqvist 2007). Successful FRP strengthening

applications have been made for steel, timber, and masonry structures. The benefits of using FRP in strengthening operations includes simplicity of handling (the availability of any length and the ability to be transported in rolls), cutting and installation (adhesively bonded), the versatile design of systems, small changes in strengthened structural member's dimensions, reduced maintenance cost, and reduced construction periods (Khan et al. 2004; Lundqvist 2007). Unlike many traditional repair methods, FRP repairs cause less disturbance to regular service during the repair process since FRPs are typically glued in place rather than requiring bolting or welding. Moreover, repairs made by bonding FRP contribute minimal additional weight to the structure and introduce less stress concentrations as compared to mechanical fastening (Al-Mosawe et al. 2016; Al-Salih et al. 2020; Al-Salih et al. 2020; Alwash and AL-Salih 2013; Ghahremani et al. 2015; Khan et al. 2004; Liu et al. 2009; Lundqvist 2007; MAPEI 2011; Wu et al. 2012).

Many researchers have studied the behavior of cracked steel members strengthened with FRP composites under quasi-static or cyclic fatigue loading. Some key studies are summarized in the following.

Wang et al. (2014) conducted a finite element (FE) study on the fatigue behavior of cracked steel plates strengthened with different configurations of FRP materials. Three different FRP configurations designed with equivalent tensile stiffnesses were investigated to determine the best configuration for extending the fatigue life of a small steel plate with a central crack. The study found that FRP configurations have a significant effect on reducing the stress intensity factor at the crack tip and crack growth rate. Applying FRP over the crack was found to be more effective than applying it to either tip of the center crack, for equivalent FRP tensile stiffness. A small FRP layer directly over the crack was more effective for a small central crack and thin FRP layers,

while a larger FRP layer was more effective for larger central cracks and thick FRP layers, for equivalent FRP tensile stiffness.

Wang et al. (2016) examined the effectiveness of different CFRP systems and configurations for repairing fatigue cracks in steel plates. Tensile fatigue tests were conducted on 10 small steel specimens with either a single edge crack or a center hole with slots. Parameters studied included CFRP type, elastic modulus, repair configuration, and tensile stiffness. The researchers concluded that the CFRP systems were able to decrease the crack propagation rate and significantly extend the fatigue life of cracked steel plates. Fatigue life was extended by a factor of 3.5–4.9x for central cracked specimens and 6.9–11.3x for edge-cracked specimens. The efficacy of CFRP plates was found to be better than that of CFRP sheets for equivalent CFRP tensile stiffnesses.

Al-Mosawe et al. (2016) performed an experimental and numerical investigation on strengthening steel members subjected to impact loading using ultrahigh modulus CFRP. Quasi-static and dynamic tensile loads were applied to steel double-strap joint specimens strengthened with ultrahigh modulus CFRP. Eighty-seven specimens were tested to investigate the effect of high loading rates on the strain distribution along the bond interface between the ultrahigh modulus CFRP and steel plates, ultimate joint capacity, failure mode, and effective bond length. A significant decrease in effective bond length was observed under dynamic loading. The results also indicated an increase in ultimate joint capacity and slight increase in ultimate strain values with increasing load rate.

Chen et al. (2019) conducted an experimental study on mixed-mode fatigue behavior of center cracked steel plates repaired with CFRP. Fatigue tests were conducted on small steel specimens with a center hole with slots. Mixed mode I and II fatigue tests were achieved by varying the load

application angles between 0, 15, and 30 degrees. Results indicated that the CFRP repair was able to effectively decrease the crack propagation rate and extend the fatigue life of the cracked steel plates under mixed mode loading. All repaired specimens failed by fracture in the CFRP materials. The results also indicated that the repair efficacy increased with increasing crack length and decreased with increasing load application angle.

Tavakkolizadeh and Saadatmanesh (2003) investigated the retrofitting of notched steel beams retrofitted with CFRP patches under medium-cycle fatigue loading. Twenty-one specimens made of S12734.5 (A36) steel beams were prepared and tested. Unretrofitted beams were also tested as control specimens. Four-point loading was used to test all the beams under loading rates of 5-10 Hz. The length and thickness of the patch were held constant for all the retrofitted specimens. The number of cycles to failure, changes in stiffness, crack initiation and growth were monitored in this experiment. It was found that for both the retrofitted and the unretrofitted beams, crack growth was stable up to a length of 20 mm and stable crack growth rates decreased by an average of 65% under the retrofit. The average number of cycles to failure after crack initiation for retrofitted specimens was 3.5 times that for unretrofitted specimens, and retrofitted specimens were able to carry a few additional cycles even after the tension flange had completely cracked.

Nozaka et al. (2005) conducted experimental tests using a new type of effective bond length test specimen while varying pre-cured CFRP laminates adhesives and bonding configurations. They determined the minimum bond length required to ensure the maximum strength of the repair. A total of 27 specimens were tested. Twenty-four of the specimens were one-layer, three were two-layer, and one was a three-layer specimen. CFRP and adhesive material, crack width, bond configuration, and bond length were the main variables in these tests. Since specimen strength can be affected by the existence of sharp corners in the adhesive layer, several different geometries of

the bond area and plate separation were created to relieve stress concentrations in the adhesive. The experimental results showed that high ductility adhesive is needed to ensure redistribution of stresses within the adhesive layer during loading. A simple analytical solution for the shear strain distribution in the adhesive layer was proposed for estimating effective bond length, and the results were verified with computational analyses.

Kaan et al. (2012) investigated a method of improving fatigue performance of welded connections in steel bridge girders by developing carbon-fiber reinforced polymer (CFRP) overlay elements. To quantify the effect of the CFRP overlays elements on fatigue crack initiation life of welded connections, a total of seven specimens were tested. The specimens were tested under cyclic fatigue in three-point bending; four were CFRP-strengthened while the other three were control specimens. For the specimens tested at high stress ranges, the CFRP overlays significantly reduced stress demands at the welds, which in turn led to an increase in fatigue initiation life. The effectiveness of the CFRP-overlay elements was found to depend primarily on bond strength under cyclic loading, which in turn was found to be affected by the composition and thickness of the adhesive layer used to bond the CFRP overlay to the steel.

Wu et al. (2012) conducted an experimental study to investigate the fatigue behavior of notched steel beams strengthened with four different types of materials, including a high-modulus carbon-fiber-reinforced polymer (HM-CFRP) plate, high-strength CFRP (HS-CFRP) plate, steel-wire basalt-fiber-reinforced polymer (SW-BFRP) plate, and welded steel plate. The material type, number of HS-CFRP layers, configuration of HS-CFRP, and interface treatment of SW-BFRP were key parameters in the study. The results showed that the application of a fiber reinforced composite plate was able to delay crack initiation, decrease crack growth rate, prolong fatigue life, and reduce stiffness decay and residual deflection. Increasing the layers of strengthening material

was found to significantly improve the fatigue behavior of steel beams. For equivalent tensile stiffnesses, fiber-reinforced composite plate were found to extend the fatigue life of the steel beam more effectively than the traditional welded steel plate. The fatigue life of the steel beams strengthened by fiber-reinforced composite plates was 3.33–5.26x that of the unstrengthened beam, whereas the fatigue life of the steel beam strengthened by a welded steel plate was only 1.74x that of the unstrengthened beam. Among the tested strengthening materials, HM-CFRP produced the best strengthening effects, whereas SW-BFRP possessed the best performance-to-price ratio.

Liu et al. (2009) conducted a series of experiments to investigate the effectiveness of CFRP sheet composites on reducing fatigue crack propagation propensity. Two types of fibers, MBrace CF130 and MBrace CF530, were used as patching systems. The fibers are unidirectional and were placed in the longitudinal direction of the plate; both single-sided and double-sided repairs were included in the study. The investigated parameters were CFRP modulus, bond width, patch thickness, patch length, and patch configuration. Experimental results showed that the fatigue life of the double-sided repair scheme increased by 2.2–2.7x over relative to an un-patched steel plate when normal modulus CFRP sheets were used, and by 4.7–7.9x when high modulus CFRP sheets were used. Increasing the CFRP modulus and bond width was found to be much more efficient for double-sided repairs.

Al-Zubaidy et al. (2013) conducted a three-dimensional finite element study to investigate CFRP-steel double strap joints with one and three CFRP layers per side. Tests were conducted using quasi-static loading as well as three dynamic tensile loading rates of 3.35, 4.43, and 5 m/s (10.99, 14.53, 16.4) ft/s. Both implicit and explicit codes in the non-linear finite element (FE) program ABAQUS were utilized in the simulations. The steel plate was modeled as an elastic–plastic

material, and CFRP and adhesive failures were accounted for. The CFRP patch was represented by continuum shell elements, whereas the adhesive layer was represented by cohesive elements. The mixed mode failure criterion (quadratic traction damage initiation criterion, QUADSCRT) which takes into account both mode I and mode II failures was used in this simulation, since adhesively bonded joints are subjected to shear and peeling stresses which can lead to adhesive failure. Damage to CFRP sheets was modeled using one of the available material models in Abaqus software, "damage and failure for fiber-reinforced composites," which is based on continuum damage mechanisms and utilizes Hashin's failure criteria. The FE models for both types of joints were verified by comparing their quasi-static and dynamic results to earlier experimental results. The four parameters that were considered in the comparison were: ultimate joint strength, failure pattern, effective bond length and strain distribution throughout the bond length. The results showed that the FE models could predict the influence of all of these parameters for quasi-static and dynamic loading, based on good agreement with experimental test findings.

Fernando et al. (2014) present an analytical solution for the full-range behavior of CFRP-to-steel bonded joints using a ductile nonlinear adhesive. Previous studies conducted by the authors showed that the bond strength of such joints is heavily influenced by the properties of the adhesive, notably the interfacial fracture energy rather than the tensile strength. It was also previously observed that the bond-slip curves for nonlinear ductile adhesives had a trapezoidal form. Closed-form formulations for the interfacial-shear stress distribution and the load-displacement response were developed. The analytical solution predictions were compared to test data to illustrate their validity and were found to closely match the interfacial-shear stress distributions at various loading/deformation stages. The CFRP-steel bond strength was closely estimated using the analytical solution, with an average error of 2%. The approach is directly applicable to intermediate

debonding that occurs at a local weakness (crack, defect, or concentrated yielding) of FRP-strengthened steel beams, which are usually dominated by interfacial-shear stresses. The analytical solution may also serve as an essential first step in modeling more sophisticated scenarios where the influence of peel stresses becomes substantial, such as plate-end debonding.

Teng et al. (2015) proposed a finite element (FE) approach predicting flexural debonding failures in simply-supported steel I-beams with a bonded CFRP plate, with a focus on plate-end debonding. Bilinear traction–separation models were used to simulate interfacial behavior under pure mode-I and mode-II loadings. A mixed-mode cohesive law was used in the proposed FE approach to represent interfacial behavior under a combination of normal stresses (i.e. mode-I loading) and shear stresses (i.e. mode-II loading). The proposed coupled cohesive zone model for CFRP-to-steel interfaces consists of three components: a bond-slip model for mode-II loading, a bond separation model for mode-I loading, and a mixed-mode cohesive law. A quadratic strength criterion was used to define damage initiation, while a linear fracture energy-based criterion was used to characterize damage evolution, both of which consider mixed-mode loading. Detailed FE models of steel beams were created using Abaqus, and their predictions were in good agreement with experimental results from the literature. Four steel I-beams each with a 1100-mm (43.3-in.) span were studied: one control beam with no CFRP strengthening, and three that were reinforced with 3-mm (0.118-in.) thick CFRP plates of different lengths, 300 mm, 400 mm, and 1000 mm (11.81, 15.75, 39.37 in.) The results showed that ultimate load carrying capacity and plate-end debonding were negatively impacted when elastic modulus or thickness of the CFRP was increased. Using a shorter CFRP plate was found to increase the likelihood of plate-end debonding, while using a longer CFRP plate may change the failure mode to intermediate debonding or other failure modes.

Bocciarelli et al. (2018) conducted a study to evaluate notched I-shaped steel beams reinforced with composite materials under fatigue stresses to estimate how fatigue crack propagation was influenced by the bond interface. To analyze the stress and strain distribution in the CFRP reinforcement for a given crack length, numerical and analytical models for elasto-brittle adhesives were suggested. The proposed methodologies were validated through comparisons with experimental test results from the literature. The commercial finite element software Abaqus was used to examine debonding of the CFRP reinforcement. All the materials (CFRP reinforcement and steel beam) were linear-elastic, isotropic, and homogenous. A finite element model with a damaging cohesive interface that provided the ability to track progressive debonding of the reinforcement for a given fracture length and increasing load was presented. There was good agreement between the analytical, numerical, and experimental data in terms of strain distribution in the CFRP material. A parametric study was carried out to explore the effect of various design parameters on the axial strain distribution in the CFRP, showing that crack length in the notched steel beam had no effect on axial strain along the debonded zone, but having a substantial influence on the debonded zone length and a minor influence on axial strain at the elastic limit. Axial strain in the CFRP tended to decrease with increasing CFRP elastic stiffness; however, the CFRP elastic modulus had a minor influence on debonded zone length.

Kabir et al. (2016) conducted an experimental and numerical investigation for studying the structural behavior of circular hollow section (CHS) beams reinforced with varied layer orientations of CFRP sheets under four-point bending. A comprehensive three-dimensional FE model was created for unstrengthened and reinforced beams, validated against the experimental portion of the study. The mixed-mode failure criterion, the quadratic traction damage criterion (QUADS), was considered for both mode I and mode II loading. To give an accurate comparison

of the numerical model to the experimental findings, damage initiation and propagation of an elastic–brittle material with isotropic behavior were adopted by implementing the Hashin damage model in Abaqus. Parametric studies were carried out to investigate the effect of different factors such as bond length, section type, CFRP tensile modulus, adhesive layer thickness, and adhesive type. The finite element model closely estimated the ultimate load, midspan load-deflection curves, and failure mode for unstrengthened and strengthened CFRP beams with varied layer orientations. The parametric analysis results revealed that the section parameters, such as outer diameter and thickness, had a significant impact on the strength increase of CFRP-enhanced CHS steel beams. CFRP reinforcement with greater tensile modulus and adhesive with greater thickness performed better under bending by increasing stiffness and ultimate load carrying capability. In terms of ultimate load and stiffness, adhesive with high tensile modulus and stiffness parameters (K) performed best.

5.3 Objective and scope

The objective of this study was to characterize the behavior of a CFRP-strengthened cracked steel plate under quasi-static load and to examine the effectiveness of CFRP strengthening in reducing propensity for crack propagation in cracked steel plates. To accomplish this, a suite of finite elements models were used to investigate the behavior of cracked steel plate with and without CFRP strengthening. Different conditions were investigated, including: an infinite vs. finite steel plate, stationary vs. propagating cracks using the XFEM modeling technique, isotropic vs. lamina (orthotropic) material models for the CFRP, and modeling of damage and damage evolution for the CFRP and adhesive materials.

The computational models were created using the commercially-available finite-element analysis software Abaqus (SIMULIA 2016) to model the small-scale steel plate with a single edge crack. The modeling approach adopted drew upon available data from the literature and aimed to predict the efficacy of the CFRP strengthening and failure mechanism of the repair.

Strengthening steel structures using Carbon Fiber Reinforced Polymers (CFRP) has received considerable attention over the last decade; however, little research into the effect of damage modeling parameters for cracked steel members strengthened with CFRP materials has been carried out. Therefore, another key objective of this study was to investigate the influence of various parameters used when modeling CFRP strengthening with damage initiation and evolution.

5.4 Numerical Modelling Approach

5.4.1 Geometry of Model

To study the effectiveness of CFRP in reducing stress at the crack tip and reducing crack growth rate, a steel plate with a single edge crack was adopted. The steel plate dimensions were 102x203x5 mm (4x8x0.2 in.) with a single edge crack 20-mm (0.8-in.) long. CFRP laminates with dimensions 102x203x2 mm (4x8x0.08 in.) were attached to both sides of the steel plate using an epoxy layer that was 102x203x0.25 mm (4x8x0.01in). Figure 5-1 and Table 5-1 show the dimensions of the models.

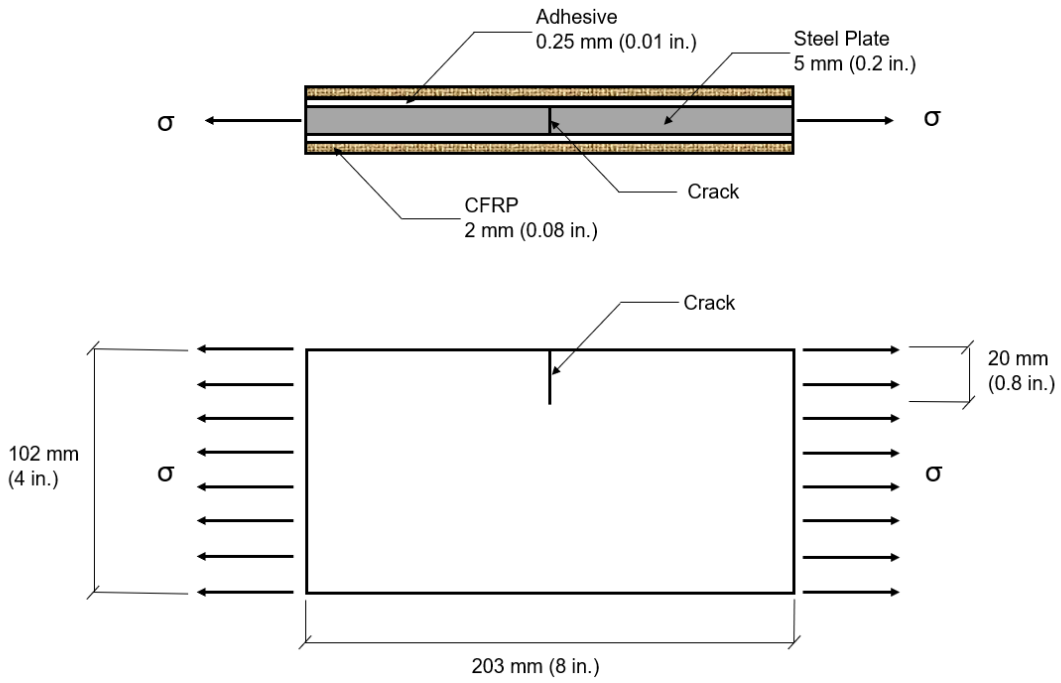

Figure 5-1 Dimensions for the steel plate with single edge crack

Cracks were modeled using the Extended Finite Element Method (XFEM) in Abaqus 2016. In the XFEM method cracks can be placed anywhere, unrestricted by elements boundaries. Moreover, various crack shapes can be modeled without influencing the mesh in the region of interest (SIMULIA 2016)**.** Two types of cracks were modeled: a stationary crack (non-growing crack) and a propagatable crack. Models of steel plates that did not include CFRP composites are referred to here as bare steel plates, while models of steel plates strengthened with CFRP composites are referred to as strengthened steel plates.

Table 5-2 Dimensions for the steel plate, CFRP, adhesive, and crack

Part	**Length** mm (in.)	**Width** mm (in.)	**Thickness** mm (in.)
Steel Plate	203 (8)	102 (4)	5 (0.2)
CFRP	203 (8)	102 (4)	2 (0.08)
Adhesive	203 (8)	102 (4)	0.25(0.01)
Crack	20 (0.8)	5 (0.2)	0 (0)

5.4.2 FE modelling suites

In total, 135 models were created and analyzed, including steel plates modeled with a stationary crack and steel plates modeled with a crack that was able to propagate. For each crack type, the following configurations were studied: a bare steel plate, a steel plate strengthened with CFRP with isotropic material properties, and a steel plate strengthened with CFRP with lamina (orthotropic) material properties. A parametric study was conducted on the steel plate with a propagatable crack strengthened with lamina CFRP. Investigated parameters included the elastic and the damage parameters of the materials. Figure 5-2 presents a flow chart for the modeling matrix.

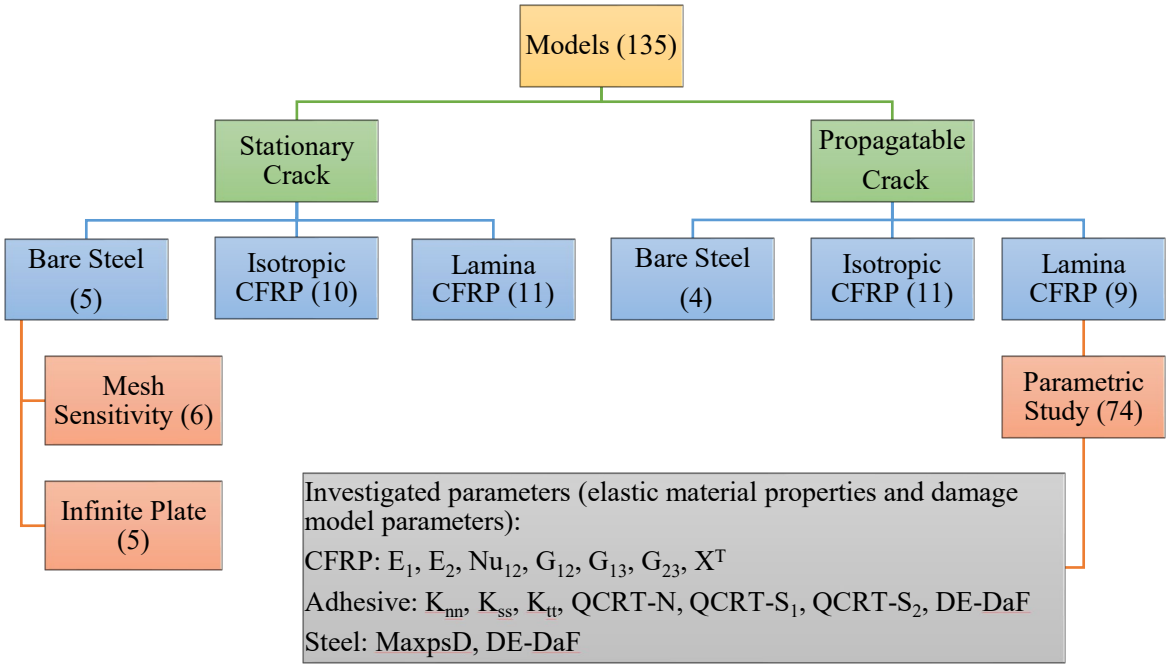

Figure 5-2 FE modelling suite, number between parentheses represent the number of models

5.4.3 Boundary conditions and loading

The models were supported such that all x-, y- and z- degrees of freedom (DOFs) were restricted at a point on the left edge of the steel plate at mid-thickness and mid-height. Additionally, y- and z- DOFs were restrained along the right edge of the steel plate, leaving only displacements free along the x-direction. A tensile pressure load was applied along both edges of the steel plate in the x- direction, as shown in Figure 5-3.

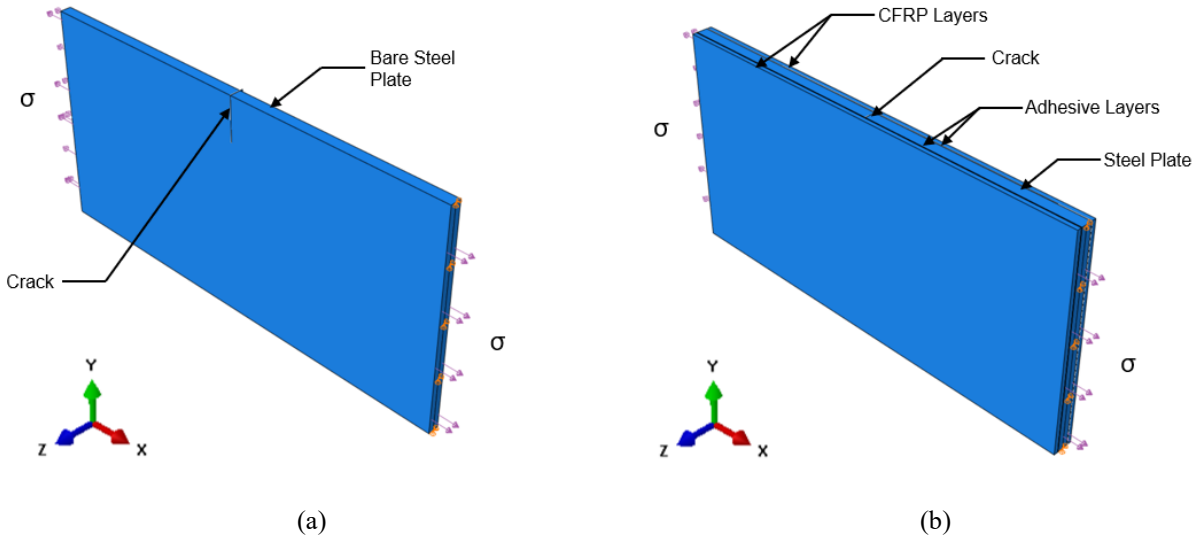

(a) (b)

Figure 5-3 Boundary conditions and loading for steel plate with single edge crack: (a) bare steel plate, (b) strengthened steel plate

5.4.4 Mesh sensitivity analysis and element selection

The steel and isotropic CFRP parts were modeled using hexahedral (C3D8R) elements, while the lamina CFRP was modeled using a continuum shell element (SC8R), with cohesive elements (COH3D8) used to model the epoxy layer. XFEM was used to model the crack in the steel substrate. A mesh convergence study was performed for the bare steel plate model with stationary

crack, resulting in the selection of a minimum element size of 2.54 mm (0.1 in.) and a total of 6400 elements in the bare steel plate model, as shown in Figure 5-4 and Figure 5-5.

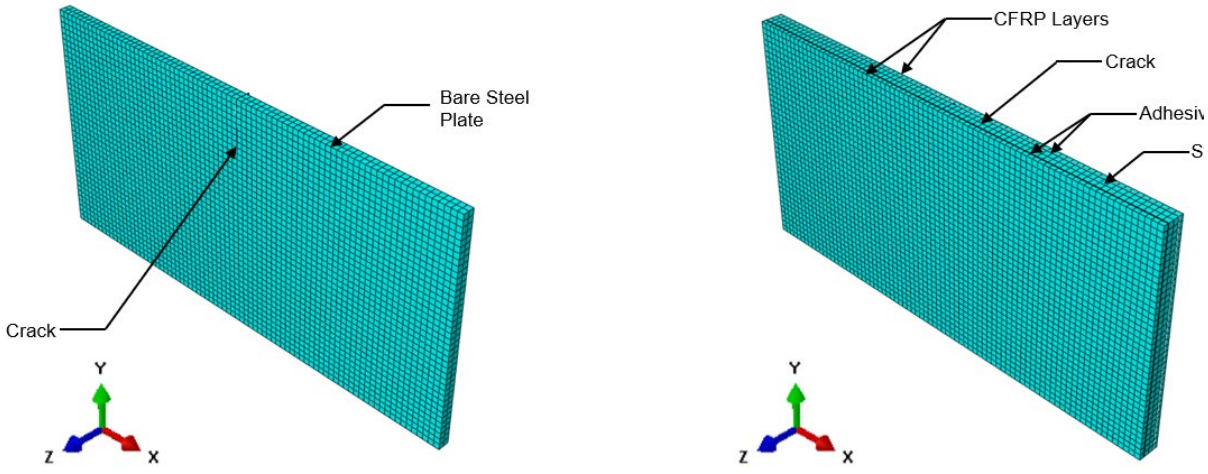

(a) (b)

Figure 5-4 Meshing for steel plate with single edge crack: (a) bare steel plate, (b) strengthened steel plate

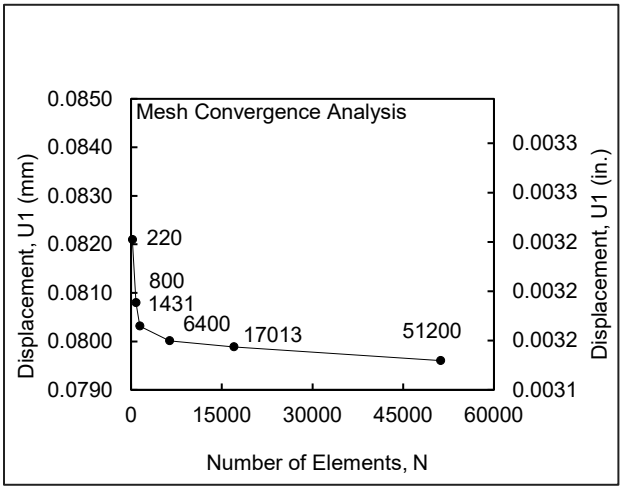

Figure 5-5 Mesh sensitivity results, for bare steel model

5.4.5 Modelling of damage and failure behavior

Adhesively bonded composite materials are typically controlled by failure occurring in the composite material and/or in the bonding material. Damage to both the CFRP and adhesive materials have been considered in this study, as well as damage in the steel substrate (crack propagation).

The failure behavior of the materials was defined using the following damage and failure models available in Abaqus: Hashin's failure criteria for CFRP, the quadratic strain damage criterion for the adhesive material, and maximum principal stress damage criterion for crack propagation in the steel substrate. Each failure mechanism consists of three key properties: a damage initiation criterion, a damage evolution law, and an option to remove damaged element(s) upon reaching a completely damaged state (SIMULIA 2016)**.**

5.4.5.1 Damage Initiation (Theory of failure)

5.4.5.1.1 Damage Initiation in the Adhesive:

Damage to the adhesive bond interface occurs when mode-II shear stress in the bond layer surpasses the peak bond shear resistance of the adhesive material; likewise, when normal stress exceeds the peak bond normal stress resistance under pure mode-I loading, damage begins (Fernando 2010). To define the initiation of damage under mixed-mode loading, a damage criterion that considers the interaction between mode-I and mode-II loading should be used.

In Abaqus, the process of degradation is modeled as beginning when stresses and/or strains reach certain user-specified damage initiation criteria. A value of 1 or higher indicates that the damage initiation criterion has been met. Damage initiation in the adhesive layer was modeled

using the available material models in Abaqus, namely traction-separation laws. Three stress-based and three strain-based damage initiation criteria are readily available for use within traction-separation laws (SIMULIA 2016)**:**

- Maximum principal stress (MAXPS) and maximum principal strain (MAXPE)
- Maximum nominal stress (MAXS) and maximum nominal strain (MAXE)
- Quadratic nominal stress (QUADS) and quadratic nominal strain (QUADE)

The first two criteria assume that adhesive damage occurs when the maximum stress or strain approaches the maximal capacity of the adhesive. The third criteria accounts for the combined effect of stresses or strains, and assumes damage occurs when a sum quadratic interaction function involving the nominal stresses or strain ratios achieves a value of one. The quadratic damage initiation criteria has been adopted by numerous researchers to simulate damage in adhesives [Abd-El-Meguid (2008); Al-Zubaidy et al. (2013); Kabir et al. (2016); Teng et al. (2015)], and is represented in equation (5-1) (SIMULIA 2016):

$$\{\frac{\langle \varepsilon_n \rangle}{\varepsilon_n^o}\}^2 + \{\frac{\varepsilon_s}{\varepsilon_s^o}\}^2 + \{\frac{\varepsilon_t}{\varepsilon_t^o}\}^2 = 1 \qquad (5\text{-}1)$$

where $\mathcal{E}^o_n$, $\mathcal{E}^o_s$, and $\mathcal{E}^o_t$ are the peak values of nominal strain when deformation is either purely normal to the interface or purely in the first or the second shear direction, respectively. $\mathcal{E}_n$, $\mathcal{E}_s$, and $\mathcal{E}_t$ denote the strains in three directions of the adhesive layer (normal, first and second shear direction). The Macaulay bracket $\langle\ \rangle$ is a symbol that indicates that compressive stresses do not cause damage (i.e., when $\mathcal{E}_n$ is negative, $\langle \mathcal{E}_n \rangle$ is zero). This mixed mode failure criteria accounts for both mode I and mode II failures, and was adopted for use in this simulation since the adhesive is subject to complex stress states.

5.4.5.1.2 Damage Initiation in the Steel Substrate:

Maximum principal stress damage initiation criterion was utilized to model damage causing the crack in the steel substrate to propagate using traction-separation laws in Abaqus, as previously described for adhesive damage initiation.

5.4.5.1.3 Damage Initiation in the CFRP:

Damage initiation in the CFRP material with lamina behavior was modeled using another available material model in Abaqus, "damage and failure for fiber-reinforced composites," which is based on continuum damage mechanisms and utilizing Hashin's failure criteria. Plasticity of CFRP composites is ignored when using this material model, and damage is detected and defined based on stiffness loss. Hashin's failure criteria can be used to numerically achieve material degradation because it provides numerical simulation of composite material damage. Fiber rupture in tension, fiber buckling in compression, matrix cracking under transverse tension and shearing, and matrix crushing under transverse compression are the four basic failures that cause damage to the CFRP layer. The parameters used in Abaqus to facilitate Hashin's damage criteria are: Longitudinal tensile and compressive strength, which represent ultimate tensile and compressive strength (X^T and X^C) of the CFRP in the fiber direction; transverse tensile and compressive strength, which represent ultimate tensile and compressive strength (Y^T and Y^C) of the CFRP in the transverse direction; and longitudinal shear and transverse shear strength (S^L and S^T) (Al-Zubaidy et al. 2013; Hashin 1980; Hashin and Rotem 1973; Kabir et al. 2016; Naghipour et al. 2009; SIMULIA 2016).

5.4.5.2 Damage Evolution (Post-peak behavior)

A damage evolution law describes the rate at which material stiffness is degraded once the corresponding initiation criterion has been reached. There are two approaches to simulating the evolution of damage (SIMULIA 2016)**:**

- Damage evolution based on displacement
- Damage evolution based on energy

Either approach could be either based on a single mode of loading (e.g., pure mode I or mode II) or a mixed mode. Moreover, the damage evolution relationship can be linear or exponential. Both approaches are viable and, in this study, the below approaches were investigated based on the availability of the required data for each material.

The triangle traction-separation law, the most popular of the traction-separation laws for cohesive elements that is included in Abaqus, has been adopted in this study. For a single mode, it is defined by the following key parameters: elastic stiffness (K), maximum traction (T_{max}), and failure separation displacement (δ_{fail}). The applied stress on the cohesive element grows linearly with the slope of K up to the element's strength T_{max} at which point the damage initiation starts (T_{max} occur at displacement of δ_{init}) and then decays linearly until achieves failure displacement (δ_{fail}) in the triangular shape model. The displacement at failure (DaF), for the triangle traction-separation model, represents failure displacement, δ_{fail}, relative to damage initiation displacement, $\delta_{init,}$ see equation (5-2). The fracture energy, for the triangle traction-separation model, is computed from the area under the traction-separation curve (SIMULIA 2016).

$$\mathrm{DaF} = \delta_{fail} - \delta_{init} \tag{5-2}$$

5.4.5.2.1 Damage Evolution in the Adhesive:

In this study, damage evolution of the adhesive was characterized using a linear independent displacement-based damage evolution. A scalar damage variable, *D*, represents the overall damage sustained in the adhesive and captures the combined effects of all the active mechanisms. The value of this variable ranges from 0 in the undamaged state to 1 in the completely damaged state, and it initially has a value of 0. If damage evolution is modeled, *D* monotonically evolves from 0 to 1 upon further loading after damage has been initiated. The Abaqus output QUADE represents damage initiation criterion, and SDEG represents the overall value of the scalar variable, *D* (SIMULIA 2016).

5.4.5.2.2 Damage Evolution in the Steel Substrate:

Similar to the adhesive damage modeling, a linear independent displacement-based damage evolution was also used to model damage evolution in the steel substrate. A scalar damage variable, *D*, represents the overall damage sustained in the steel substrate and captures the combined effects of all the active mechanisms.

5.4.5.2.3 Damage Evolution in the CFRP:

A linear fracture energy-based damage evolution that considers mixed-mode loading was used to characterize damage evolution in the CFRP materials. Damage occurs in the CFRP when the fracture energy exceeds the maximum resistance in any of the four basic failure criteria that cause damage to the CFRP layer. The fracture energy can be defined as an input parameter in Abaqus as longitudinal tensile and compressive fracture energy and/or as transverse tensile and compressive fracture energy. Once damage occurs, three non-negative parameters, d_f, d_m, and d_s, quantitatively reduce the CFRP laminate stiffness in the longitudinal, transverse, and shear directions until the

final failure point is achieved (Kabir et al. 2016; SIMULIA 2016), where d_f is the current state of fiber damage, d_m describes the current state of matrix damage, and d_s describes the current state of shear damage.

5.4.6 Material properties

Most material properties used in the finite element models in this study were obtained from the existing literature. Material properties and damage parameters used for epoxy, which was modeled as a cohesive element, and material properties and damage parameters for CFRP were obtained from Abd-El-Meguid (2008) (Table 5-3 and Table 5-5.)**.** The properties used for steel are presented in Table 5-4)

Table 5-3 Elastic and damage coefficients for adhesive materials (Abd-El-Meguid 2008),

Interfacial elastic stiffness, Normal, MPa (ksi)	K_{nn}	200,000 (29,006) [1]
Interfacial elastic stiffness, 1st Direction, MPa (ksi)	K_{ss}	75,188 (10,904) [1]
Interfacial elastic stiffness, 2nd Direction, MPa (ksi)	K_{tt}	75,188 (10,904) [1]
Normal Strain Normal Mode Only, mm/mm (in/in)	*QCRT-N*	2.50E-05 (2.50E-05)
Normal Strain Shear-Only Mode (1st Direction), mm/mm (in/in)	$QCRT\text{-}S_1$	6.65E-05 (6.65E-05)
Normal Strain Shear-Only Mode (2nd Direction), mm/mm (in/in)	$QCRT\text{-}S_2$	6.65E-05 (6.65E-05)
Displacement at failure, mm(in.)	*DaF*	1.17 (0.046) [2]

[1] Based on cohesive element initial thickness of unity (which is the default value in Abaqus), $K_{nn}= E$, $K_{ss}= G_1$, *and* $K_{tt}= G_2$

[2] Assumed value based on the Epibond 420 A/B (Araldite 420 A/B) structural adhesive datasheet (Huntsman Corporation 2017)

Table 5-4 Elastic and damage coefficients for steel materials

Young's Modulus MPa (ksi)	*E*	207000 (30000)
Poisson's ratio	*v*	0.3 (0.3)
Max Principal Stress MPa (ksi)	*MaxpsD*	248.3 (36) [1]
Displacement at failure mm (in)	*DaF*	0.508 (0.02) [2]

[1] Assumed reasonable value, this value was varied during the parametric study from 138MPa to 689.5 MPa (20 ksi-100 ksi)

[2] Based on literature: Choe et al technical report (Choi et al. 2011)

Table 5-5 Elastic and damage coefficients for CFRP materials (Abd-El-Meguid 2008),

Elastic modulus in longitudinal direction, MPa (ksi)	E_1	231000 (33495)
Elastic modulus in transverse direction, MPa (ksi)	E_2	200000 (29000)
Poisson's ratio	Nu_{12}	0.1 (0.1) [1]
Shear modulus, MPa (ksi)	G_{12}	6000 (870)
Shear modulus, MPa (ksi)	G_{13}	0 [2]
Shear modulus, MPa (ksi)	G_{23}	0 [2]
Longitudinal Tensile Strength, MPa (ksi)	X^T	3790 (550)
Longitudinal compressive Strength, MPa (ksi)	X^c	2000 (290)
Transverse Tensile Strength, MPa (ksi)	Y^T	1800 (261)
Transverse compressive Strength, MPa (ksi)	Y^C	1000 (145)
Longitudinal shear Strength, MPa (ksi)	S^L	500 (72.5)
Transverse shear Strength, MPa (ksi)	S^T	500 (72.5)
Longitudinal Tensile Fracture Energy = Fiber Tension Fracture Energy, μ J (in·kips)	G^c_{ft}	50 (4.43E-07)
Longitudinal compressive Fracture Energy = Fiber Compression Fracture Energy μ J (in·kips)	G^c_{fc}	50 (4.43E-07)
Transverse Tensile Fracture Energy = Matrix Tension Fracture Energy, μ J (in·kips)	G^c_{mt}	10 (8.85E-08)
Transverse compressive Fracture Energy = Matrix Compression Fracture Energy, μ J (in·kips)	G^c_{mc}	10 (8.85E-08)

[1] Based on literature: Sandia National Laboratories Report 2018 (Sandia National Laboratories 2018)
[2] To model the Lamina CFRP using continuum shell with G_{13} and G_{23}=0, Abaqus requires defining transverse shear stiffness K_{11}, K_{12}, K_{22}; this study is based on the minimum values to keep G_{13} and G_{23} close to zero, therefore, the assumed values were K_{11}=1, K_{12}=1, K_{22}=2.

5.4.7 Parametric Analysis

Forty-four models were constructed and executed to study the sensitivity of different parameters on the overall behavior of a cracked steel plate strengthened with CFRP laminate. A model of a steel plate with a propagatable single edge crack (PSEC) subjected to a 40 ksi tensile load was adopted in this analysis. The parametric study on steel parameters aimed to capture the influence of different grades of steel. The parametric study on CFRP parameters aimed to capture the effect of different kinds of CFRP composites (such as normal modulus CFRP, high modulus CFRP, ultrahigh modulus CFRP). The parametric study on adhesive parameters aimed to capture the influence of different types of adhesives. Target values for these parameters were determined from

existing literature and ranges were investigated below and above the target values, as shown in Table 5-6.

Table 5-6 Parametric study details

Material	Type of Parameter	Parameter Description	Symbol and Units	No. of Models	Range of Values
CFRP	Elastic	Modulus of elasticity in longitudinal direction	E_1 MPa (ksi)	9	165,480-689,500 (24,000-100,000)
		Modulus of elasticity in transverse direction	E_2 MPa (ksi)	5	10,342-200,000 (1,500-29,000)
		Poisson's ratio	Nu_{12}	6	(0-0.5)
		Shear modulus	G_{12} MPa (ksi)	5	3,696-13,793 (536-2,000)
		Shear modulus	$G_{13}=G_{23}$ MPa (ksi)	3	0-6,000 (0-870)
	Damage	Longitudinal tensile strength	X^T MPa (ksi)	4	1,600-5,171 (232-750)
Adhesive	Elastic	Traction- separation stiffness, normal (initial slop of bond separation curve)	K_{nn} MPa (ksi)	4	75,183-275,862 (10,904-40,000)
		Traction separation stiffness,1st and 2nd (initial slop of bond slip curve)	$K_{ss}=K_{tt}$ MPa (ksi)	5	75,183-200,000 (10,904-29,006)
	Damage	Normal Strain Normal Mode Only	*QCRT-N*	5	(1e-5) - (8e-5)
		Normal Strain Shear-Only Mode (1st Direction) = (2nd Direction)	*QCRT-*$S_1=S_2$	7	(5e-5) - (12e-5)
		Displacement at Failure	*DE-DaF* mm (in)	5	0.25-2.28 (0.01-0.09)
Steel	Damage	Damage for traction separation law (Maxps Damage)	*MaxpsD* MPa (ksi)	9	227.6-689.5 (33-100)
		Displacement at Failure	*DE-DaF* mm (in)	7	0.2-2.54 (0.008-0.1)

5.5 Results and Discussion

5.5.1 Model Validation

To determine validity of the FE models, model results were compared against closed-form solutions based on fracture mechanics principles. Two models were created for this purpose, both bare steel plates without CFRP or adhesive. A model of a finite plate was created with dimensions described previously (same original steel plate model having dimensions 203x102x5mm (8x4x0.2

in.) with a 20-mm (0.8-in) crack), and a wide steel plate was also modeled with a single edge crack (610x610x5mm (24x24x0.2 in.) with 20-mm (0.8-in.) crack), representing an infinite plate.

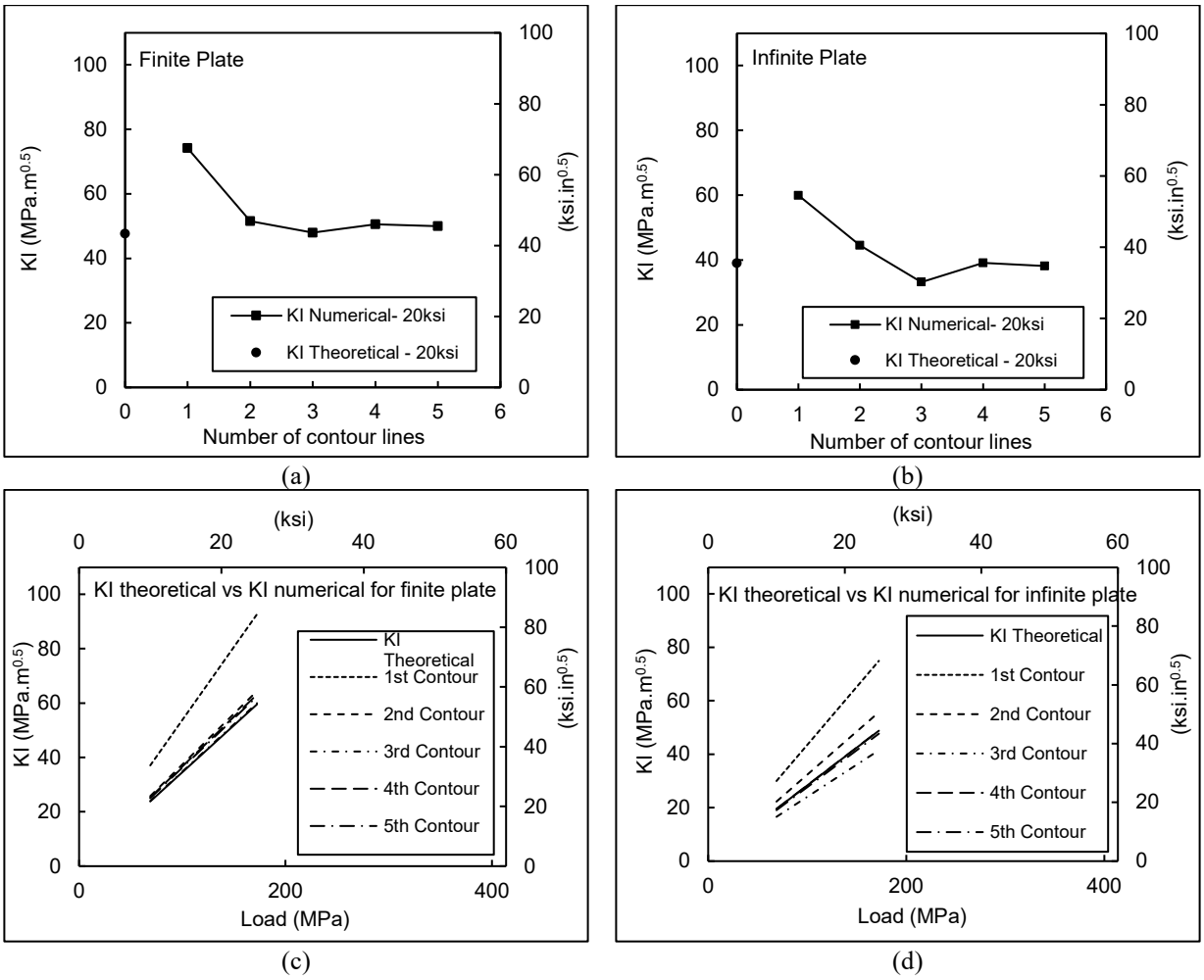

Figure 5-6 Comparison of numerical vs theoretical values *KI* for bare steel plate with stationary crack: (a) *KI* variation along 5 contours from the crack tip for finite plate at load value of 20 ksi; (b) *KI* variation along 5 contours from the crack tip for infinite plate at load value of 20 ksi; (c) *KI* variation with different loads for 5 contours for finite plate; (d) *KI* variation with different loads for 5 contours for infinite plate;

The numerical Mode I stress intensity factor, *KI*, computed from the models was compared to the closed form solution determined by equation (5-3) and equation (5-4)(5-2 (Barsom and Rolfe 1999) for a single edge crack in a finite plate and a single edge crack in an infinite plate, respectively:

$$KI = 1.12 \times \sigma \times \sqrt{(\pi a)} \times k(\frac{a}{b}) \quad (5\text{-}3)$$

$$KI = 1.12 \times \sigma \times \sqrt{(\pi a)} \quad (5\text{-}4)$$

where σ is nominal stress, a is crack length, and b is plate width. A comparison of the numerical results extracted from the first five contours and theoretical values of *KI* for the finite and infinite plate models are shown in Figure 5-6. Based on the model results, the second contour values were adopted for numerically-obtained *KI*.

5.5.2 Model Results and Discussion

Six cases were considered in the computational simulations:

- Bare steel plate with a stationary crack;
- Steel plate with a stationary crack strengthened with isotropic CFRP;
- Steel plate with a stationary crack strengthened with lamina CFRP;
- Bare steel plate with a propagatable crack;
- Steel plate with a propagatable crack strengthened with isotropic CFRP; and
- Steel plate with a propagatable crack strengthened with lamina CFRP.

As a basis for comparison between simulations, maximum principal stress and total displacement were extracted from the finite element models for all the six cases under different values of the applied tensile pressure load. The Maximum principal stresses were extracted at the crack tip for the steel plate, at the location aligning with the crack mouth for the CFRP layer, and at the ends of the adhesive layer. The total displacement was extracted at the free end of the steel plate. Moreover, the stress intensity factor *KI* was extracted for the stationary crack cases, and crack length, *a*, was recorded for models with a propagatable crack.

The variation of *KI* over 5 contours from the crack tip is presented in Figure 5-7, as a comparison between the bare steel plate with a stationary crack and the steel plate with a stationary crack strengthened with isotropic CFRP. Contour plots showing the variation of maximum principal stress on the steel plate are presented in Figure 5-8 for the bare steel plate and for the strengthened steel plate, both subjected to an applied tensile load of 138 MPa (20ksi). A comparison of the capacity of the bare steel plate and strengthened steel plate is shown in Figure 5-9. Damage initiation and damage evolution in the steel plate strengthened with lamina CFRP under tensile loading of 303 MPa (44 ksi) is presented in Figure 5-10. Moreover, a comparison of maximum principal stress, stress intensity factor, and crack length between the bare and strengthened steel plates for both stationary crack and propagatable crack cases are presented in Figure 5-11.

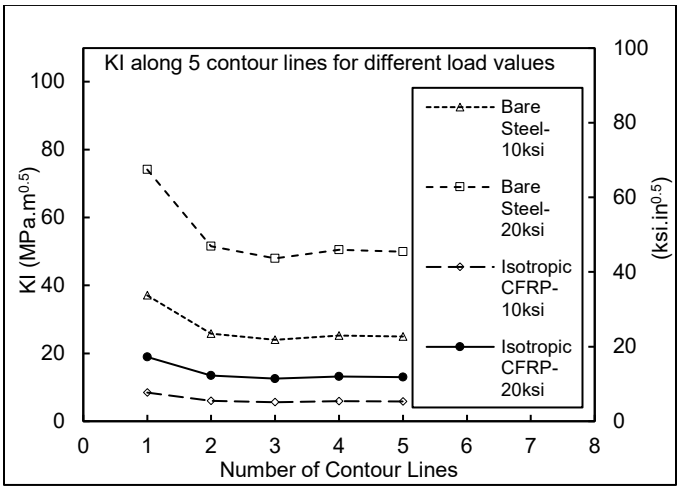

Figure 5-7 Comparison of stress intensity factor (KI) variation along 5 contours from the crack tip for bare steel plate with stationary crack against steel plate with stationary crack and strengthened with isotropic CFRP at different load values.

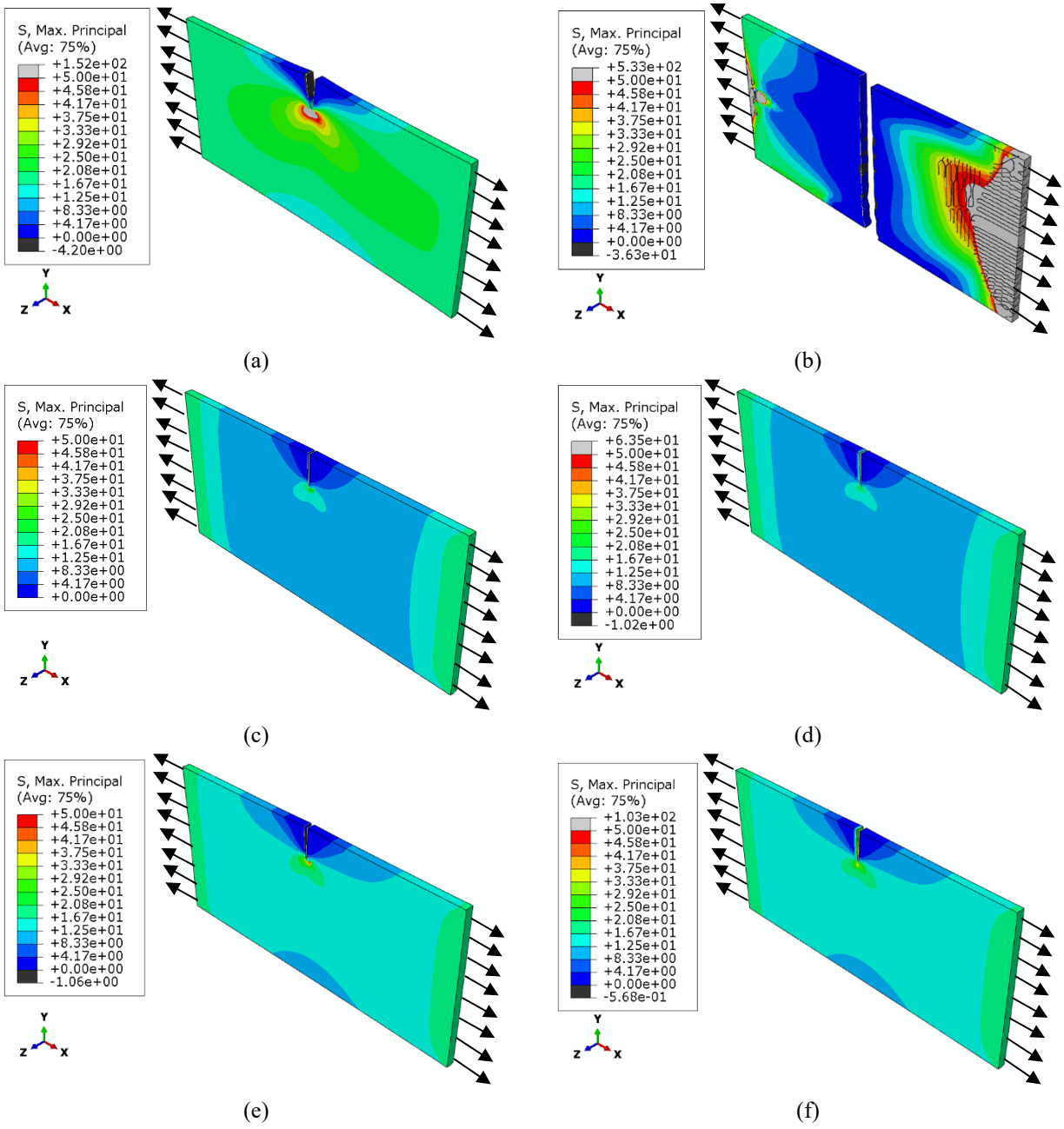

Figure 5-8 Max principal stress contours under 20 ksi pressure load (note that CFRP and adhesive layers are hidden for clarity): (a) Bare steel plate with stationary crack; (b) Bare steel plate with propagatable crack; (c) Steel plate with stationary crack strengthened with isotropic CFRP; (d) Steel plate with propagatable crack strengthened with isotropic CFRP; (e) Steel plate with stationary crack strengthened with Lamina CFRP; (f) Steel plate with propagatable crack strengthened with Lamina CFRP

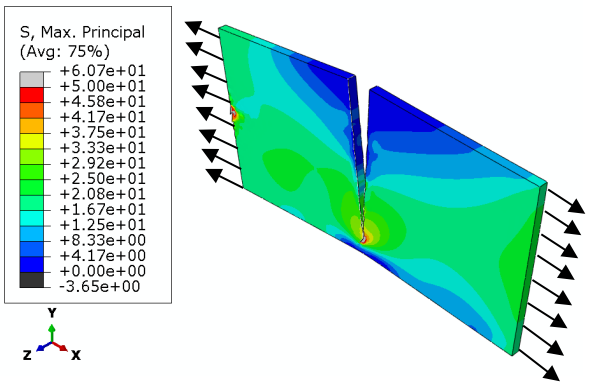

(a)

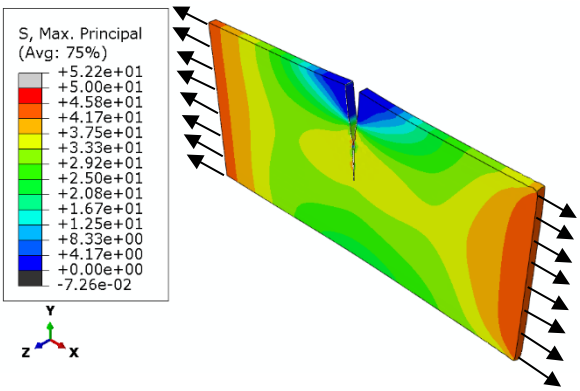

(b)

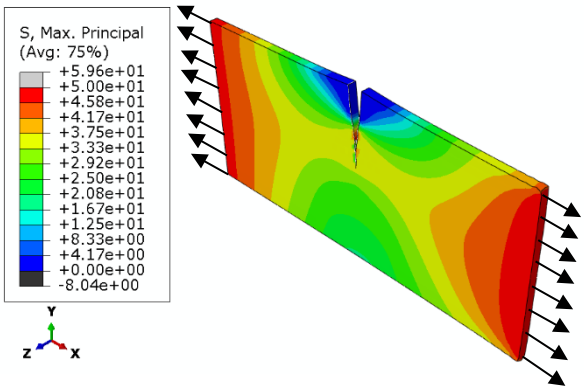

(c)

Figure 5-9 Comparison of maximum principal stresses and maximum load capacity of bare steel plate and strengthened steel plates (note that CFRP and adhesive layers are hidden for clarity): (a) Bare cracked steel plate under 131MPa (19ksi) applied load; (b) Cracked steel plate strengthened with Lamina CFRP under 303MPa (44ksi) applied load; (c) Cracked steel plate strengthened with Isotropic CFRP under 331MPa (48ksi) applied load

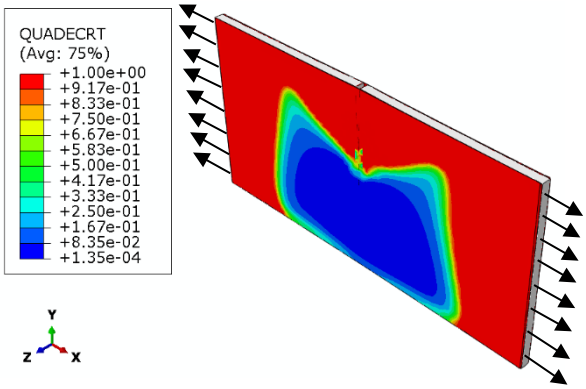

(a)

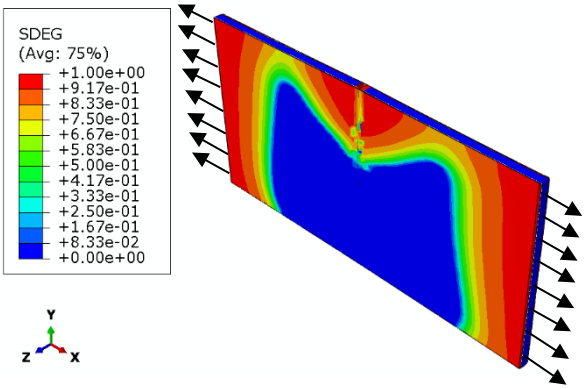

(b)

Figure 5-10 Damage initiation and damage evolution in steel plate strengthened with lamina CFRP under tensile load of 303MPa (44ksi) (note that CFRP layers are hidden for clarity): (a) Damage initiation: red color represents the damage initiation criteria (QUADECRT=1); (b) Damage evolution: red color represents the damage evolution (SDEG=1)

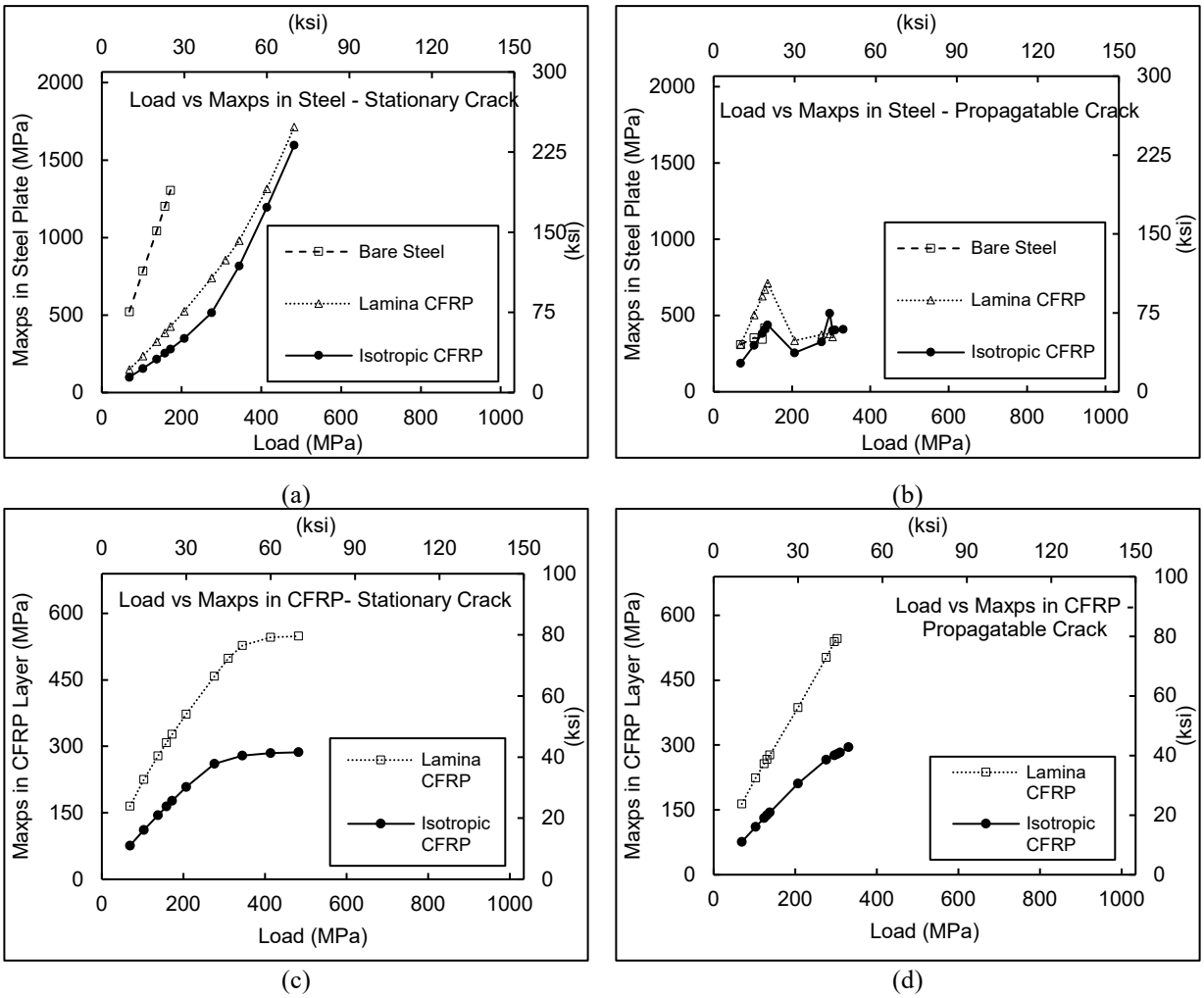

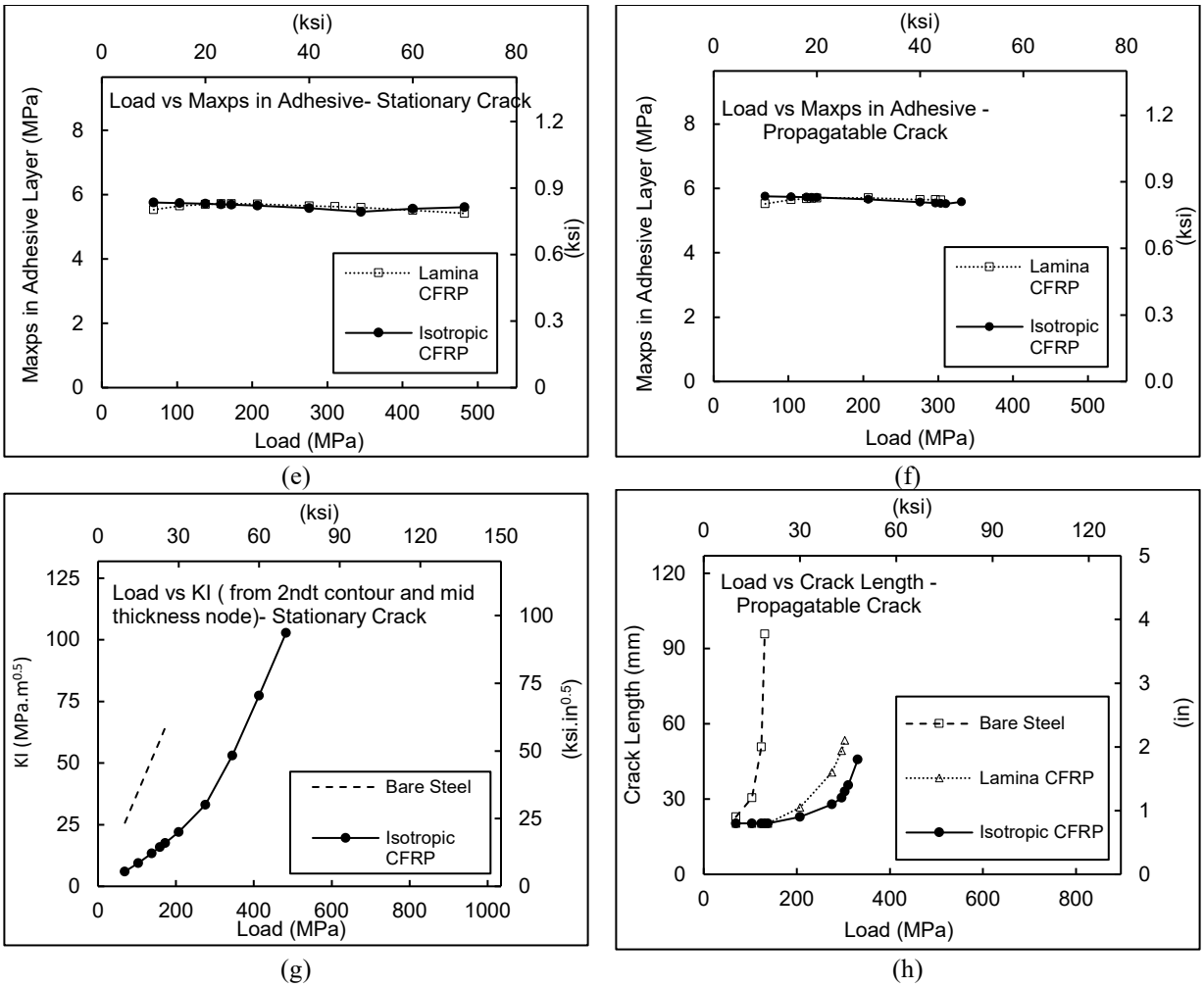

Figure 5-11 Comparison of bare cracked steel plate against cracked steel plate strengthened with isotropic CFRP or Lamina CFRP at different loads: (a) Maximum principal stress in steel plate for stationary crack; (b) Maximum principal stress in steel plate for propagatable crack; (c) Maximum principal stress in CFRP for stationary crack; (d) Maximum principal stress in CFRP for propagatable crack; (e) Maximum principal stress in adhesive for stationary crack; (f) Maximum principal stress in adhesive for propagatable crack; (g) Stress intensity factor (KI) for stationary crack; (h) Crack propagating length for propagatable crack

It is clear from the results that the CFRP strengthening reduces maximum principal stress at the crack tip, reduces stress intensity factor at the crack tip, and prevents or reduces crack propagation. For the steel plate with a stationary crack, addition of CFRP significantly reduced the stress intensity factor at the crack tip. For example, for the same applied load of 138 MPa (20 ksi), *KI* reduced from 51.5 MPa√m (46.9 ksi√in.) for the bare steel plate to 13.4 MPa√m (12.2 ksi√in.) for the strengthened steel plate case, an approximate 300% decrease in the stress intensity factor

(Figure 5-7 and Figure 5-11g). Strengthening with CFRP also significantly reduced the maximum principal stress; for instance, under the same applied load of 138 MPa (20 ksi), the maximum principal stress decreased from 1,045 MPa (151.5ksi) for the bare steel plate to 217 MPa (31.43 ksi) for the strengthened steel plate, which is a 380% reduction (Figure 5-8 a, b and Figure 5-11a).

For the steel plate with a propagatable crack, strengthening with CFRP reduced the amount of crack propagation. For the same applied load of 138 MPa (20 ksi) the crack length, *a*, reduced from 101.6 mm (4 in.) (full separation of the steel plate) for the bare steel plate to 20 mm (0.8 in) (original crack length) for the strengthened steel plate (see Figure 5-8 c, d). Moreover, strengthening with CFRP increased the required load for full steel plate separation from 20 ksi for the bare steel plate to 303 MPa (44 ksi) for the steel plate strengthened with Lamina CFRP and to 331 MPa (48 ksi) for the steel plate strengthened with Isotropic CFRP, which is an increase in load carrying capacity of 150% (Figure 5-9 and Figure 5-11h). Furthermore, CFRP strengthening increased the load required for crack propagation. As an example, the crack propagated at load of 69 MPa (10 ksi) for the bare steel plate, but propagated at load of 207 MPa (30 ksi) for the CFRP-strengthened case, which is a 200% increase in the load required for crack propagation (Figure 5-11h).

From a comparison of maximum principal stress between the bare and strengthened steel plate with a propagatable crack (Figure 5-11b), both show “zig-zag” behavior. This may be attributed to the crack propagation damage modeling technique, wherein stress at the crack tip continues increasing until the specified damage criteria is met; at this point, the crack propagates a small amount, leading to a decrease in stress at the crack tip. This mechanism repeats itself until complete separation occurs (102mm (4 in) crack).

5.5.3 Parametric Analysis Results and Discussion

The effect of the CFRP elastic and damage parameters on crack propagation behavior are presented in Figure 5-12, while the effect of the adhesive elastic and damage parameters on crack propagation behavior are presented in Figure 5-13. Lastly, Figure 5-14 presents the effect of steel damage parameters on the crack propagation.

It is clear from Figure 5-12 that most of the CFRP-modeling parameters did not have a major effect on crack propagation, except the modulus of elasticity in the longitudinal direction *E1*. Increasing *E1* was associated with significant reductions in crack length. However, it provided diminishing returns beyond 517 GPa (75,000 ksi). A high-modulus CFRP such as 3K plain weave carbon fiber from Fibre Glast has *E1* range of 227-240 GPa (33,000-35,000 ksi) (Fibre Glast Developments Corporation 2017)), and ultrahigh modulus carbon fiber laminate like MBrace from BASF has *E1* of 457GPa (66,381 ksi) (Al-Mosawe et al. 2016).

Figure 5-13 shows that increasing the adhesive traction separation stiffness (K_{ss} and K_{tt}) and nominal shear strain were associated with significant reductions in crack length. However, they showed diminishing returns at higher values. Figure 5-13 shows that reducing the displacement at failure (DaF) in the adhesive below 0.76 mm (0.03in) has a significant effect in increasing crack propagation. Therefore, this is a value that requires significant attention in creating high-fidelity models intended to predict adhesive debonding.

It can be seen from Figure 5-14 that increasing the maximum principal stress responsible for triggering damage initiation in the steel substrate was associated with large reductions in crack length; this is not surprising, since this is the value that represents the onset of damage initiation.

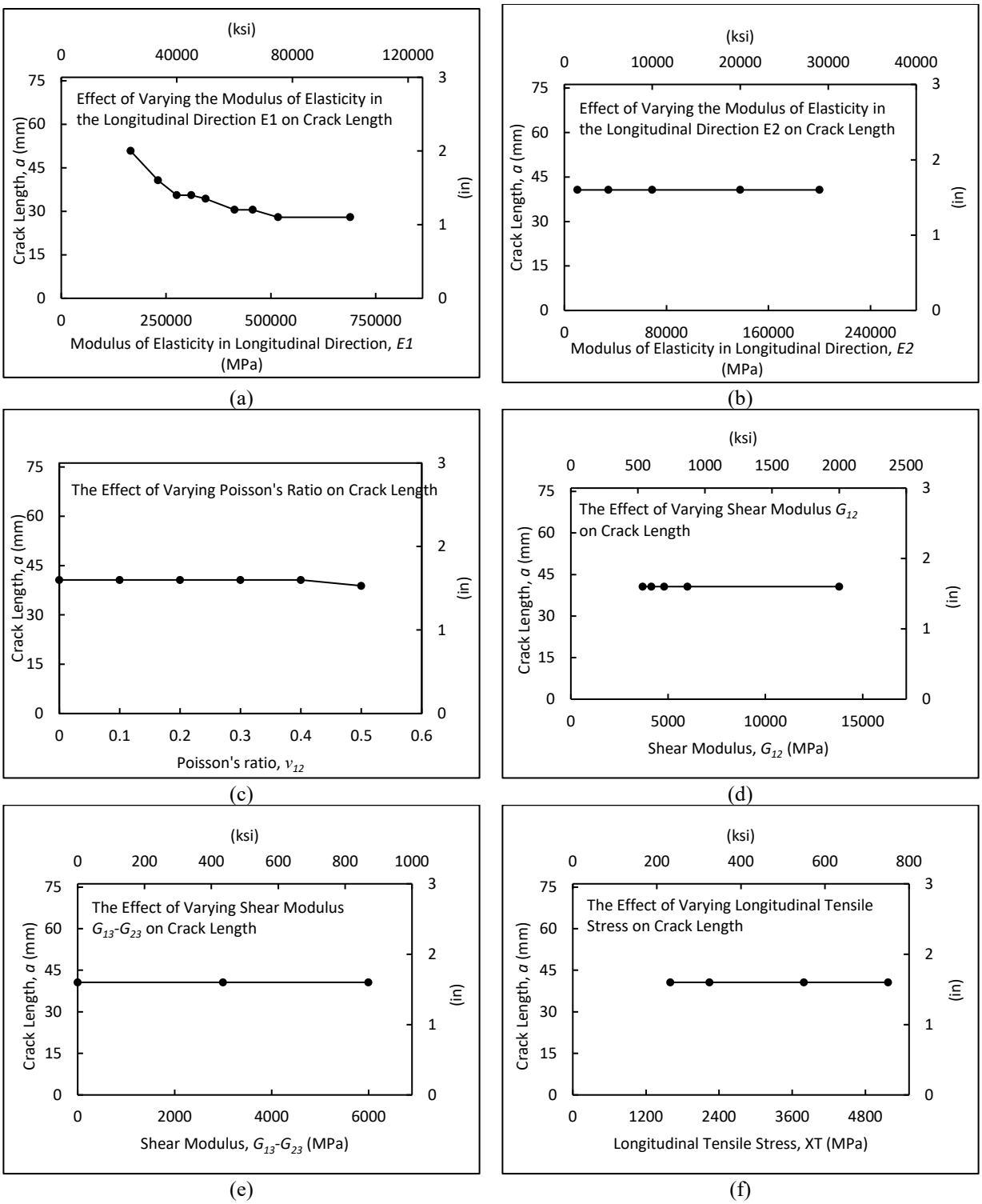

Figure 5-12 Effect of CFRP elastic and damage parameters on crack propagation: (a) Modulus of elasticity in longitudinal direction; (b) Modulus of elasticity in transverse direction; (c) Poisson's ratio; (d) Shear modulus, G_{12}; (e) Shear modulus G_{13}=G_{23}; (f) Longitudinal tensile strength

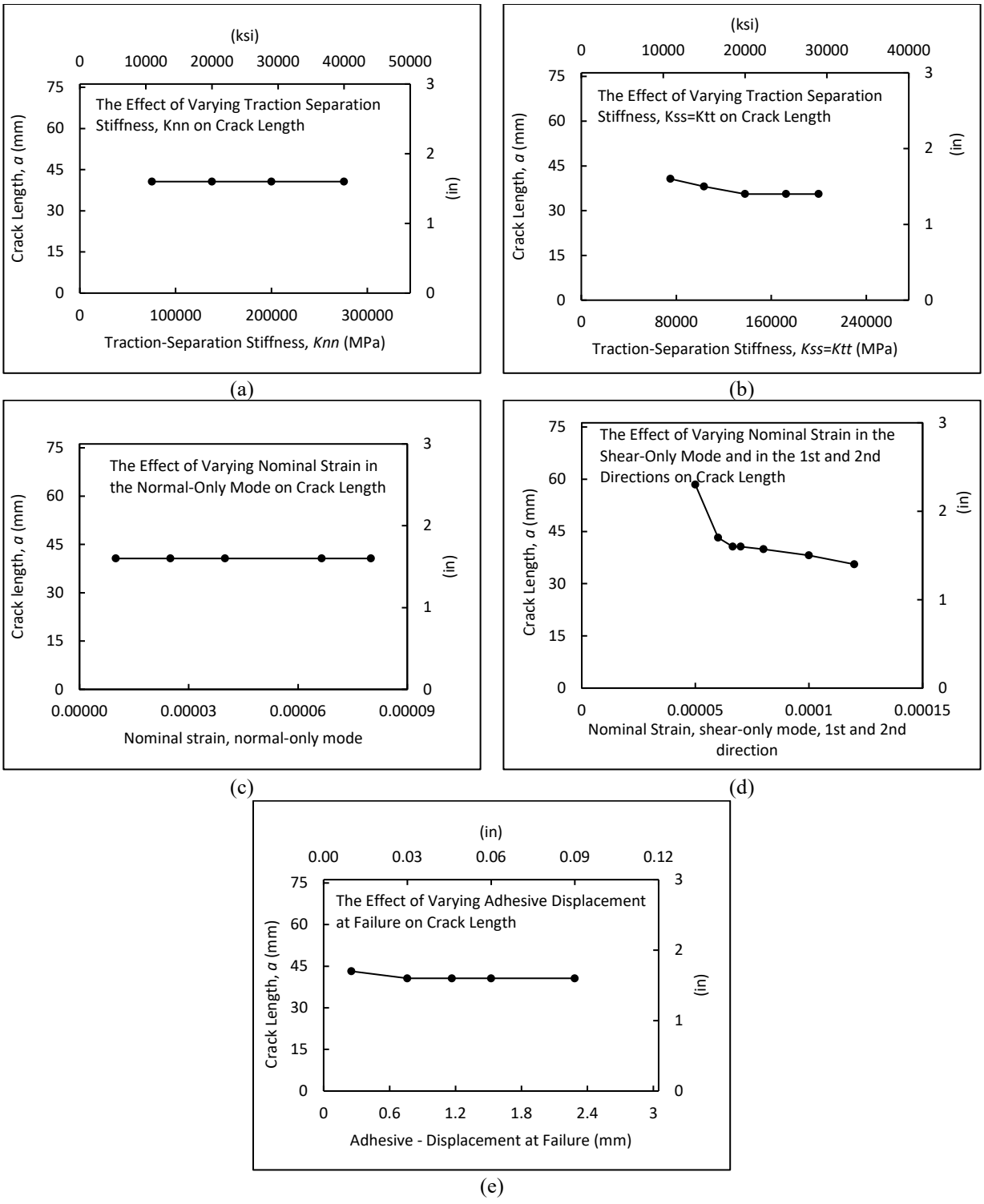

Figure 5-13 Effect of adhesive elastic and damage parameters on the crack propagation: (a) Traction-separation stiffness, normal (initial slope of bond separation curve); (b) Traction-separation stiffness,1st and 2nd (initial slope of bond-slip curve); (c) Normal strain normal mode only; (d) Normal strain shear-only mode (1st Direction= 2nd Direction); (e) Displacement at failure in the adhesive determined as shown in equation (5-2)

Reducing the displacement at failure (DaF) criterion below 0.51 mm (0.02in) increased crack propagation slightly.

A summary of the parametric analysis, ranges of the parameters studied, and their effects on crack propagation is presented in Table 5-7.

Table 5-7 Summary of the parametric analysis, range of the parameter values and their effects

Material			**No. of Model**	**Range of Values**	**Results and Conclusions**
CFRP	Elastic	E_1, MPa (ksi)	9	165,480-689,500 (24,000-100,000)	Increasing *E1* effectively reduce the crack growing. Significantly increase in CFRP Maxps Slightly decrease in steel Maxps
		E_2, MPa (ksi)	5	10,342-200,000 (1,500-29,000)	No significant effect
		Nu_{12}	6	(0-0.5)	No significant effect
		G_{12}, MPa (ksi)	5	3,696-13,793 (536-2,000)	No significant effect
		$G_{13}=G_{23}$, MPa (ksi)	3	0-6,000 (0-870)	No significant effect
	Damage	$X^{T,}$ MPa (ksi)	4	1,600-5,171 (232-750)	No significant effect of crack growing length
Adhesive	Elastic	K_{nn} ,MPa (ksi)	4	75,183-275,862 (10,904-40,000)	No significant effect
		$K_{ss}=K_{tt,}$ MPa (ksi)	5	75,183-200,000 (10,904-29,006)	Reducing $K_{ss}=K_{tt}$ below 137900MPa (20000 ksi), increases the crack growing and the Maxps at crack tip No significant effect above 137900MPa (20000 ksi) Increasing $K_{ss}=K_{tt}$ significantly increase in CFRP Maxps Significantly increase in adhesive Maxps
	Damage	*QCRT-N*	5	(1e-5) – (8e-5)	Slightly increase in adhesive Maxps Increasing $S_1=S_2$ effectively reduce the crack growing Significantly increase in CFRP Maxps Significantly increase in adhesive Maxps
		QCRT-S1=S2	7	(5e-5) - (12e-5)	
		DE-DaF, mm (in)	5	0.25-2.28 (0.01-0.09)	Reducing DE-DaF below 0.76mm (0.03 in), increases the crack growing slightly No significant effect above 0.76 mm (0.03in)
Steel	Damage	*MaxpsD*, MPa (ksi)	9	227.6-689.5 (33-100)	Increasing MaxpsD effectively reduce the crack growing Significantly increase in steel Maxps Slightly decrease in CFRP Maxps
		DE-DaF, mm (in)	7	0.2-2.54 (0.008-0.1)	Reducing DE-DaF below 0.51 mm (0.02 in), increases the crack growing slightly No significant effect above 0.51 mm (0.02in)

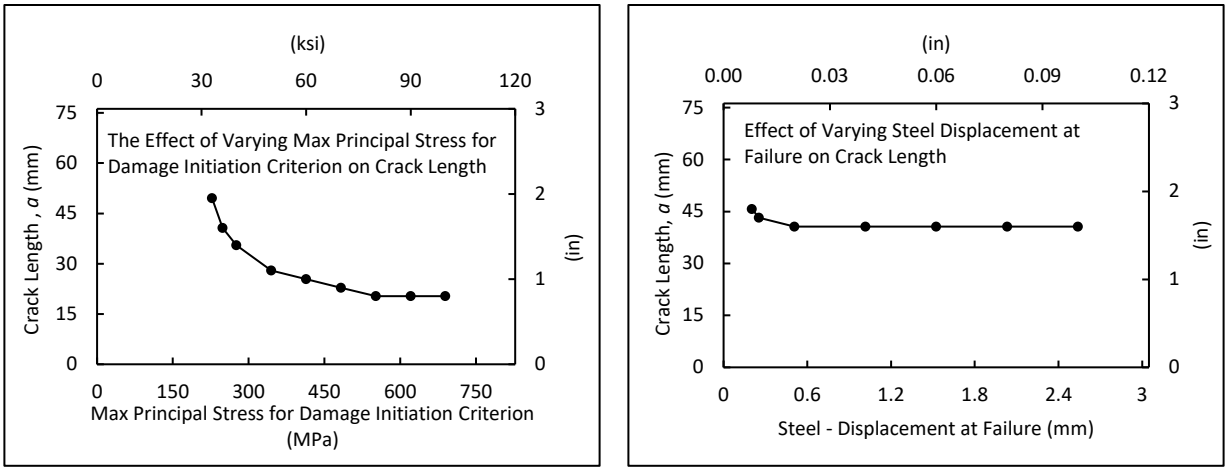

(a) (b)

Figure 5-14 Effect of steel damage parameters on crack propagation: (a) Max principal stress at damage initiation, (b) Displacement at failure at damage evolution determined as shown in equation (5-2)

5.6 Conclusions

A total of 135 finite elements models of a steel plate with a single edge crack were created to investigate the effectiveness of CFRP in reducing stress demand, stress intensity factor at the crack tip, and reducing crack propagation. Different modeling techniques and parameters were investigated to capture the CFRP performance, including an infinite and finite steel plate, stationary cracks and propagatable cracks using the XFEM modeling technique, isotropic and lamina CFRP materials, and modeling of damage initiation and damage evolution for steel, CFRP, and adhesive materials. Based on the results, the following key conclusions can be drawn:

1. For all the cases and loads modeled in the study, CFRP strengthening reduced the maximum principal stress at the crack tip by 380%. Additionally, analysis results showed that the addition of CFRP made a large reduction, up to 285%, in the stress intensity factor, K_I, at the crack tip.

2. Results indicated that strengthening the steel plate with CFRP led to an increase in maximum load carrying capacity up to 150%.

3. Strengthening with CFRP increased in the load required for crack propagation by 200%, and completely halted the crack propagation at a load of 138 MPa (20 ksi).

4. The parametric study on the CFRP modeling parameters showed that increasing elastic modulus in the longitudinal direction of the CFRP ($E1$) led to an increase in the capacity and reduced crack propagation length.

5. The parametric study on the adhesive modeling parameters indicated that increasing the adhesive traction separation stiffness (K_{ss} and K_{tt}) and nominal shear strain were also associated with significant reductions in crack length.

6. The parametric study on the steel modeling parameters indicated that increasing the maximum principal stress responsible for triggering damage initiation in the steel substrate was associated with large reductions in crack length. Result also indicated that reducing the displacement at failure (DaF) below 0.51 mm (0.02in) increased crack propagation slightly.

CFRP composites are a promising mitigation measure for cracked steel members, as illustrated in this analytical study for a steel plate with single edge crack under tensile pressure load. Although previous research has examined the efficacy of CFRP to halt fatigue cracking, little prior research into the effect of damage modeling parameters for cracked steel members strengthened with CFRP materials has been carried out. The study described in this paper constitutes an important and novel contribution to understanding the effect of different elastic and damage modeling parameters on the efficacy of CFRP in halting crack propagation that added to the available body of knowledge and literature.

Further investigations are recommended to study the effect of different steel plate thicknesses, crack locations, initial crack length, adhesive thicknesses, CFRP thicknesses, and CFRP bond length. Additionally, experimental tests are recommended to confirm the numerical results and conclusions of this study.

5.7 References

Abd-El-Meguid, A. S. (2008). "Strengthening and rehabilitation of steel bridge girders using CFRP laminates." Birmingham, Ala. : University of Alabama at Birmingham.

Al-Mosawe, A., Al-Mahaidi, R., and Zhao, X.-L. (2016). "Experimental and Numerical Study on Strengthening of Steel Members Subjected to Impact Loading Using Ultrahigh Modulus CFRP." *Journal of Composites for Construction*, 20(6).

Al-Salih, H., Bennett, C., and Matamoros, A. (2020). "Evaluation of Novel Combined CFRP-Steel Retrofit for Repairing Distortion-Induced Fatigue." *Journal of Constructional Steel Research* (in review).

Al-Salih, H., Bennett, C., Matamoros, A., Collins, W., and Li, J. (2020). "Repairing Distortion-Induced Fatigue in Steel Bridges Using a CFRP-Steel Retrofit." *Structures Congress 2020*, 273-284.

Al-Zubaidy, H., Al-Mahaidi, R., and Zhao, X.-L. (2013). "Finite element modelling of CFRP/steel double strap joints subjected to dynamic tensile loadings." *Composite Structures*, 99, 48-61.

Alwash, N. A., and AL-Salih, H. I. (2013). "Experimental Investigation on Behavior of SCC Filled Steel Tubular Stub Columns Strengthened with CFRP." *Construction Engineering*, 1(2), 37-51.

Barsom, J. M., and Rolfe, S. T. (1999). *Fracture and Fatigue Control in Structures: Application of Fracture Mechanics*, ASTM, West Conshohocken, PA.

Bocciarelli, M., Colombi, P., D'Antino, T., and Fava, G. (2018). "Intermediate crack induced debonding in steel beams reinforced with CFRP plates under fatigue loading." *Engineering Structures*, 171, 883-893.

Carolin, A. (2003). "Carbon fibre reinforced polymers for strengthening of structural elements." Luleå.

Chen, T., Huang, C., Hu, L., and Song, X. (2019). "Experimental study on mixed-mode fatigue behavior of center cracked steel plates repaired with CFRP materials." *Thin-Walled Structures*, 135, 486-493.

Choi, M.-K., Kim, T.-H., and Villani, C. (2011). "Fracture toughness test and its simulation for brittle and ductile steel." *Technical report*, Purdue University.

Fernando, D., Yu, T., and Teng, J. G. (2014). "Behavior of CFRP Laminates Bonded to a Steel Substrate Using a Ductile Adhesive." *Journal of Composites for Construction*, 18(2), 04013040.

Fernando, N. D. (2010). "Bond Behaviour and debonding Failures in CFRP-strengthened members." Ph.D. Thesis, The Hong Kong Polytechnic University, Hong Kong, China.

Fibre Glast Developments Corporation (2017). "3K, Plain Weave Carbon Fiber." *Product Data Sheet,* Brookville, Ohio.

Fukuyama, H., Nakai, H., Tanigaki, M., and Uomoto, T. "JCI State-of œthe-Art on retrofiting by CFRM part1. Materials, Construction and Application." *Proc., Non-Metallic (FRP) Reinforcement for Concrete Structures, Proceedings of the Third Symposium*, 605-612.

Ghahremani, K., Walbridge, S., and Topper, T. (2015). "Inhibiting Distortion-Induced Fatigue Damage in Steel Girders by Using FRP Angles." *Journal of Bridge Engineering*, 20(6).

Hashin, Z. (1980). "Failure criteria for unidirectional fiber composites."

Hashin, Z., and Rotem, A. (1973). "A fatigue failure criterion for fiber reinforced materials." *Journal of composite materials*, 7(4), 448-464.

Huntsman Corporation (2017). "Epibond® 420 A/B Epoxy Adhesive." *Advanced Materials Technical Datasheet,* The Woodlands, TX.

Kaan, B., Alemdar, F., Bennett, C., Matamoros, A., Barrett-Gonzalez, R., and Rolfe, S. (2012). "Fatigue Enhancement of Welded Details in Steel Bridges Using CFRP Overlay Elements." *J. Compos. Constr.*, 16(2), 138-149.

Kabir, M. H., Fawzia, S., Chan, T., Gamage, J. C., and Bai, J. (2016). "Experimental and numerical investigation of the behaviour of CFRP strengthened CHS beams subjected to bending." *Engineering Structures*, 113, 160-173.

Khan, A., Baluch, M., and Al-Gadhib, A. "Repair and strengthening of reinforced concrete structures using CFRP plates." *Proc., Proceedings of international Bhurban conference on applied sciences and technology v. 2*.

Liu, H., Al-Mahaidi, R., and Zhao, X.-L. (2009). "Experimental study of fatigue crack growth behaviour in adhesively reinforced steel structures." *Composite Structures*, 90(1), 12-20.

Lundqvist, J. (2007). "Numerical analysis of concrete elements strengthened with carbon fiber reinforced polymers." Luleå tekniska universitet.

MAPEI (2011). "Fiber Reinforced Polymer (FRP) Composite Systems."

Meier, U. (1987). "Bridge “Repair with high performance Composite Materials”, Material und Technik, v4, 125128." German.

Naghipour, P., Schneider, J., Bartsch, M., Hausmann, J., and Voggenreiter, H. (2009). "Fracture simulation of CFRP laminates in mixed mode bending." *Engineering Fracture Mechanics*, 76(18), 2821-2833.

Nordin, H. (2003). "Flexural strengthening of concrete structures with prestressed near surface mounted CFRP rods." *Licentiate Thesis, Lulea University of Technology, Lulea, Sweden*.

Nozaka, K., Shield, C., and Hajjar, J. (2005). "Effective Bond Length of Carbon-Fiber-Reinforced Polymer Strips Bonded to Fatigued Steel Bridge I-Girders." *J. Bridge Eng.*, 10(2), 195-205.

Sandia National Laboratories (2018). "Mechanical Properties of Woven Composites at Ambient Temperature." Sandia National Laboratories, Livermore, California 94550.

SIMULIA (2016). "SIMULIA™ Support Documentation - Dassault Systèmes®, Abaqus, Version 2016." <http://simulia.com>.

Tavakkolizadeh, M., and Saadatmanesh, H. (2003). "Fatigue Strength of Steel Girders Strengthened with Carbon Fiber Reinforced Polymer Patch." *J. Struct. Eng.*, 129(2), 186-196.

Teng, J. G., Fernando, D., and Yu, T. (2015). "Finite element modelling of debonding failures in steel beams flexurally strengthened with CFRP laminates." *Engineering Structures*, 86, 213-224.

Wang, H.-T., Wu, G., and Jiang, J.-B. (2016). "Fatigue Behavior of Cracked Steel Plates Strengthened with Different CFRP Systems and Configurations." *Journal of Composites for Construction*, 20(3).

Wang, H.-T., Wu, G., and Wu, Z.-S. (2014). "Effect of FRP Configurations on the Fatigue Repair Effectiveness of Cracked Steel Plates." *Journal of Composites for Construction*, 18(1).

Wu, G., Wang, H., Wu, Z., Liu, H., and Ren, Y. (2012). "Experimental Study on the Fatigue Behavior of Steel Beams Strengthened with Different Fiber-Reinforced Composite Plates." *J. Compos. Constr.*, 16(2), 127-137.

Chapter 6: **Evaluation of Novel Combined CFRP-Steel Retrofit for Repairing Distortion-Induced Fatigue**

Hayder Al-Salih[1], Caroline Bennett[2], Ph.D., P.E., and Adolfo Matamoros, Ph.D., P.E. [3]

[1]Graduate Research Assistant, University of Kansas, Department of Civil, Environmental, and Architectural Engineering, 1530 W. 15th St., Lawrence, Kansas, 66045, E-mail: hia@ku.edu

[2]Professor, University of Kansas, Department of Civil, Environmental, and Architectural Engineering, 1530 W. 15th St., Lawrence, Kansas, 66045, E-mail: crb@ku.edu (Corresponding Author)

[3]Professor, University of Texas San Antonio, Department of Civil and Environmental Engineering

6.1 Abstract

Distortion-induced fatigue damage at crossframe-to girder connections affects many steel bridges built before the mid-1980s. This type of damage is associated with a prevalent detailing practice at the time which avoided welding connection plates to girder flanges to avoid fatigue cracks. The lack of connectivity and out-of-plane motion of the crossframe produce a flexible gap region in the girder web where fatigue cracks often develop, requiring frequent inspections, costly maintenance, and repairs.

This paper presents a study evaluating the use of CFRP in conjunction with steel sections to repair complex patterns of distortion-induced fatigue cracks in steel bridge web gaps, without the need for bolting to the flange or concrete deck removal. A steel girder-to-crossframe subassembly was tested in distortion-induced fatigue to evaluate the performance of the retrofit measure. Realistic crack patterns were introduced by applying fatigue loading, and the efficacy of the repair method was evaluated by monitoring crack growth with the repair in place. Twelve test trials were performed: five in the unretrofitted condition to propagate the cracks, and seven in the retrofitted condition to evaluate the performance of the repair. The study evaluated multiple crack patterns, different configurations of the retrofit, presence or absence of mechanical anchorage to the flange,

footprint of the CFRP relative to the steel retrofit elements, and different surfaces connected by the CFRP.

The results showed that the combined CFRP-steel retrofit measure was effective in preventing distortion-induced fatigue crack initiation and propagation.

Keywords:

steel bridges; fatigue; distortion-induced fatigue; fatigue repair; retrofit; CFRP; composite; carbon fiber.

6.2 Introduction and Background

Fatigue damage in steel bridges is classified according to cause in two broad categories: in-plane fatigue damage, caused by primary stresses, and distortion-induced fatigue, caused by secondary stresses. For many aging bridges built prior to the mid-1980s, common detailing practice was to leave connection plates unconnected to the adjacent girder flange to prevent fatigue cracks in the flange (i.e., web gap regions were created to avoid welding to the tension flange). This practice resulted in flexible web-gap regions susceptible to localized bending and a connection detail vulnerable to fatigue cracking, as illustrated in Figure 6-1 (Hartman et al. 2013; Hassel et al. 2010).

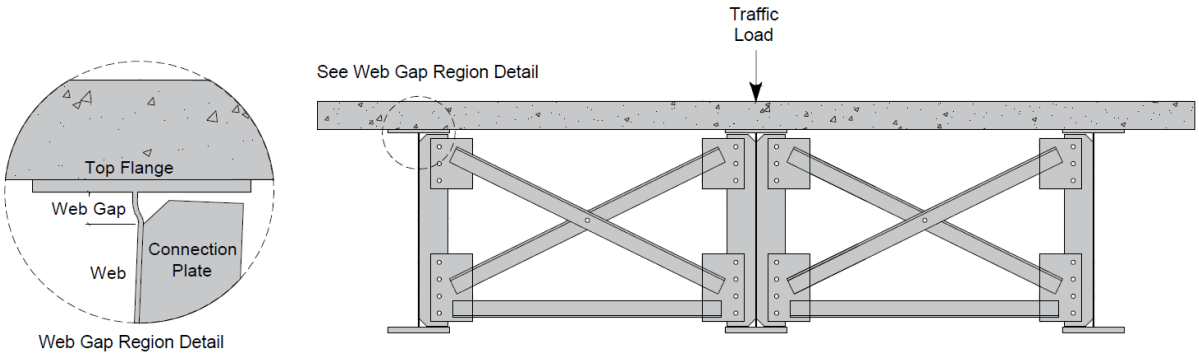

Figure 6-1 Distortion-induced fatigue in web-gap regions caused by relative displacement of adjacent girders under live loads

Dexter and Ocel (Dexter and Ocel 2013) and Connor and Lloyd (Connor and Lloyd 2017) summarize repair techniques available for distortion-induced fatigue and provide a discussion on advantages and disadvantages of each method. Commonly-used repair methods for web-gap regions damaged by distortion-induced fatigue are grouped into three categories: (1) crack repair, which can be accomplished by grinding and re-welding, adding doubler plates, and/or drilling crack-arrest holes; (2) connection softening, which can be accomplished by diaphragm or crossframe removal or repositioning, bolt removal or loosening, and removal of material around the web-gap region to soften the area through coping or large hole-drilling; and (3) connection stiffening, which has traditionally been accomplished by providing positive attachment through welding and/or bolting (Connor and Lloyd 2017; Dexter and Ocel 2013).

The most common method of repair for distortion-induced fatigue is to reduce localized stresses in the web gap region by attaching the connection plate (CP) and the top flange with bolted steel angles. This repair requires removal of the concrete deck to make the bolted connection, which causes disruption to the traveling public (Hassel et al. 2010). This retrofit is shown in Figure 6-2a.

The angles-with-plate retrofit is a more recent attachment technique that avoids interference with the concrete deck so installation can proceed with minimal disruption to traffic (Alemdar et al. 2014; Hartman et al. 2013). Connection between the girder web and connection plate is provided using a pair of angles instead of connecting the flange and the CP, and utilizes a backing plate to distribute out-of-plane stresses over a wide area of the girder web (see Figure 6-2b). For connections with a crossframe on both sides of the girder, as is often the case for interior girders, the backing plate can be replaced by a second pair of angles. Experiments have shown that the angles-with-plate retrofit measure drastically reduces crack propagation rates in the region surrounding the connection plate as well as in cracks of moderate length near the web-to-flange

weld. However, this retrofit measure was not effective in girders with long, aggressive web-to-flange cracks (>203 mm [8 in.]), where its use was not recommended based on the experimental results.

Increased use of composite materials over the past two decades has sparked interest on strengthening steel structures with externally bonded carbon fiber reinforced polymers (CFRP), including fatigue applications. Despite a growing body of literature on this topic, there are very few studies investigating repair of distortion-induced fatigue damage in steel bridges with CFRP materials. The features that make CFRP materials appealing for strengthening structures include high tensile strength and stiffness, low weight, corrosion resistance, and adhesive bonding. Unlike traditional repair methods for distortion-induced fatigue that rely on the attachment of standard shapes, CFRP materials introduce potential for less intrusive repairs and reduced needs for heavy equipment because they can be glued in place. Also, adhesive bonding of CFRPs distributes connection forces over larger areas and eliminates residual stresses caused by mechanical fastening and welding (Al-Mosawe et al. 2016; Al-Zubaidy et al. 2012; Ghahremani et al. 2015; Liu et al. 2009; Wu et al. 2012).

A study conducted by Ghahremani et al. (2015) at the University of Waterloo investigated the use of glass fiber reinforced polymer (GFRP) angles for repairing distortion-induced fatigue in steel bridge girders. Fatigue tests were performed on specimens designed to simulate the web gap region of a crossframe-to-girder connection in a steel girder bridge. Angles were adhesively bonded to the steel, which eliminated the need for concrete deck removal, drilling holes in the girder, and bolting. Results of the study showed that fatigue life of the connection was extended by several hundred percent, and that debonding of the GFRP angles was the dominant mode of failure. Performance of the repair was improved by using a highly ductile adhesive, which delayed

debonding. Tests by Ghahremani et al. showed that the main limitation of composite repairs is the tendency of the composite material to debond from the steel under fatigue loading. Debonding renders the repair ineffective, and monitoring the composite-steel interface is challenging under field conditions.

Other researchers have investigated composite repairs where attachment between composite materials and steel is not achieved solely by gluing. Bun (2014) and Bonet (2014) conducted pilot studies investigating the use of cast-in-place composite blocks to mitigate distortion-induced fatigue cracks in steel bridge girders, and showed that the bond between the blocks and the girder could be maintained in the presence of mechanical attachment for numbers of cycles similar to infinite fatigue life.

This study addresses significant limitations of previous research on the repair of distortion-induced fatigue damage: the ineffectiveness of the angles-with-plate retrofit in connections with long horizontal web-to-flange weld cracks due to lack of simultaneous attachment to the surfaces of the web, flange, and connection plate; cases where fatigue cracking extends beyond the boundaries of the angles-with-plate steel components; and the loss of bond at composite-steel interfaces under fatigue loading that renders FRP repairs ineffective and unable to restrain crack opening.

6.3 Objective and Scope

The goal of this study was to investigate the performance of the angles-with-plate retrofit used in combination with CFRP materials for repairing distortion-induced fatigue cracks. The scope of the study included the development of a novel CFRP-steel retrofit that simultaneously engages the surfaces of the girder web, flange and connection plate in an unobtrusive manner. A combined

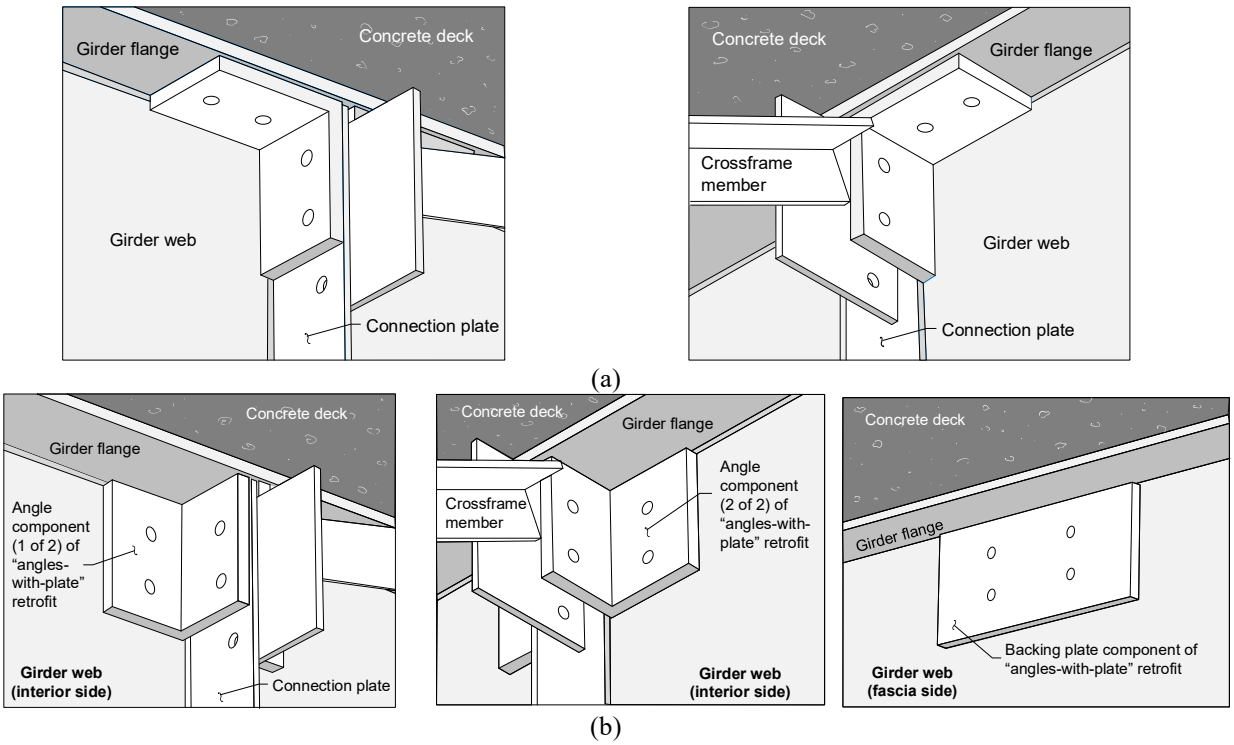

Figure 6-2 Existing retrofits for distortion induced fatigue: (a) Angle to flange retrofit ; (b) Angles-with-plate retrofit

CFRP-steel retrofit has potential to address various limitations of the angles-with-plate retrofit, particularly in cases that include long web-to-flange cracks, or in cases where cracks may extend beyond the edges of a steel-only retrofit. The addition of CFRP in different configurations with the steel angles-with-plate elements may offer a solution to these challenges, as a combined CFRP-steel retrofit provides connectivity to the flange without necessarily requiring fasteners or concrete deck removal, and also allows for the CFRP components to extend beyond the steel components in cases where cracks are very long. The mechanical properties of CFRP, including its high tensile strength and stiffness and good resistance to fatigue loading, make it a valuable material for investigation in this application.

Fatigue tests were performed on a 2845-mm (9-ft) long steel plate girder-crossframe subassembly to evaluate the efficiency of different CFRP and angles-and-plate retrofit configurations for repairing distortion-induced fatigue damage in steel bridges. The experimental program consisted

of 12 trials with different cracks patterns and lengths, CFRP configurations, and steel retrofit configurations. A single girder specimen was used for the 12 test trials, therefore the cumulative number of fatigue cycles applied to the girder increased with each consecutive test trial.

6.4 Experimental Configuration

6.4.1 Girder Subassembly Dimensions and Overall Test Configuration

A built-up, welded I-shaped steel plate girder and crossframe subassembly was used in the experimental study. The girder, shown in Figure 6-3 , was cyclically loaded to initiate and propagate fatigue cracks in the web gap region of the girder. The cracked specimen was repaired with different variants of a CFRP-steel retrofit over a series of test trials, and crack propagation was monitored under fatigue loading to evaluate effectiveness of the repair variants in mitigating distortion-induced fatigue damage. The dimensions of the girder are presented in Figure 6-4 , which shows a schematic of the girder-crossframe subassembly.

The entire girder-crossframe subassembly was manufactured using Gr. A36 steel. The subassembly was tested upside-down such that the bottom flange of the specimen, fixed to the laboratory reaction floor using a series of post-tensioned channels, simulated the top flange of a bridge girder connected to a concrete deck. Two post-tensioned channels were removed from under the center of the subassembly during the first three trials to accommodate interference with the steel with bolts repair configuration. The reinstallation of the two C130x13 (C5x9) channels under the center of the girder in later trials provided increased constraint to the bottom flange, discussed further in the Results section.

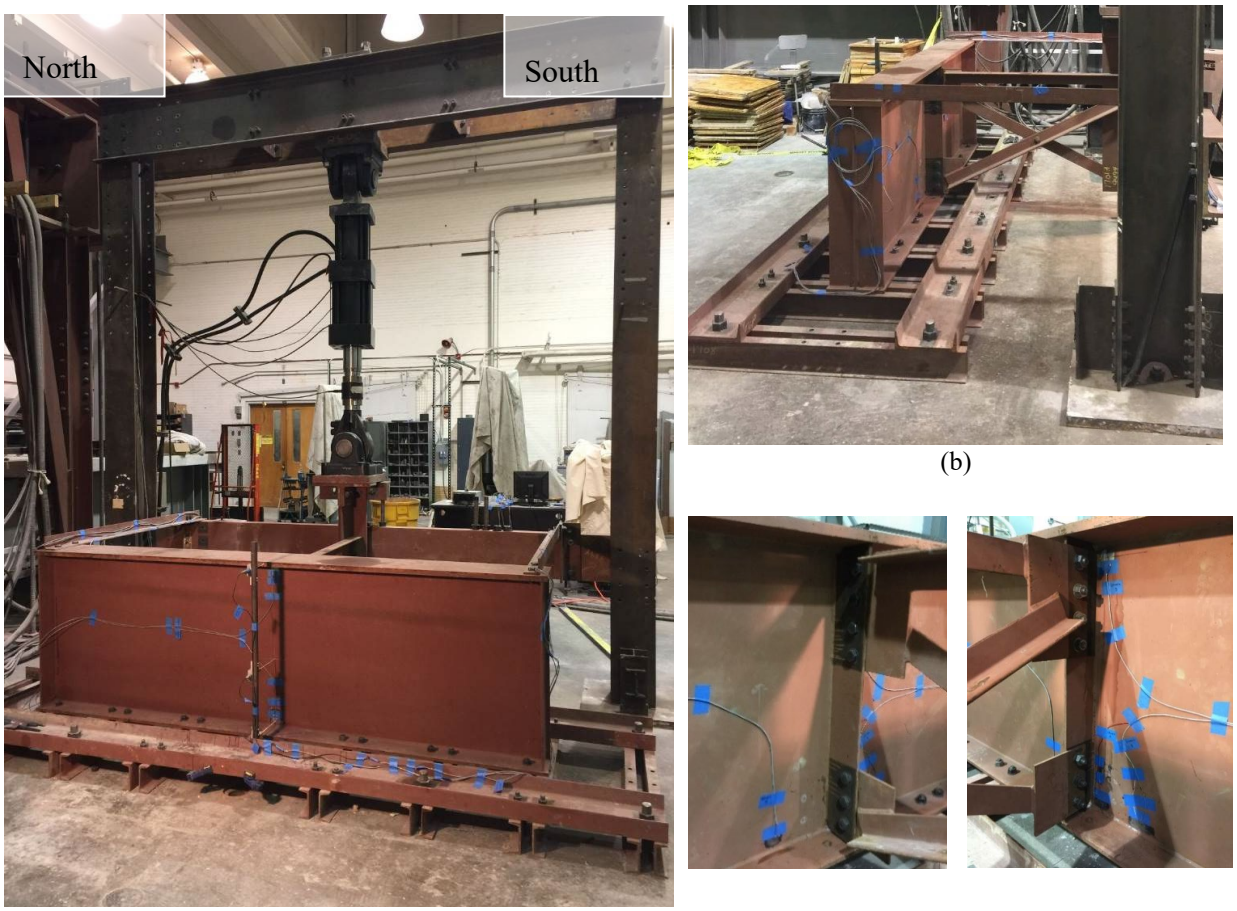

(a) (b) (c)

Figure 6-3 Photographs of load-reaction system employed in the tests: (a) Front view showing the test frame, actuator, girder fascia side, LVDTs on the fascia side, angles restraining lateral motion at the girder ends, and bolted connections to the rigid floor tie-down system; (b) Side view of the girder subassembly; (c) Connection plate side view showing the crossframe-to-girder connection and strain gauges in the web gap region.

The crossframe was connected to the girder via the connection plate at midspan. The connection plate was welded to the web at the centerline of the girder with a 5-mm (3/16-in.) fillet weld, without any connection between it and the girder flange. The connection plate had a 32 mm (1-1/4 in.) clip at each end and a gap of 3-mm (1/8-in.) with respect to the bottom flange; the cropped end of the connection plate formed a flexible web gap region that was susceptible to distortion-induced fatigue damage. The connection plate was fabricated mill-to-bear against the inside face of the top flange of the subassembly. The girder was restrained from lateral deflections by two angles each attached to the loading frame at one end and the top flange of the girder at the other end (Figure 6-3). Cyclic fatigue loading was applied in the upwards direction at the far end of the crossframe,

using an MTS servo-controlled actuator with 489-kN (110-kip) capacity (Figure 6-3 and Figure 6-4). Alemdar et al. (2014) provide more details about the configuration of the reaction system used in the experimental program, and describe comparisons with computational simulations of full-scale bridges performed by Hassel et al. (2013) to validate the stress field in the subassembly. Detailed descriptions of the testing procedure and loading protocol are provided in Section 6.4.3.

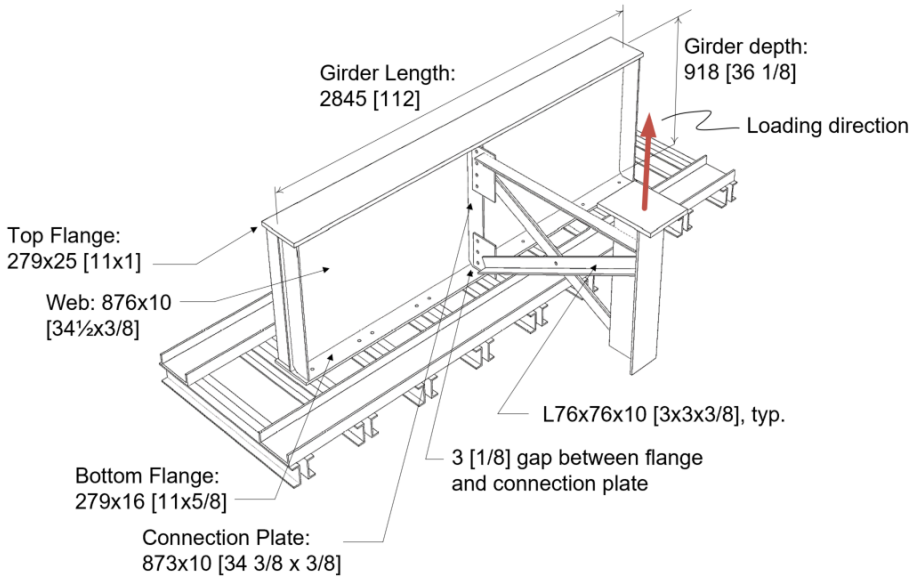

Figure 6-4 Schematic of the girder-to-crossframe subassembly, mm[in.]. (Note that the load frame and lateral restraining angles are not shown here for clarity, refer to photographs in Figure 6-3.)

6.4.2 Instrumentation of Girder Subassembly

Three linear variable differential transformers (LVDTs) were used to record out-of-plane displacements at discrete locations over the girder depth. They were installed at midspan on the fascia side; one LVDT was placed at the top flange, one near mid-depth of the web, and one in the bottom web gap region behind the bottom of the connection plate, as illustrated in Figure 6-5 .

Seven Micro-Measurements L2A-06-250LW-350 strain gauges were attached to the girder to record strain in web of the girder in the vicinity of the connection plate, as depicted in Figure 6-5. The gauge positions were selected as corresponding with regions of high stress demand in the web

gap region, as established from crack patterns in prior physical tests as well as finite element modeling results (Alemdar et al. 2014), while avoiding regions of severe stress gradient to minimize error that could be introduced with small differences in gauge placement across test trials.

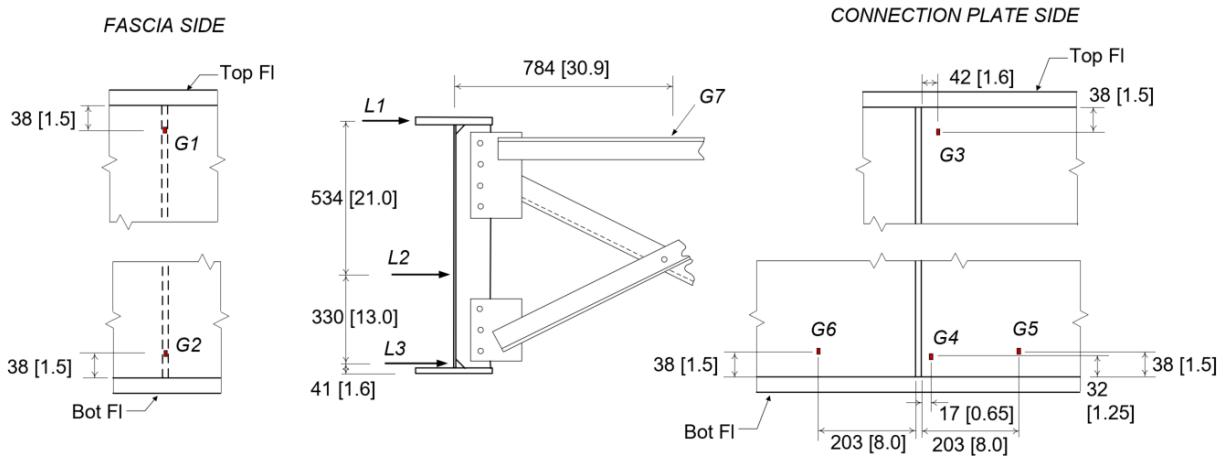

Figure 6-5 Instrumentation placement on girder specimen. *G* indicates strain gauge placement; *L* indicates LVDT placement. All dimensions are provided in mm [in.].

6.4.3 Test Procedure and Loading Protocol

The crossframe-to-girder connection was subjected to cyclic fatigue loading through a crossframe attached to the girder at midspan. The opposite end of the crossframe was connected to an MTS 489-kN (110-kip) servo-controlled hydraulic actuator, used to simulate the differential motion of an adjacent girder under traffic loading. The fatigue cycles were sinusoidal with a frequency of 0.5 Hz; the maximum applied load was 25.5 kN (5.75 kips), and the minimum load was 2.2 kN (0.5 kips) for all test trials. This loading protocol induced a stress range of 197 MPa (29 ksi) at the bottom of the web-gap region, computed from strain gauge 4 using Hooke's law, and was the same stress range used by Alemdar et al. (2014) to load similar subassemblies in their study. The load range adopted in this study is more than three times that which would be produced by the AASHTO fatigue truck in a full-scale steel girder bridge (Dellenbaugh et al. 2020) and was chosen to ensure

the tests could be completed in a reasonable amount of time. Load control, rather than displacement control, was utilized. Stresses in the web gap region would be expected to decrease across the test program if displacement control were to be used; therefore, we prioritized load control as it provides a more demanding test for retrofit evaluation.

The girder subassembly was loaded monotonically at regular intervals to monitor changes in stiffness; data were collected during monotonic loading approximately every 5,000 cycles in unretrofitted trials and every 20,000 cycles in retrofitted trials. The protocol for monotonic loading consisted of slowly increasing actuator force from 0-26.7 kN (0-6 kips) while force, displacement, and strain were recorded using the instrumentation array.

6.4.4 CFRP and Epoxy Properties

The composite material used in this study was a high-modulus carbon fiber fabric commercially marketed under the name *3K Plain Weave Carbon Fiber* manufactured and supplied by Fiber Glast Developments Corporation (Fibre Glast Developments Corporation 2017). This type of composite fabric is a bidirectional carbon fiber sheet with 3K tow (3000 carbon filaments per fiber) designated as a 12.5x12.5 fabric, meaning it has 12.5 weaves/25mm [/ 1 in.] in both the wrap and fill direction. The fabric has a nominal thickness of 0.305 mm (0.012 in.) and a unit weight of 196.7 g/m^2 [5.8 oz/yd^2]. It has high tensile strength, fatigue resistance, fire resistance, and is dimensionally stable (Fibre Glast Developments Corporation 2017). Table 6-1 presents the mechanical properties of the carbon fiber fabric used.

Table 6-1. CFRP and Epoxy Mechanical Properties (Fibre Glast Developments Corporation 2017; Huntsman Corporation 2017)

Properties	CFRP	Adhesive
Tensile Strength, MPa [ksi]	4205-4378 [610-635]	35.9 [5.2]
Tensile Modulus, GPa [ksi]	227-240 [33000-34900]	1.6 [238]
Elongation, %	1.4-1.95	4.2

The bonding adhesive was a two-part modified epoxy marketed as Epibond 420 A/B (Araldite 420 outside the United States) and manufactured by Huntsman in the U.S. Epibond 420 A/B is a thermosetting polymer matrix structural adhesive in paste form, curable at room temperature, suitable for metal and fiber reinforced composite bonding applications. Due to its toughness, resiliency, and high shear strength it is recommended by the manufacturer for applications requiring high shear and peel strength. The specified manufacturer properties of the adhesive are presented in Table 6-1.

6.4.5 Repair Method

The crossframe-to-girder connection was evaluated in six different conditions, one without repair and five others with different types of repair as described in Table 6-2 and Figure 6-6: C1S1, C1S2, C2S0, C2S2, and C3S2. The naming convention refers to the number of surfaces connected with CFRP (designated with "C" and a numeral) and whether the steel retrofit elements were mechanically connected to the flange (S1), not mechanically attached (S2), or not present at all (S0). In one of the repairs (C2S0 in Table 6-2), CFRP fabric was used without steel components to examine the effectiveness of the CFRP by itself in mitigating distortion induced fatigue cracks. The four remaining types of repair (C1S1, C1S2, C2S2, and C3S2 in Table 6-2) consisted of permutations of three different CFRP and two different steel shape configurations. These different configurations are described in detail in the following.

C1S1

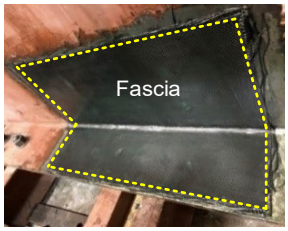

C1 – CFRP connects web and flange

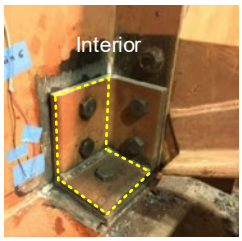

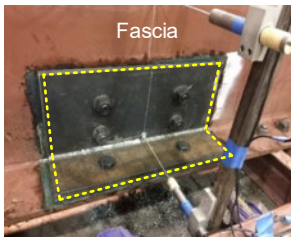

S1 – Bolted to flange

(a)

C1S2

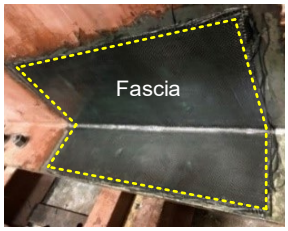

C1 – CFRP connects web and flange

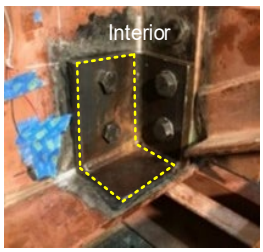

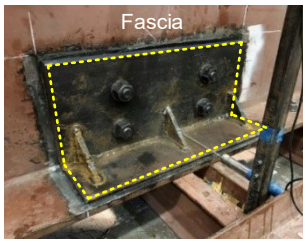

S2 – Not bolted to flange

(b)

C2S2

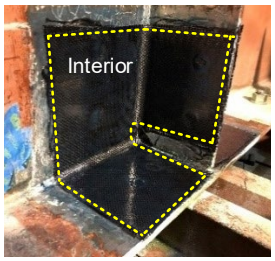

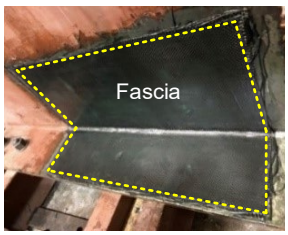

C2 – CFRP connects web and flange, and web and CP

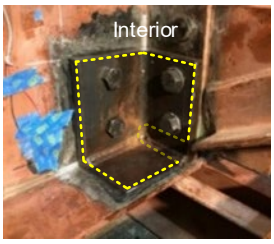

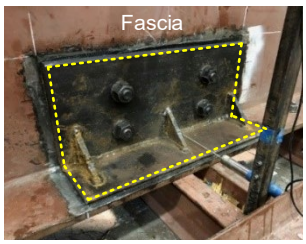

S2 – Not bolted to flange

(c)

C2S0

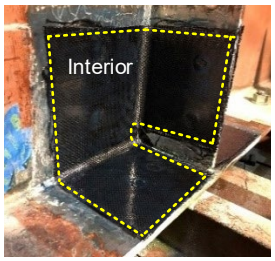

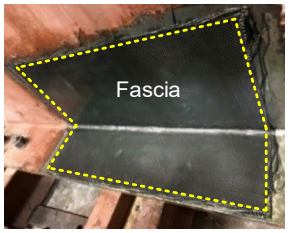

C2 – CFRP connects web and flange, and web and CP

S0 – No steel

(d)

C3S2

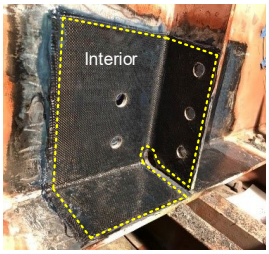

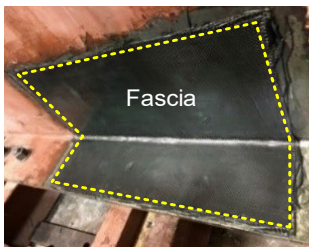

C3 - CFRP connects web and flange, and web and CP; C3 is taller than C2 on the interior side

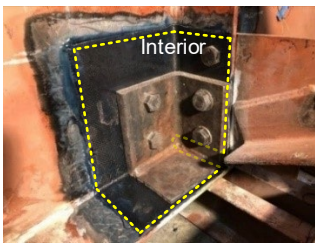

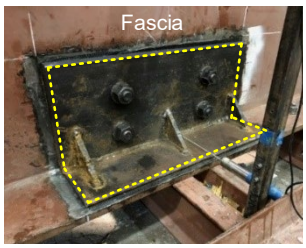

S2 – Not bolted to flange

(e)

Figure 6-6 Description of repair configurations; the extents of the CFRP are shown in dashed lines

Table 6-2 Repair Configurations Evaluated

Retrofit Measure	CFRP Configuration	Steel Configuration	Test Trials
None	-----	-----	1, 3, 6, 8, 11
C1S1	C1: web-to-flange wrap on interior and fascia	S1: with flange bolts	2, 4
C1S2	C1: web-to-flange wrap on interior and fascia	S2: without flange bolts	5, 7
C2S2	C2: CP-web-flange wrap on interior; web-to-flange wrap on fascia	S2: without flange bolts	9
C2S0	C2: CP-web-flange wrap on interior; web-to-flange wrap on fascia	S0: No steel retrofit elements	10
C3S2	C3: extended CP-web-flange wrap on interior; web-to-flange wrap on fascia	S2: without flange bolts	12

The CFRP was configured in three different ways in the five total repair variants, differing in the area covered by CFRP fabric and the surfaces that the CFRP fabric was attached to. In configuration C1 (Figure 6-6 a,b) the CFRP fabric was attached only to the girder web and flange. In configuration C2 (Figure 6-6 c,d) the CFRP fabric was epoxied to the flange, web, and connection plate. In configuration C3 (Figure 6-6 e) the CFRP fabric was also epoxied to the flange, web, and connection plate, but was applied over a larger area than in configuration C2. In configurations C1 and C2, the dimensions of the CFRP fabric were 5.1 mm (0.2 in.) smaller on all sides than the dimensions of the steel components. This was done to ensure that the fabric was completely covered by the steel retrofit measure and its edges were in contact with the steel retrofit. In configuration C3, the CFRP was extended beyond the edge of the steel retrofit by 89 mm (3.5 in) in the vertical direction and 64 mm (2.5 in) in the horizontal direction, on the interior (connection plate) side of the web only. The CFRP fabric was extended beyond the edges of the angle in C3S2 because the crack tip had propagated beyond the height of the angle in Trial 12, and this crack configuration provided an excellent opportunity to evaluate the ability of the CFRP fabric to arrest cracks that extend beyond the steel retrofit. For all the CFRP configurations (C1, C2, and C3), continuous sheets of CFRP were used for each layer, cut to continuously wrap from

one component to another. Further details regarding surface preparation and layup technique are provided in Sections 6.3.6 and 6.3.7.

Results from Kaan et al. (2012) showed that extending the adhesive layer beyond the extent of the CFRP fabric resulted in a reduction in the tensile stress at the resin-steel interface, significantly increasing the number of cycles at which debonding of the adhesive layer initiated. This technique was implemented in all the CFRP configurations evaluated in this study, by extending the epoxy adhesive layer approximately 25 mm (1 in.) on the steel surface of the girder beyond the extents of the CFRP fabric.

In repairs that included CFRP fabric and steel shapes (C1S1, C1S2, C2S2, and C3S2), the modified angles-with-plate retrofit measure (Figure 6-7) was installed over the CFRP. The previously developed angles-with-plate retrofit measure shown in Figure 6-2b was modified to provide a bearing surface between the steel retrofit elements and the CFRP fabric epoxied to the girder flange. The modification consisted of welding an orthogonal steel plate to the backing plate to form an "L" shape, and a third steel plate to both of the angle components of the angles-with-plate retrofit, as shown in Figure 6-7. The purpose of the modifications was to ensure that regardless of the relative rotation of the crossframe with respect to the horizontal, contact would be maintained between retrofit components and the girder flange on at least one side of the girder web.

Two different connection schema for the steel angles-with-plate retrofit measure were evaluated in this study. In steel configuration S1, used in repair C1S1 (Figure 6-6), the angles-with-plate retrofit measure was connected to the girder web, girder flange, and connection plate using Gr. A325 bolts. This configuration was only evaluated in Trials 2 and 4 to establish a baseline for the mechanically-anchored condition, keeping in mind that one of the goals of this study was to

evaluate retrofit configurations that *avoid* a mechanical connection to the flange. In this configuration, 9.5-mm (3/8-in.) thick shim plates were placed between the flange and the steel retrofit elements to prevent interference with the fillet weld. The central two channels of the floor tie-down system were removed from under the girder while this repair was evaluated to eliminate interference with the flange bolts.

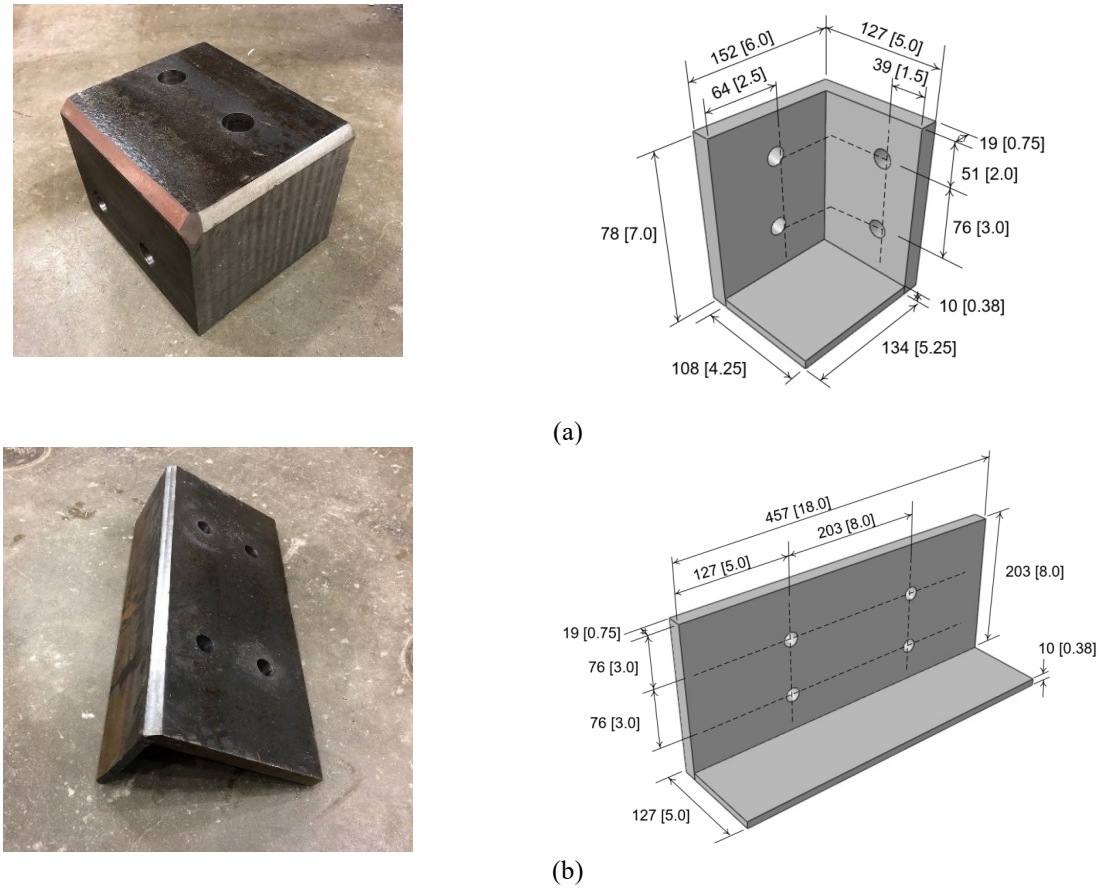

Figure 6-7 Modified steel retrofit geometry and dimensions for the combined CFRP-steel retrofit: (a) Modified angles to the south of the CP; (b) Modified backing plate

In steel configuration S2, used in repairs C1S2, C2S2, and C3S2, the angles-with-plate retrofit measure was bolted only to the girder web and connection plate (no bolted connection to the flange). To bring the S2 steel retrofit in contact with the portion of the CFRP wrap on the girder flange, the corners of the steel elements were chamfered to avoid interference with the fillet weld such that the retrofit would fit tightly over the CFRP, as illustrated in Figure 6-7; this eliminated

the need for shim plates. Three small triangular stiffeners were welded to the backing plate to prevent rotation between its two components. This steel configuration was evaluated in Trials 5, 7, 9, and 12.

6.4.6 Surface Preparation

Debonding between composite materials and the steel substrate is a significant concern and one of the most important barriers to implementation of CFRP repairs because it usually occurs rapidly and leads to a complete failure of the repair (Kim and Brunell 2011). Surface preparation is key for bond performance, so in this study it was performed very carefully. First, steel surfaces were cleaned with acetone to remove traces of dye penetrant, dust, and any other contaminants. After cleaning, steel surfaces were thoroughly prepared with hand and power cleaning tools, to remove the paint and achieve grade St2 surface preparation as described in ISO 8501-1 (International Organization for Standardization ISO 8501 2007). The hand and power tools used included power grinders, power sanders, and power wire brushes. Also, a die grinder was used for the tight corner, the welds, and to roughen the whole surface. The last step consisted of cleaning the surfaces again with acetone prior to bonding the CFRP layers (Al-Mosawe et al. 2016; Al-Salih et al. 2020; Al-Zubaidy et al. 2012; Alwash and AL-Salih 2013; Kadhim et al. 2018; Kadhim et al. 2019; Liu et al. 2009; Wu et al. 2012). Figure 6-8 shows the surface of the steel girder after preparation. The same tools were used and St2 surface preparation procedures were followed when CFRP and adhesive materials were removed between test trials; care was taken to not over-process the steel substrate.

6.4.7 CFRP Fabric Application

CFRP fabric layers were attached to the girder using the wet hand lay-up technique; many researchers have adopted this method of application, including (Al-Mosawe et al. 2016; Al-Salih et al. 2020; Al-Zubaidy et al. 2012; Alwash and AL-Salih 2013; Jawdhari et al. 2018; Jawdhari et al. 2018; Kadhim et al. 2018; Kadhim et al. 2019; Liu et al. 2009; Wu et al. 2012; Zaki et al. 2020). First, the CFRP layers were detailed and cut to the prescribed shape and dimensions of the bond area. Second, a thin uniform layer of Epibond 420 A/B epoxy was applied onto the previously-prepared, dry steel surface using a brush. Accumix cartridges pre-filled with 200 ml of Epibond were used to mix parts A and B of the epoxy and to apply it. This method of mixing and application was adopted to ensure that correct mixing proportions were maintained (2:1 parts by volume), to avoid batching large quantities of epoxy that may cause exceedance of its workable pot life, and to avoid corruption of leftovers. Cartridges had a static mixing nozzle to ensure that manufacturer recommended mixing procedures were followed (Huntsman Corporation 2017). The adhesive was distributed uniformly along the bond area and extended approximately 25 mm (1 in) beyond the footprint of the CFRP as recommended by Kaan, et al. (Kaan et al. 2012). Care was taken to apply the adhesive layer with uniform thickness. Third, a CFRP layer was saturated with the Epibond 420 A/B epoxy using a scraper. Fourth, the saturated CFRP layer was applied on top of the steel surface previously coated with epoxy. This was done as quickly as possible to ensure that the application was performed while the resin was still workable. Fifth, a bristle roller was used to apply uniform pressure over the placed CFRP fabric, to ensure that the CFRP sheet was immersed in the epoxy, expel small air bubbles/pockets, and eliminate any excessive adhesive. The CFRP preparation and application processes are illustrated in Figure 6-8 and Figure 6-9. The same procedure was used to add the remaining two CFRP layers.

(a) (b) (c)

Figure 6-8 Material preparation for CFRP application: (a) Steel girder surface after preparation; (b) CFRP detailing; (c) CFRP configuration C1 dimensions

(a) (b) (c)

Figure 6-9 Application of the CFRP to the steel girder: (a) CFRP saturation; (b) CFRP application; (c) hole drilling

After installation, the CFRP was cured at room temperature for approximately five days. In girders where both CFRP and steel sections were added, preparation continued by drilling holes for bolting. As shown in Figure 6-8, holes in the steel girder web and flange were drilled prior to

installation of the CFRP using a magnetic drill press, and the corresponding holes in the CFRP were drilled after installation using a cordless drill (Figure 6-9).

6.4.8 Description of Test Trials

The experimental program consisted of a total of 12 test trials on one specimen, examining the effectiveness of different retrofit configurations, as listed in Table 6-3. The fatigue loading was stopped at the end of each test trial for different retrofits to be removed and installed. Five of the trials (Trials 1, 3, 6, 8, and 11) were conducted in the unretrofitted condition to provide a baseline for the crack propagation rates and to allow the cracks to grow so retrofit performance could be examined for different cracks patterns and lengths. The length of unretrofitted trials (in terms of number of cycles applied) was not fixed, but was based on achieving new crack growth beyond the prior test trial to establish a clean start for the next trial.

Six trials (Trials 2, 4, 5, 7, 9, and 12) were conducted with both composite and steel retrofit measures in place to evaluate the performance of different configurations of the combined retrofit measure. In two of the retrofitted trials (Trials 2 and 4), 19-mm (3/4-in) diameter Gr. A325 structural bolts were used to fasten the CFRP-steel retrofit to the flange to provide a basis of comparison with the subsequent trials. The remaining four retrofitted trials (Trials 5, 7, 9, and 12) were conducted to examine the performance of the retrofit without a bolted connection to the flange. CFRP Configuration C1 was used in Trials 2, 4, 5, and 7; CFRP Configuration C2 was used in Trials 9 and 10; and CFRP Configuration C3 was used in Trial 12. One trial (Trial 10) was conducted with only CFRP, without the addition of the steel retrofit measure, to examine the performance of the CFRP in distortion-induced fatigue. Retrofitted trials were each conducted over

1,200,000 cycles, corresponding approximately to the number of cycles in the AASHTO S-N curves at which a Category A detail will runout under a stress range of 200 MPa (29 ksi).

Table 6-3 Matrix of test trials

Trial Number	Retrofit Measure	CFRP Retrofit Configuration	Steel Retrofit Configuration	Cumulative number of cycles
Trial 1	No Retrofit	-----	-----	50,000
Trial 2	C1S1	C1: web-to-flange wrap on interior and fascia	S1: with flange bolts	1,200,000
Trial 3	No Retrofit	-----	-----	1,250,000
Trial 4	C1S1	C1: web-to-flange wrap on interior and fascia	S1: with flange bolts	2,450,000
Trial 5	C1S2	C1: web-to-flange wrap on interior and fascia	S2: without flange bolts	3,651,700
Trial 6	No Retrofit	-----	-----	4,051,700
Trial 7	C1S2	C1: web-to-flange wrap on interior and fascia	S2: without flange bolts	5,251,700
Trial 8	No Retrofit	-----	-----	6,456,000
Trial 9	C2S2	C2: CP-web-flange wrap on interior; web-to-flange wrap on fascia	S2: without flange bolts	7,656,000
Trial 10	C2S0	C2: CP-web-flange wrap on interior; web-to-flange wrap on fascia	-----	8,866,000
Trial 11	No Retrofit	------	-----	9,201,600
Trial 12	C3S2	C3: extended CP-web-flange wrap on interior; web-to-flange wrap on fascia	S2: without flange bolts	10,409,500

6.5 Results and Discussions

6.5.1 Crack Initiation and Propagation Behavior

The test protocol consisted of applying fatigue cycles to the girder subassembly in accordance with the loading protocol as described in Section 6.4.3 and periodically performing inspections of the girder. Crack growth was monitored at regular intervals throughout testing by visual inspection aided with dye penetrant and a blacklight. The first crack was observed at 6,500 cycles on the interior side of the girder (CP side), in the bottom web-gap region, to the north of the CP (see Figure 6-10a). The crack occurred between the web and CP, at the toe of the weld on the CP side

of the weld, and it had a length of 13-mm (½-in.). As loading continued, the crack propagated through the throat of the weld towards the opposite weld toe on the side of the web (Figure 6-10b). At 13,300 cycles the crack started to grow vertically along the weld toe in the web base metal, (Figure 6-10c). At 29,000 cycles the first spider-cracking formed, small cracks that bifurcated from the vertical CP-to-web crack and moved into the web metal (see Figure 6-10d); at 37,800 cycles the longest spider crack measured 1.6 mm (0.0625 in.) (see Figure 6-10e). A similar crack pattern was observed on the south side of the connection plate with somewhat shorter crack lengths (Figure 6-10f). A horizontal web-to-flange weld crack 9.5-mm (3/8-in.) long was detected on the fascia side of the girder at 8,500 cycles, this crack did not propagate further during Trial 1 (see Figure 6-10g). At 29,000 cycles the web-to-flange crack was detected on the interior side (see Figure 6-10d) to the north of the CP with a length of 19.1 mm (3/4 in.). An overall butterfly-shaped crack pattern was observed on the fascia side of the girder near the end of Trial 1 (47,000 cycles), as shown in Figure 6-10g. This crack pattern consisted of several short cracks that bifurcated from a similar origin, each approximately 7.6-mm (0.3-in.) long. The cracks in that pattern furthest from the flange extended through-thickness and coincided with the cracks on the interior of the girder, while the remaining appeared to be partial-thickness cracks not visible on the interior side of the girder.

A naming convention to describe crack segments was adopted, as follows: Horizontal web-to-flange weld cracks (*FL*); vertical cracks that propagated along the CP-to-web weld (*CP*); and spider shaped cracks (*S*) that bifurcated from the vertical crack and moved into the web at an inclined or horizontal angle. These cracks were either on the fascia side (*Fascia*), or on the interior, connection plate side (*Int.*). Therefore, the designation FL_{Int} represents a horizontal web-to-flange crack on the interior of the girder; $CP_{1,Int}$ represents the first vertical crack that developed along

the connection plate weld on the interior of the girder; $S_{2,Fascia}$ represents the second crack of the spider shaped pattern observed on the fascia side, and so on. Figure 6-11 presents the crack pattern at the end of Trial 8 (6,456,000 total cycles had been applied, of which 1,700,000 cycles were in the unretrofitted condition); note that $S_{5,Int}$ and $S_{6,Fascia}$ were detected at the end of Trial10 and they are depicted here for the sake of illustration.

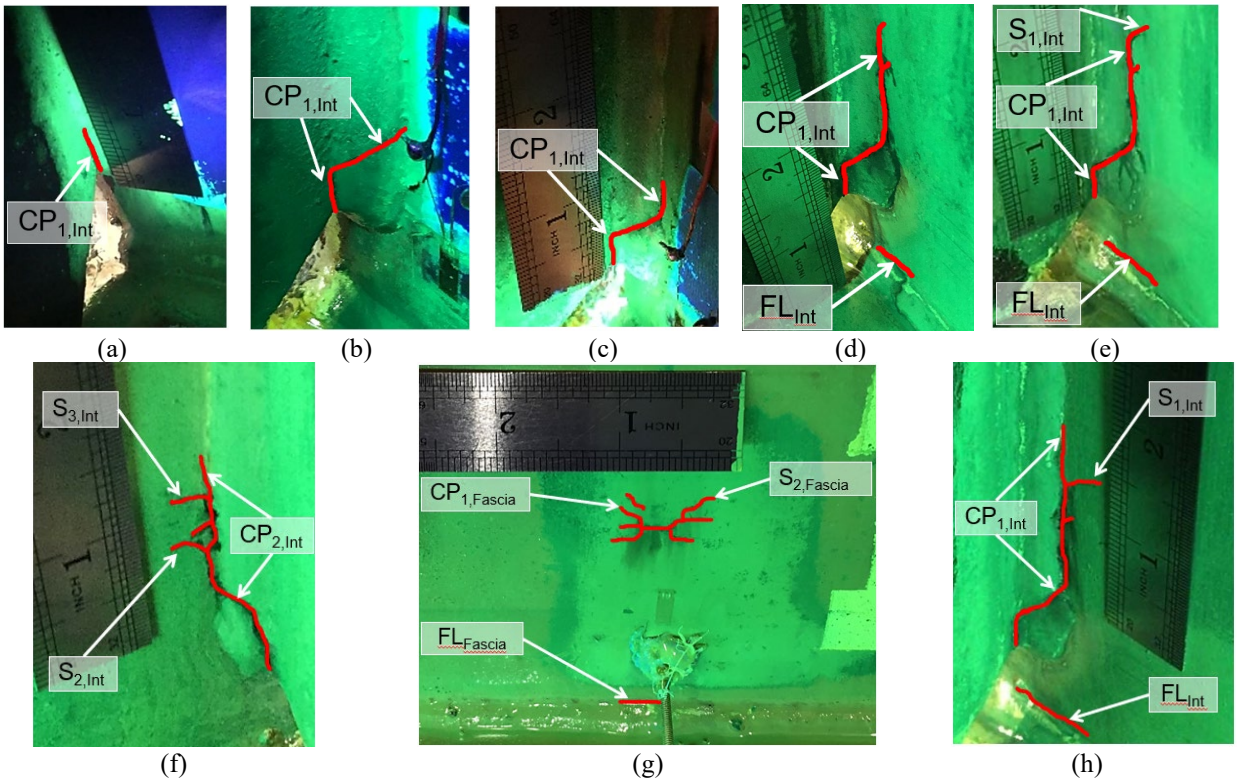

Figure 6-10 Crack pattern during Trial 1: (a) Interior of the girder, north side of CP at 6,500 cycles; (b) Interior of the girder, north side of CP at 12,600 cycles; (c) Interior of the girder, north side of CP at 17,000 cycles; (d) Interior of the girder, north side of CP at 29,000 cycles; (e) Interior of the girder, north side of CP at 37,800 cycles; (f) Interior of the girder, south side of CP at 47,000 cycles; (g) Fascia side at 47,000 cycles; (h) Interior of the girder, north side of CP at 47,000 cycles

Table 6-4 and Figure 6-12 show crack propagation in relation to applied fatigue cycles for cracks around the connection plate-to-web weld and at the horizontal flange-to-web weld, on the interior of the girder. Table 6-5 and Figure 6-13 show the relationship between crack propagation and number of cycles for cracks on the fascia side. In unretrofitted Trials 1 and 3, the propagation rate for cracks around the CP was greater than the propagation rate for the horizontal crack at the bottom flange-to-web weld. However, in Trial 6, which was also unretrofitted, the propagation

rate for the web-to-flange was very high and nearly exceeded the growth rate observed for other cracks. This is attributed to the reinstallation of the two C130x13 (C5x9) channels under the center of the girder, providing greater constraint to the bottom flange and increasing demand at the web-to-flange crack. It should also be noted that the crack opening displacement at the flange-to-web weld was extremely small and nearly invisible, making it very hard to inspect and measure, particularly during early test trials when the crack was short.

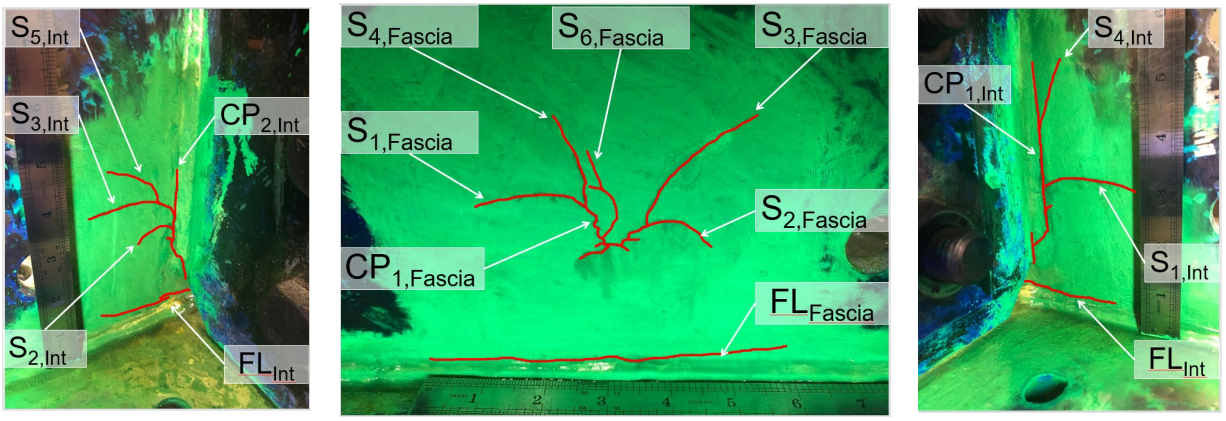

(a) (b) (c)

Figure 6-11 Crack patterns at the end of Trial 8 (6,456,000 cumulative cycles): (a) Interior of the girder, south side of the CP; (b) Fascia side; (c) Interior of the girder, north side of the CP

The observed crack patterns were similar to those noted in fields observations and also aligned well with observations from many other studies on distortion-induced fatigue (Alemdar et al. 2014; Bonet 2014; Bun 2014; Hartman et al. 2013). It is important to note that the applied load range in this study was significantly greater than what would be experienced by a bridge in practice; a high load range was adopted to accelerate the crack propagation rate and reduce the duration of the tests. Consequently, the crack propagation rate in the unretrofitted subassembly trials was much faster than the crack rate expected to occur in bridges under normal traffic loading, where it may take many years to propagate the cracks.

Table 6-4 Crack length measurements on connection plate side

Trial	Retrofit Measure	No. of Cycles (N) in Trial	Cumulative No. of Cycles	FL_{Int}	Cracking Around CP South Side (mm)				Cracking Around CP North Side (mm)		
					$CP_{2,Int}$	$S_{2,Int}$	$S_{3,Int}$	$S_{5,Int}$	$CP_{1,Int}$	$S_{1,Int}$	$S_{4,Int}$
1	No Retrofit	50,000	50,000	19.1	59.4	6.4	0.00	0.0	68.2	11.4	0.0
2	C1S1	1,150,000	1,200,000	19.1	59.4	6.4	0.00	0.0	68.2	11.4	0.0
3	No Retrofit	50,000	1,250,000	24.1	79.4	24.1	25.4	0.0	105.0	30.5	0.0
4	C1S1	1,201,500	2,451,500	24.1	79.4	24.1	25.4	0.0	105.0	30.5	0.0
5	C1S2	1,200,200	3,651,700	24.1	79.4	24.1	25.4	0.0	105.0	30.5	0.0
6	No Retrofit	400,000	4,051,700	95.3	83.2	27.9	44.5	0.0	105.0	54.6	17.8
7	C1S2	1,200,000	5,251,700	95.3	83.2	27.9	44.5	0.0	105.0	54.6	17.8
8	No Retrofit	1,204,300	6,456,000	127.0	83.2	30.5	62.2	0.0	105.0	59.7	43.2
9	C2S2	1,200,800	7,656,800	127.0	83.2	30.5	62.2	0.0	105.0	59.7	43.2
10	C2S0	1,210,000	8,866,800	127.0	83.2	30.5	62.2	43.2	105.0	66.0	81.3
11	No Retrofit	338,200	9,205,000	161.3	83.2	30.5	66.0	53.3	105.0	66.0	116.8
12	C3S2	1,200,000	10,405,000	161.3	83.2	30.5	66.0	53.3	105.0	66.0	116.8

Table 6-5 Crack length measurements on fascia side

Trial	Retrofit Measure	No. of Cycles(N) in Trial	Cumulative No. of Cycles (N)	FL_{Fascia}	Cracking Around CP South Side (mm)		Cracking Around CP North Side (mm)			
					$S_{2,Fascia}$	$S_{3,Fascia}$	$CP_{1,Fascia}$	$S_{1,Fascia}$	$S_{4,Fascia}$	$S_{6,Fascia}$
1	No Retrofit	50,000	50,000	9.5	9.5	0.0	0.0	9.5	0.0	0.0
2	C1S1	1,150,000	1,200,000	9.5	9.5	0.0	0.0	9.5	0.0	0.0
3	No Retrofit	50,000	1,250,000	45.7	29.2	30.5	19.1	25.4	0.0	0.0
4	C1S1	1,201,500	2,451,500	45.7	29.2	30.5	19.1	25.4	0.0	0.0
5	C1S2	1,200,200	3,651,700	45.7	29.2	30.5	19.1	25.4	0.0	0.0
6	No Retrofit	400,000	4,051,700	129.5	29.2	45.7	29.2	36.8	15.2	0.0
7	C1S2	1,200,000	5,251,700	129.5	29.2	45.7	29.2	36.8	15.2	0.0
8	No Retrofit	1,204,300	6,456,000	157.5	34.3	61.0	29.2	47.0	26.7	0.0
9	C2S2	1,200,800	7,656,800	157.5	34.3	61.0	29.2	47.0	26.7	0.0
10	C2S0	1,210,000	8,866,800	210.8	34.3	76.2	29.2	47.0	68.6	22.9
11	No Retrofit	338,200	9,205,000	246.4	34.3	80.0	29.2	47.0	88.9	48.3
12	C3S2	1,200,000	10,405,000	246.4	34.3	80.0	29.2	47.0	88.9	48.3

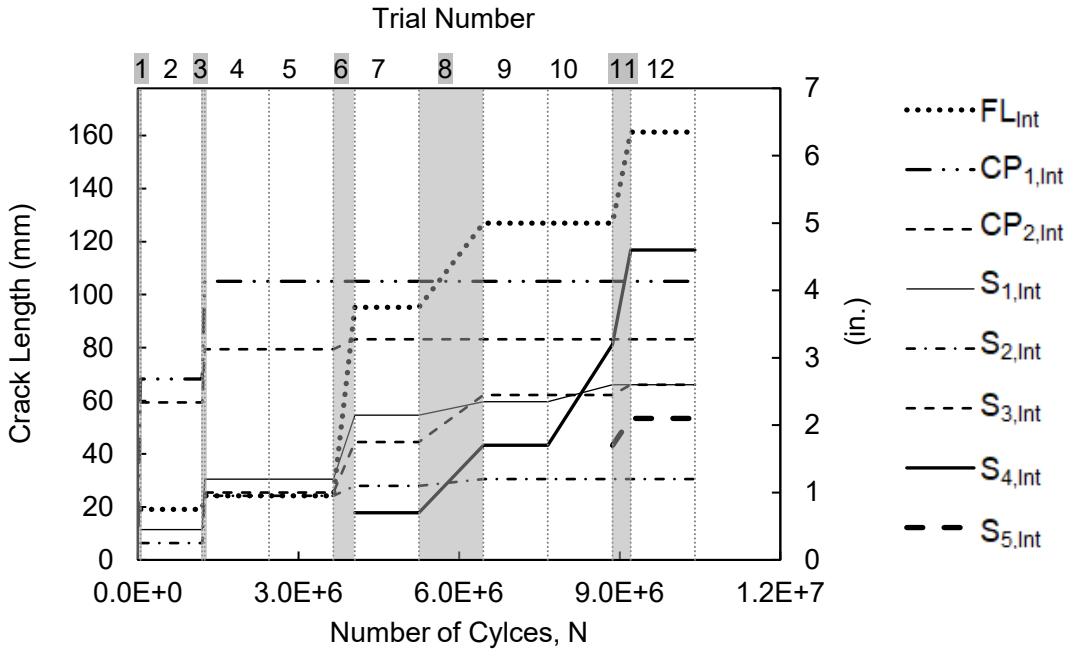

Figure 6-12 Crack propagation on the interior of the girder for all trials (unretrofitted trials are differentiated with shading)

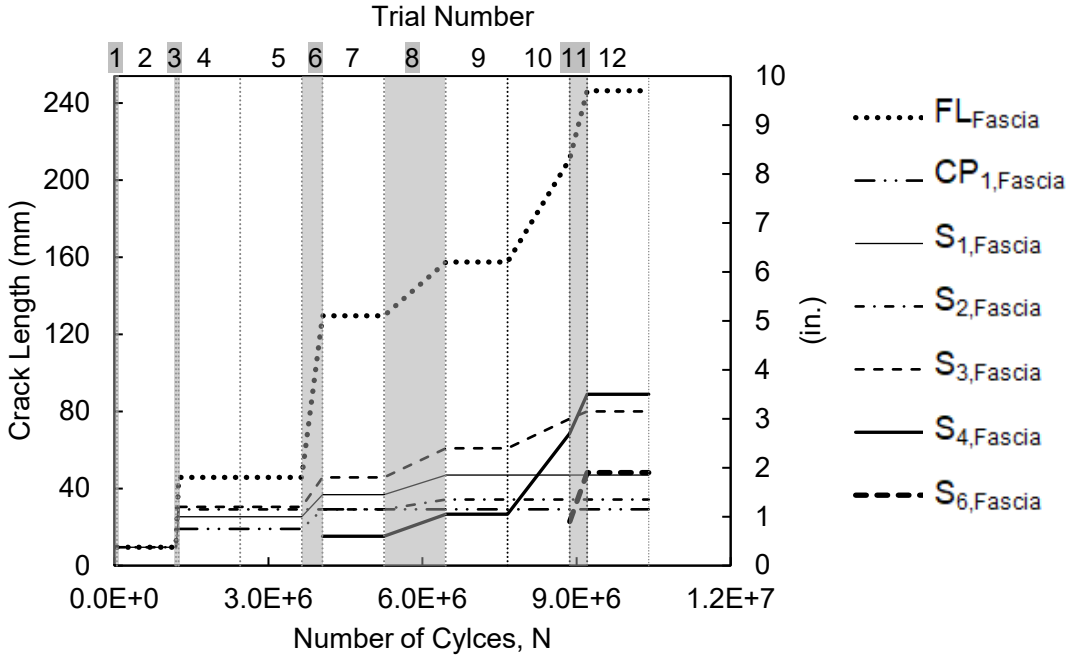

Figure 6-13 Crack propagation on the fascia side for all trials (unretrofitted trials are differentiated with shading)

Figure 6-14 and Figure 6-15 show the crack propagation rates for only unretrofitted trials for the interior and fascia sides of the girder, respectively. It can be observed that crack growth rates were steep for nearly all cracks during Trials 1, 3 and 6, and started to stabilize at Trial 8, then increased

again during Trial 11. This behavior can be attributed to the relaxation and the stress relief associated with crack extension under distortion-induced fatigue, as well as non-uniform crack propagation in a complex overall crack pattern subjected to mixed-mode fracture behavior. Although distortion-induced fatigue occurs in complex geometries and under a complex load path, it is still useful to consider the basic stress intensity factor formula (Equation 6-1):

$$K = \alpha\sigma\sqrt{a} \tag{6-1}$$

where the stress intensity factor, K, is a function of crack size a, stress in the crack vicinity σ, and a constant factor represented here as α, which depends on geometric shape and loading conditions. Although a increases as a crack propagates, stresses in the web gap region may be relieved as loads redistribute. Furthermore, the stress intensity factor is proportional to the square root of crack length, meaning that crack extension has a lesser effect on stress intensity factor than stresses at the crack vicinity. This framework helps to shed light on the crack propagation behavior noted for the girder in the unretrofitted condition.

Paris' Law, presented in Equation (6-2), establishes the relationship between crack growth rate (da/dN) and the stress intensity range (ΔK):

$$\frac{da}{dN} = C(\Delta K)^m \tag{6-2}$$

where C and m are experimentally derivable constants for a given material, geometric detailing, and loading conditions. For crack sizes below a critical threshold, a reduction in the stress intensity factor causes crack propagation rate to decrease. When the critical crack size is reached, crack propagation rate increases rapidly causing sudden failure due to fracture.

Results from strain gauge measurements, discussed in detail later in this section, show that stress demands were very high at the edge of the web gap region prior to crack initiation, particularly at

the CP-to-web weld toes (established from strain gauge 4). After cracks initiated and propagated, making it no longer possible to transfer forces across the crack, stress demands due to out-of-plane forces dropped significantly near the weld toe of the CP-to-web weld, at both sides of the fatigue crack. Demands remained high at the crack tip, where the sharp discontinuity caused highly localized stresses, and at the uncracked region ahead of the crack tip. The presence of fatigue cracks also decreased the stiffness of the web gap and caused the out-of-plane load path to shift locations, away from the cracks in the web gap. Stiffness of the web gap region decreased with increased cracking, and the location of the load path drifted further away from the beam flange. The change in location of the load path and decreased web gap stiffness caused a reduction of stresses in the web gap region, leading to stress reduction at the crack tips. Hence, the stress intensity factor decreased, reducing crack growth rates as observed in Trial 6 and 8. As cracks grew further, they began to grow increasingly unstable and crack growth rates increased rapidly as observed in Trial 11. FL_{Fascia}, $FL_{Int.}$ $S_{4,Fascia}$ and $S_{4,Int.}$ cracks exhibited high rates of propagation during Trial 11 compared to other cracks and previous trials.

6.5.2 Stress in Web Gap Region

The relationship between stress demand in the web gap region and monotonically applied load is shown in Figure 6-16 for measurements corresponding to five different points in time early in the overall test program, as cracking initiated and propagated in the unretrofitted web gap. Stress demands were computed from strain readings at the discrete location of strain gage 4 using Hooke's Law. Stress in the web gap region was found to decrease as cracks propagated, and the stress-load relationship gradually changed from linear to nonlinear as cracks grew. Readings from strain gauge 2, on the fascia side of the girder, exhibited a similar trend in behavior as cracks appeared on the fascia side.

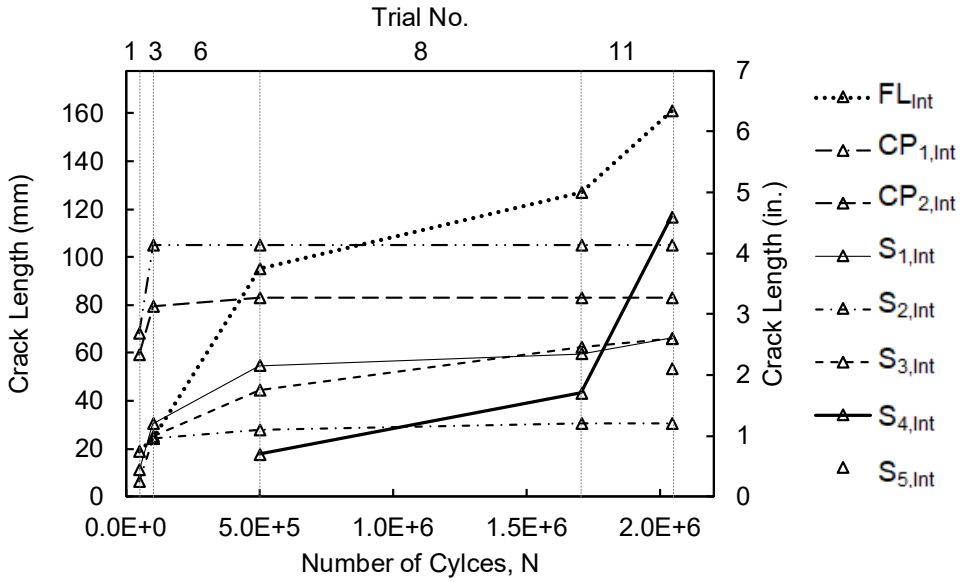

Figure 6-14 Crack propagation rates on the interior (connection plate side) for unretrofitted trials

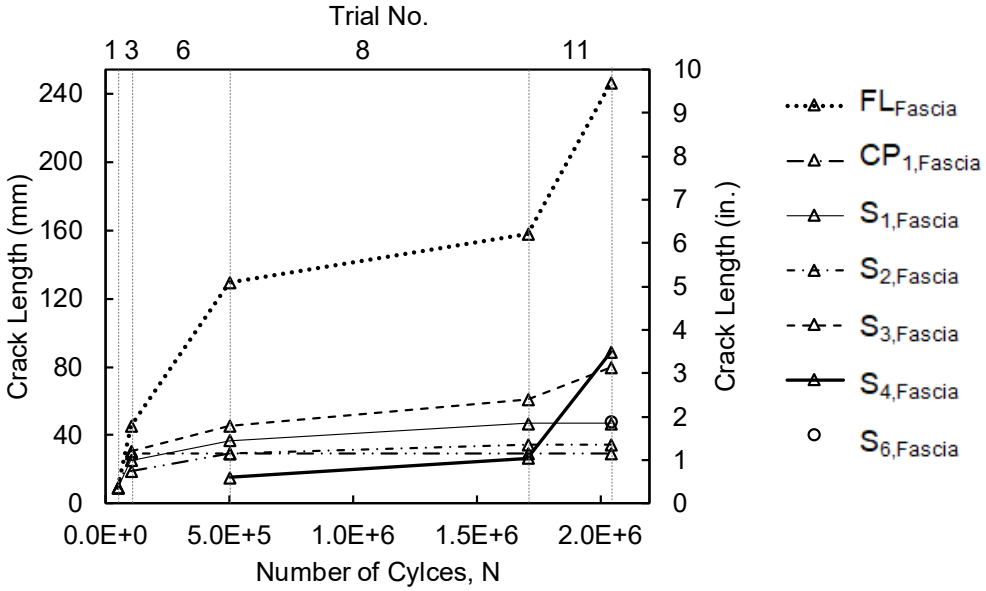

Figure 6-15 Crack propagation rates on the fascia side for unretrofitted trials

These observations indicate that stresses computed from strain gauge readings can be used as indicators of crack growth and confirm that complex changes took place in the stress field at the web gap region as cracks propagated, consistent with crack propagation measurements. The spatial variation of stress in the web gap region from finite element analysis of the test configuration performed by (Liu 2015) for an uncracked unretrofitted girder is shown in Figure 6-17.

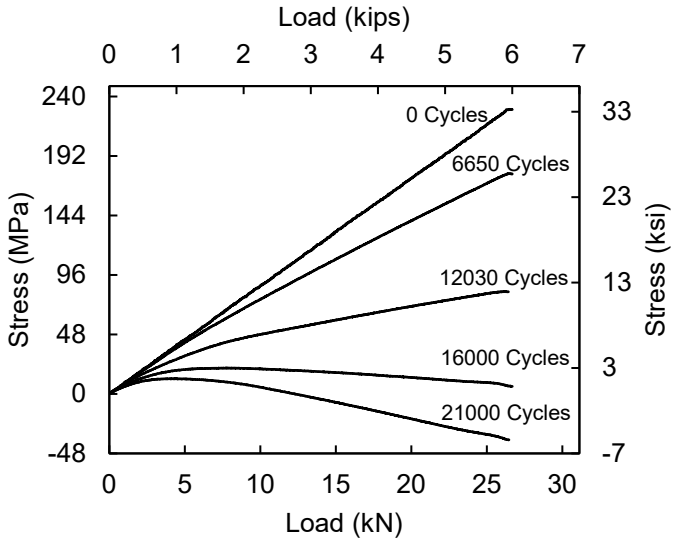

Figure 6-16 Local stress in the web gap region, stress from strain gauge 4 with increasing cycle count.

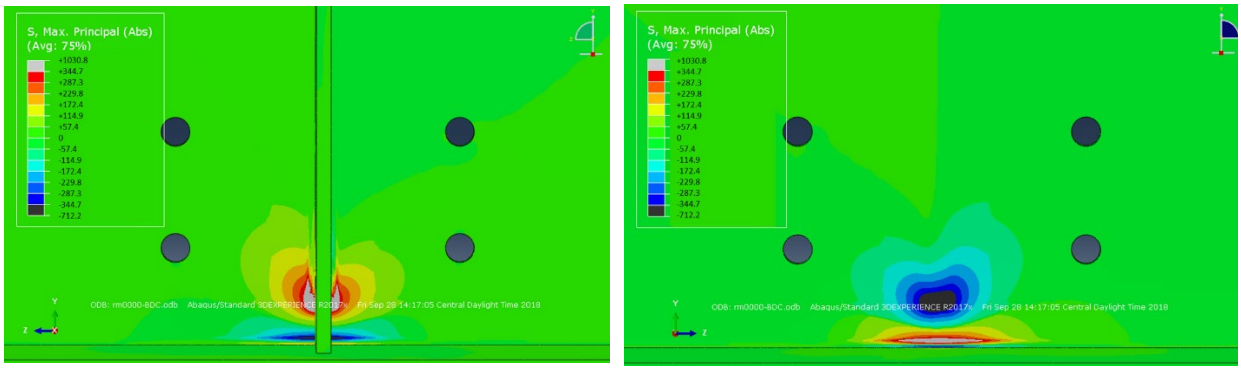

(a) (b)

Figure 6-17: Absolute maximum principal stress [MPa] contours of the web gap region of the uncracked unretrofitted girder: (a) on the interior side; (b) on the fascia side

6.5.3 Out-of-Plane Displacements of the Girder

Figure 6-18 shows girder out-of-plane displacement profiles for different number of fatigue cycles, measured upon completion of each test trial. All measurements correspond to an applied load of 23.4 kN (5.25 kips). Figure 6-18 includes reference data for the intact girder measured at the beginning of Trial 1 before any cracking was sustained. Comparisons of out-of-plane displacements between the retrofitted and unretrofitted condition are shown between Trials 3 (unretrofitted) and 4 (C1S1), and Trials 6 (unretrofitted) and 7 (C1S2), to describe how retrofit

application influenced the displacement characteristics of the girder. These comparisons are representative of the displacement behavior observed between unretrofitted and retrofitted conditions for the overall suite of CFRP-steel variants studied. Additionally, out-of-plane displacements are presented for Trial 10 (C2S0), which was the CFRP-only retrofit.

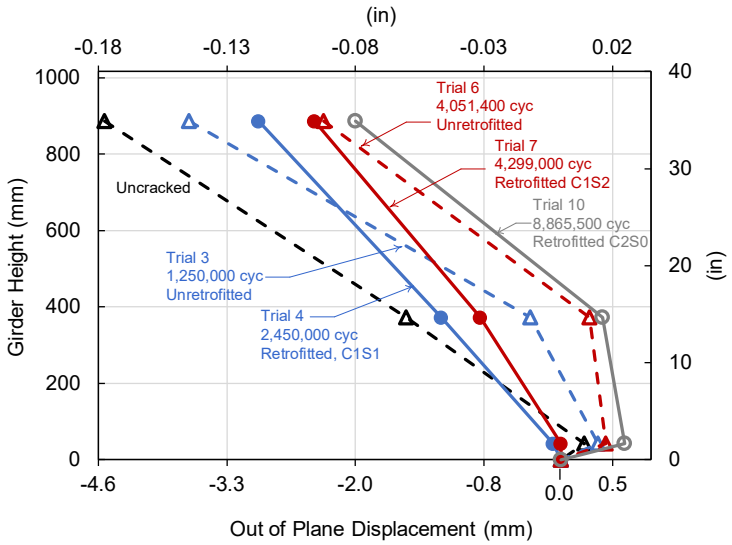

Figure 6-18 Out-of-plane displacement along the girder height with increasing cycles for: (a) unretrofitted trials; (b) retrofitted trials

The results show that in the uncracked, unretrofitted condition, the displacement profile exhibited significant 'hinging' localized in the web gap; however, the girder deformed shape was linear above that point. As the girder developed fatigue cracks that increased in length, the out-of-plane deformation response of unretrofitted girders became increasingly nonlinear across the girder height, as evidenced by comparing deformation responses for "uncracked," "Trial 3," and "Trial 6" in Figure 6-18. At midspan, the girder can be idealized as being composed of three rigid parts (the bottom flange, the stiffened portion of the web, and the top flange), connected by springs at the bottom and top web gaps. Before cracks initiated, the portion of the unretrofitted girder above the bottom web gap deformed as a rigid element, and the deformed shape of the girder had a linear pattern. As cracks developed and propagated in the bottom web gap, the position of the center of

rotation of the stiffened web shifted upwards. Because the center of rotation shifted upwards and the web gap deformation pattern changed during this process, deformations at the top of the girder modestly decreased with increased cycles. The deformed shape changed from a linear pattern before cracking, associated primarily with rotation of the girder web, to a nonlinear pattern where lateral deformations in the stiffened segment of the web (stiffened with the CP) had opposite direction deformations in the top and bottom web gaps. Although deformation at the top of the girder decreased, the cumulative effect was that the girder became more flexible because of increased flexibility at the web gaps, as demonstrated by the strain gauge readings in Figure 6-16. The LVDT-derived plots in Figure 6-18 do not completely reveal this behavior, because the instrumentation array only had three LVDTs over the girder height, and because lateral deflections at the web gaps were highly localized which made them difficult to measure. Nonetheless, the data in Figure 6-18 are very valuable in considering the linearity (or not) of the deformations across the girder depth, and also in considering the relative deformations in the web gap as measured by LVDT3 (L3).

All configurations with the combined CFRP-steel retrofit exhibited stiffer responses than the unretrofitted girder, and all CFRP-steel retrofitted configurations exhibited a nearly linear distribution for out-of-plane displacements measured over the girder depth, indicating that the retrofit was effective in reducing localized deformations in the web gap region. The combined CFRP-steel retrofit was able to dramatically reduce the highly localized out-of-plane deformations in the web gap (Figure 6-18), reducing the overall magnitude of out-of-plane displacements measured by LVDT L3, and bringing the system to a nearly-linear deformed shape. Furthermore, there was not a significant difference between deformations in the web gap when steel components were bolted to the flange vs. unbolted. In fact, the bolted retrofit measure (e.g., Trial 4, C1S1)

demonstrated a less stiff response than unbolted retrofits (e.g., Trial 7, C1S2), which is attributed to the removal of two post-tensioned channels from under the center of the subassembly to accommodate interference with the steel bolts used to attach the retrofit measure to the girder flange, rather than to the presence (or not) of the bolts.

The effect of the steel components of the retrofit on stiffness is clear in Figure 6-18, which shows that the CFRP-only retrofit (C2S0, Trial 10) had a deformation pattern similar to that of the unretrofitted condition. Without the steel components, the CFRP fabric was ineffective increasing the stiffness of the crossframe-to-girder connection and restoring a near-linear deformed shape for out-of-plane displacements at midspan.

6.5.4 Performance of Retrofit Variants

Crack growth rates in Figure 6-12 and Figure 6-13 show that cracks propagated very rapidly during unretrofitted trials (shaded areas in the curves), while no cracks initiated or propagated during trials with the combined CFRP-steel retrofit measure in place. These results show that all variations of the combined CFRP-steel retrofit were effective in stopping crack propagation and protecting web gap regions with fatigue cracks from further distortion-induced fatigue damage, under extremely demanding load conditions.

Trials 4 and 5 were conducted back-to-back without propagating cracks in the unretrofitted condition between the two. The reason for this sequence was to investigate the performance of the retrofit measure without flange bolts (C1S2, Trial 5) relative to the performance of the retrofit with flange bolts (C1S1, Trial 4) under the same loading conditions, crack pattern, and crack lengths. The CFRP was carefully inspected for signs of partial debonding at the conclusion of both trials, and none was noted. Results from Trials 4 and 5 show that the retrofit measure without bolted

attachment between the steel angles and the girder flange (C1S2) was equally effective to the retrofit measure with bolted attachment between the angles and the flange (C1S1). This finding suggests that it is possible to forgo the use of bolts to anchor the retrofit to the flange, which has significant advantages in terms of cost.

The use of the combined CFRP-steel retrofit measure without mechanical attachment to the girder flange was also evaluated in Trials 7 and 9. In Trial 7, the CFRP was attached only to the girder web and flange (C1S2), while in Trial 9, the CFRP was attached to the girder web, girder flange, and CP (C2S2). In both Trials 7 and 9, the area where CFRP fabric was glued to the girder was smaller than the footprint of the steel retrofit elements. Cracks did not initiate or propagate in Trial 7 or 9, showing that the combined CFRP-steel retrofit continued to perform well without mechanical attachment to the flange, even as it was tested over increasingly long cracks in the web gap. No debonding of the CFRP components was observed for either CFRP configuration, indicating reliable behavior under very demanding fatigue loading conditions, and that performance was not sensitive to the configuration of the CFRP fabric.

The test trial with the longest fatigue cracks was Trial 12, performed after cracks propagated beyond the footprint of the steel retrofit elements. In this trial, the CFRP was attached to the CP, web and flange, similar to Trial 9. The main difference with the retrofit configuration evaluated in Trial 12 and other variants is that CFRP fabric dimensions were larger than those of the steel element to ensure that the crack pattern was completely covered by CFRP (C3S2). Similar to Trial 9, the steel components of the retrofit measure were not bolted to the girder flange, but the steel elements remained present to bear against it. The C3S2 version of the combined CFRP-steel retrofit was also found to be successful in halting crack initiation and propagation, reinforcing the finding that mechanical attachment to the flange can be avoided even for long web-to-flange cracks

(>203 mm [8 in.]). No debonding of the CFRP was noted at the end of the test trial, indicating that the area of application of CFRP fabric can be extended beyond the edges of the steel retrofit components and still be effective in arresting cracks. This result is particularly important in light of the results from Trial 10, which examined the performance of a CFRP-only retrofit measure, C2S0.

Trial 10, in which the girder was repaired with the CFRP-only retrofit measure (C2S0), was performed immediately after Trial 9 to allow for a direct comparison of retrofit performance over identical initial crack lengths; this was possible because cracks did not propagate while the C2S2 retrofit was in place during Trial 9. This sequence permitted a direct comparison between the performance of a CFRP-only retrofit measure and a combined CFRP-steel retrofit measure, under the same loading conditions and crack patterns/lengths. Crack propagation measurements in Figure 6-12 and Figure 6-13 show that the CFRP-only retrofit measure (Trial 10, C2S0) was ineffective in preventing crack propagation for cracks $S_{3,FASCIA}$, $S_{4,INT}$, $S_{4,FASCIA}$, and FL_{FASCIA} (Figure 6-12). Also, the CFRP-only retrofit measure differed from all other retrofit variants studied in that C2S0 was unable to restore a near-linear displacement profile for out-of-plane displacements (Figure 6-18). The CFRP fabric layers used in this repair method were thin relative to the thicknesses of the girder web and flange, and unable to increase the out-of-plane stiffness of the web gap region sufficiently to reduce out-of-plane distortions. As a result, the web gab region continued to experience highly-localized bending, and the arresting effect of the composite fabric was insufficient to prevent the fatigue cracks from propagating. Although the CFRP-only C2S0 retrofit was unable to arrest crack growth, debonding was not observed at the edges of the fabric by the end of the trial, which indicates that although there may have been localized debonding near crack

tips, it did not propagate along the bonding layer-steel interface. This constitutes an important result from the standpoint of fatigue robustness of the repair method.

Considered in combination with other test trials, results from Trial 10 (C2S0) provide important context for the results of the experimental program, highlighting the importance of the stiffness imparted to the web gap region by the steel retrofit components. The stiff steel components provide an alternative load path for out-of-plane forces imposed by the crossframe, reducing stress demands in the web gap region. The reduced stress demands allowed the composite fabric to effectively arrest crack growth under very high stress ranges, and without any crack-arrest hole measures to blunt the tip of fatigue cracks. Without the reduction in stress demand afforded by the steel components, the CFRP was unable to arrest crack growth in all cracks, although crack growth rates were lower than those observed immediately following in Trial 11, without any retrofit measure. Results from retrofitted Trials 5, 7, 9, and 12 showed that the CFRP bond could be successfully maintained without mechanical anchorage to the steel retrofit and girder flange of a combined CFRP-steel retrofit, even for fatigue cracks that extended beyond the edges of the steel retrofit. These findings support a tangible benefit in the combined use of CFRP and steel elements for repair of distortion-induced fatigue damage.

6.6 Conclusions

A total of 12 fatigue test trials were conducted on a girder-to-crossframe subassembly to evaluate the efficacy of combined CFRP-steel retrofit measures to repair distortion-induced fatigue damage in web gap regions of steel bridges. The test program included five test trials with the girder subassembly in the unretrofitted condition to establish a baseline for girder behavior with different crack patterns, and seven trials with different retrofit measures in-place to evaluate the

performance of each repair measure for mitigating fatigue damage. Several variants of the combined CFRP-steel retrofit were considered in the study. Parameters of the experimental program included connectivity between the CFRP and the girder web, flange, and steel retrofit components, whether fatigue cracks and the CFRP extended beyond the steel retrofit elements, and whether the steel retrofit elements were mechanically fastened to the girder flange. The following conclusions are drawn from the study:

1. As cracks propagated in the web gap region, the distribution of out-of-plane displacements over the height of the girder became increasingly nonlinear. All variants of the combined CFRP-steel retrofit resulted in dramatically reduced out-of-plane deformations in the web gap region as established from LVDT measurements, and also produced a near-linear out-of-plane displacement distribution over the girder height. Additionally, the combined CFRP-steel retrofit was able to reduce overall out-of-plane displacements in the girder and web gap.

2. For the crack patterns and lengths evaluated in this study, all configurations of the CFRP-steel retrofit measure were found to be effective in stopping distortion-induced fatigue crack propagation, even for long crack lengths with aggressive propagation rates. While further testing is needed at very low stress ranges to establish fatigue performance over a range of stress demands, the results are very encouraging that the retrofit may effectively repair damaged web gaps for the duration of their remaining life.

3. The combined CFRP-steel retrofit measures without mechanical anchorage to the girder flange (C1S2, C2S2, and C3S2) were found to be as effective as the retrofit measure with mechanical anchorage to the girder flange (C1S1).

4. The combined CFRP-steel retrofit measure with CFRP fabric attached beyond the edges of the steel elements was found to be effective in preventing the growth of cracks that extended beyond the steel elements, the longest evaluated in the study. This particular combination (C3S2) highlighted the benefits of using a combined CFRP-steel retrofit measure, where the stiffness imparted by the steel elements reduces the stress range and

the CFRP arrests crack growth without the need to blunt crack tips. This approach is particularly beneficial for complex crack patterns, such as those encountered in this study that have many crack tips, where drilling appropriately sized crack arrest holes in all of them could significantly weaken the web gap region. Because of the excellent performance of the C3S2 variant over aggressive, long fatigue cracks, its use is recommended from the variants studied.

5. A CFRP-only retrofit measure was ineffective in preventing propagation of some cracks for the tested crack pattern and lengths. Without the steel elements, the CFRP fabric was insufficient to reduce deformations in the web gap and decrease the stress range to a magnitude where the CFRP could effectively prevent crack growth, as it did in the combined CFRP-steel retrofit measures, even in cases where the cracks extended beyond the steel components. Out-of-plane deformation patterns of the CFRP-only retrofit measure were similar to those of cracked unretrofitted girders, exhibiting a nonlinear distribution over girder height.

6. Notably, no debonding between the CFRP fabric and steel substrate was observed at the edges of the application region in any of the fatigue trials, even for the CFRP-only retrofit measure. This finding indicates excellent bond tenacity and durability under demanding loading conditions, and should provide engineers with additional confidence to use CFRPs to repair fatigue damage.

The combined CFRP-steel retrofit is a promising mitigation measure for distortion-induced fatigue damage in steel bridges, particularly in cases that include long web-to-flange cracks or in cases where cracks extend beyond the edges of steel shapes added to provide connectivity. This technique can be applied with relative ease and, more importantly, can be implemented without removing the concrete deck and disrupting traffic. A commonly stated barrier to applying CFRP as a fatigue retrofit measure on steel bridges has been bond tenacity; this work demonstrated excellent bond tenacity under demanding loading. Because of this, future research should consider cases in which steel-only retrofits are adhesively-bonded over web gaps to study an extreme of

bond performance. Overall, the developed technique combines the unique strengths of CFRP and steel to arrive at a robust and effective solution for repairing steel bridges that have experienced cracking due to distortion-induced fatigue. It is worth mentioning that field applications are also subject to variations in temperature, humidity, moisture, UV, deicing agents, etc. that may affect the CFRP behavior, and further investigation regarding in-situ durability of the CFRP-steel retrofit should be conducted in future research.

6.7 Acknowledgements

The authors are grateful for support from Ministry of Higher Education and Scientific Research of Iraq (MOHESR).

6.8 References

Al-Mosawe, A., Al-Mahaidi, R., and Zhao, X.-L. (2016). "Experimental and Numerical Study on Strengthening of Steel Members Subjected to Impact Loading Using Ultrahigh Modulus CFRP." *Journal of Composites for Construction*, 20(6).

Al-Salih, H., Bennett, C., Matamoros, A., Collins, W., and Li, J. (2020). "Repairing Distortion-Induced Fatigue in Steel Bridges Using a CFRP-Steel Retrofit." *Structures Congress 2020*, 273-284.

Al-Zubaidy, H., Al-Mahaidi, R., and Zhao, X.-L. (2012). "Experimental investigation of bond characteristics between CFRP fabrics and steel plate joints under impact tensile loads." *Composite Structures*, 94(2), 510-518.

Alemdar, F., Nagati, D., Matamoros, A., Bennett, C., and Rolfe, S. (2014). "Repairing Distortion-Induced Fatigue Cracks in Steel Bridge Girders Using Angles-with-Plate Retrofit Technique. I: Physical Simulations." *Journal of Structural Engineering*, 140(5).

Alwash, N. A., and AL-Salih, H. I. (2013). "Experimental Investigation on Behavior of SCC Filled Steel Tubular Stub Columns Strengthened with CFRP." *Construction Engineering*, 1(2), 37-51.

Bonet, E. (2014). "Utilizing Fiber-Reinforced Polymers to Retrofit Steel Bridge Girders Damaged by Fatigue Loading." C. Bennett, A. Matamoros, R. Barrett-Gonzalez, R. Lyon, and S. Rolfe, eds., ProQuest Dissertations Publishing.

Bun, S. (2014). "Retrofit techniques for distortion-induced fatigue damage in steel bridge girders." C. R. Bennett, A. Matamoros, and S. Rolfe, eds., ProQuest Dissertations Publishing.

Connor, R. J., and Lloyd, J. B. (2017). "Maintenance actions to address fatigue cracking in steel bridge structures: Proposed guidelines and commentary, West Lafayette, IN: Purdue University."

Dellenbaugh, L., Kong, X., Al-Salih, H., Collins, W., Bennett, C., Li, J., and Sutley, E. J. (2020). "Development of a Distortion-Induced Fatigue Crack Characterization Methodology Using Digital Image Correlation." *Journal of Bridge Engineering*, 25(9), 04020063.

Dexter, R. J., and Ocel, J. M. (2013). "Manual for Repair and Retrofit of Fatigue Cracks in Steel Bridges." FHWA Publication No. FHWA-IF-13-020.

Fibre Glast Developments Corporation (2017). "3K, Plain Weave Carbon Fiber." *Product Data Sheet,* Brookville, Ohio.

Ghahremani, K., Walbridge, S., and Topper, T. (2015). "Inhibiting Distortion-Induced Fatigue Damage in Steel Girders by Using FRP Angles." *Journal of Bridge Engineering*, 20(6).

Hartman, A., Bennett, C., Matamoros, A., and Rolfe, S. (2013). "Innovative Retrofit Technique for Distortion Induced Fatigue Cracks in Steel Girder Web Gaps." *Bridge Structures*, 9, 57-71.

Hassel, H. L., Bennett, C. R., Matamoros, A. B., and Rolfe, S. T. (2013). "Parametric Analysis of Cross-Frame Layout on Distortion-Induced Fatigue in Skewed Steel Bridges." *J. Bridge Eng.*, 18(7), 601-611.

Hassel, H. L., Hartman, A. S., Bennett, C., Matamoros, A., and Rolfe, S. (2010). "Distortion-Induced Fatigue in Steel Bridges: Causes, Parameters, and Fixes." *Proceedings of the 2010 ASCE/SEI Structures Congress*, Orlando,FL, May 12-15, 2010.

Huntsman Corporation (2017). "Epibond® 420 A/B Epoxy Adhesive." *Advanced Materials Technical Datasheet,* The Woodlands, TX.

International Organization for Standardization ISO 8501 (2007). "Preparation of steel substrates before application of paints and related products — Visual assessment of surface cleanliness ".

Jawdhari, A., Harik, I., and Fam, A. (2018). "Behavior of reinforced concrete beams strengthened with CFRP rod panels CRP 195." *Structures*, 16, 239-253.

Jawdhari, A., Peiris, A., and Harik, I. (2018). "Experimental study on RC beams strengthened with CFRP rod panels." *Engineering Structures*, 173, 693-705.

Kaan, B., Alemdar, F., Bennett, C., Matamoros, A., Barrett-Gonzalez, R., and Rolfe, S. (2012). "Fatigue Enhancement of Welded Details in Steel Bridges Using CFRP Overlay Elements." *J. Compos. Constr.*, 16(2), 138-149.

Kadhim, M. M. A., Wu, Z., and Cunningham, L. S. (2018). "Experimental study of CFRP strengthened steel columns subject to lateral impact loads." *Composite Structures*, 185, 94-104.

Kadhim, M. M. A., Wu, Z., and Cunningham, L. S. (2019). "Experimental and Numerical Investigation of CFRP-Strengthened Steel Beams under Impact Load." *Journal of Structural Engineering*, 145(4), 04019004.

Kim, Y. J., and Brunell, G. (2011). "Interaction between CFRP-repair and initial damage of wide-flange steel beams subjected to three-point bending." *Composite Structures*, 93(8), 1986-1996.

Liu, H. (2015). "A Finite-Element-Based Approach to Modeling Cracking & Repairs for Distortion-Induced Fatigue in Steel Bridges."Ph.D., University of Kansas, Ann Arbor.

Liu, H., Al-Mahaidi, R., and Zhao, X.-L. (2009). "Experimental study of fatigue crack growth behaviour in adhesively reinforced steel structures." *Composite Structures*, 90(1), 12-20.

Wu, C., Zhao, X., Duan, W., Emdad, M. R., and Al-Mahaidi, R. (2012). "Fatigue of Center Cracked Steel Plates with UHM CFRP Plate Strengthening." *Proc. of Third Asia-Pacific Conference on FRP in Structures (APFIS)*, Sapporo, Japan, 02-04 February 2012.

Zaki, M. A., Rasheed, H. A., Roukerd, R. R., and Raheem, M. (2020). "Performance of reinforced concrete T beams strengthened with flexural CFRP sheets and secured using CFRP splay anchors." *Engineering Structures*, 210, 110304.

Chapter 7: **Conclusions**

In this dissertation, a Digital Image Correlation (DIC) based crack characterization methodology for detecting and monitoring Distortion Induced Fatigue (DIF) in steel bridges was developed and evaluated to quantify the multiple geometrically-complex bifurcated cracks. In addition, a numerical analysis of three types of finite element (FE) analysis computational measures (Hot Spot Stress (HSS) analysis, *J*-integrals, and Stress Intensity Factors (K)) was carried out to assess their predictive capabilities for characterizing DIF cracking propensity. Moreover, a numerical study of a steel plate with a single edge crack strengthened with CFRP composites was conducted to assess the effectiveness of the CFRP in reducing stress concentration at the crack tip, as well as reducing crack growth rate. Furthermore, a novel CFRP-Steel retrofit to repair complex patterns of DIF cracks in steel bridge web gaps without the use of bolting to the flange or the removal of the concrete deck was experimentally evaluated. From all these studies the following key conclusions can been drawn; detailed conclusions for each study are provided at the end of each chapter.

Based on the results of developing a DIC-based crack characterization methodology for detecting and monitoring DIF study, the following key conclusions were drawn:

- The DIC methodology can adequately characterize fatigue cracks, both under in-plane and out-of-plane loading, in terms of crack length.
- Results of in-plane testing indicated convergence between 90% and 95% corresponding to the actual crack length.
- For the load cases examined, 90% convergence resulted in a -9% error in crack length prediction, while 95% convergence produced an average crack length prediction only 1% beyond the known crack length for the out-of-plane DIF cracks.

From the results of evaluating the DIC-based crack characterization methodology for detecting geometrically-complex multi-segment DIF cracks, the following key conclusions were drawn:

- A convergence of 98% was found to provide a more accurate estimation of the crack length on a steel girder loaded out-of-plane with complex fatigue crack geometry compared with 95% convergence.
- The methodology was found to result in more accurate results when V-direction displacements were used rather than U- and W-direction displacements.
- On average, 98% convergence based on V-direction displacement data resulted in underprediction of crack lengths with 5%, 13%, and 17% error for the Vertical Crack, Branched Crack 1, and Branched Crack 2, respectively.
- The crack characterization methodology was found to not converge well for the horizontal web-to-flange crack under this mode of loading. This was because the web-to-flange crack experienced crack closure on the interior face of the girder, and relative displacements were extremely small along the crack length.
- Load cases with low load levels resulted in greater error in terms of crack length determination. The threshold of adequate loading for use with this technique appears to be between LC4 and LC5 for the Vertical Crack, LC5 and LC6 for Branched Crack 1, and LC6 and LC7 for Branched Crack 2, as load levels below this did not produce crack opening along the full length of the crack.

The simulation results of the three types of finite element (FE) analysis computational measures (HSS, K, J) to assess their predictive capabilities for characterizing DIF cracking propensity were compared to experimental findings and the following conclusions have been drawn based on the comparison and the parametric study:

- All evaluated numerical techniques, HSS, K, and *J*-integral, corresponded well with findings from the experimental study and indicate all methods are suitable for estimating crack propagation likelihood in DIF. The results of this study indicate that engineers can use adapted hot-spot stress techniques, rather than more complicated fracture mechanics principles, when evaluating the effectiveness of fatigue repairs.
- Numerical results indicated that equivalent Mode I stress intensity, $K_{Ieq(Ks)}$, values computed from a combination of K_I, K_{II}, K_{III}, are equivalent to those obtained from the *J*-integral, $K_{Ieq(J)}$, with both correlating well with experimental behavior.

- Numerical results indicated that $K_{I,eq(J)}$, $K_{I,eq(Ks)}$ and HSS had higher magnitudes in the unretrofitted condition and much lower magnitudes when the retrofit is in place, aligning well with the experimental data as no crack propagation occurred in the retrofitted condition for any crack length.

Based on the results of the numerical study on a steel plate with a single edge crack strengthened with CFRP composites to assess the effectiveness of the CFRP in reducing stress concentration at the crack tip, as well as reducing crack growth rate, the following key conclusions were drawn:

- For all the cases and loads modeled in the study, CFRP strengthening reduced the maximum principal stress at the crack tip by 380%. Additionally, analysis results showed that the addition of CFRP made a large reduction, up to 285%, in the stress intensity factor, K_I, at the crack tip.

- Results indicated that strengthening the steel plate with CFRP led to an increase in maximum load carrying capacity up to 150%.

- Strengthening with CFRP increased in the load required for crack propagation by 200%, and completely halted the crack propagation at a load of 138 MPa (20 ksi).

- The parametric study on the CFRP modeling parameters showed that increasing elastic modulus in the longitudinal direction of the CFRP ($E1$) led to an increase in the capacity and reduced crack propagation length.

- The parametric study on the adhesive modeling parameters indicated that increasing the adhesive traction separation stiffness (K_{ss} and K_{tt}) and nominal shear strain were also associated with significant reductions in crack length.

- The parametric study on the steel modeling parameters indicated that increasing the maximum principal stress responsible for triggering damage initiation in the steel substrate was associated with large reductions in crack length. Result also indicated that reducing the displacement at failure (DaF) below 0.51 mm (0.02in) increased crack propagation slightly.

From the findings of the experimental study to develop and evaluate a novel CFRP-Steel retrofit to repair complex patterns of DIF cracks in steel bridge web gaps without the use of bolting to the flange or the removal of the concrete deck, the following key conclusions were drawn:

- All configurations of the CFRP-steel retrofit measure were found to be effective in stopping DIF crack propagation, even for long crack lengths with aggressive propagation rates, for the crack patterns and lengths evaluated in this study.
- The combined CFRP-steel retrofit measure with CFRP fabric attached beyond the edges of the steel elements was found to be effective in preventing the growth of cracks that extended beyond the steel elements, the longest evaluated in the study.

- A CFRP-only retrofit measure was ineffective in preventing propagation of some cracks for the tested crack pattern and lengths. Without the steel elements, the CFRP fabric was insufficient to reduce deformations in the web gap and decrease the stress range to a magnitude where the CFRP could effectively prevent crack growth, as it did in the combined CFRP-steel retrofit measures, even in cases where the cracks extended beyond the steel components.
- Notably, no debonding between the CFRP fabric and steel substrate was observed at the edges of the application region in any of the fatigue trials, even for the CFRP-only retrofit measure.

Appendix A: **Different Stresses Contours of the Web Gap Region on the Interior Side and Fascia Side of the Girder**

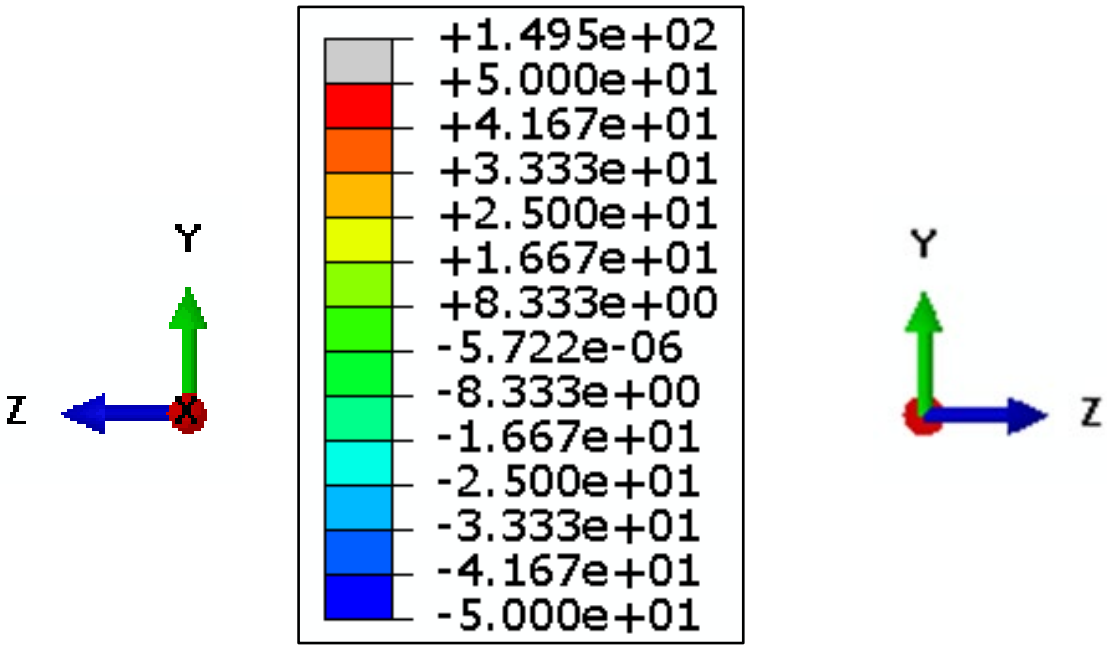

(a) (b) (c)

Figure A-1 Stress limits and coordinates directions convention for all figures in this Appendix: (a) Coordinate direction on the interior side of the girder; (b) Stress limits (-50 ksi to +50 ksi); (c) Coordinate direction on the fascia side of the girder

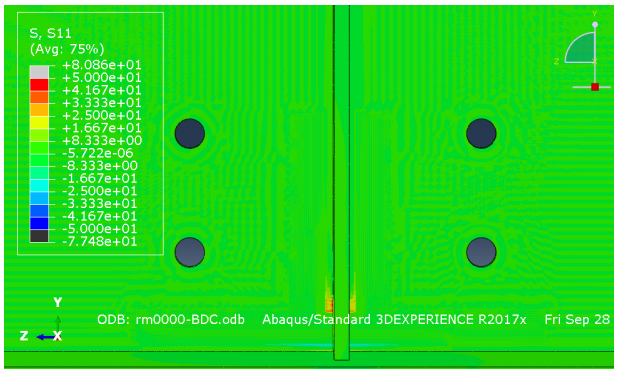
S, S11
(Avg: 75%)
+8.086e+01
+5.000e+01
+4.167e+01
+3.333e+01
+2.500e+01
+1.667e+01
+8.333e+00
-5.722e-06
-8.333e+00
-1.667e+01
-2.500e+01
-3.333e+01
-4.167e+01
-5.000e+01
-7.748e+01
ODB: rm0000-BDC.odb Abaqus/Standard 3DEXPERIENCE R2017x Fri Sep 28

(a)

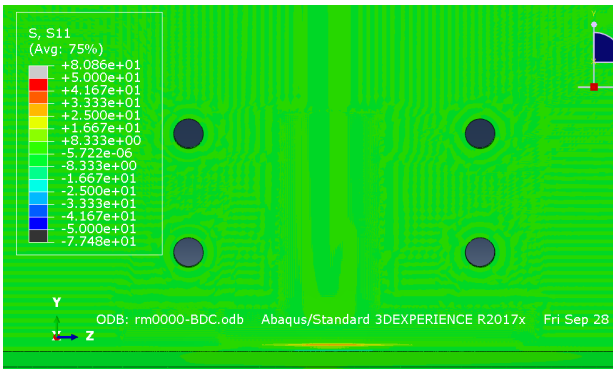
S, S11
(Avg: 75%)
+8.086e+01
+5.000e+01
+4.167e+01
+3.333e+01
+2.500e+01
+1.667e+01
+8.333e+00
-5.722e-06
-8.333e+00
-1.667e+01
-2.500e+01
-3.333e+01
-4.167e+01
-5.000e+01
-7.748e+01
ODB: rm0000-BDC.odb Abaqus/Standard 3DEXPERIENCE R2017x Fri Sep 28

(b)

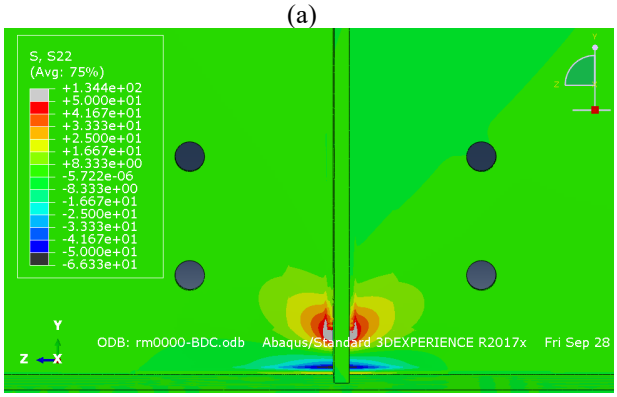
S, S22
(Avg: 75%)
+1.344e+02
+5.000e+01
+4.167e+01
+3.333e+01
+2.500e+01
+1.667e+01
+8.333e+00
-5.722e-06
-8.333e+00
-1.667e+01
-2.500e+01
-3.333e+01
-4.167e+01
-5.000e+01
-6.633e+01
ODB: rm0000-BDC.odb Abaqus/Standard 3DEXPERIENCE R2017x Fri Sep 28

(c)

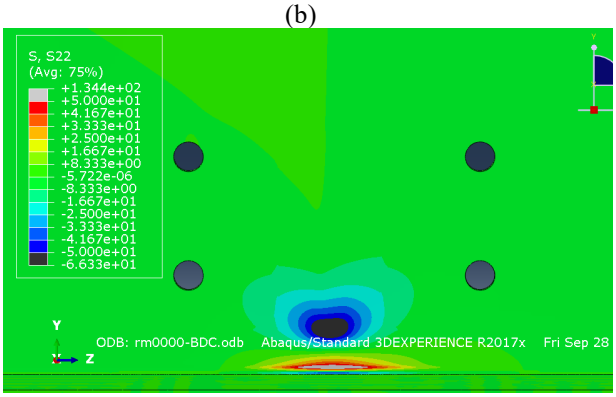
S, S22
(Avg: 75%)
+1.344e+02
+5.000e+01
+4.167e+01
+3.333e+01
+2.500e+01
+1.667e+01
+8.333e+00
-5.722e-06
-8.333e+00
-1.667e+01
-2.500e+01
-3.333e+01
-4.167e+01
-5.000e+01
-6.633e+01
ODB: rm0000-BDC.odb Abaqus/Standard 3DEXPERIENCE R2017x Fri Sep 28

(d)

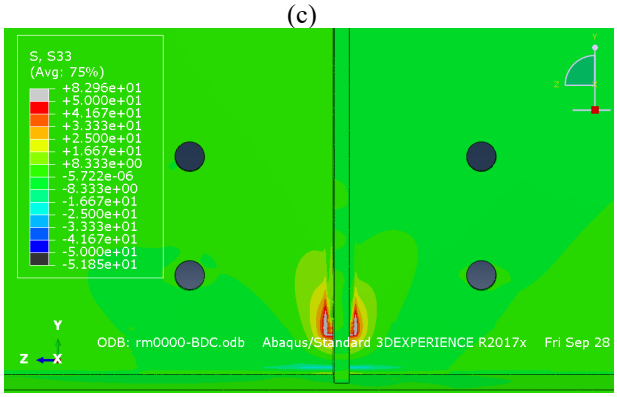
S, S33
(Avg: 75%)
+8.296e+01
+5.000e+01
+4.167e+01
+3.333e+01
+2.500e+01
+1.667e+01
+8.333e+00
-5.722e-06
-8.333e+00
-1.667e+01
-2.500e+01
-3.333e+01
-4.167e+01
-5.000e+01
-5.185e+01
ODB: rm0000-BDC.odb Abaqus/Standard 3DEXPERIENCE R2017x Fri Sep 28

(e)

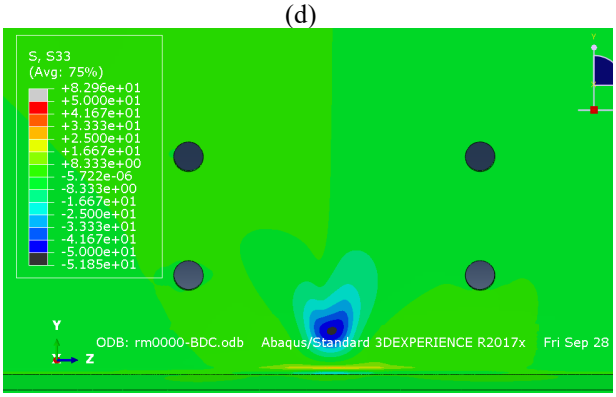
S, S33
(Avg: 75%)
+8.296e+01
+5.000e+01
+4.167e+01
+3.333e+01
+2.500e+01
+1.667e+01
+8.333e+00
-5.722e-06
-8.333e+00
-1.667e+01
-2.500e+01
-3.333e+01
-4.167e+01
-5.000e+01
-5.185e+01
ODB: rm0000-BDC.odb Abaqus/Standard 3DEXPERIENCE R2017x Fri Sep 28

(f)


S, Mises
(Avg: 75%)
+1.163e+02
+5.000e+01
+4.167e+01
+3.333e+01
+2.500e+01
+1.667e+01
+8.333e+00
-5.722e-06
-8.333e+00
-1.667e+01
-2.500e+01
-3.333e+01
-4.167e+01
-5.000e+01

(g)

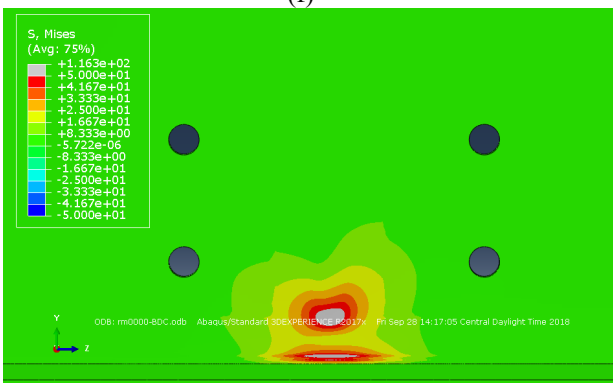
S, Mises
(Avg: 75%)
+1.163e+02
+5.000e+01
+4.167e+01
+3.333e+01
+2.500e+01
+1.667e+01
+8.333e+00
-5.722e-06
-8.333e+00
-1.667e+01
-2.500e+01
-3.333e+01
-4.167e+01
-5.000e+01

(h)

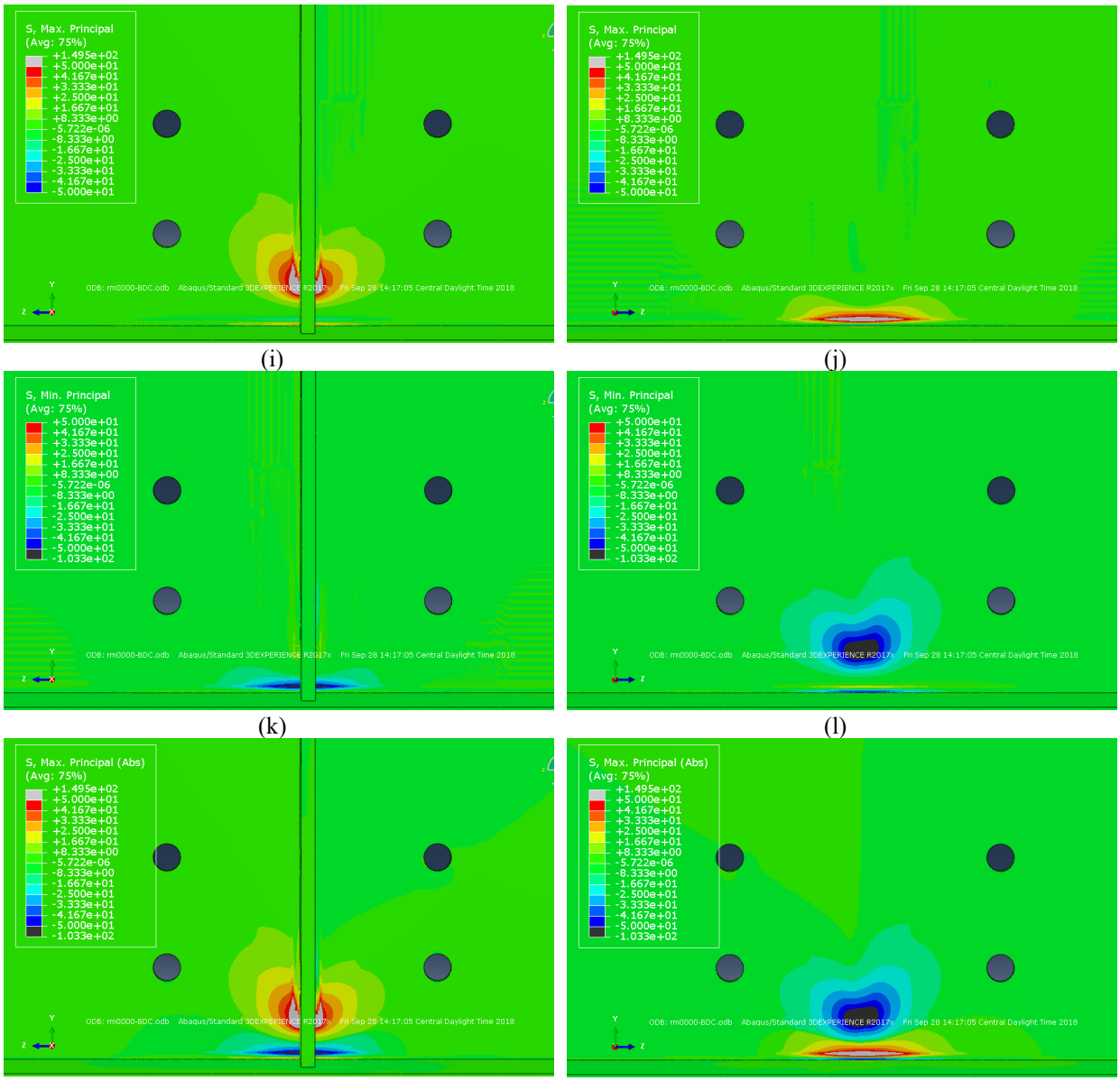

(i) (j)

(k) (l)

(m) (n)

Figure A-2: Different stresses contours of the web gap region on the interior side and fascia side of the girder for UR-UC (a1=a2=0) model: (a) S11 on the interior side; (b) S11 on the fascia side; (c) S22 on the interior side; (d) S22 on the fascia side; (e) S33 on the interior side; (f) S33 on the fascia side; (g) Von Mises on the interior side; (h) Von Mises on the fascia side; (i) Max principal stress on the interior side; (j) Max principal stress on the fascia side; (k) Min principal stress on the interior side; (l) Min principal stress on the fascia side; (m) Absolute max principal stress on the interior side; (m) Absolute max principal stress on the fascia side

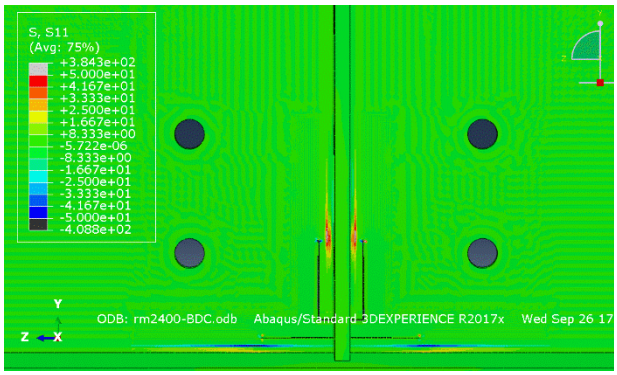
S, S11
(Avg: 75%)
+3.843e+02
+5.000e+01
+4.167e+01
+3.333e+01
+2.500e+01
+1.667e+01
+8.333e+00
-5.722e-06
-8.333e+00
-1.667e+01
-2.500e+01
-3.333e+01
-4.167e+01
-5.000e+01
-4.088e+02
ODB: rm2400-BDC.odb Abaqus/Standard 3DEXPERIENCE R2017x Wed Sep 26 17

(a)

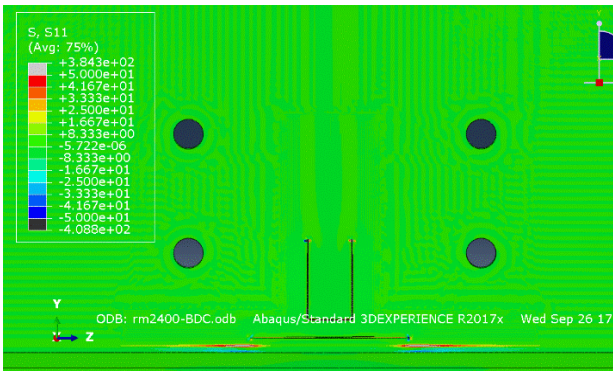
S, S11
(Avg: 75%)
+3.843e+02
+5.000e+01
+4.167e+01
+3.333e+01
+2.500e+01
+1.667e+01
+8.333e+00
-5.722e-06
-8.333e+00
-1.667e+01
-2.500e+01
-3.333e+01
-4.167e+01
-5.000e+01
-4.088e+02
ODB: rm2400-BDC.odb Abaqus/Standard 3DEXPERIENCE R2017x Wed Sep 26 17

(b)

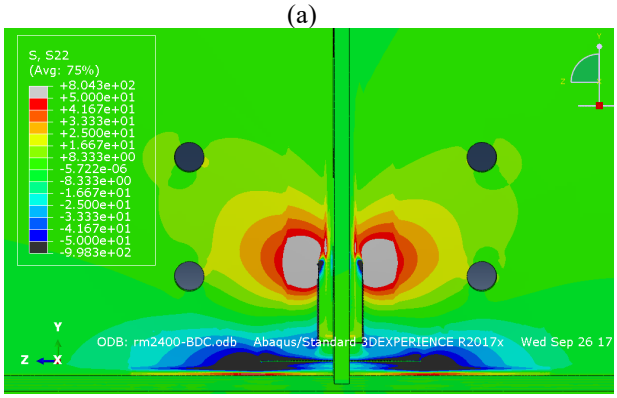
S, S22
(Avg: 75%)
+8.043e+02
+5.000e+01
+4.167e+01
+3.333e+01
+2.500e+01
+1.667e+01
+8.333e+00
-5.722e-06
-8.333e+00
-1.667e+01
-2.500e+01
-3.333e+01
-4.167e+01
-5.000e+01
-9.983e+02
ODB: rm2400-BDC.odb Abaqus/Standard 3DEXPERIENCE R2017x Wed Sep 26 17

(c)

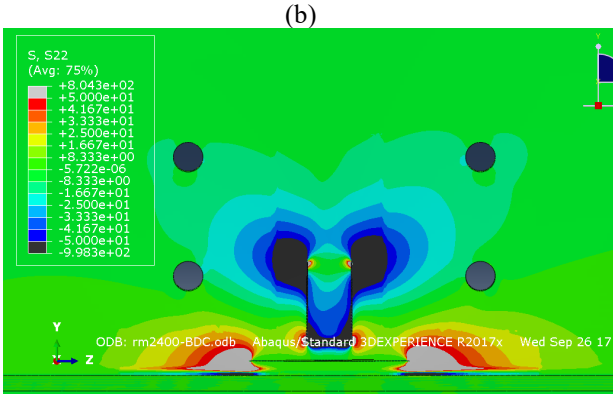
S, S22
(Avg: 75%)
+8.043e+02
+5.000e+01
+4.167e+01
+3.333e+01
+2.500e+01
+1.667e+01
+8.333e+00
-5.722e-06
-8.333e+00
-1.667e+01
-2.500e+01
-3.333e+01
-4.167e+01
-5.000e+01
-9.983e+02
ODB: rm2400-BDC.odb Abaqus/Standard 3DEXPERIENCE R2017x Wed Sep 26 17

(d)

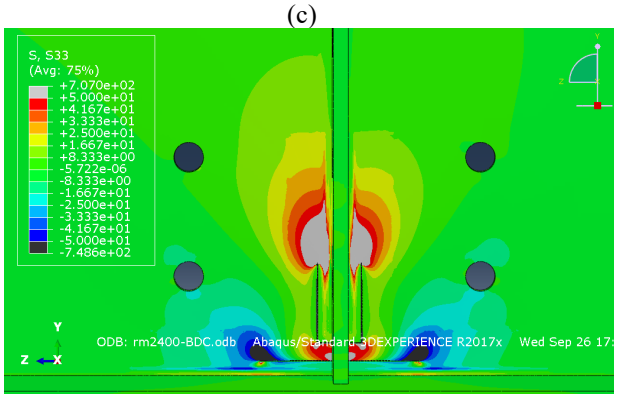
S, S33
(Avg: 75%)
+7.070e+02
+5.000e+01
+4.167e+01
+3.333e+01
+2.500e+01
+1.667e+01
+8.333e+00
-5.722e-06
-8.333e+00
-1.667e+01
-2.500e+01
-3.333e+01
-4.167e+01
-5.000e+01
-7.486e+02
ODB: rm2400-BDC.odb Abaqus/Standard 3DEXPERIENCE R2017x Wed Sep 26 17

(e)

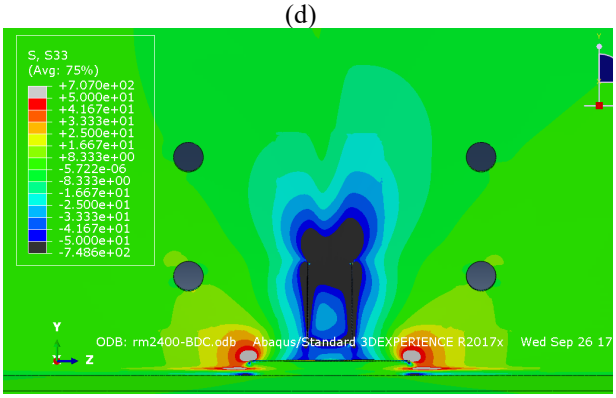
S, S33
(Avg: 75%)
+7.070e+02
+5.000e+01
+4.167e+01
+3.333e+01
+2.500e+01
+1.667e+01
+8.333e+00
-5.722e-06
-8.333e+00
-1.667e+01
-2.500e+01
-3.333e+01
-4.167e+01
-5.000e+01
-7.486e+02
ODB: rm2400-BDC.odb Abaqus/Standard 3DEXPERIENCE R2017x Wed Sep 26 17

(f)

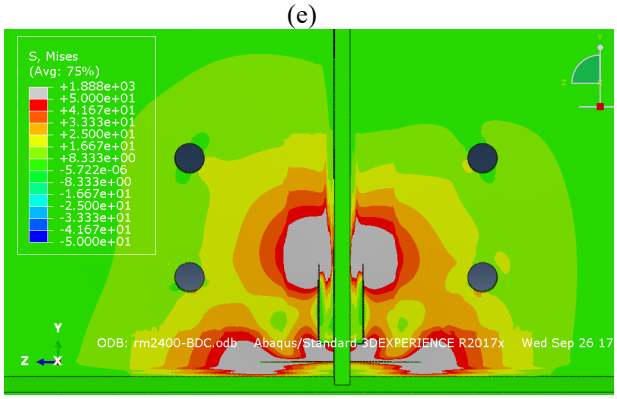
S, Mises
(Avg: 75%)
+1.888e+03
+5.000e+01
+4.167e+01
+3.333e+01
+2.500e+01
+1.667e+01
+8.333e+00
-5.722e-06
-8.333e+00
-1.667e+01
-2.500e+01
-3.333e+01
-4.167e+01
-5.000e+01
ODB: rm2400-BDC.odb Abaqus/Standard 3DEXPERIENCE R2017x Wed Sep 26 17

(g)

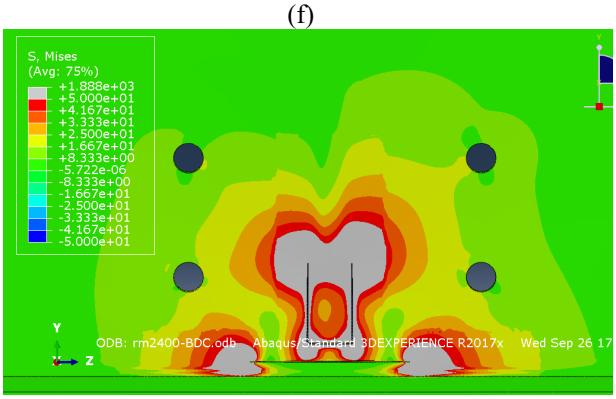
S, Mises
(Avg: 75%)
+1.888e+03
+5.000e+01
+4.167e+01
+3.333e+01
+2.500e+01
+1.667e+01
+8.333e+00
-5.722e-06
-8.333e+00
-1.667e+01
-2.500e+01
-3.333e+01
-4.167e+01
-5.000e+01
ODB: rm2400-BDC.odb Abaqus/Standard 3DEXPERIENCE R2017x Wed Sep 26 17

(h)

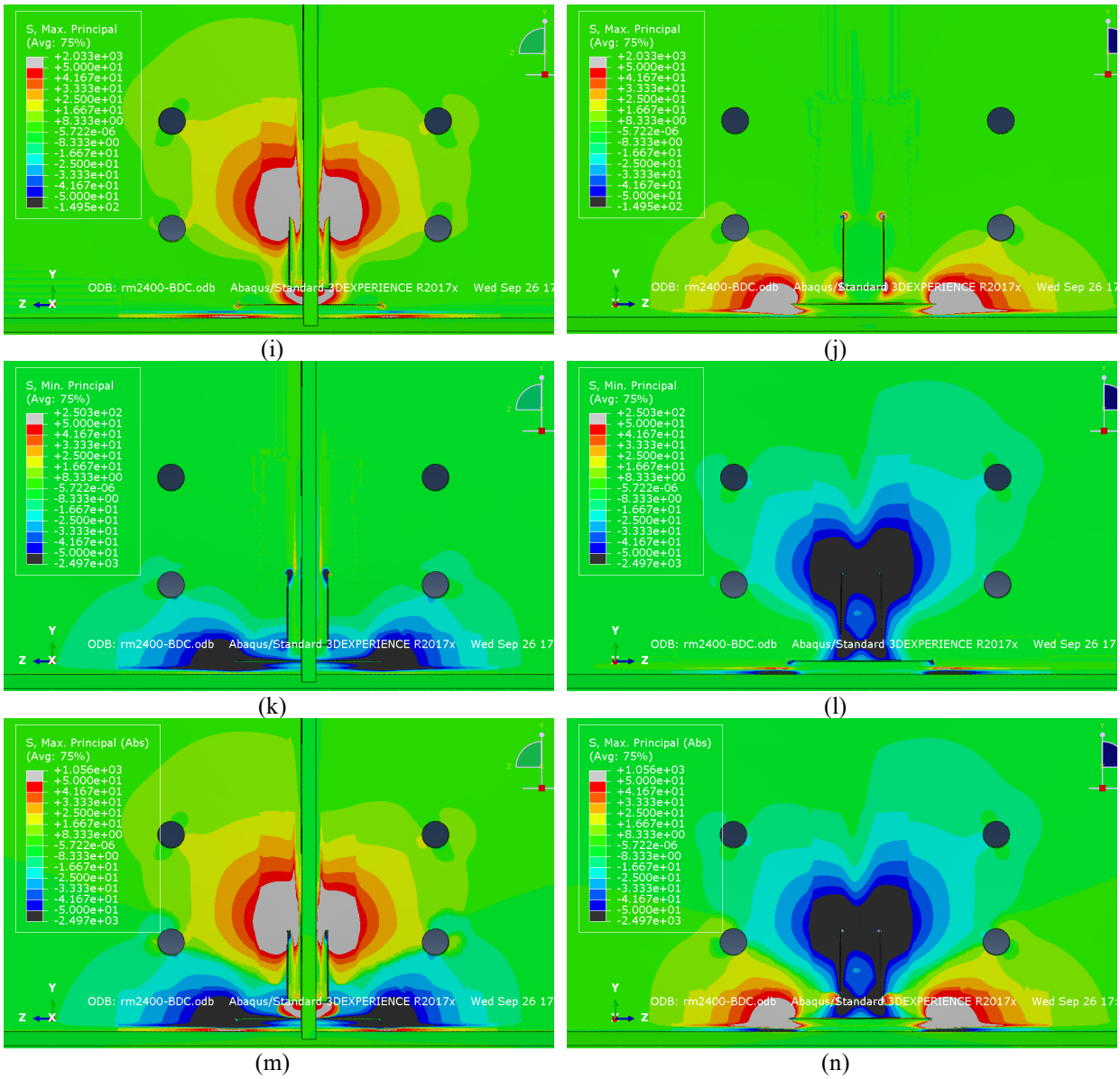

Figure A-3: Different stresses contours of the web gap region on the interior side and fascia side of the girder for UR-a1=a2=2 model: (a) S11 on the interior side; (b) S11 on the fascia side; (c) S22 on the interior side; (d) S22 on the fascia side; (e) S33 on the interior side; (f) S33 on the fascia side; (g) Von Mises on the interior side; (h) Von Mises on the fascia side; (i) Max principal stress on the interior side; (j) Max principal stress on the fascia side; (k) Min principal stress on the interior side; (l) Min principal stress on the fascia side; (m) Absolute max principal stress on the interior side; (m) Absolute max principal stress on the fascia side

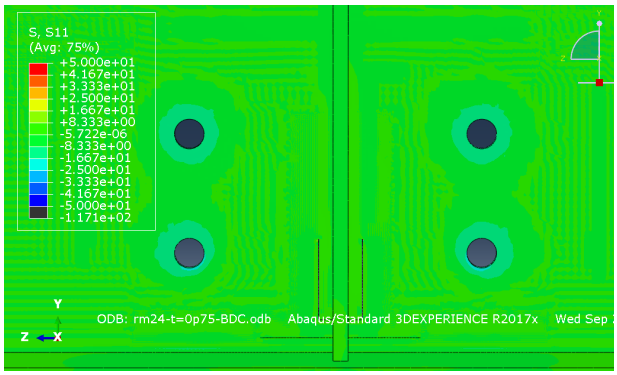
S, S11
(Avg: 75%)
+5.000e+01
+4.167e+01
+3.333e+01
+2.500e+01
+1.667e+01
+8.333e+00
-5.722e-06
-8.333e+00
-1.667e+01
-2.500e+01
-3.333e+01
-4.167e+01
-5.000e+01
-1.171e+02
ODB: rm24-t=0p75-BDC.odb Abaqus/Standard 3DEXPERIENCE R2017x Wed Sep

(a)

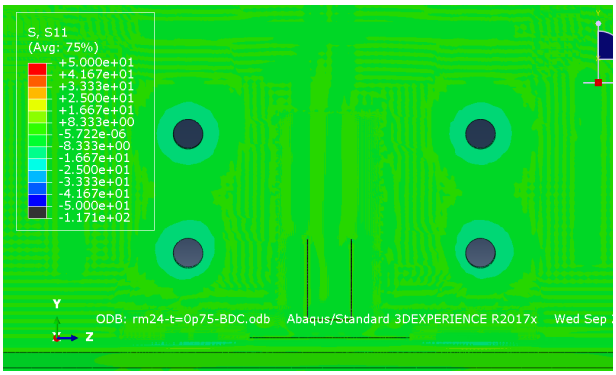
S, S11
(Avg: 75%)
+5.000e+01
+4.167e+01
+3.333e+01
+2.500e+01
+1.667e+01
+8.333e+00
-5.722e-06
-8.333e+00
-1.667e+01
-2.500e+01
-3.333e+01
-4.167e+01
-5.000e+01
-1.171e+02
ODB: rm24-t=0p75-BDC.odb Abaqus/Standard 3DEXPERIENCE R2017x Wed Sep

(b)

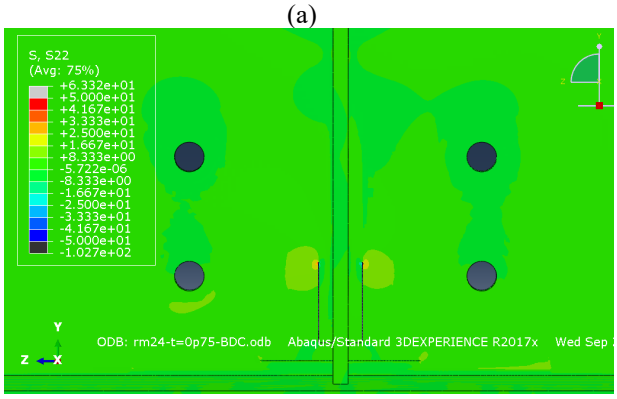
S, S22
(Avg: 75%)
+6.332e+01
+5.000e+01
+4.167e+01
+3.333e+01
+2.500e+01
+1.667e+01
+8.333e+00
-5.722e-06
-8.333e+00
-1.667e+01
-2.500e+01
-3.333e+01
-4.167e+01
-5.000e+01
-1.027e+02
ODB: rm24-t=0p75-BDC.odb Abaqus/Standard 3DEXPERIENCE R2017x Wed Sep

(c)

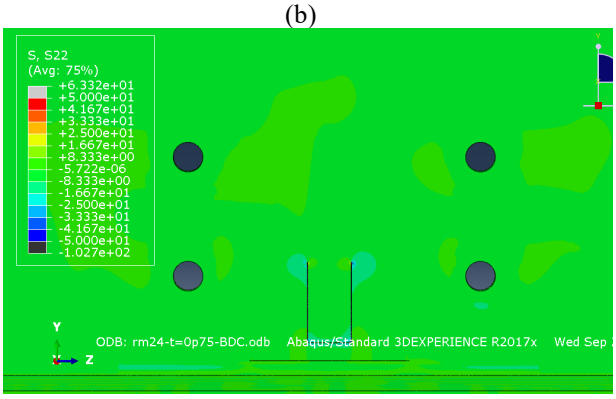
S, S22
(Avg: 75%)
+6.332e+01
+5.000e+01
+4.167e+01
+3.333e+01
+2.500e+01
+1.667e+01
+8.333e+00
-5.722e-06
-8.333e+00
-1.667e+01
-2.500e+01
-3.333e+01
-4.167e+01
-5.000e+01
-1.027e+02
ODB: rm24-t=0p75-BDC.odb Abaqus/Standard 3DEXPERIENCE R2017x Wed Sep

(d)

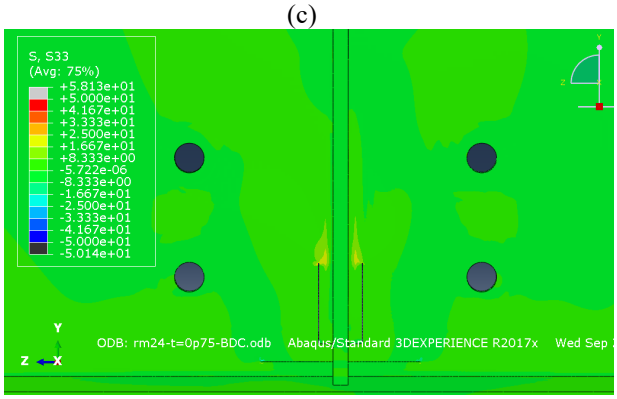
S, S33
(Avg: 75%)
+5.813e+01
+5.000e+01
+4.167e+01
+3.333e+01
+2.500e+01
+1.667e+01
+8.333e+00
-5.722e-06
-8.333e+00
-1.667e+01
-2.500e+01
-3.333e+01
-4.167e+01
-5.000e+01
-5.014e+01
ODB: rm24-t=0p75-BDC.odb Abaqus/Standard 3DEXPERIENCE R2017x Wed Sep

(e)

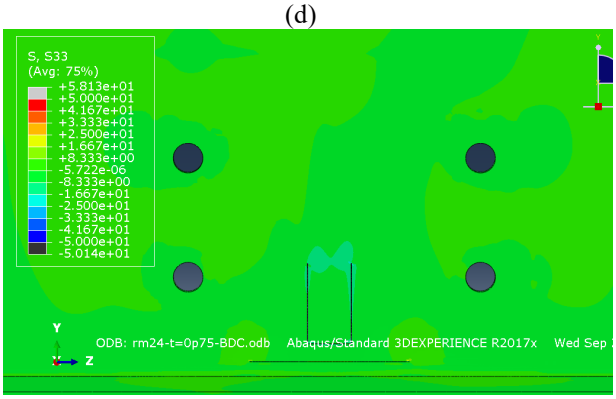
S, S33
(Avg: 75%)
+5.813e+01
+5.000e+01
+4.167e+01
+3.333e+01
+2.500e+01
+1.667e+01
+8.333e+00
-5.722e-06
-8.333e+00
-1.667e+01
-2.500e+01
-3.333e+01
-4.167e+01
-5.000e+01
-5.014e+01
ODB: rm24-t=0p75-BDC.odb Abaqus/Standard 3DEXPERIENCE R2017x Wed Sep

(f)

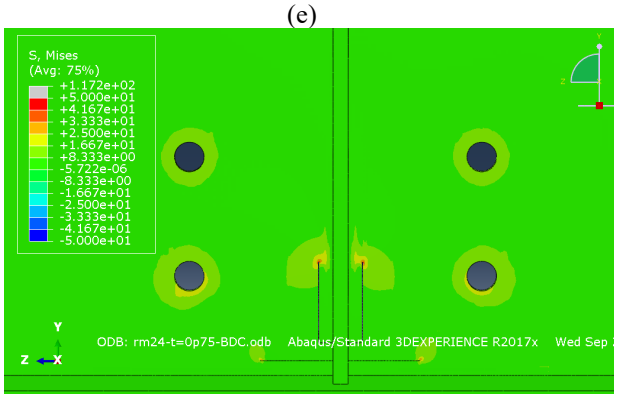
S, Mises
(Avg: 75%)
+1.172e+02
+5.000e+01
+4.167e+01
+3.333e+01
+2.500e+01
+1.667e+01
+8.333e+00
-5.722e-06
-8.333e+00
-1.667e+01
-2.500e+01
-3.333e+01
-4.167e+01
-5.000e+01
ODB: rm24-t=0p75-BDC.odb Abaqus/Standard 3DEXPERIENCE R2017x Wed Sep

(g)

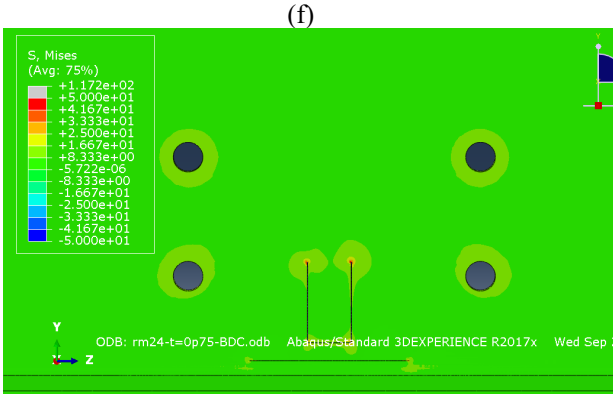
S, Mises
(Avg: 75%)
+1.172e+02
+5.000e+01
+4.167e+01
+3.333e+01
+2.500e+01
+1.667e+01
+8.333e+00
-5.722e-06
-8.333e+00
-1.667e+01
-2.500e+01
-3.333e+01
-4.167e+01
-5.000e+01
ODB: rm24-t=0p75-BDC.odb Abaqus/Standard 3DEXPERIENCE R2017x Wed Sep

(h)

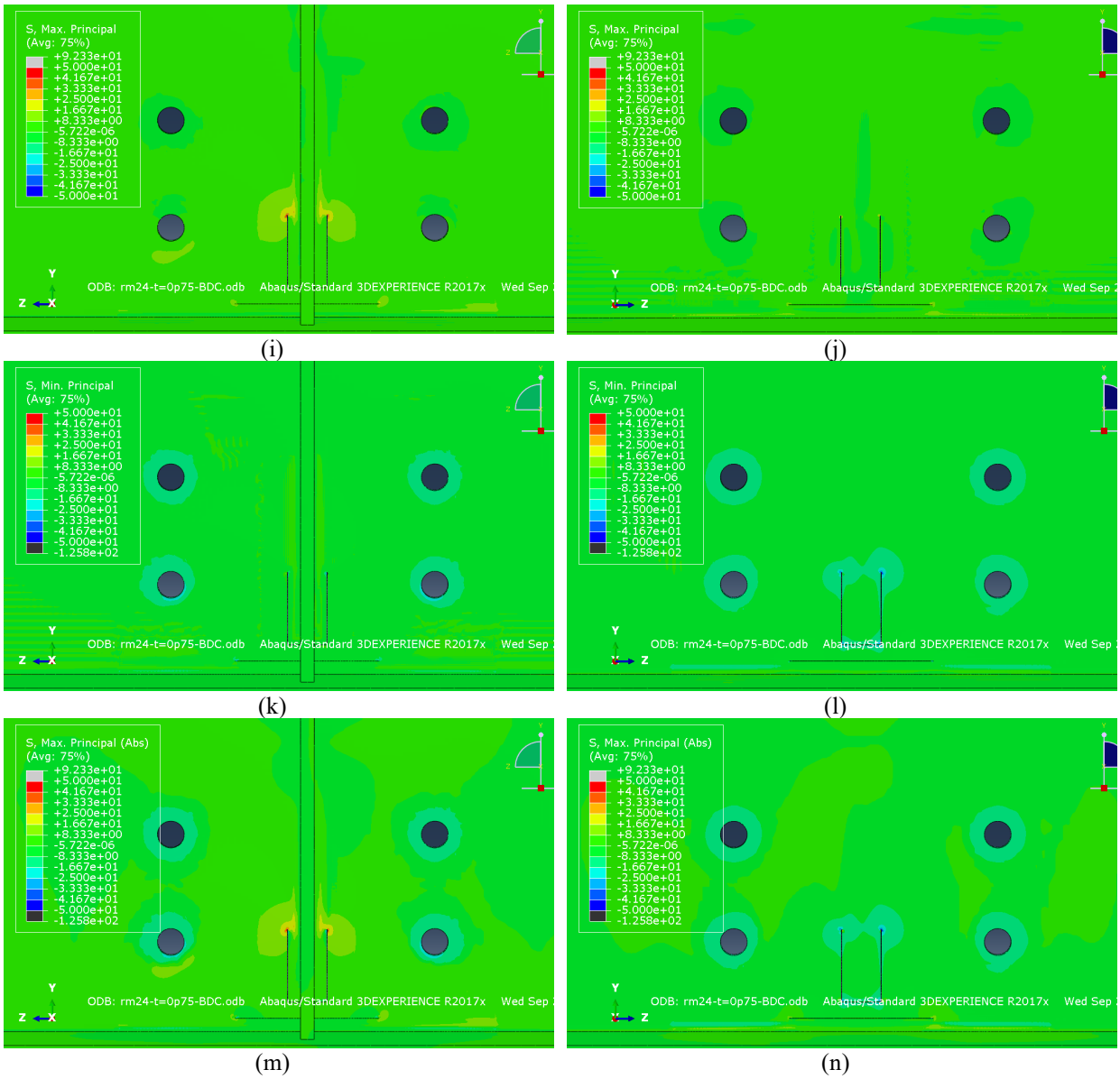

Figure A-4: Different stresses contours of the web gap region on the interior side and fascia side of the girder for 0.75R-a1=a2=2 model: (a) S11 on the interior side; (b) S11 on the fascia side; (c) S22 on the interior side; (d) S22 on the fascia side; (e) S33 on the interior side; (f) S33 on the fascia side; (g) Von Mises on the interior side; (h) Von Mises on the fascia side; (i) Max principal stress on the interior side; (j) Max principal stress on the fascia side; (k) Min principal stress on the interior side; (l) Min principal stress on the fascia side; (m) Absolute max principal stress on the interior side; (m) Absolute max principal stress on the fascia side

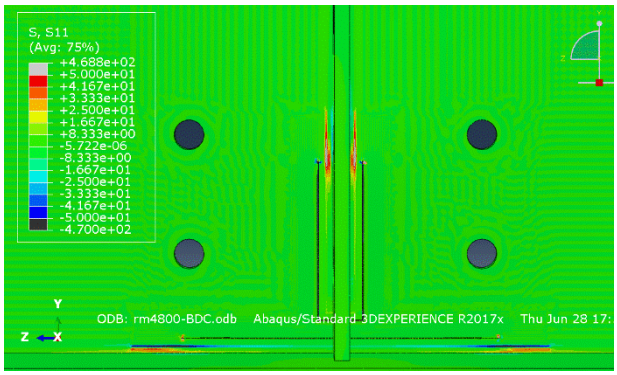
S, S11
(Avg: 75%)
+4.688e+02
+5.000e+01
+4.167e+01
+3.333e+01
+2.500e+01
+1.667e+01
+8.333e+00
-5.722e-06
-8.333e+00
-1.667e+01
-2.500e+01
-3.333e+01
-4.167e+01
-5.000e+01
-4.700e+02
ODB: rm4800-BDC.odb Abaqus/Standard 3DEXPERIENCE R2017x Thu Jun 28 17:

(a)

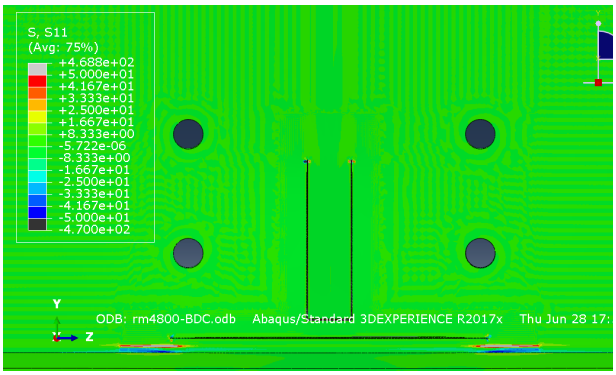
S, S11
(Avg: 75%)
+4.688e+02
+5.000e+01
+4.167e+01
+3.333e+01
+2.500e+01
+1.667e+01
+8.333e+00
-5.722e-06
-8.333e+00
-1.667e+01
-2.500e+01
-3.333e+01
-4.167e+01
-5.000e+01
-4.700e+02
ODB: rm4800-BDC.odb Abaqus/Standard 3DEXPERIENCE R2017x Thu Jun 28 17:

(b)

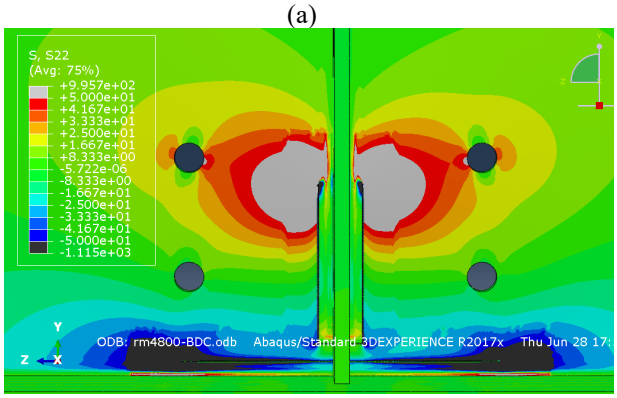
S, S22
(Avg: 75%)
+9.957e+02
+5.000e+01
+4.167e+01
+3.333e+01
+2.500e+01
+1.667e+01
+8.333e+00
-5.722e-06
-8.333e+00
-1.667e+01
-2.500e+01
-3.333e+01
-4.167e+01
-5.000e+01
-1.115e+03
ODB: rm4800-BDC.odb Abaqus/Standard 3DEXPERIENCE R2017x Thu Jun 28 17:

(c)

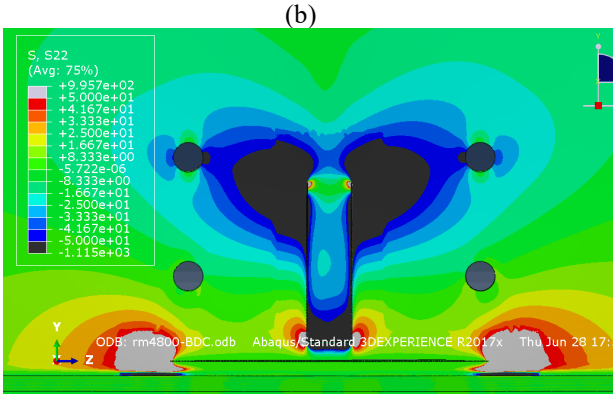
S, S22
(Avg: 75%)
+9.957e+02
+5.000e+01
+4.167e+01
+3.333e+01
+2.500e+01
+1.667e+01
+8.333e+00
-5.722e-06
-8.333e+00
-1.667e+01
-2.500e+01
-3.333e+01
-4.167e+01
-5.000e+01
-1.115e+03
ODB: rm4800-BDC.odb Abaqus/Standard 3DEXPERIENCE R2017x Thu Jun 28 17:

(d)

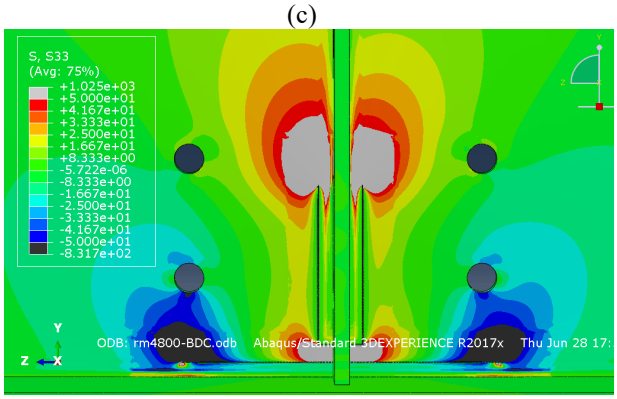
S, S33
(Avg: 75%)
+1.025e+03
+5.000e+01
+4.167e+01
+3.333e+01
+2.500e+01
+1.667e+01
+8.333e+00
-5.722e-06
-8.333e+00
-1.667e+01
-2.500e+01
-3.333e+01
-4.167e+01
-5.000e+01
-8.317e+02
ODB: rm4800-BDC.odb Abaqus/Standard 3DEXPERIENCE R2017x Thu Jun 28 17:

(e)

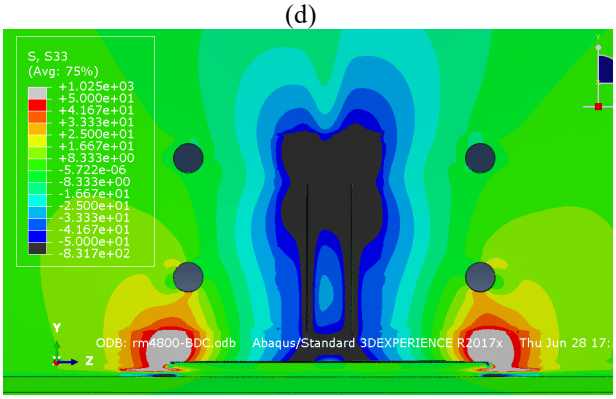
S, S33
(Avg: 75%)
+1.025e+03
+5.000e+01
+4.167e+01
+3.333e+01
+2.500e+01
+1.667e+01
+8.333e+00
-5.722e-06
-8.333e+00
-1.667e+01
-2.500e+01
-3.333e+01
-4.167e+01
-5.000e+01
-8.317e+02
ODB: rm4800-BDC.odb Abaqus/Standard 3DEXPERIENCE R2017x Thu Jun 28 17:

(f)

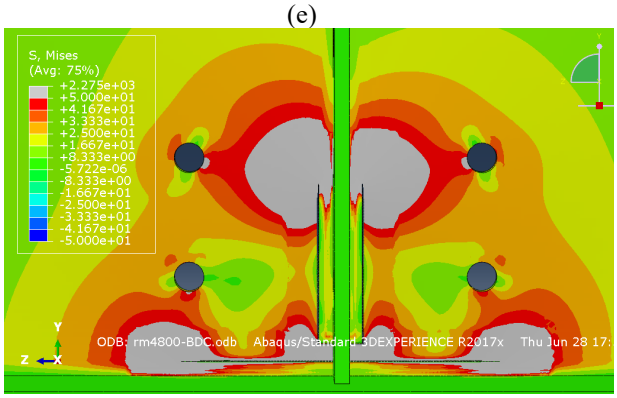
S, Mises
(Avg: 75%)
+2.275e+03
+5.000e+01
+4.167e+01
+3.333e+01
+2.500e+01
+1.667e+01
+8.333e+00
-5.722e-06
-8.333e+00
-1.667e+01
-2.500e+01
-3.333e+01
-4.167e+01
-5.000e+01
ODB: rm4800-BDC.odb Abaqus/Standard 3DEXPERIENCE R2017x Thu Jun 28 17:

(g)

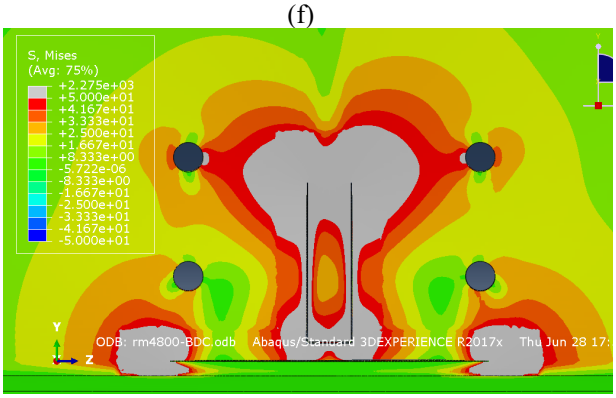
S, Mises
(Avg: 75%)
+2.275e+03
+5.000e+01
+4.167e+01
+3.333e+01
+2.500e+01
+1.667e+01
+8.333e+00
-5.722e-06
-8.333e+00
-1.667e+01
-2.500e+01
-3.333e+01
-4.167e+01
-5.000e+01
ODB: rm4800-BDC.odb Abaqus/Standard 3DEXPERIENCE R2017x Thu Jun 28 17:

(h)

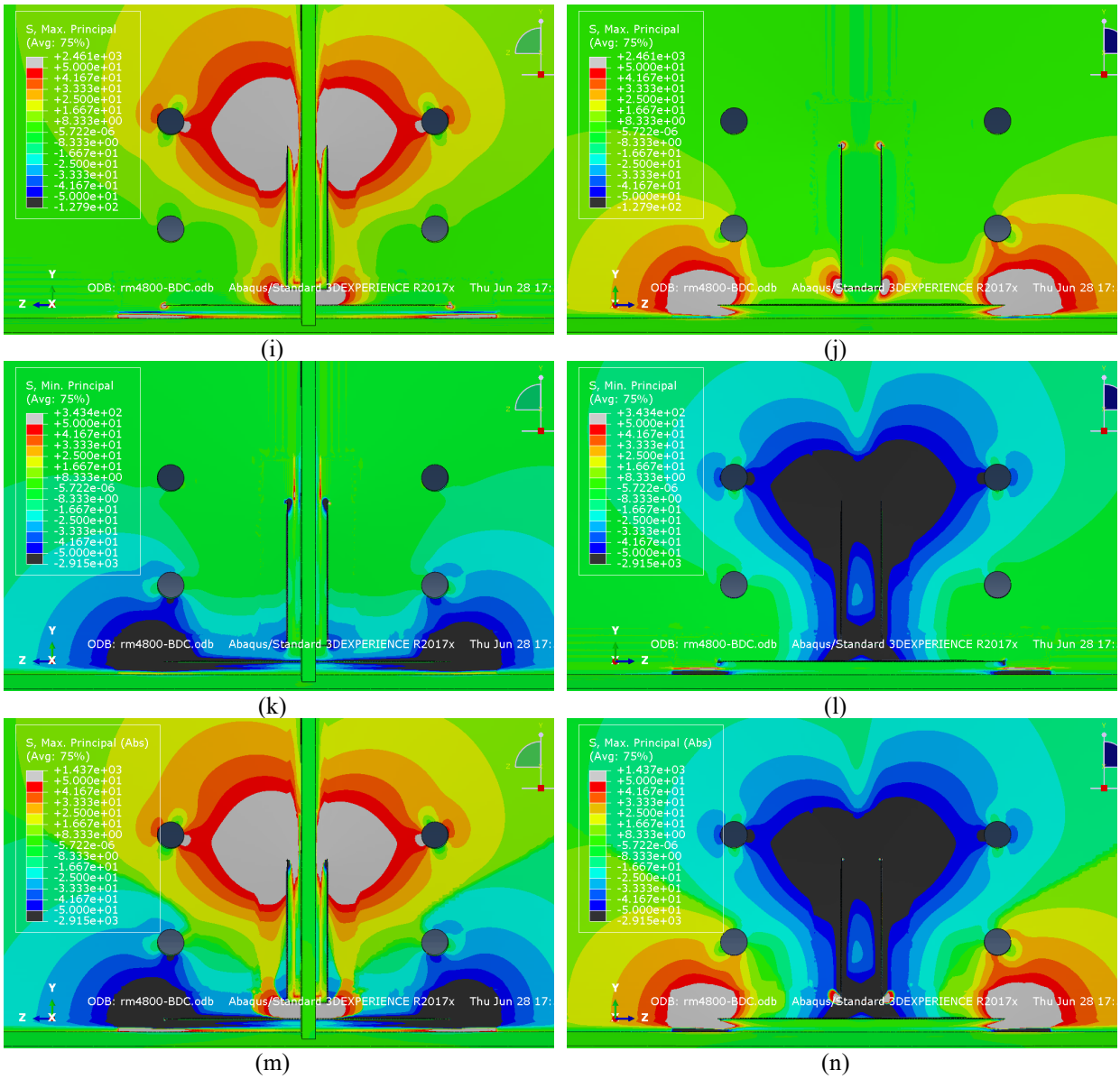

Figure A-5: Different stresses contours of the web gap region on the interior side and fascia side of the girder for UR-a1=a2=4 model: (a) S11 on the interior side; (b) S11 on the fascia side; (c) S22 on the interior side; (d) S22 on the fascia side; (e) S33 on the interior side; (f) S33 on the fascia side; (g) Von Mises on the interior side; (h) Von Mises on the fascia side; (i) Max principal stress on the interior side; (j) Max principal stress on the fascia side; (k) Min principal stress on the interior side; (l) Min principal stress on the fascia side; (m) Absolute max principal stress on the interior side; (m) Absolute max principal stress on the fascia side

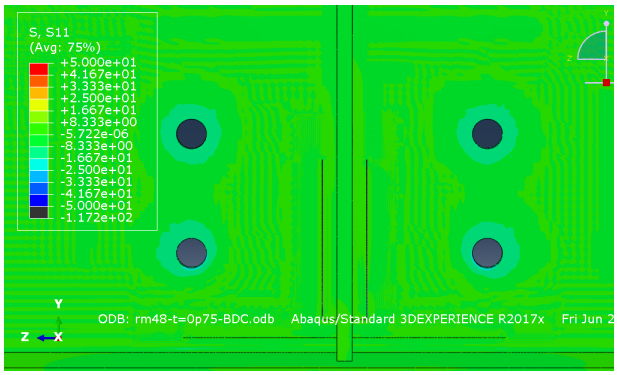
S, S11
(Avg: 75%)
+5.000e+01
+4.167e+01
+3.333e+01
+2.500e+01
+1.667e+01
+8.333e+00
-5.722e-06
-8.333e+00
-1.667e+01
-2.500e+01
-3.333e+01
-4.167e+01
-5.000e+01
-1.172e+02
ODB: rm48-t=0p75-BDC.odb Abaqus/Standard 3DEXPERIENCE R2017x Fri Jun 2

(a)

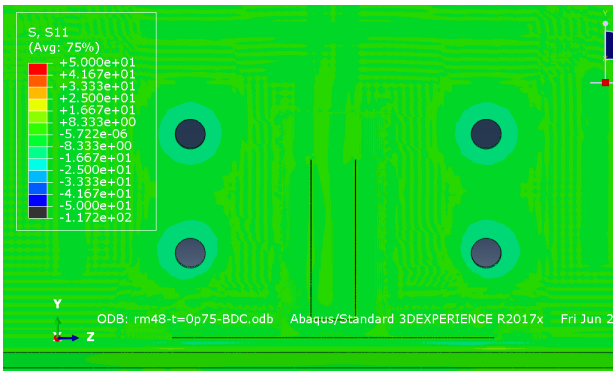
S, S11
(Avg: 75%)
+5.000e+01
+4.167e+01
+3.333e+01
+2.500e+01
+1.667e+01
+8.333e+00
-5.722e-06
-8.333e+00
-1.667e+01
-2.500e+01
-3.333e+01
-4.167e+01
-5.000e+01
-1.172e+02
ODB: rm48-t=0p75-BDC.odb Abaqus/Standard 3DEXPERIENCE R2017x Fri Jun 2

(b)

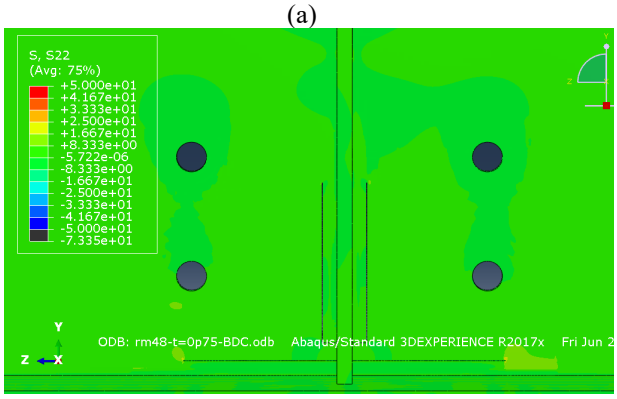
S, S22
(Avg: 75%)
+5.000e+01
+4.167e+01
+3.333e+01
+2.500e+01
+1.667e+01
+8.333e+00
-5.722e-06
-8.333e+00
-1.667e+01
-2.500e+01
-3.333e+01
-4.167e+01
-5.000e+01
-7.335e+01
ODB: rm48-t=0p75-BDC.odb Abaqus/Standard 3DEXPERIENCE R2017x Fri Jun 2

(c)

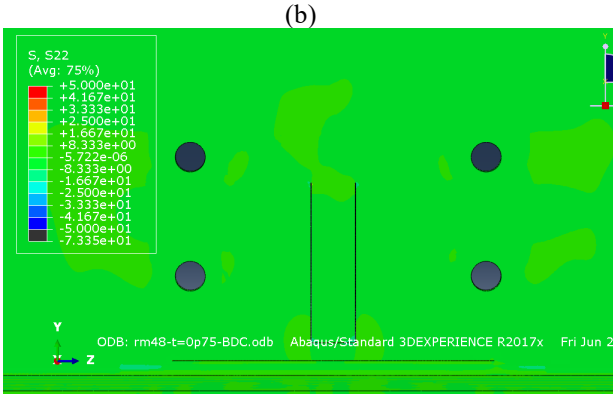
S, S22
(Avg: 75%)
+5.000e+01
+4.167e+01
+3.333e+01
+2.500e+01
+1.667e+01
+8.333e+00
-5.722e-06
-8.333e+00
-1.667e+01
-2.500e+01
-3.333e+01
-4.167e+01
-5.000e+01
-7.335e+01
ODB: rm48-t=0p75-BDC.odb Abaqus/Standard 3DEXPERIENCE R2017x Fri Jun 2

(d)

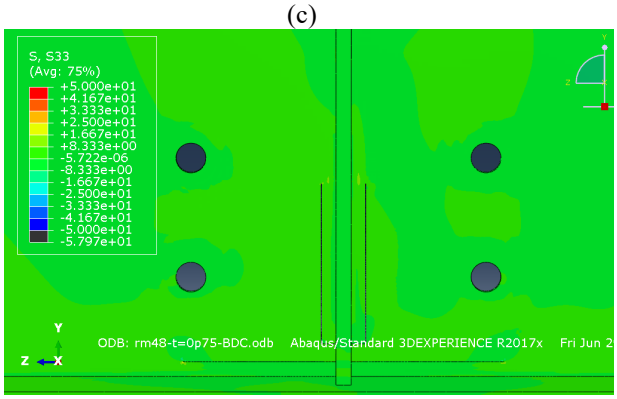
S, S33
(Avg: 75%)
+5.000e+01
+4.167e+01
+3.333e+01
+2.500e+01
+1.667e+01
+8.333e+00
-5.722e-06
-8.333e+00
-1.667e+01
-2.500e+01
-3.333e+01
-4.167e+01
-5.000e+01
-5.797e+01
ODB: rm48-t=0p75-BDC.odb Abaqus/Standard 3DEXPERIENCE R2017x Fri Jun 2

(e)

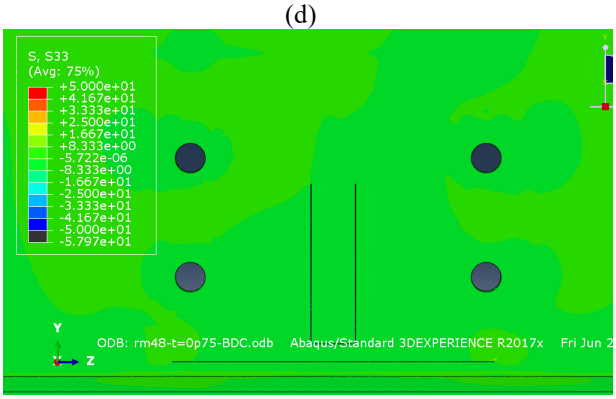
S, S33
(Avg: 75%)
+5.000e+01
+4.167e+01
+3.333e+01
+2.500e+01
+1.667e+01
+8.333e+00
-5.722e-06
-8.333e+00
-1.667e+01
-2.500e+01
-3.333e+01
-4.167e+01
-5.000e+01
-5.797e+01
ODB: rm48-t=0p75-BDC.odb Abaqus/Standard 3DEXPERIENCE R2017x Fri Jun 2

(f)

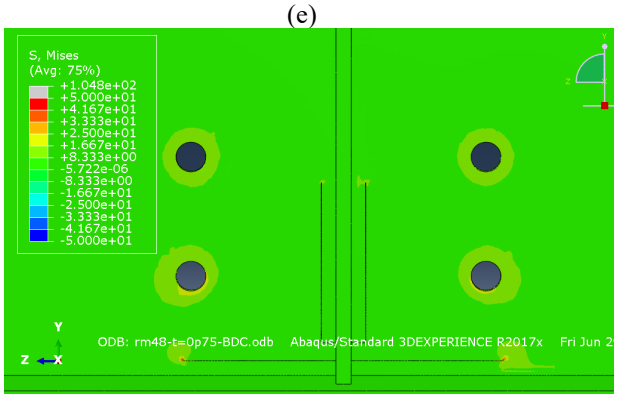
S, Mises
(Avg: 75%)
+1.048e+02
+5.000e+01
+4.167e+01
+3.333e+01
+2.500e+01
+1.667e+01
+8.333e+00
-5.722e-06
-8.333e+00
-1.667e+01
-2.500e+01
-3.333e+01
-4.167e+01
-5.000e+01
ODB: rm48-t=0p75-BDC.odb Abaqus/Standard 3DEXPERIENCE R2017x Fri Jun 2

(g)

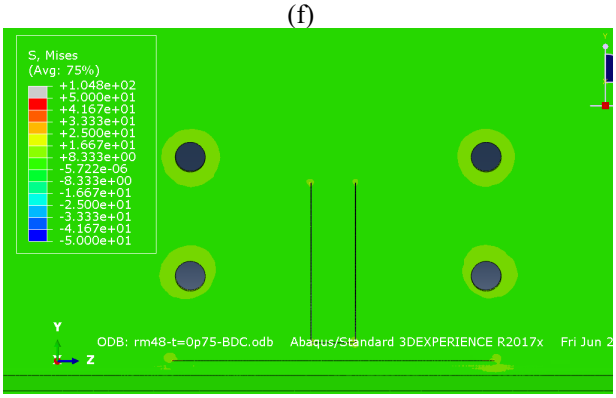
S, Mises
(Avg: 75%)
+1.048e+02
+5.000e+01
+4.167e+01
+3.333e+01
+2.500e+01
+1.667e+01
+8.333e+00
-5.722e-06
-8.333e+00
-1.667e+01
-2.500e+01
-3.333e+01
-4.167e+01
-5.000e+01
ODB: rm48-t=0p75-BDC.odb Abaqus/Standard 3DEXPERIENCE R2017x Fri Jun 2

(h)

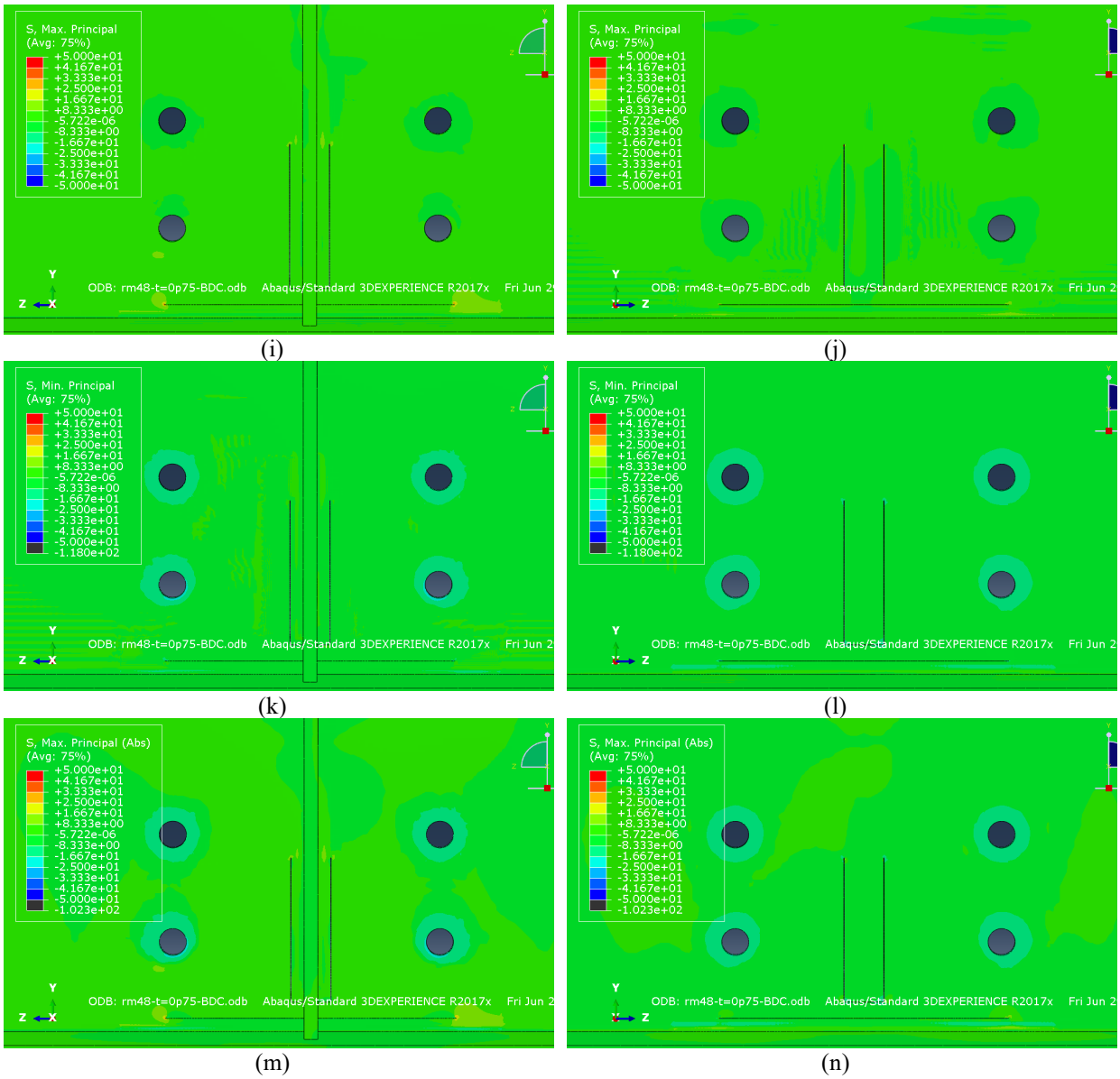

(i) (j)

(k) (l)

(m) (n)

Figure A-6: Different stresses contours of the web gap region on the interior side and fascia side of the girder for 0.75R-a1=a2=4 model: (a) S11 on the interior side; (b) S11 on the fascia side; (c) S22 on the interior side; (d) S22 on the fascia side; (e) S33 on the interior side; (f) S33 on the fascia side; (g) Von Mises on the interior side; (h) Von Mises on the fascia side; (i) Max principal stress on the interior side; (j) Max principal stress on the fascia side; (k) Min principal stress on the interior side; (l) Min principal stress on the fascia side; (m) Absolute max principal stress on the interior side; (m) Absolute max principal stress on the fascia side

Appendix B: **Summary of Key Literature Review about CFRP Strengthening**

Table B-1 Summary of Some of University of Kansas Research

Research Title	Reference Information	Type of FRP	Type of Epoxy	Description of study	Results Highlights
Fatigue Enhancement of Welded Details in Steel Bridges Using CFRP Overlay Elements	Kaan, B., Alemdar, F., Bennett, C., Matamoros, A., Barrett-Gonzalez, R., and Rolfe, S. (2012). "Fatigue Enhancement of Welded Details in Steel Bridges Using CFRP Overlay Elements," *Journal of Composites for Construction*, American Society of Civil Engineers (ASCE), 16(2) 138-149.	CFRP	Hysol (Loctite 9412) between CFRP and Steel	A flange/CP detail was retrofitted with CFRP doubler element, and loaded in 3-pt bending fatigue. Bond layer thickness, fabrication methods, retrofit shape, and application method of the CFRP reinforcement were varied. (Exp. & Numerical)	· Bonding CFRP reinforcements to damage-vulnerable welds lowered stress and increased stiffness in the welds, thereby suppressing crack initiation · Effectiveness of the reinforcement was very dependent on a strong bond between the composites and the steel · Adding extra resin around the edge of the CFRP and adding polyester fibers to the interface layer were both very effective at ensuring the required strong bond between the composites and steel · The characteristics of shear and peel stresses were investigated numerically · Peel strength was measured through monotonic testing
Use of Bolted CFRP Overlays to Prevent Fatigue Damage in Welded Steel Cover Plates	Alemdar, F., Matamoros, A., Bennett, C., Barrett-Gonzalez, R., and Rolfe, S. (2012). "Use of CFRP Overlays to Strengthen Welded Connections under Fatigue Loading," *Journal of Bridge Engineering*, American Society of Civil Engineers (ASCE), 17(3), 420-431. Nigam, D. (2012). M.S. thesis, Department of Civil, Environmental, and Architectural Engineering, Univ. of Kansas, Lawrence, KS. Wheeler, J. (2013). "Use of Bolted CFRP Overlay Elements for Fatigue Enhancement of Welded Coverplates in Steel Bridge Girders," M.S. thesis, Department of Civil, Environmental, and Architectural Engineering, Univ. of Kansas, Lawrence, KS.	E = 2000 ksi v = 0.1	E = 300 ksi v = 0.15	A flange/CP detail was studied with bolted CFRP doubler element, and loaded in 3-pt bending fatigue. The following were varied: Thickness of overlay; Bolt spacing; Presence of a resin pool (Numerical)	· Configurations with thinner overlays showed the largest compressive stresses at the interface layer. · Reducing the bolt spacing led to higher compressive stresses over a shorter region of the overlay. · A resin pool of 25-mm (1-in.), extending from the edge of the composite, led to a significant reduction in the tensile stress at the edge of the resin-steel interface.
Use of CFRP Overlays to Repair Fatigue Damage in Steel	Gonzalez, R., Rolfe, S., and Liu, H. (2014). "Use of CFRP Overlays to Repair Fatigue Damage in Steel Plates under Tension Loading," ASCE *Journal of Composites for Construction*, American Society of Civil Engineers (ASCE), 18 (4).	CFRP overlays made of bidirectional pre-impregnated	Hysol (Loctite 9412) between CFRP and steel	Dogbone-type specimens with a hole at the center were loaded in tensile fatigue. CFRP overlays and CFRP chopped-fiber overlays were evaluated as retrofits.	· As stress range was increased, a greater stiffness ratio was required for infinite fatigue life · Best SR = 1.0 and SR > 1.0 had limited benefits · Modulus of elasticity of the CFRP and the thickness of the overlay had significant effect on fatigue-crack propagation life

Plates under Tension Loading		impregnated CFRP plies or carbon chopped fiber		The following were evaluated: Modulus of CFRP; Thickness of CFRP; Length of CFRP overlay; Thickness of bond layer; Effect of stiffness ratio; Thickness of steel; Different stress ranges (Exp. & Numerical)	· Shear demand in resin and tensile demand in resin to steel interface were used to gauge the potential for debonding · Debonding only occurred in 1 of the 14 fatigue tests – the thickest steel plate combined with the thickest overlay.
Use of CFRP Combined with Steel Angles and Back Plate for Repairing Distortion-Induced Fatigue Damage at Cross-Frame Connection Plates	Bun, S. H. (2014). "Retrofit techniques for distortion-induced fatigue damage in steel bridge girders." M.S.Thesis, University of Kansas, Lawrence, Kansas.	Two layers of graphite fiber	West Systems two-part epoxy	A girder specimen was loaded in distortion-induced fatigue. The effectiveness of adding a layer of 1/16-in thick CFRP material to angles-back plate retrofit was investigated over a very deep web crack. (Exp. & Numerical)	· The cracks did not propagate under the retrofit · No debonding was noted.
Use of Composite Block Retrofit for Repairing Distortion–Induced Fatigue Damage at Cross-Frame Connection Plates	Bun, S., Bonet, E., Matamoros, A., Bennett, C., Rolfe, S., Barrett-Gonzalez, R. (2014). "Repair of Distortion-Induced Fatigue Damage in Steel Bridges using Composite Materials." *Proc. European Bridge Conference*, London, U.K.	Conventional mat fiberglass	West System™ two-part epoxy (West System™ 105 Epoxy Resin and West System™ 206 Slow Hardener)	A girder specimen was loaded in distortion-induced fatigue. A fiberglass composite block retrofit in the web gap region was used in conjunction with threaded rods (Exp. & Numerical)	· Significant reduction in crack growth propensity. · FRP block composite shown to significantly slow crack propagation rate but did not completely stop the crack from reinitiating · Some debonding was noted
Utilizing Fiber-Reinforced Polymers to Retrofit Steel Bridge Girders Damaged by Fatigue Loading.	Bonet, E. (2014). "Utilizing Fiber-Reinforced Polymers to Retrofit Steel Bridge Girders Damaged by Fatigue Loading." M.S. thesis, Department of Civil, Environmental, and Architectural Engineering, Univ. of Kansas, Lawrence, KS. Bun, S., Bonet, E., Matamoros, A., Bennett, C., Rolfe, S., Barrett-Gonzalez, R. (2014). "Repair of Distortion-Induced Fatigue Damage in Steel Bridges using Composite Materials." *Proc. European Bridge Conference*, London, U.K.	Chopped Carbon fiber	West Systems two-part epoxy	A girder specimen was loaded in distortion-induced fatigue. A chopped carbon fiber composite block retrofit in the web gap region was investigated when used with studs placed in the flanges of the girder. (Exp. & Numerical)	· Significant reduction in crack growth propensity · The girder was loaded under extreme levels of distortion-induced fatigue loading, but no debonding of the block was noted during testing.

Table B-2 Summary of Some of Zhao & Al Mahaidi Research (Australia-based)

Research Title	Year	Researchers	Type of Research/ method/approach	Loading Procedures or Behavior	Specimens Type/Shape	Number of Specimens	Type of Steel	Type of FRP	Type of Epoxy	Investigated Variables	Findings about Bond Behavior
Experimental Study on Bond Behavior between UHM CFRP Laminate and Steel	2010	Wu et al.	Exp.	Monotonic tension	Double strap joints (2 steel plates) 300x50x20 mm for each steel plate)	12	HA300 F_y=300 MPa	MBrace laminate *(UHM CFRP plates)*	Araldite 420 Sikadur 30	adhesives types bond length	· Failure mode for Araldite was either delamination or rupture, while for Sikadur was cohesive failure. · Araldite 420 achieved greater bond strength than Sikadur 30 in this application
Bond–slip models for double strap joints strengthened by CFRP	2010	Fawzia et al.	Exp. & Numerical	Tension	Double strap joints (2 steel plates) 400x50x10mm or 400x50x6mm for each steel plate	27	.....	Normal modulus CFRP; High modulus CFRP	Araldite 420 Sikadur 30 MBrace Saturant	adhesives types, CFRP type, CFRP layers, steel thickness, bond length	· Shear stresses decreased away from edge · Adhesive thickness affected bond-slip model proportionally · Adhesive peak strain affected only the max slip not initial slip nor shear stress
Experimental study of fatigue crack growth behaviour in adhesively reinforced steel structures	2009	Liu et al.	Exp.	Tensile fatigue	Steel plate with center hole and slots 500x90x10 mm	21	F_y =297 MPa	MBrace CF130 (normal); Mbrace CF530 (high); *both are unidirectional CFRP sheets*	Araldite 420	CFRP type, one side, two side, Patch system, thickness, length, width, and configuration	· Normal modulus CFRP, debonding failure; high modulus CFRP, fiber breakage failure · Bond width had a considerable influence of crack growth life
The Effect of Fatigue Loading on Bond Strength of CFRP Bonded Steel Plate Joints	2005	Liu et al.	Exp.	Tensile fatigue	Steel plate joints (2 steel plates) 210x50x5mm for each steel plate	12	F_y =359 MPa	MBrace CF130 (normal); Mbrace CF530 (high) *both are unidirectional CFRP sheets*	Araldite 420	CFRP type bond length CFRP layers	· Reduction in bond slip stiffness due to accumulated fatigue damage · Failure modes not affected by fatigue loading except for high-modulus CFRP
Experimental and Numerical Study on Strengthening of Steel Members Subjected to	2016	Al-Mosawe et al.	Exp. & Numerical	Quasi-static tension; High-impact tension	Double strap joints (2 steel plates) 200x40x16 mm for each steel plate	87	mild steel	MBrace laminate 460/1500 *(UHM CFRP Laminate)* (BASAF)	Araldite 420	quasi Static to dynamic high rates tensile load bond length	· Decrease in effective bond length under dynamic load · Increase in ultimate joint capacity; ultimate strain values

Impact Loading Using Ultrahigh Modulus CFRP										
Mechanical Behaviour of Normal Modulus Carbon Fibre Reinforced Polymer (CFRP) and Epoxy under Impact Tensile Loads	2011	Al-Zubaidy et al.	Exp.	Quasi-static tension; Medium-impact tension	Coupons ASTM: D3039/D 3039M-07	40	……..	MBrace CF130 (normal modulus) *unidirectional CFRP sheets*	Araldite 420	strain rates effects on tensile stress, tensile stiffness and strain at failure	· For Araldite 420, the increase in tensile stress was ~220% and the increase in modulus of elasticity was ~100%. · However, a reduction (up to 55%) in strain at failure was observed.
Experimental investigation of bond characteristics between CFRP fabrics and steel plate joints under impact tensile loads	2012	Al-Zubaidy et al.	Exp.	Static tension; Impact tension	Double strap joints (2 steel plates) 210x50x5mm for each steel plate	56	A36	MBrace CF130 (normal modulus) *unidirectional CFRP sheets*	Mbrace Saturant	Static and dynamic bond length CFRP layers	· For all loading rates, joint strength showed a higher degree of increase when the bond length was below the effective bond length. · 3 layers of CFRP showed insignificant difference in the joint capacity enhancement ratio, compared with joints with 1 CFRP ply.
Fatigue Tests of Cracked Steel Plates Strengthened with UHM CFRP Plates	2012	Wu et al.	Exp.	Tensile fatigue	Steel plate with center hole and slots 550x90x10 mm	11	300+ grade steel F_y =335 MPa	MBrace laminate 460/1500 *(UHM CFRP plates)*	Araldite 420	Bond width, length, location	· Bond length, width and location had considerable influence on the fatigue behavior of the strengthened steel plates.

Table B-3 Summary of Some Researches about Cracked Steel Plate

Research Title	Year	Researchers	Type of Research/method/approach	Loading Procedures or Behavior	Specimens Type/Shape	Specimens Number	Specimens Dimensions	Type of Steel	Type of FRP	Type of Epoxy	Investigated Variables	Measured Parameters	Interesting Findings
Effect of FRP Configurations on the Fatigue Repair Effectiveness of Cracked Steel Plates	2014	Wang et al	Numerical	Tensile Fatigue test	Steel plate with central crack	3	700x120x10 mm	E = 206 GPa; v = 0.3	orthotropic, E1 = 165 GPa; E2 = E3 = 10 GPa G12 = G13 = 5 GPa; G23 = 2.5 GPa v12 = v13 = 0.28; v23 = 0.35	G = 900 MPa; v = 0.35	FRP configuration	Stress intensity factor Crack growth life	*Applying the FRP over the crack was more effective than applying it to either end of the crack, especially as FRP thickness and initial crack length increased *A thin FRP directly over the crack is more effective if small while a thick FRP directly over the crack is more effective if large
Fatigue Behavior of Cracked Steel Plates Strengthened with Different CFRP Systems and Configurations	2016	Wang et.al	Experimental and Numerical	Tensile Fatigue test	* Steel plate with center hole and slots * Steel plate with single edge crack	6 4	* 700x120x10 mm *700x100x10 mm	Fy=385 Mpa (Q345B)	* Unidirectional pultruded CFRP plates (Sika CarboDur S514) * CFRP sheets manufactured by Mitsubishi Rayon	* Two component epoxy paste adhesive (Araldite 2015) to bond the CFRP plates *Two-component epoxy resin (Sanyu L-500) to bond the CFRP sheets	* CFRP plate vs CFRP sheet * Normal vs high modulus * CFRP configuration	* Failure mode * Crack propagation and fatigue life * Stiffness change * Effect of CFRP type, modulus and configuration	* CFRP can effectively decrease the crack growth rate and prolong the fatigue life of cracked steel plates * For the central-cracked specimens, the fatigue life can be extended by 3.5–4.9 times * For the edge-cracked specimens, the extension ratio of the fatigue life was 6.9–11.3. * Under the equivalent CFRP tensile stiffness, the repair effect of the CFRP plates was better than that of the CFRP sheets * The specimens were close to failure if an obvious decrease in stiffness was observed.
Experimental study on mixed-mode fatigue behavior of center cracked steel plates repaired with CFRP materials	2019	Chen et al	Experimental	*mixed mode I and II fatigue tests *load applied at 0, 15, and 30 degrees	* Steel plate with center hole and slots	12	500x90x8 mm	Fy = 480 Mpa E = 213 GPa	*carbon fibre FTS-C8–30 *E = 681 GPa	epoxy adhesive Araldite 420	*load application angle *initial crack length *reinforced vs unreinforced	*crack propagation *trajectory *failure mode	*CFRP repair signficantly reduced crack growth rate in all cases *increased load application angle reduced repair effectiveness *repairing specimens increased deviation angles

Fatigue Behavior of Cracked High-Strength Steel Plates Strengthened by CFRP Sheets	2016	Hu et al	Experimental	*sine cyclic loading	*Steel plate with center hole and slots	*10 unstrengthened (2 Q345, 4 Q460, 4 Q690), *9 strengthened (2 Q345, 3 Q450, 4 Q690)	*400x70 mm *Q 345 is 16 mm thick * Q460 is 12 mm thick *Q 690 is 14 mm thick	Q345, Q460, and Q690	*CFRP sheet (UM46) * E = 435 GPa	*E2500S resin *E = 2.36 Gpa	*type of steel *reinforced vs unreinforced	*Failure mode *Fatigue life	*grain refinement is effective at strengthening steel without hurting fatigue behavior *lower stress ranges cause longer fatigue life *CFRP reinforcement is efficient and effective if there is no debonding *Beach marking was effective at monitoring crack growth
Fatigue behaviour of CFRP strengthened open-hole steel plates	2017	Wang et al	Experimental and Numerical	*50kN tensile fatigue test	*steel plate with open central hole		300×30×6 mm	Fy = 388 MPa E = 2.1x10^5 Mpa	*unidirectional carbon fibre fabric UT70-30 *E = 2.52x10^5 Mpa	epoxy resin/ adhesive (Sikadur-330a)	*repaired vs unrepaired *repair method *CFRP configuration	*failure modes *local strain evolution *stiffness degradation behavior	*local debonding was more likely to occur when more layers of carbon fiber were applied *theory provided a good prediction of strain around the hole *single layer CFRP improved fatigue life by 20% while triple layer CFRP improved fatigue life by 60% *FEA was effective at predicting stress concentrations
Fatigue Behaviour of CFRP Strengthened Out-of-Plane Gusset Welded Joints with Double Cracks	2015	Yu et al	Experimental and Numerical	*tensile cyclic loading; 10 Hz	*main plate with two gusset plates; notched holes in weld toes	8	*main plate: 700x80x8 mm *gusset plates: 100x80x8 mm	Q345	*CFC3-1.2-50 *Carbolam THM450 50x1.2	Araldite 420	*stress range *single- or double-sided strengthening *modulus of CFRP materials	*failure mode *fatigue life *stress intensity factor *crack opening displacement	*the fatigue life of all specimens was significantly improved, with the high stress range specimen repaired on both sides with a high strength CFRP showing the greatest improvement *double sided repairs are most effective because secondary bending is reduced *FEA showed that crack opening displacement and stress intensity factor were reduced by repair *Numerical prediction and experimental results agree well
Fatigue behaviour of CFRP strengthened steel plates with different degrees of damage	2013	Yu et al	Experimental and Numerical	*tensile fatigue test	*steel plate with central hole and two notches	6	*500x100x8 mm	Q345	E = 1.91 x 10^2 GPa	E = 3.32 GPa	*initial crack length	*fatigue life	*CFRP repair was extremely effective at improving fatigue life of pre cracked specimens *beach marking was effective at recording crack shapes *Numerical predictions and experimental results agreed well *Early repair was found to be most effective at extending fatigue life, but repair

													was still effective at all levels of damage tested
Fatigue Performance of Tension Steel Plates Strengthened with Prestressed CFRP Laminates	2010	Huawen et al	Experimental and Numerical	*constant amplitude tensile loading at 15 Hz	*double-edge-notched steel plates	14	*1200x150x10 mm	mild carbon steel S355	E = 165 GPa	S&P Resin 220	*level of prestressing of CFRP repair *applied stress range *CFRP laminate stiffness	*fatigue life *secondary crack propagation *debonding behavior of adhesive	*Prestressing a CFRP reinforcement significantly improved the fatigue life of the steel specimens compared to non-stressed reinforcements *Theoretical predictions and experimental results were in agreement *Preempting crack development with reinforcement is most effective at prolonging fatigue life *a greater prestress level reduced debonding area by nearly 50% *A secondary crack was caused by high prestress levels
Numerical analysis of fatigue performance of CFRP–repaired steel plates with central inclined cracks	2019	Li et al	Experimental and Numerical	*tensile fatigue test	*steel plate with central hole and two angled notches	13	*700x90x8 mm	E = 205.35 GPa, Fy = 372 MPa	CFRP strand sheets, FSS-HM-900	FB-E9S(ST) adhesive	*initial crack inclination angle	*stress intensity factor *fatigue life	*Crack inclination angle had no significant effect on fatigue life below an angle of 70 degrees for unrepaired specimens and 60 degrees for double sided repaired specimens. *The fatigue life of specimens with different angles were largely determined early on in crack propagation *Tail slots in front of the crack tips only reduced the effects of KII early on in crack propagation *CFRP repair significantly increased fatigue life in all cases

Progressive damage modeling in fiber-reinforced materials	2007	Lapczyk and Hurtado	Numerical		*GLARE material		*300x50x1.406 mm	aluminum, isotropic elastic–plastic with isotropic hardening	E = 55000 MPa	E = 2000 MPa	*failure mode (fiber tension, fiber compression, matrix tension, and matrix compression)	*Behavior of elastic-brittle materials that fail without showing major plastic deformation	*a model predicting four different failure modes in elastic-brittle materials is presented and applied to an example finite element model of a blunt notched GLARE specimen *Numerical results from this study agree well with experimental results of a related study.
Strength prediction in CFRP woven laminate bolted single-lap joints under quasi-static loading using XFEM	2014	Ahmad et al	Experimental and Numerical	*Increasing tensile load until carbon fiber laminate failure	CFRP strip with a bolt hole	table 2 shows 48 configurations tested 3 times each but the conclusion mentions 72 configurations	*varying sizes	specimens secured to high yield strength stainless steel, but steel not tested	Toray T300 high strength carbon fibres (plain weave and five harness satin weave)	Vantico MY750	*type of carbon fiber laminate being tested (two-layer cross-ply plain weave, four-layer cross-ply plain weave, two-layer cross-ply five harness satin weave, four-layer five harness satin weave, four-layer quasi-isotropic plain weave, eight-layer quasi-isotropic plain weave, twelve layer quasi-isotropic five harness satin weave) *hole diameter *clamp torque *width of specimen/hole diameter	*bearing stress at failure *failure behavior *analytical model's agreement with experiment	*net-tension failures were likely to occur at low values of W/d while bearing or pull-through failures were more likely to occur at higher values *Five-harness satin weave specimens demonstrated lower bolted joint strengths than plain weave or cross ply weave specimens *applied bolt clamping torque affects transition values of W/d *Finite element model predictions agreed within 15% of experimental values about 60% of the time

Tensile behaviour of open-hole and bolted steel plates reinforced by CFRP strips	2016	Wang et al	Experimental and Numerical	*increasing tensile load until failure	*Steel plate with central bolt hole; reinforced by CFRP and bolted washer clamp up	39	*300x30 mm *various thicknesses	steel conforming to Chinese standards GB/T700 [23] and GB/T1591	carbon fiber UT70-30, manufactured by Toray Industries, Inc	Sikadur-330 epoxy resin	*CFRP layers *Bolt torque *washer length	*failure mode	*Unreinforced specimens deform plastically, while reinforced specimens' primary failure modes are adhesive failure or CFRP rupture *additional CFRP layers increase the specimen's tensile strength linearly while decreasing deformability along a second order polynomial. *The interface between the steel and CFRP was prone to failure under tensile load *The washer clamp up process increased the specimen's strength. *Longer washers reduce deformability linearly. *Increased bolt torque significantly enhanced strength. *The model developed agreed well with experiment.

Table B-4 Summary of Various Adhesives & Research Applications

Manufacturer	Type	Tensile Strength (psi)	Tensile Modulus (psi)	Elongation %	Shear Strength (psi)	Shear Modulus (psi)	Peel Strength	Working Time (Pot Life) or Gel time	Viscosity (cp)	Notes	References
FYFE Tyfo	Tyfo S (Saturant Epoxy)	10,500	461,000	5				3-6 hrs	600-700	· Provide wet lay up	
	Tyfo TC Epoxy -Tack coat)	3,285	174,000	1.88				1-2 hrs	55,000	· Vertical and overhead application	
	Tyfo TC-1 (Tack coat)	2,408		8.9				0.5-1 hr	46,000	· Vertical and overhead application	
	Tyfo MB-3 (High performance adhesive)	3,285	174,000	1.88				1-2 hrs	55,000	· Metals; vertical and overhead application	Abd El-Meguid, Alabama
BASF	BASF, MBRACE Saturant	8,000	440,000	3.5				15-200 min	900-2,500	· Can be used for vertical, overhead, steel	Zhao and AlMahaidi group, Australia
HUNTSMAN	Araldite 420 A/B	4,206	216,831	4.6	4,351	105,878		60 min	35,000-45,000	· Very high lap shear and peel strength; · Extremely tough and resilient · Structural applications	Zhao and AlMahaidi group, Australia The US version of Araldite 420 A/B, H. Al-Salih / C. Bennett, U. Kansas
	Epibond 420 A/B	5,200	238,000	4.2	4,500			70 min	Semi-paste	· High shear and good peel strength · Extremely tough and resilient	
Loctite	Loctite Hysol 9412				4,000		35	65min	600-900	· Low viscosity, self-leveling, flowable	B. Kaan / F. Alemdar / C. Bennett, U. Kansas
West System	West System (105 Epoxy Resin/206 Slow Hardener)	7,300	460,000	4.5				20-25min	725	· Coating, bonding applications	S. Hak Bun (block glass fiber); S. Hak Bun (pre-preg graphite fiber, E. Bonet (chopped fiber block), U. Kansas
Sika	SikaFast -3131S	1,300	14,500	50				7 min	150,000-350,000	· High ductility paste · Bonding sidewall panels, roofs, floors, aluminum, steel, fiber reinforced polymers	K. Ghahremani / S. Walbridge, U. Waterloo
	Sikadur 30	3,600	650,000	1	3,600			70 min	Non-sag paste	· High modulus, high strength paste · Bonding composite laminate · Bonding steel to concrete · Vertical and overhead applications	
	Sikadur 300	8,000	250,000	3				long	500	· High modulus, high strength · Used as pre-preg resin · Excellent adhesion to metals	
	Sikadur Hex 300	7,500	280,000	3.2				3-4 hrs	500-750	· High modulus, high strength · Used as pre-preg resin	

						• Excellent adhesion to metals
Sikadur 301	8,000	290,000	3.5	40 min	2,700	• High modulus, high strength • Used as pre-preg resin • Excellent adhesion to metals
Sikadur 330 US	4,900	-----	1.2	57 min	Non-sag paste	• High modulus, high strength • Used as pre-preg resin • Excellent adhesion to metals
Sikadur 340	5,580	270,000	1.5	90 min	300-500	• High modulus, high strength • Primer with presaturated system • Excellent adhesion to metals

Appendix C: **Parametric Analysis Results**

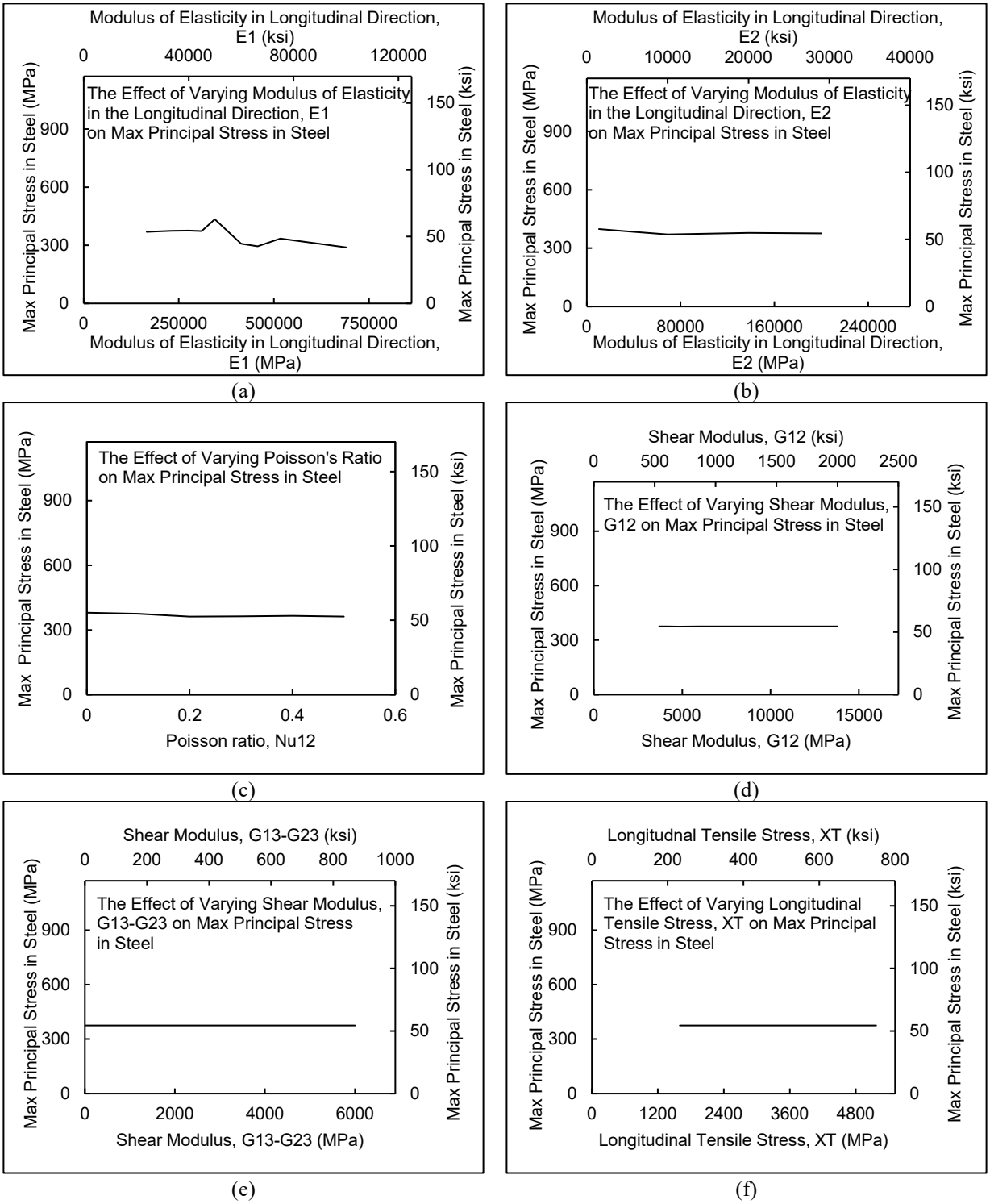

Figure C-1 Effect of CFRP elastic and damage parameters on the maximum principal stress in steel plate: (a) Modulus of elasticity in longitudinal direction; (b) Modulus of elasticity in transverse direction; (c) Poisson ratio; (d) Shear modulus, G12; (e) Shear modulus G13=G23; (f) Longitudinal tensile strength

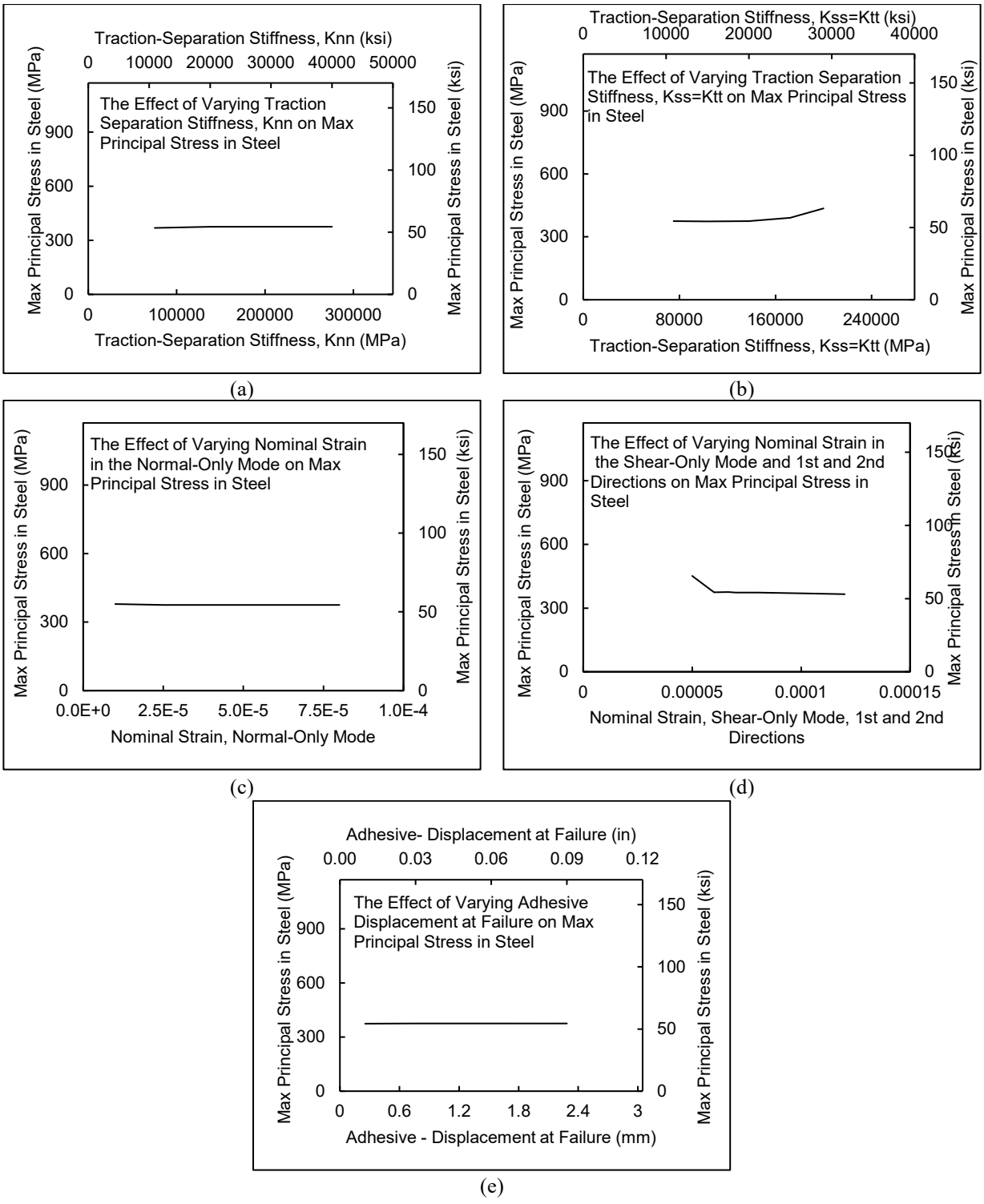

Figure C-2 Effect of adhesive elastic and damage parameters on the maximum principal stress in steel plate: (a) Traction- separation stiffness, normal (initial slop of bond separation curve); (b) Traction separation stiffness,1st and 2nd (initial slop of bond slip curve); (c) Normal Strain Normal Mode Only; (d) Normal Strain Shear-Only Mode (1st Direction= 2nd Direction); (e) Displacement at Failure

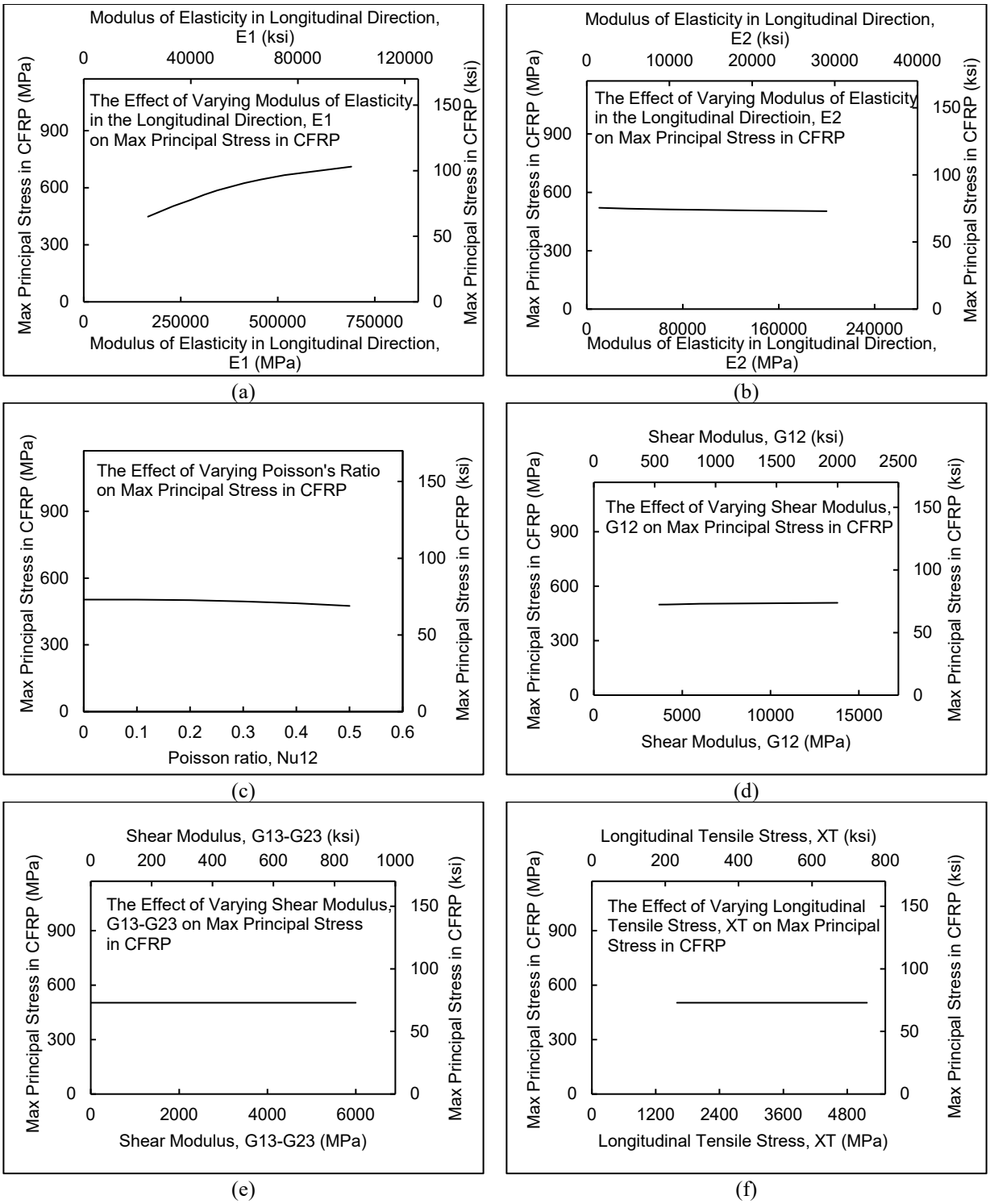

Figure C-3 Effect of CFRP elastic and damage parameters on the maximum principal stress in CFRP: (a) Modulus of elasticity in longitudinal direction; (b) Modulus of elasticity in transverse direction; (c) Poisson ratio; (d) Shear modulus, G12; (e) Shear modulus G13=G23; (f) Longitudinal tensile strength

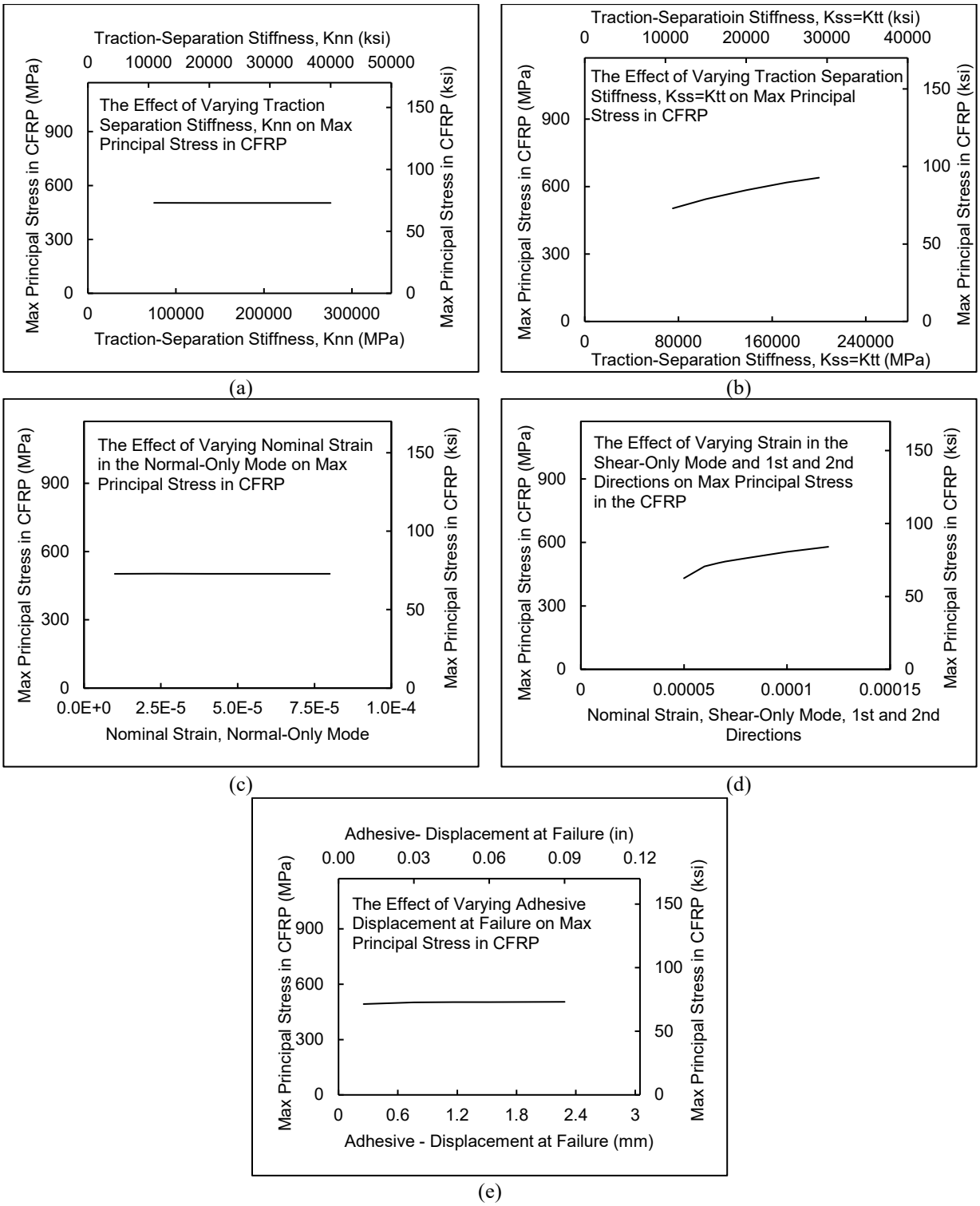

Figure C-4 Effect of adhesive elastic and damage parameters on the maximum principal stress in CFRP: (a) Traction- separation stiffness, normal (initial slop of bond separation curve); (b) Traction separation stiffness,1st and 2nd (initial slop of bond slip curve); (c) Normal Strain Normal Mode Only; (d) Normal Strain Shear-Only Mode (1st Direction= 2nd Direction); (e) Displacement at Failure

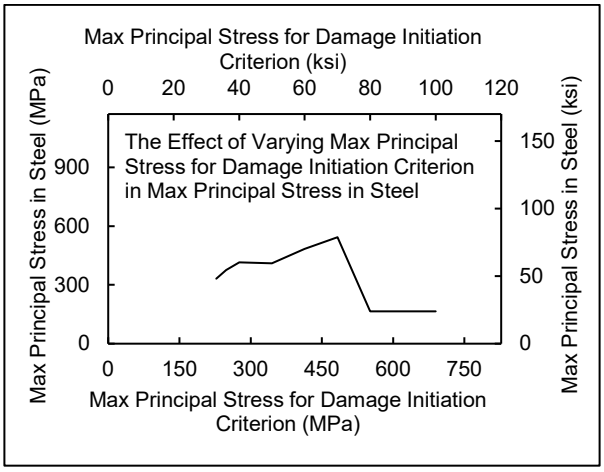

(a)

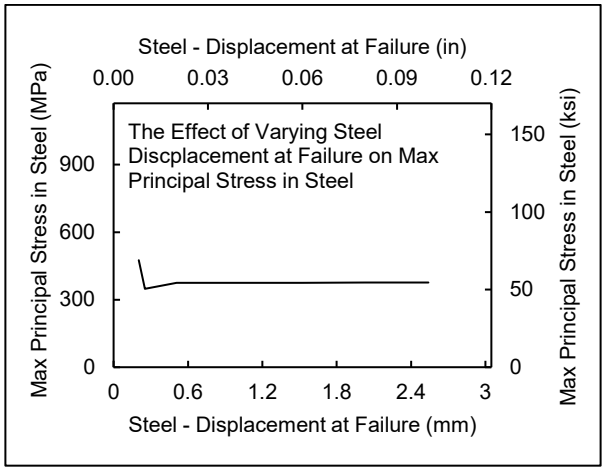

(b)

Figure C-5 Effect of steel damage parameters on the maximum principal stress in steel plate: (a) Max principal stress at damage initiation, (b) Displacement at failure at damage evolution

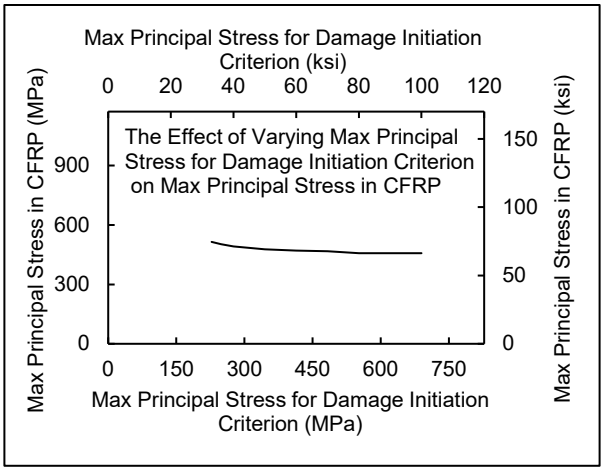

(a)

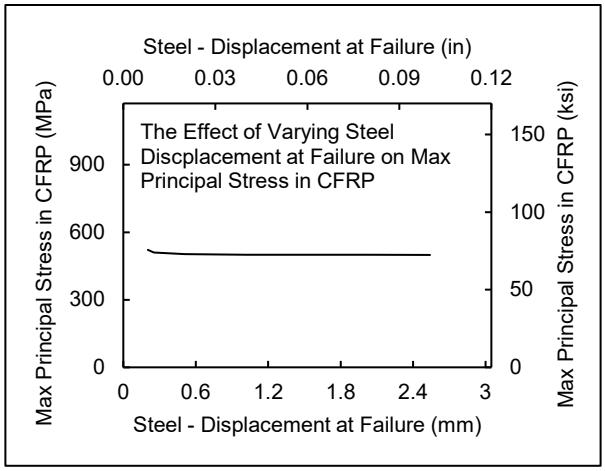

(b)

Figure C-6 Effect of steel damage parameters on the maximum principal stress in CFRP: (a) Max principal stress at damage initiation, (b) Displacement at failure at damage evolution

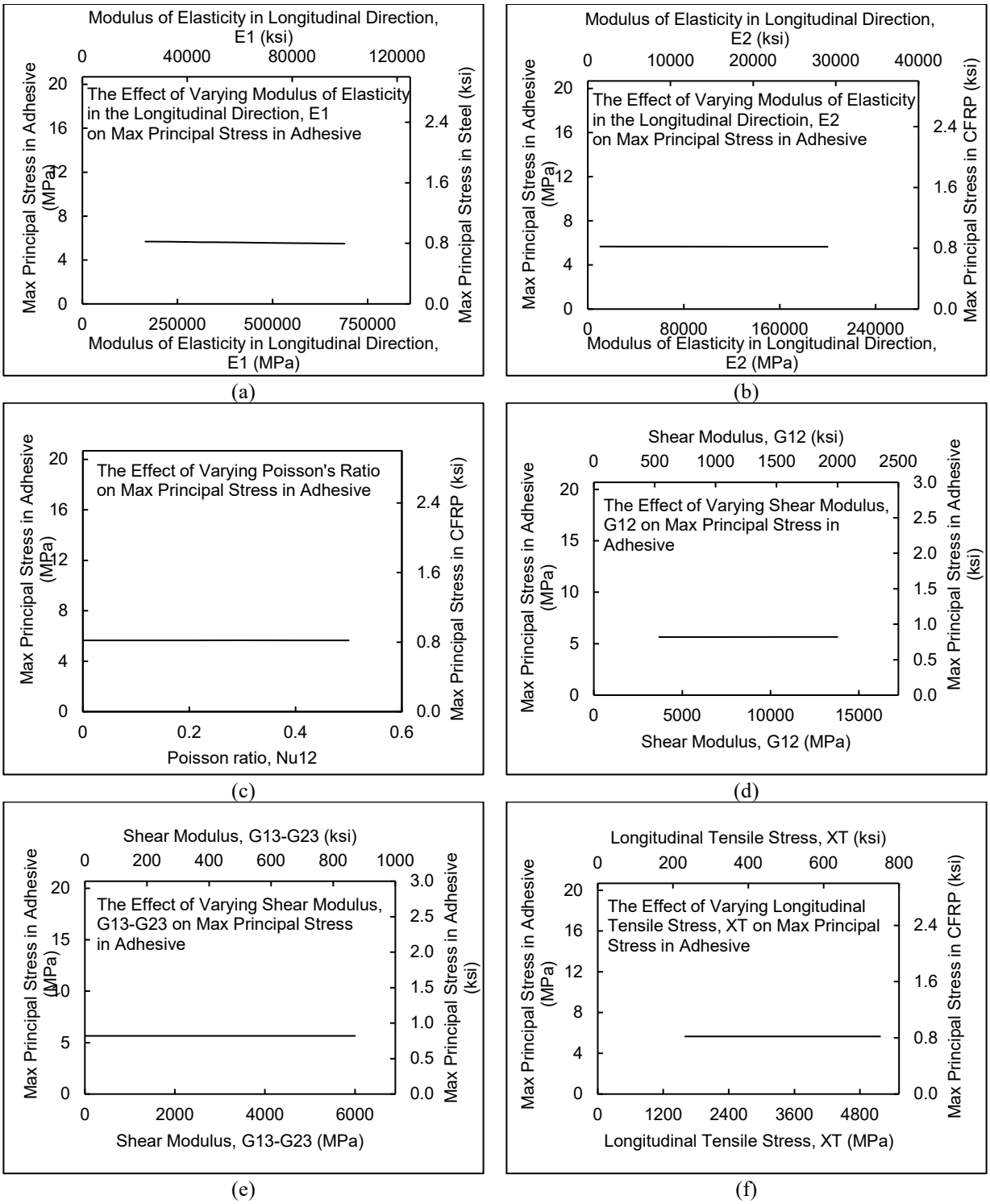

Figure C-7 Effect of CFRP elastic and damage parameters on the maximum principal stress in Adhesive: (a) Modulus of elasticity in longitudinal direction; (b) Modulus of elasticity in transverse direction; (c) Poisson ratio; (d) Shear modulus, G12; (e) Shear modulus G13=G23; (f) Longitudinal tensile strength

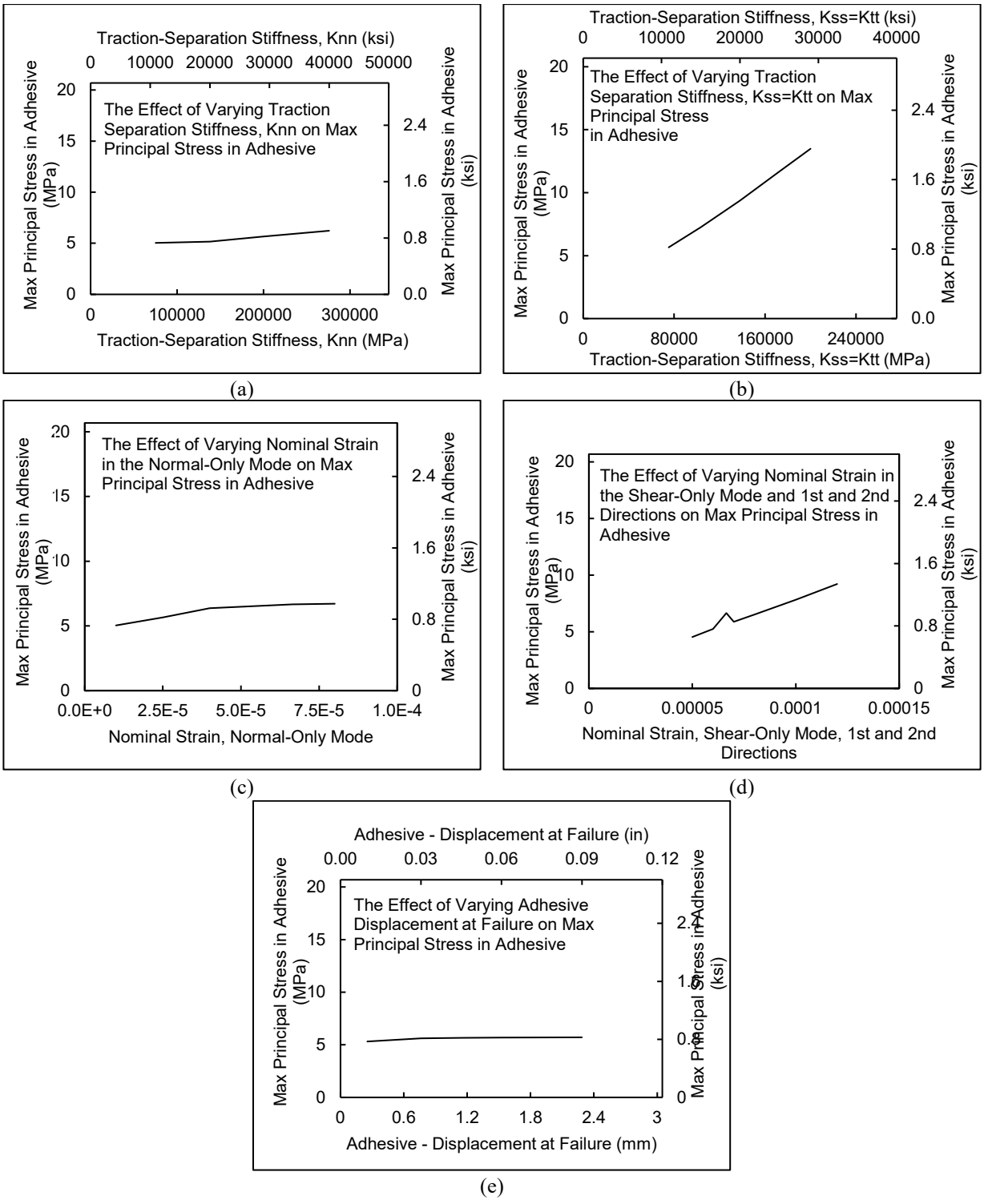

Figure C-8 Effect of adhesive elastic and damage parameters on the maximum principal stress in Adhesive: (a) Traction- separation stiffness, normal (initial slop of bond separation curve); (b) Traction separation stiffness,1st and 2nd (initial slop of bond slip curve); (c) Normal Strain Normal Mode Only; (d) Normal Strain Shear-Only Mode (1st Direction= 2nd Direction); (e) Displacement at Failure

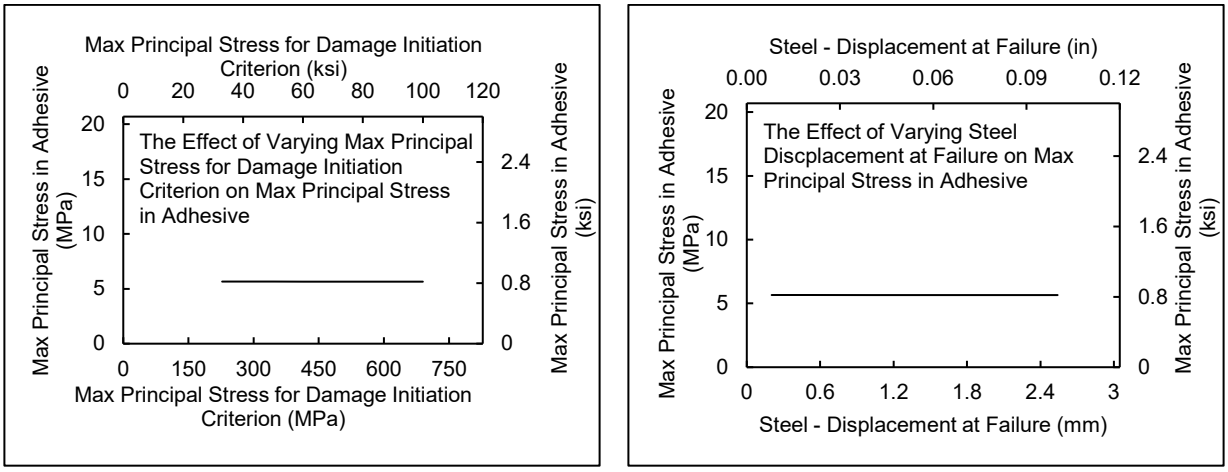

(a) (b)

Figure C-9 Effect of steel damage parameters on the maximum principal stress in Adhesive: (a) Max principal stress at damage initiation, (b) Displacement at failure at damage evolution